Cambridge University

Doctoral Thesis

On the Simulation of Boson Stars in General Relativity

Author: Robin Croft

Supervisor: Dr. Ulrich Sperhake

UNIVERSITY OF CAMBRIDGE

Contents

Chapter 1

Introduction to Differential Geometry and General Relativity

1.1 Introduction

1.1.1 Introduction to General Relativity

general gr shit? mention einstein derivation (hilbert derivation a potentially earlier but vacuum), karl schwarzshild (ironicaly meaning black shield), then low mass limit, photon deflection and mercury perihelion around sun. mention cosmology, gravitational waves, more black holes, minkowski. more compact objects.

The modern theory of gravity, published by Albert Einstein in 1915, is general relativity (GR). It is a geometric theory relying on curved spaces and differential geometry. GR is a generalisation of Einstein's theory of special relativity (SR) to include matter and gravity. Where the main idea behind SR was that the laws of physics are identical in any non-accelerating frame, GR includes the gravitational force (and subsequently matter) by postulating that the laws of phsyics are identical in any free-falling frame. In a universe without gravity or matter, also called a vaccum universe, GR is equivalent to SR.

GR also supercedes Newton's theory of gravity when gravity becomes stronger. In Newtonian theory, two masses orbit each other in a constant circle or ellipse; the ellipses can precess in the presence of extra masses. However, the calculated precession rate of Mercury about the sun using Newton's theory of gravity was much to slow; Einstien correctly calculated the precession rate using GR. This initial success proved to the world that Einstein's theory was the best current describtion of gravity. In the weak gravity limit, GR perfectly replicates Newton's theory of gravity; the precession of Mercury is the most stark deviation from Newton's theory as it is closest to the sun where gravity is the strongest.

Other new effects predicted by GR including gravitational time dilation and light ray deflection. Gravitational time dilation is similar to time dilation in SR which states that an observer at rest would age more quickly (in their own frame) compared to a quickly moving observer. Gravitational time dilation states that an observer in a stronger gravitational field will age slower than one in a weaker gravitational field; this effect has been verified by comparing two atomic clocks where one is left on the surface of the earth and one is elevated. Light ray deflection occurs when a beam of light passes close by an object with a strong gravitational field - the stronger the field the more the light beam is deflected. This can be seen when distant bright objects pass behind matter, for example black holes or even the sun.

In the moderately strong gravity regime, Newtons theory starts to become quite innacurate. After many orbits of two (or more) heavy objects the time averages separtion can be seen to decrease, hence the objects are inspiralling. The orbital energy lost is released as a gravitational wave (GW) signal. Inspiralling and radiation becomes more pronounced at lower separtions and with heavier objects. If the inspiralling becomes significantly fast compared to an orbit time, then Newton's theory of gravity can fail to accurately simulate the binary; approxiations to GR can be used in this regime, for example post newtonian (PN) theory.

In the strong gravity regime GR deviaties entirely from Newtonian theory leading to a plethora of exotic results. One example is the neutron star (NS), an object so dense that all of the electons in an atom are forced to combine with nearby protons and reduce all matter to a dense lattice of neutrons. The gravitational field on the surface of a NS is of order 10^{11} times stronger than on earth. Another example is the black hole (BH), an even denser object with such a strong gravitational pull that even light cannot escape. These dense objects can be produced by the collapse of large dying stars, implosions of supernovae, and collisions of very dense objects.

At the centre of a black hole, GR predicts a singularity; a single infinitely dense point surrounded by vacuum. it is presumed that Einstein's theory breaks down towards a singularity which is deemed unphysical. Theories such as loop quantum gravity (LQG) and string theory (ST) try to reconcile GR with quantum mechanics which is thought might aleviate this problem. Sadly there is no definive answeras to what happens near a gravitational singularity, this is in part due to the lack of experimental data to draw from. The weak cosmic sensorship hypothesis states that all physical singularities are hidden inside an event horizon; a surface which contains all points that are cannot send information to an observer infinitely far away in the infinite future. This is called causally disconnected.

Black holes in the universe generally spin, this is due to any black hole forming from the collapse of matter will inherit the angular momentum of the matter as it collapses. Rotating black holes were first described by Roy Kerr in 1963, and therefore are called Kerr black holes. The collisions of black holes (with or without spin) is also successfully described by GR, however this phenomenon is far too complicated to solve analytically. Numerical relativity (NR), the exact simulation of GR using methods to solve partial differential equations (PDEs), is needed to describe black hole collisions and inspirals.

GR also describes physics at the largest scales, not just compact regions and objects as discussed so far. The application of GR to the entire universe is called Cosmology. Cosmology can be used to describe the big bang, early universe expansion, and late universe inflation. Cosmology can also be used to describe a universe with small matter and gravitational perturbations ontop of a uniform background, this is the best current description of the universe.

One final noteworthy prediction of GR is gravitational waves (GWs). In 2015 GWs were detected by the Laser Interferometer Gravitational-Wave Observatory (LIGO) which lead to the 2017 nobel prize in physics. Many subsequent signals from inspiralling black hole-black hole and black hole-neutron star inspirlas have been measured which agree with the waveforms predicted by NR simulations and PN theories.

1.1.2 Introduction to Compact Objects and Boson Stars

The first non-trivial solution to Einstein's equation found was that of the spherically symmetric, static and asymptotically flat vacuum spacetime by Karl Schwarzschild in 1916. The solution was designed to be used outside a spherically symmetric, non-spinning, body of mass; however it turned out to provide use in describing black holes. This metric was then modified by Tolman, Oppenheimer and Volkov in 1939 to describe the non-vacuum case of a constant density neutron star. This turned out to give an unphysical estimate of $0.7M_{\odot}$ for the upper limit of neutron star mass due to the equation of state.

The study of compact exotic objects can be traced back to John Wheeler who investigated Geons in 1955 for their potential similarity to elementary particles. Geons are gravito-electromagnetic objects with the name arising from "gravitational electromagnetic entity". In 1968 David Kaup published [] describing what he called "Klein-Gordon Geons", nowadays referred to as boson stars. Importantly, boson stars are a localised complex Klein-Gordon configuration, with the real counterparts being unstable. Many variants such as (Spin 1) proca stars [], electromagnetically charged boson stars and many others have been studied.

Interest in boson stars remains for many reasons. Given the recent discovery of the higgs boson, we know that scalar fields exist in nature and any gravitational wave signals created by compact objects could theoretically be detected with modern gravitational wave interferometers. Secondly, boson stars are a good candidate for dark matter haloes. Boson stars are also useful as a proxy to other compact objects in general relativity; there is a lot of freedom in the construction of different types of boson star and they can be fine tuned to model dense neutron stars for one example. The advantage this would have over simulating a real fluid is that the Klein Gordon equation is linear in the principal part meaning smooth data must always remain smooth; thus avoiding shocks and conserving particle numbers relatively well with less sophisticated numerical schemes.

On a slightly different topic, collisions of boson stars could be a natural method to produce scalar hair around black holes which will be discussed later in more detail. [CHECK THIS IS DISCUSSED]

1.1.3 Conventions

Throughout this thesis physical quantities will be expressed as a dimensionless ratio of the Planck length, time and mass L_{pl}, T_{pl} and M_{pl} respectively; consequently the constants c, G and $\hbar$ evaluate numerically to 1. As an example, Newtons equation of gravity would be recast like

$$F = \frac{GMm}{r^2} \rightarrow \left(\frac{F}{F_{pl}}\right) = \frac{\left(\frac{M}{M_{pl}}\right)\left(\frac{m}{M_{pl}}\right)}{\left(\frac{r}{L_{pl}}\right)^2} \tag{1.1.1}$$

where $F_{pl} = M_{pl}L_{pl}T_{pl}^{-2}$ is the Planck force. $c = G = \hbar = 1$, unless stated otherwise. The metric signature will always be $(-,+,+,+)$.

Tensors and tensor fields will be denoted using bold font for index free notation and normal font for the components. The dot product between two vectors or vector fields will be written interchangeably as $\boldsymbol{A}\cdot\boldsymbol{B} \leftrightarrow A_\mu B^\mu$ for readability. Additionally, ∇_μ denotes the covariant derivative and ∂_μ is the partial derivative, both with respect to coordinate x^μ.

When considering the ADM decomposition, as in [REF SECT], objects can be associated with both the 3+1 dimensional manifold $\mathcal{M}$ or the 3 dimensional hypersurface Σ. To differentiate here, standard Roman letters such as R represent the object belonging to $\mathcal{M}$ and calligraphic letters such as $\mathcal{R}$ correspond to the projected object belonging to Σ. [MAYBE JUST REMOVE THIS BIT AND MAKE IT OBVIOUS IN THE ACTUAL 3+1 SECTION].

Finally, unless stated otherwise, Greek indices such as $\{\alpha,\beta,...,\mu,\nu,...\}$ label four dimensional tensor components whereas late Latin indices such as $\{i,j,k,...\}$ label three dimensional tensor components and early Latin indices such as $\{a,b,...\}$ label two dimensional ones. When the index range is unspecified and unimportant Greek letters will also be used.

EINSTEIN SUMMATION CONV

make explicit th inner product, dot product, outer product (otimes) and wedge product (for forms, antisymm)

Conventions (from q)

Throughout this work the metric has sign $\{-,+,+,+\}$ and physical quantities will be expressed as a dimensionless ratio of the Planck length L_{pl}, time T_{pl} and mass M_{pl} unless stated otherwise; for example Newtons equation of gravity would be written as

$$F = \frac{GMm}{r^2} \quad \rightarrow \quad \left(\frac{F}{F_{pl}}\right) = \frac{\left(\frac{M}{M_{pl}}\right)\left(\frac{m}{M_{pl}}\right)}{\left(\frac{r}{L_{pl}}\right)^2}, \tag{1.1.2}$$

where $F_{pl} = M_{pl}L_{pl}T_{pl}^{-2}$ is the Planck force. Consequently c, G and $\hbar$ take the numerical value of 1. Additionally, tensor fields will be denoted using bold font for index free notation and normal font for the components. The dot product between two vector fields will be written interchangeably as $\boldsymbol{A}\cdot\boldsymbol{B} \leftrightarrow A^\mu B_\mu$ for readability. Additionally, ∇_μ denotes the covariant derivative and ∂_μ is the partial derivative, both with respect to coordinate x^μ. Finally, unless stated otherwise, Greek indices such as $\{\alpha,\beta,...,\mu,\nu,...\}$ label four dimensional tensor components whereas late Latin indices such as $\{i,j,k,...\}$ label three dimensional tensor components and early Latin indices such as $\{a,b,...\}$ label two dimensional ones.

PROBABLY DELETE THIS

1.2 Differential Geometry

1.2.1 Introduction to Geometry and Manifolds

Everyones first encounter with geometry will cover Pythagoras' theorem; arguably the most famous and useful equation in existance. Pythagoras' equation relates the sidelengths of a right angled triangle, it says that $s^2 = x^2 + y^2$ for a triangle with height y, width x and hypotenuse length s. This can be shown very simply by looking at Fig. 1.1. The area of the partially rotated square is s^2, but we can also calculate it from the the area of the larger square A_{sq} and subtracting four times the area of one of the triangles A_{tr}. Given that $A_{sq} = (x+y)^2$ and $A_{tr} = \frac{1}{2}xy$, then

$$s^2 = (x+y)^2 - 2xy = x^2 + y^2, \tag{1.2.1}$$

and we have proved Pythagoras' theorem. Using an infinitessimally small triangle, we can write $\mathrm{d}s^2 = \mathrm{d}x^2 + \mathrm{d}y^2$ and this can be trivially extended to arbitrary dimensions like

$$\mathrm{d}s^2 = \mathrm{d}x^2 + \mathrm{d}y^2 + \mathrm{d}z^2 + ... \;. \tag{1.2.2}$$

The infinitessimal form of Pythagoras' theorem is very powerful as it can be used to calculate the length of a generic curve by approximating the curve as a collection of infinitessimally small straight lines with length $\mathrm{d}s$. So far we have assumed that space is flat meaning Eq. (1.2.2) is true for all points in space, this is an assumpion we will have to drop if we want to study the curved spaces arising in strong gravity. In the next sections we will explore the generalisation of Pythagoras' equation to curved spaces and use it to measure curve lengths answell as volumes and areas.

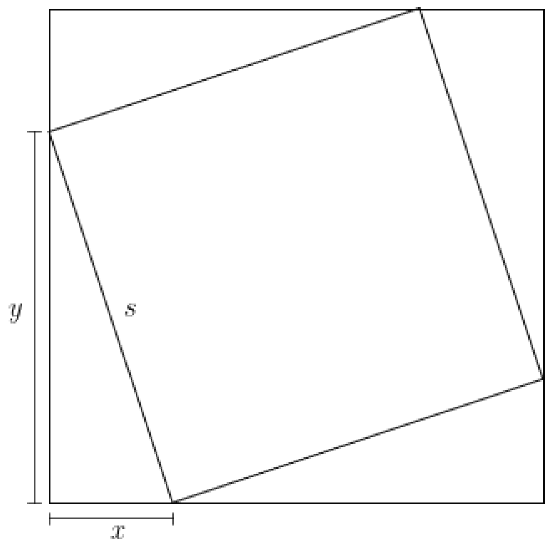

Figure 1.1: Diagram for proof of Pythagoras' theorem.

Differential Geometry (DG) is the extension of calculus, linear algebra and multilinear algebra to curved geometries. Einstein's Theory of Relativity is written using the language of DG as it is the natural way to deal with curves, tensor calculus and differential tensor equations in curved spaces. For a basic introduction to DG, we should start with a manifold $\mathcal{M}$ which is an N dimensional space that locally looks like $\mathbb{R}^N$, N dimensional Euclidean space. This is important as at a point $p \in \mathcal{M}$ we can find infinitesimally close neighbouring points $p + \delta p \in \mathcal{M}$. In the following sections we will explore curves, functions, tensors and calculus on manifolds using DG.

1.2.2 Functions, Curves and Tensors on Manifolds

A real scalar function f over $\mathcal{M}$ maps any point $p \in \mathcal{M}$ to a real number, denoted $f : p \to \mathbb{R}$. An important example of a set of scalar functions is the coordinate system ϕ, $\phi : p \to \mathbb{R}^N$, this is normally written x^μ where $\mu \in \{0, 1, ..., N-1\}$ is an index labelling the coordinate. The map ϕ is called a chart, and unlike Euclidean space one chart may not be enough to cover the entire manifold; in this case a set of compatible charts should be smoothly joined, collectively known as an atlas.

Now that functions have been discussed, the next simplest object we can discuss is a curve, or path, through $\mathcal{M}$. A curve Γ is a set of smoothly connected points $p(\lambda) \in \mathcal{M}$ that smoothly depend on an input parameter $\lambda \in [\lambda_0, \lambda_1]$. This can be expressed in terms of coordinates as $x^\mu(\lambda)$ where $\phi : p(\lambda) \to x^\mu(\lambda)$. Differentiating a function f along Γ with respect to λ gives

$$\frac{\mathrm{d}}{\mathrm{d}\lambda} f(x^\mu(\lambda)) = \frac{\mathrm{d}x^\nu}{\mathrm{d}\lambda} \frac{\partial f(x^\mu)}{\partial x^\nu} = \frac{\mathrm{d}x^\nu}{\mathrm{d}\lambda} \partial_\nu f, \tag{1.2.3}$$

where the Einstein summation convention was invoked, summing over all values of ν, and $\partial_\nu = \partial/\partial x^\nu$. Equation (1.2.3) was derived independantly of the choice of f, therefore we can generally write

$$\frac{\mathrm{d}}{\mathrm{d}\lambda} = \frac{\mathrm{d}x^\nu}{\mathrm{d}\lambda} \partial_\nu. \tag{1.2.4}$$

The operator $\mathrm{d}/\mathrm{d}\lambda$ can act on any function f and return a new function $\tilde{f}$ over $\mathcal{M}$, this is written as $\mathrm{d}/\mathrm{d}\lambda(f) = \tilde{f}$ where $\tilde{f} : p \to \mathbb{R}$ for $p \in \mathcal{M}$. We can also think of $\mathrm{d}/\mathrm{d}\lambda$ as a vector $\boldsymbol{X}$ with components $X^\mu = \mathrm{d}x^\mu/\mathrm{d}\lambda$ and basis vectors $\boldsymbol{e}_\mu := \partial_\mu$ taken from Eq. (1.2.4). The vector $\boldsymbol{X}$ can be written as $\boldsymbol{X} = X^\mu \boldsymbol{e}_\mu$ and can act on a general function f over $\mathcal{M}$ as $\boldsymbol{X}(f) = X^\mu \boldsymbol{e}_\mu(f) = X^\mu \partial_\mu f$. Considering the set of all possible curves through a points $p \in \mathcal{M}$, the tangent vector components $\mathrm{d}x^\mu/\mathrm{d}\lambda$ span an N dimensional space with basis $\boldsymbol{e}_\mu = \partial_\mu$; this space is called the tangent space and is denoted as $\mathcal{T}_p(\mathcal{M})$ at a point $p \in \mathcal{M}$.

The next object to discuss is the co-vector which is defined as a map from vectors to real numbers; not to be confused with the dot product in section 1.2.3. Similarly to vectors, a co-vector $\boldsymbol{\omega}$ can be expressed as a sum of components ω_μ and basis co-vectors $\boldsymbol{\theta}^\mu$ like $\boldsymbol{\omega} = \omega_\mu \boldsymbol{\theta}^\mu$. Contrary to vectors, co-vector components have downstairs indeces and the basis has upstairs indeces; this choice improves the readability of tensor equations when working with components. A co-vector can map a vector to a real number like $\boldsymbol{\omega} : \boldsymbol{X} \to \mathbb{R}$ or $\boldsymbol{\omega}(\boldsymbol{X}) \to \mathbb{R}$. Vectors are equally able to map co-vectors to real numbers, denoted as $\boldsymbol{X} : \boldsymbol{\omega} \to \mathbb{R}$. Co-vectors are defined such that $\boldsymbol{\theta}^\mu : \boldsymbol{e}_\nu = \delta^\mu_\nu$ where δ^μ_ν are the components of the Kroneka delta equating to zero unless $\mu = \nu$ in which case they are one. The operation of a generic co-vector $\boldsymbol{\omega}$ on a generic vector $\boldsymbol{X}$ is

$$\boldsymbol{\omega} : \boldsymbol{X} = \omega_\mu X^\nu \boldsymbol{\theta}^\mu : \boldsymbol{e}_\nu = \omega_\mu X^\nu \delta^\mu_\nu = \omega_\mu X^\mu \in \mathbb{R}. \tag{1.2.5}$$

This map is linear and identical under reversing the order of operation; $\boldsymbol{\omega} : \boldsymbol{X} = \boldsymbol{X} : \boldsymbol{\omega}$. Similarly to vectors, the set of all possible co-vectors at a point $p \in \mathcal{M}$ span an N-dimensional space called the co-tangent space, written as $\mathcal{T}^*_p(\mathcal{M})$.

Multilinear Maps and Tensors

Generalising the previous linear maps between vectors and co-vectors gives the multilinear map. Consider a tensor $\boldsymbol{T}$, this can be expressed in component form like

$$\boldsymbol{T} = T^{\alpha\beta,...}_{\mu\nu,...} \boldsymbol{e}_\alpha \otimes \boldsymbol{e}_\beta \otimes ... \otimes \boldsymbol{\theta}^\mu \otimes \boldsymbol{\theta}^\nu \otimes ... \tag{1.2.6}$$

for an arbitrary number of outer products of vector and co-vector bases. A tensor with m co-vector bases and n vector bases is called an (m, n) tensor and has a rank of $m + n$. Vectors, co-vectors and scalars are $(1, 0)$, $(0, 1)$ and $(0, 0)$ tensors respectively. Tensors can act as multilinear maps between tensors. We have already seen how a vector and co-vector can map each other to a scalar, let's extend this with an example. An $(0, 2)$ tensor, $\boldsymbol{T} = T_{\mu\nu} \boldsymbol{\theta}^\mu \otimes \boldsymbol{\theta}^\nu$ at $p \in \mathcal{M}$, can map two vectors $\boldsymbol{X}$ and $\boldsymbol{Y}$ to a scalar as shown,

$$\begin{aligned}
\boldsymbol{T}(\boldsymbol{X},\boldsymbol{Y}) &= T_{\mu\nu}X^{\alpha}Y^{\beta}\boldsymbol{\theta}^{\mu}\otimes\boldsymbol{\theta}^{\nu}(\boldsymbol{e}_{\alpha},\boldsymbol{e}_{\beta}), && (1.2.7)\\
&= T_{\mu\nu}X^{\alpha}Y^{\beta}(\boldsymbol{\theta}^{\mu}:\boldsymbol{e}_{\alpha})(\boldsymbol{\theta}^{\nu}:\boldsymbol{e}_{\beta}), && (1.2.8)\\
&= T_{\mu\nu}X^{\alpha}Y^{\beta}\delta^{\mu}_{\alpha}\delta^{\nu}_{\beta}, && (1.2.9)\\
&= T_{\mu\nu}X^{\mu}Y^{\nu}. && (1.2.10)
\end{aligned}$$

The multilinear map can also output generic tensors, for example consider

$$\boldsymbol{T}(\boldsymbol{X},\star) = T_{\mu\nu}X^{\alpha}(\boldsymbol{\theta}^{\mu}:\boldsymbol{e}_{\alpha})\boldsymbol{\theta}^{\nu} = T_{\mu\nu}X^{\mu}\boldsymbol{\theta}^{\nu}, \tag{1.2.11}$$

which uses the $(0,2)$ tensor $\boldsymbol{T}$ to map the vector $\boldsymbol{X}$ to a co-vector $\boldsymbol{W}$ with components $W_{\mu} = T_{\mu\nu}X^{\mu}$.

One final example of a mapping is from a single tensor to a lower rank tensor, this is called contraction. To illustrate this, let's take a $(1,3)$ tensor $\boldsymbol{Z} = Z^{\alpha}{}_{\mu\nu\rho}\boldsymbol{e}_{\alpha}\otimes\boldsymbol{\theta}^{\mu}\otimes\boldsymbol{\theta}^{\nu}\otimes\boldsymbol{\theta}^{\rho}$. We can choose to use the basis vector $\boldsymbol{e}_{\alpha}$ to act on any of the three co-vector bases, choosing $\boldsymbol{\theta}^{\mu}$ this is

$$Z^{\alpha}{}_{\mu\nu\rho}(\boldsymbol{e}_{\alpha}:\boldsymbol{\theta}^{\mu})\boldsymbol{\theta}^{\nu}\otimes\boldsymbol{\theta}^{\rho} = Z^{\mu}{}_{\mu\nu\rho}\boldsymbol{\theta}^{\nu}\otimes\boldsymbol{\theta}^{\rho} = \tilde{Z}_{\nu\rho}\boldsymbol{\theta}^{\nu}\otimes\boldsymbol{\theta}^{\rho}, \tag{1.2.12}$$

where $\tilde{Z}_{\nu\rho} = Z^{\mu}{}_{\mu\nu\rho}$.

1.2.3 The Inner Product and the Metric

To introduce the notion of length on a tanget plane $\mathcal{T}_p(\mathcal{M})$ at a point $p\in\mathcal{M}$ the metric tensor $\boldsymbol{g}$ is introduced. The metric tensor has componenets,

$$g_{\mu\nu} = \boldsymbol{e}_{\mu}\cdot\boldsymbol{e}_{\nu}, \tag{1.2.13}$$

where $\boldsymbol{e}_{\mu}\cdot\boldsymbol{e}_{\nu}$ represents the inner product (or dot product) on $\mathcal{T}_p(\mathcal{M})$; clearly the metric is symmetric by construction as $\boldsymbol{e}_{\mu}\cdot\boldsymbol{e}_{\nu} = \boldsymbol{e}_{\nu}\cdot\boldsymbol{e}_{\mu}$. The inner product can be thought of as a multilinear map,

$$\boldsymbol{g}:(\boldsymbol{X},\boldsymbol{Y})\to\mathbb{R}, \quad \text{or} \quad \boldsymbol{g}(\boldsymbol{X},\boldsymbol{Y}) = g_{\mu\nu}X^{\mu}Y^{\nu}, \tag{1.2.14}$$

where $\boldsymbol{X}\in\mathcal{T}_p(\mathcal{M})$, $\boldsymbol{Y}\in\mathcal{T}_p(\mathcal{M})$ and $\boldsymbol{g}\in\mathcal{T}^*_p(\mathcal{M})\otimes\mathcal{T}^*_p(\mathcal{M})$. The inner product can also be represented by a second map

$$\boldsymbol{X}:\boldsymbol{Y}\to\mathbb{R}, \quad \text{or} \quad \boldsymbol{X}\cdot\boldsymbol{Y} = X^{\mu}Y^{\nu}\boldsymbol{e}_{\mu}\cdot\boldsymbol{e}_{\nu} = X^{\mu}Y^{\nu}g_{\mu\nu}, \tag{1.2.15}$$

which is a new mapping. The inner product also gives the length $|\boldsymbol{X}|$ or magnitude of any vector $\boldsymbol{X}\in\mathcal{T}_p(\mathcal{M})$ as,

$$|\boldsymbol{X}|^2 = \boldsymbol{X}\cdot\boldsymbol{X} = g_{\mu\nu}X^{\mu}X^{\nu}. \tag{1.2.16}$$

Another way to think of the inner product is that the metric maps a vector $\boldsymbol{X}$ to an equivalent or *dual* co-vector $\boldsymbol{\Xi}$ such that $\boldsymbol{X}:\boldsymbol{\Xi} = X^{\mu}\Xi_{\mu} = g_{\mu\nu}X^{\mu}X^{\nu}$. In component form $\boldsymbol{\Xi}$ is

$$\Xi_{\mu} = g_{\mu\nu}X^{\nu}; \tag{1.2.17}$$

this use of the metric to map a vector to it's corresponding co-vector (and vica versa) is extremely useful. Without loss of information we can write $\Xi_{\nu} = X_{\nu}$ to make it obvious that $X_{\nu} = X^{\mu}g_{\mu\nu}$ and this convention will be used from now on.

The metric also assigns an inner product and a length measure on the co-tangent plane $\mathcal{T}^*_p(\mathcal{M})$ but instead using the inverse components $g^{\mu\nu} = (g^{-1})_{\mu\nu}$,

$$g^{\mu\nu} = \boldsymbol{\theta}^{\mu}\cdot\boldsymbol{\theta}^{\nu}. \tag{1.2.18}$$

Similarly to before the inner product of two co-vectors $\boldsymbol{\omega}$ and $\boldsymbol{\sigma}$ is

$$\boldsymbol{\omega} \cdot \boldsymbol{Y} = \omega_\mu \sigma_\nu \boldsymbol{\theta}^\mu \cdot \boldsymbol{\theta}^\nu = \omega_\mu \sigma_\nu g^{\mu\nu} = \omega_\mu \sigma^\mu. \tag{1.2.19}$$

The reason that $g^{\mu\nu}$ must be the inverse matrix to $g_{\mu\nu}$ is as follows. For a vector $X^\mu \boldsymbol{e}_\mu$ and a co-vector $\omega_\mu \boldsymbol{\theta}^\mu$ we would like,

$$\boldsymbol{X} : \boldsymbol{\omega} = \boldsymbol{g}(\boldsymbol{X}, \star) : \boldsymbol{g}^{-1}(\boldsymbol{\omega}, \star), \tag{1.2.20}$$

$$X^\mu \omega_\mu = X_\mu \omega^\mu, \tag{1.2.21}$$

$$= X^\rho g_{\rho\mu} g^{\mu\sigma} \omega_\sigma \tag{1.2.22}$$

which is only true if $g_{\rho\mu} g^{\mu\sigma} = \delta^\sigma_\rho$ which is true by definition if $(g^{-1})_{\mu\nu} = g^{\mu\nu}$.

Not only has the metric provided us with an inner product and a length on tangent planes and cotangent planes, but it has also given a mapping between the two and can raise and lower indeces on general tensors such as

$$T^{\mu\nu\dots}_{\alpha\beta} = g^{\mu\rho} g_{\beta\sigma} T_\rho{}^\nu{}_\alpha{}^{\sigma\dots}. \tag{1.2.23}$$

1.2.4 Maps Between Manifolds

In section we will be interested in the maps between two manifolds M and N. This has many uses such as pushing and pulling tensors between manifolds, allowing us to calculate a Lie derivative of tensor fields and finding the metric (or any tensor field) on an embedded surface; this very importantly allowed us to perform the 3+1 decomposition on a spacetime as in section 2.1.2.

Define a smooth map $\Phi : M \to N$ between manifolds on some coordinate patch labelling coordinates $x^\mu \in M$ and $y^\mu \in N$. The map $\Phi : x^\mu \to y^\mu$ gives $y^\mu = \Phi^\mu(x^\nu)$, or equivalently $y^\mu(x^\nu)$. Scalar functions must also map trivially $f_N(y^\mu(x^\nu)) = f_M(x^\mu)$ where $f_N \in N$ and $f_M \in M$, thus we will no longer identify which manifold a function is on. The map Φ allows us to push the vector $\boldsymbol{X} \in \mathcal{T}_p(M)$ to $\Phi_* \boldsymbol{X} \in \mathcal{T}_q(N)$, where $q = \Phi(p)$, in a way such that it's action on a function f is the same in either manifold.

$$\boldsymbol{X}(f)\Big|_p = \Phi_* \boldsymbol{X}(f)\Big|_q, \tag{1.2.24}$$

$$X^\mu \frac{\partial f}{\partial x^\mu} = (\Phi_* X)^\nu \frac{\partial f}{\partial y^\nu}, \tag{1.2.25}$$

$$\left(X^\mu \frac{\partial y^\nu}{\partial x^\mu} \right) \frac{\partial f}{\partial y^\nu} = (\Phi_* X)^\nu \frac{\partial f}{\partial y^\nu}, \tag{1.2.26}$$

and hence the components of the push-foreward $\Phi_* \boldsymbol{X}$ can be read off,

$$(\Phi_* X)^\mu = \frac{\partial y^\mu}{\partial x^\nu} X^\nu. \tag{1.2.27}$$

Given a co-vector field $\boldsymbol{\omega} \in \mathcal{T}^*_p(N)$ we can pull the field back from $\mathcal{T}^*_p(M) \leftarrow \mathcal{T}^*_q(N)$, denoted $\Phi^* \boldsymbol{\omega}$, by demanding that $\Phi^* \boldsymbol{\omega}(\boldsymbol{X})\big|_p = \boldsymbol{\omega}(\Phi_* \boldsymbol{X})\big|_q$. Evaluating this gives

$$\Phi^* \boldsymbol{\omega}(\boldsymbol{X})\Big|_p = \boldsymbol{\omega}(\Phi_* \boldsymbol{X})\Big|_q, \tag{1.2.28}$$

$$(\Phi^* \omega)_\mu X^\mu = \omega_\nu (\Phi_* X)^\nu, \tag{1.2.29}$$

$$(\Phi^* \omega)_\mu X^\mu = \omega_\nu \frac{\partial y^\nu}{\partial x^\mu} X^\mu, \tag{1.2.30}$$

and the components of the pull-back $\Phi_* \boldsymbol{\omega}$ can be read off,

$$(\Phi^* \omega)_\mu = \omega_\nu \frac{\partial y^\nu}{\partial x^\mu}. \tag{1.2.31}$$

Considering an $(0,2)$ tensor $\boldsymbol{T} \in N$, the pullback $\Phi^*\boldsymbol{T} \in M$ follows simply from demanding that $\boldsymbol{T}(\Phi_*\boldsymbol{X}, \Phi_*\boldsymbol{Y})|_q = \Phi^*\boldsymbol{T}(\boldsymbol{X}, \boldsymbol{Y})|_p$ where $\boldsymbol{X}$ and $\boldsymbol{Y}$ are vector fields on M. The components of the pull-back of $\boldsymbol{T}$ are therefore

$$(\Phi^*T)_{\mu\nu} = \frac{\partial y^\rho}{\partial x^\mu}\frac{\partial y^\sigma}{\partial x^\nu}T_{\rho\sigma}. \tag{1.2.32}$$

The pull-back of a generic $(0,q)$ tensor and the push-foreward of a generic $(p,0)$ tensor can be found similarly by contracting with an extra $\frac{\partial y^\mu}{\partial x^\nu}$ for each downstairs index or $\frac{\partial x^\mu}{\partial y^\nu}$ for each upstairs index.

Diffeomorphisms

So far we have only discussed the one way mapping $\Phi : M \to N$ which is requires a well behaved $\partial y^\nu/\partial x^\mu$. A diffeomorphism is an isomorphism[1] between smooth manifolds $\Phi : M \to N$, meaning M and N have the same number of dimensions. Two infinitessimally close points $\{p, p+\delta p\} \in \mathcal{M}$ map to two infinitessimally close points $(q, q+\delta q) \in \mathcal{N}$ meaning that open sets are preserved. Given that a diffeomorphism is smooth bijective map then it must be invertible with inverse map $\Phi^{-1} : N \to M$, and $y^\nu(x^\mu)$ has a smooth inverse $x^\nu(y^\mu)$. When an inverse map Φ^{-1} is defined then the pull-back of $(p,0)$ tensors from N to M along with the push-foreward of $(0,q)$ tensors from M to N is possible. This means it is possible to push or pull generic tensors between M and N in any direction. The tangent spaces associated with $p \in \mathcal{M}$ or $q \in \mathcal{N}$ are therefore also preserved under mapping meaning that local structure on the manifold is preserved under the mapping. Two common examples of diffeomorphisms are coordinate changes and translations.

Projection Mappings

As mentioned, maps between manifolds can be used to project tensors to lower dimensional embedded surfaces. This requires us to consider an m dimensional manifold M with metric $g_{\mu\nu}$ and coordinates x^μ aswell as an embedded n dimensional surface N where $n < m$. We can treat N as a separate n dimensional manifold with metric $h_{\mu\nu}$. As before, we can define a map $\Phi : x^\mu \to y^\mu$ and the pullback of the metric demands that,

$$^{(m)}h_{\rho\sigma} = {}^{(n)}h_{\mu\nu}\frac{\partial y^\mu}{\partial x^\rho}\frac{\partial y^\nu}{\partial x^\sigma}, \tag{1.2.33}$$

where $^{(m)}\boldsymbol{h}$ represents m-dimensional the tensor on M and $^{(n)}\boldsymbol{h}$ represents n-dimensional the tensor on N; of course $^{(n)}\boldsymbol{h}$ and $\boldsymbol{h}$ are completely identical.

In the case that $n = m-1$, which is a projection into one less dimension, a convenient form for $^{(n)}\boldsymbol{h}$ can be found. If the image of N in M has everywhere an m-dimensional unit normal $\boldsymbol{n}$, then a vector $\boldsymbol{X} \in \mathcal{T}_p(\mathcal{M})$ for $p \in N$ can be projected onto N like,

$$({}^{(m)}\overrightarrow{X})^\mu = (\delta^\mu_\nu \mp n^\mu n_\nu)X^\nu, \tag{1.2.34}$$

where the sign is negative if $|\boldsymbol{n}|^2 = 1$ and positive if $|\boldsymbol{n}|^2 = -1$. It should be noted that strictly, $\overrightarrow{\boldsymbol{X}} \in \mathcal{T}_p(\mathcal{M})$. To avoid confusion we will denote the m-dimensional projected vector as $^{(m)}\overrightarrow{\boldsymbol{X}}$ and vector existing in the n-dimensional manifold N as $^{(n)}\overrightarrow{\boldsymbol{X}}$. The projection guarentees that,

$$\begin{aligned}
{}^{(n)}\boldsymbol{h}({}^{(n)}\overrightarrow{\boldsymbol{X}}, {}^{(n)}\overrightarrow{\boldsymbol{X}}) &= \boldsymbol{g}({}^{(m)}\overrightarrow{\boldsymbol{X}}, {}^{(m)}\overrightarrow{\boldsymbol{X}}), && (1.2.35)\\
&= {}^{(m)}h_{\mu\nu}(\delta^\mu_\alpha \mp n^\mu n_\alpha)X^\alpha(\delta^\nu_\beta \mp n^\nu n_\beta)X^\beta, && (1.2.36)\\
&= {}^{(m)}\boldsymbol{h}(\boldsymbol{X}, \boldsymbol{X}), && (1.2.37)
\end{aligned}$$

which gives a formula for the projected metric $^{(m)}\boldsymbol{h} \in \mathcal{M}$,

$$^{(m)}h_{\mu\nu} = g_{\mu\nu} \mp n_\mu n_\nu. \tag{1.2.38}$$

[1]An isomorphism is a structure preserving bijective map between sets.

The use of this projected metric to project general tensors to lower dimensions is explored in detail in section 2.1.2.

Mapping to lower dimensional surface of d dimensions can be done similarly by adding an extra mutually-orthogonal unit vector for each reduced dimension like,

$$^{(d)}h_{\mu\nu} = g_{\mu\nu} \mp n^{(1)}_{\mu} n^{(1)}_{\nu} \mp n^{(2)}_{\mu} n^{(2)}_{\nu} + \dots \, . \tag{1.2.39}$$

The metric $\boldsymbol{h}$ on an arbitrary a-dimensional sub-surface $A \in \mathcal{M}$ can be explicitly calculated from the pushforeward of $^{(m)}\boldsymbol{h}$ considering the diffeomorphism Φ^A that maps the image of A embedded in $\mathcal{M}$ to an a-dimensional manifold $\mathcal{A}$. The resulting metric is,

$$(\Phi^A_* g)_{ij} = h_{ij} = \frac{\partial x^\mu}{\partial z^i}\frac{\partial x^\nu}{\partial z^j} {}^{(m)}h_{\mu\nu} = \frac{\partial x^\mu}{\partial z^i}\frac{\partial x^\nu}{\partial z^j}\left(g_{\mu\nu} \mp n^{(1)}_{\mu} n^{(1)}_{\nu} \mp n^{(2)}_{\mu} n^{(2)}_{\nu} + \dots\right), \tag{1.2.40}$$

where $n^{(i)}$ are a set of orthogonal unit vectors perpendicular to A; x^μ span $\mathcal{M}$ and z^i span $\mathcal{A}$.

1.2.5 Lie Derivatives

The Lie derivative of a tensor at a point p is the rate of change of a tensor field with respect to a pull-back from a diffeomorphism Φ mapping infinitessimally close points $p = x^\mu, q = x^\mu + \epsilon\xi^\mu \in \mathcal{M}$ like $\Phi : p \to q$ for some vector field $\boldsymbol{\xi}$. Like any good differential operator, the Lie deriviative $\mathcal{L}_\xi$ along $\boldsymbol{\xi}$ (and $\mathcal{L}_\zeta$ along vector field $\boldsymbol{\zeta}$) should obey,

$$\mathcal{L}_{a\xi+b\zeta}\boldsymbol{T} = a\mathcal{L}_\xi \boldsymbol{T} + b\mathcal{L}_\zeta \boldsymbol{T}, \tag{1.2.41}$$

$$\mathcal{L}_\xi(a\boldsymbol{T} + b\boldsymbol{W}) = a\mathcal{L}_\xi \boldsymbol{T} + b\mathcal{L}_\xi \boldsymbol{W}, \tag{1.2.42}$$

$$\mathcal{L}_\xi(f\boldsymbol{T}) = \boldsymbol{T}\mathcal{L}_\xi f + f\mathcal{L}_\xi \boldsymbol{T}, \tag{1.2.43}$$

for constant $\{a, b\}$, function f and generic tensorial objects of same type $\boldsymbol{T}$ and $\boldsymbol{W}$.

The simplest example is the Lie derivative of a scalar field ϕ, denoted $\mathcal{L}_\xi\phi$ with respect to vector field $\boldsymbol{\xi}$,

$$\mathcal{L}_\xi\phi = \lim_{\epsilon\to 0}\left[\frac{\Phi^*\phi|_q - \phi|_p}{\epsilon}\right], \tag{1.2.44}$$

$$= \lim_{\epsilon\to 0}\left[\frac{\phi(x^\mu + \epsilon\xi^\mu) - \phi(x^\mu)}{\epsilon}\right], \tag{1.2.45}$$

$$= \xi^\mu\partial_\mu\phi, \tag{1.2.46}$$

which reduces to the partial derivative of ϕ with along $\boldsymbol{\xi}$. Next let's calculate the Lie derivative of a vector field $\boldsymbol{X}$ with respect to vector field $\boldsymbol{\xi}$. Starting with the same definition as Eq. (1.2.44), and using $y^\mu = x^\mu + \epsilon\xi^\mu$, the Lie derivative of $\boldsymbol{X}$ is,

$$(\mathcal{L}_\xi X)^\mu = \lim_{\epsilon\to 0}\left[\frac{(\Phi^* X|_q)^\mu - X|_p{}^\mu}{\epsilon}\right], \tag{1.2.47}$$

$$= \lim_{\epsilon\to 0}\left[\frac{\frac{\partial x^\mu}{\partial y^\nu}X^\nu(x^\rho + \epsilon\xi^\rho) - X^\mu(x^\rho)}{\epsilon}\right], \tag{1.2.48}$$

$$= \lim_{\epsilon\to 0}\left[\frac{(\delta^\mu_\nu - \epsilon\partial_\nu\xi^\mu)X^\nu(x^\rho + \epsilon\xi^\rho) - X^\mu(x^\rho)}{\epsilon}\right], \tag{1.2.49}$$

$$= \lim_{\epsilon\to 0}\left[\frac{-\epsilon\partial_\nu\xi^\mu X^\nu(x^\rho + \epsilon\xi^\rho) + X^\mu(x^\rho + \epsilon\xi^\rho) - X^\mu(x^\rho)}{\epsilon}\right], \tag{1.2.50}$$

$$= \lim_{\epsilon\to 0}\left[\frac{-\epsilon\partial_\nu\xi^\mu X^\nu(x^\rho) + X^\mu(x^\rho + \epsilon\xi^\rho) - X^\mu(x^\rho) + \mathcal{O}(\epsilon^2)}{\epsilon}\right], \tag{1.2.51}$$

$$= \xi^\nu\partial_\nu X^\mu - X^\nu\partial_\nu\xi^\mu. \tag{1.2.52}$$

The Lie derivative for co-vectors and tensors can be derived in the same way, but can be quickly derived from the Liebnitz rule as follows. Define a scalar field ψ, vector field $\boldsymbol{X}$ and co-vector field $\boldsymbol{\omega}$, where $\psi = X^\mu \omega_\mu$, then it follows that,

$$\begin{aligned}
\mathcal{L}_\xi \psi &= \xi^\mu \partial_\mu \psi = X^\nu \xi^\mu \partial_\mu \omega_\nu + \omega_\nu \xi^\mu \partial_\mu X^\nu, && (1.2.53)\\
&= \mathcal{L}_\xi (X^\mu \omega_\mu), && (1.2.54)\\
&= \omega_\mu (\mathcal{L}_\xi X)^\mu + X^\mu (\mathcal{L}_\xi \omega)_\mu, && (1.2.55)\\
X^\mu (\mathcal{L}_\xi \omega)_\mu &= X^\nu \xi^\mu \partial_\mu \omega_\nu + \omega_\nu \xi^\mu \partial_\mu X^\nu - \omega_\mu (\mathcal{L}_\xi X)^\mu, && (1.2.56)\\
(\mathcal{L}_\xi \omega)_\mu &= \xi^\nu \partial_\nu \omega_\mu + \omega_\nu \partial_\mu \xi^\nu. && (1.2.57)
\end{aligned}$$

Derivatives of a generic tensor $\boldsymbol{T}$ follows simply, for example,

$$(\mathcal{L}_\xi T)^{\alpha\beta...}_{\mu\nu...} = \xi^\sigma \partial_\sigma T^{\alpha\beta...}_{\mu\nu...} + T^{\alpha\beta...}_{\sigma\nu...} \partial_\mu \xi^\sigma + T^{\alpha\beta...}_{\mu\sigma...} \partial_\nu \xi^\sigma + ... - T^{\sigma\beta...}_{\mu\nu...} \partial_\sigma \xi^\alpha - T^{\alpha\sigma...}_{\mu\nu...} \partial_\sigma \xi^\beta - ... . \quad (1.2.58)$$

1.2.6 Lengths on Manifolds

The natural entry point for studying curved geometry is to revisit Pythagoras' theorem. For this we need a manifold $\mathcal{M}$ equipped with a metric $\boldsymbol{g}$, written as $(\mathcal{M}, \boldsymbol{g})$ for short. The distance $\mathrm{d}s$ between two infinitessimaly close points $p \in \mathcal{M}$ and $p + \delta p \in \mathcal{M}$, with coordinates $p = x^\mu$ and $p + \delta p = x^\mu + \mathrm{d}x^\mu$, is given by

$$\mathrm{d}s^2 = \boldsymbol{g}(\mathbf{d}\boldsymbol{x}, \mathbf{d}\boldsymbol{x}) = g_{\mu\nu} \mathrm{d}x^\mu \mathrm{d}x^\nu, \quad (1.2.59)$$

where $g_{\mu\nu}$ are the components of the metric tensor. This is the generalisation of Eq. (1.2.2) to curved space; noteably the line element can now have varying coefficients from $g_{\mu\nu}$ and cross terms such as $\mathrm{d}x\mathrm{d}y$. The special choice of $g_{\mu\nu} = \delta_{\mu\nu}$ gives us flat space, also called Euclidean space, where $\delta_{\mu\nu} = 1$ if $\mu = \nu$ and vanishes otherwise. With the line elemend defined, we can immediately apply it to calculating the length of a general curve in curved space. Consider the curve Γ consisting of a set of connected points $p(\lambda) \in \mathcal{M}$ smoothly parameterised by λ. We can calculate the length Δs of the curve between $\lambda_1 \geq \lambda \geq \lambda_0$ by parameterising $\mathrm{d}s$,

$$\mathrm{d}s^2 = g_{\mu\nu} \frac{\partial x^\mu}{\partial \lambda} \frac{\partial x^\nu}{\partial \lambda} \mathrm{d}\lambda^2, \quad (1.2.60)$$

and integrating $\mathrm{d}s$ along Γ,

$$\Delta s = \int_{\lambda_0}^{\lambda_1} \sqrt{\left(g_{\mu\nu} \frac{\partial x^\mu}{\partial \lambda} \frac{\partial x^\nu}{\partial \lambda} \right)} \mathrm{d}\lambda. \quad (1.2.61)$$

In the simplified case where λ is one of the coordinates, say ξ, the length Δs becomes,

$$\Delta s = \int_{\xi_0}^{\xi_1} \sqrt{g_{\xi\xi}} \mathrm{d}\xi. \quad (1.2.62)$$

1.2.7 Volumes on Manifolds

Following from measuring the length of a curve now we can measure volumes on a manifold; of course we still require a metric $\boldsymbol{g}$ over the manifold. Let's say that in a coordinate system x^μ we can define the volume V of a subregion M by integrating some weight function $w(x^\mu)$,

$$V = \int_M w(x^\mu) \mathrm{d}x^1 \mathrm{d}x^2 ... \mathrm{d}x^n, \quad (1.2.63)$$

over M. To find $w(x^\mu)$, start by defining an orthogonal coordinate transformation $x^\mu \to \tilde{x}^\mu$ such that $\tilde{\boldsymbol{g}}$ is diagonal and $\det(\boldsymbol{g}) = \det(\tilde{\boldsymbol{g}})$; this is always possible as $\boldsymbol{g}$ is real and symmetric. In this coordinate system, the volume δV in an infinitessimal cuboid, with i'th sidelength $\delta \tilde{x}^i$, is

$$\delta V = \left(\sqrt{\tilde{g}_{11}} \delta \tilde{x}^1 \right) \left(\sqrt{\tilde{g}_{22}} \delta \tilde{x}^2 \right) ... \left(\sqrt{\tilde{g}_{nn}} \delta \tilde{x}^n \right), \quad (1.2.64)$$

where Eq. (1.2.62) was used to get the length bewteen each $\tilde{x}^i$ and $\tilde{x}^i + \delta\tilde{x}^i$. Given that $\tilde{\boldsymbol{g}}$ is diagonal we know the i'th eigenvalue $\tilde{\lambda}_i = \tilde{g}_{ii}$ and therefore $\det(\tilde{\boldsymbol{g}}) = \prod_i \tilde{g}_{ii}$. Thus the volume δV can be rewritten,

$$\delta V = \sqrt{|\det(\tilde{\boldsymbol{g}})|}\delta\tilde{x}^1\delta\tilde{x}^2...\delta\tilde{x}^n, \tag{1.2.65}$$

and the formula for the finite volume of M is,

$$V = \int_M \sqrt{|\det(\tilde{\boldsymbol{g}})|}\mathrm{d}\tilde{x}^1\mathrm{d}\tilde{x}^2...\mathrm{d}\tilde{x}^n, \tag{1.2.66}$$

and the form of the weight function in $\tilde{x}^\mu$ coordinates is $\tilde{w}(\tilde{x}^\mu) = \sqrt{|\det(\tilde{\boldsymbol{g}})|}$. We are now free to transform back from $\tilde{x}^\mu \to x^\mu$, and given that the transformation is orthogonal we know that $\det(\boldsymbol{g}) = \det(\tilde{\boldsymbol{g}})$ and the Jacobean matrix $\boldsymbol{J}$ of the coordinate transformation has $\det(\boldsymbol{J}) = 1$, therefore

$$V = \int_M \sqrt{|\det(\boldsymbol{g})|}\,\mathrm{d}x^1\,\mathrm{d}x^2\,...\,\mathrm{d}x^n\,, \tag{1.2.67}$$

which holds for any non-diagonal, real and symmetric metric $\boldsymbol{g}$. In general we will now denote the deteminant of a metric $\det(\boldsymbol{g})$ with the lower case letter g. When dealing with a pseudo-Riemannian manifold with a negative determinant, such as spacetime, it is more common to see $\sqrt{-g}$ written rather than $\sqrt{|g|}$ giving

$$V = \int_M \sqrt{-g}\,\mathrm{d}x^1\,\mathrm{d}x^2\,...\,\mathrm{d}x^n\,. \tag{1.2.68}$$

Equation (1.2.67) can also be used to find the volume (or area) of a lower dimensional sub-volume. First cover the new sub-volume A with coordinates z^μ, where $\mu \in \{1, 2, ..., m\}$ for $m < n$, and then calculate the metric $\boldsymbol{h}$ which can be done using Eq. (1.2.40). The area V_A of A is then,

$$V_A = \int_A \sqrt{|h|}\,\mathrm{d}z^1\,\mathrm{d}z^2\,...\,\mathrm{d}z^m\,, \tag{1.2.69}$$

which can be seen by mapping to an a-dimensional manifold $\boldsymbol{\mathcal{A}}$ that is diffeomorphic to A and applying Eq. (1.2.67).

1.2.8 Geodesics

For a manifold equipped with metric $(\mathcal{M}, g)$ the curve with shortest distance between two points $p, q \in \mathcal{M}$ is called a geodesic. To find the geodesic joining p and q we need to use calculus of variation on the total length Δs from Eq. (1.2.61) of a general curve between two points. Given that the integrand $\mathcal{L}$ of Eq. (1.2.61) is a function like $\mathcal{L}(x^\mu, \dot{x}^\mu)$, where the dot means differentiation by λ, we can use the Eular-Lagrange equation,

$$\frac{\partial\mathcal{L}}{\partial x^\mu} - \frac{\mathrm{d}}{\mathrm{d}\lambda}\frac{\partial\mathcal{L}}{\partial\dot{x}^\mu} = 0, \tag{1.2.70}$$

to give a differential equation with solution being a geodesic. Applyin the EL equation to the integrand of Eq. (1.2.61) is algebraically messy, it is easier[2] to square the integrand and start from $\mathcal{L}^2$ giving the same solution if $\mathrm{d}\mathcal{L}/\mathrm{d}\lambda = 0$,

$$\frac{\partial\mathcal{L}^2}{\partial x^\alpha} - \frac{\mathrm{d}}{\mathrm{d}\lambda}\frac{\partial\mathcal{L}^2}{\partial\dot{x}^\alpha} = 0, \tag{1.2.71}$$

$$\frac{\partial}{\partial x^\alpha}\left(g_{\mu\nu}\dot{x}^\mu\dot{x}^\nu\right) - \frac{\mathrm{d}}{\mathrm{d}\lambda}\frac{\partial}{\partial\dot{x}^\alpha}\left(g_{\mu\nu}\dot{x}^\mu\dot{x}^\nu\right) = 0, \tag{1.2.72}$$

$$(\partial_\alpha g_{\mu\nu})\dot{x}^\mu\dot{x}^\nu - 2\frac{\mathrm{d}}{\mathrm{d}\lambda}\left(g_{\alpha\nu}\dot{x}^\nu\right) = 0, \tag{1.2.73}$$

$$(\partial_\alpha g_{\mu\nu})\dot{x}^\mu\dot{x}^\nu - 2\left(\dot{x}^\rho\partial_\rho\left(g_{\alpha\nu}\right)\dot{x}^\nu\right) - 2\ddot{x}^\nu g_{\alpha\nu} = 0. \tag{1.2.74}$$

[2]Given that $\mathcal{L}$ is homogeneneus to degree k, $\dot{x}^i\partial\mathcal{L}/\partial\dot{x}^i = k\mathcal{L}$ for constant k, one can show that $\mathrm{d}\mathcal{L}/\mathrm{d}\lambda = 0$ if the Eular-Lagrange equation is assumed.

Rearranging and multiplying by $g^{\alpha\beta}$ gives,

$$\ddot{x}^{\beta} + \frac{1}{2} g^{\alpha\beta} \left(\partial_{\mu} g_{\alpha\nu} + \partial_{\nu} g_{\alpha\mu} - \partial_{\alpha} g_{\mu\nu}\right) \dot{x}^{\mu} \dot{x}^{\nu} = 0, \tag{1.2.75}$$

$$\ddot{x}^{\beta} + \Gamma^{\beta}{}_{\mu\nu} \dot{x}^{\mu} \dot{x}^{\nu} = 0, \tag{1.2.76}$$

where $\Gamma^{\beta}{}_{\mu\nu}$ is the components of the connection-symbol from Eq. (1.3.77). A trivial solution to Eq. (1.2.76) is in flat space using cartesian coordinates where $\Gamma^{\beta}{}_{\mu\nu} = 0$ and therefore $\ddot{x}^{\beta} = 0$ so $\dot{x}^{\beta}$ is a constant; this tells us the shortest distance between two points in flat space is a straight line. In other words, geodesics are straight lines in flat space.

Non-affine Geodesics

The equation of a geodesic given above is true for an affinely parameterised curve. An affine parameter λ is defined so that the length of a curve δs between two parameter values λ and $\lambda + \delta\lambda$ is given by $\delta s = k(\delta\lambda)$ for constant k; the arclength along a curve is linearly proportional to the value of the λ. This property was inherant in the derivation of Eq. (1.2.76) is that $\mathrm{d}\mathcal{L}/\mathrm{d}\lambda = 0$ was assumed.

A non-affine parameter μ could equally be used to describe the curve. Writing $\mu(\lambda)$ the geodesic equation is transformed as shown,

$$\frac{\mathrm{d}^2 x^{\beta}}{\mathrm{d}\lambda^2} + \Gamma^{\beta}{}_{\mu\nu} \frac{\mathrm{d}x^{\mu}}{\mathrm{d}\lambda} \frac{\mathrm{d}x^{\nu}}{\mathrm{d}\lambda} = 0, \tag{1.2.77}$$

$$\left(\frac{\mathrm{d}^2 \mu}{\mathrm{d}\lambda^2} \frac{\mathrm{d}}{\mathrm{d}\mu} + \left(\frac{\mathrm{d}\mu}{\mathrm{d}\lambda}\right)^2 \frac{\mathrm{d}^2}{\mathrm{d}\mu^2}\right) x^{\beta} + \Gamma^{\beta}{}_{\mu\nu} \frac{\mathrm{d}x^{\mu}}{\mathrm{d}\mu} \frac{\mathrm{d}x^{\nu}}{\mathrm{d}\mu} \left(\frac{\mathrm{d}\mu}{\mathrm{d}\lambda}\right)^2 = 0, \tag{1.2.78}$$

$$\frac{\mathrm{d}^2 x^{\beta}}{\mathrm{d}\mu^2} + \Gamma^{\beta}{}_{\mu\nu} \frac{\mathrm{d}x^{\mu}}{\mathrm{d}\mu} \frac{\mathrm{d}x^{\nu}}{\mathrm{d}\mu} = -\left(\frac{\mathrm{d}\mu}{\mathrm{d}\lambda}\right)^{-2} \frac{\mathrm{d}^2 \mu}{\mathrm{d}\lambda^2} \frac{\mathrm{d}x^{\beta}}{\mathrm{d}\mu}, \tag{1.2.79}$$

$$\frac{\mathrm{d}^2 x^{\beta}}{\mathrm{d}\mu^2} + \Gamma^{\beta}{}_{\mu\nu} \frac{\mathrm{d}x^{\mu}}{\mathrm{d}\mu} \frac{\mathrm{d}x^{\nu}}{\mathrm{d}\mu} = -f(\mu) \frac{\mathrm{d}x^{\beta}}{\mathrm{d}\mu}, \tag{1.2.80}$$

$$\tag{1.2.81}$$

which is the same as the affine geodesic equation except with an extra non-zero right hand side proportional to $\mathrm{d}x^{\beta}/\mathrm{d}\mu$ and some function $f(\mu)$. If μ is a linear function of λ then μ is also an affine parameter; this is reflected in the term $\mathrm{d}^2\mu/\mathrm{d}\lambda^2 = 0$ and the affine geodesic equation is returned.

MAYBE IM BETTER OFF DERIVING THE GEODESIC EQUTION FROM L NOT L SQAURED WHICH GIVES

$$\frac{1}{\mathcal{L}} \left(\dot{x}^{\mu} \dot{x}^{\nu} \partial_{\alpha} g_{\mu\nu} - 2\dot{x}^{\mu} \frac{\mathrm{d}}{\mathrm{d}\lambda} g_{\mu\alpha} - 2 g_{\mu\alpha} \ddot{x}^{\mu} + \underbrace{\frac{2}{\mathcal{L}} g_{\mu\nu} \dot{x}^{\mu} \frac{\mathrm{d}\mathcal{L}}{\mathrm{d}\lambda}}_{this\ is\ the\ non-affine\ bit} \right) = 0 \tag{1.2.82}$$

1.3 Tensor Calculus and Curvature

1.3.1 General Covariance and Coordinate transformations

Many laws of physics can be expressed as tensor field equations where a tensor field is the assignment of a tensor to each point in space. This assignment must be smooth as it is to describe physical quantities. The power of tensor algebra and tensor calculus is that if a tensor field equation can be written in one coordiante system then must hold (in index form) in all sensible coordinate system. This is a consequence of the tensor transformation law. Looking back, we can write a generic vector $\boldsymbol{X}$ as $X^{\mu} \boldsymbol{e}_{\mu} = X^{\mu} \partial_{\mu}$ and if we choose a coordinate transformation $x^\mu \to \tilde{x}^\mu$ then we see that in the transformed coordinate system the vector field $\boldsymbol{X}$, written $\tilde{\boldsymbol{X}}$, becomes

$$\begin{aligned}
\tilde{\boldsymbol{X}} &= \tilde{X}^\mu \frac{\partial}{\partial \tilde{x}^\mu}, && (1.3.1)\\
&= \tilde{X}^\mu \frac{\partial x^\nu}{\partial \tilde{x}^\mu} \frac{\partial}{\partial x^\nu}, && (1.3.2)\\
&= X^\nu \frac{\partial}{\partial x^\nu}, && (1.3.3)\\
&= \boldsymbol{X}, && (1.3.4)
\end{aligned}$$

where the components $X^\nu = \tilde{X}^\mu \frac{\partial x^\nu}{\partial \tilde{x}^\mu}$ are required to transform in order to ensure $\boldsymbol{X} = \tilde{\boldsymbol{X}}$. This says that the underlying geometric object (a vector in this case) is independant of the coordinates used to describe them; the tradeoff for this useful property is that the vectors components X^μ have to transform under the tensor transformation law, effectively opposing the transformation of the basis vectors. Working from a co-vector ω we can write it as $\omega_\mu \boldsymbol{\theta}^\mu = \omega_\mu \mathrm{d}x^\mu$ in component-basis form [REF THIS?] and the same coordinate transform gives

$$\begin{aligned}
\tilde{\boldsymbol{\omega}} &= \tilde{\omega}_\mu \mathrm{d}\tilde{x}^\mu, && (1.3.5)\\
&= \tilde{\omega}_\mu \frac{\partial \tilde{x}^\mu}{\partial x^\nu} \mathrm{d}x^\nu\,, && (1.3.6)\\
&= \omega_\nu \mathrm{d}x^\nu, && (1.3.7)
\end{aligned}$$

where the co-vector components transform like $\omega_\nu = \tilde{\omega}_\mu \frac{\partial \tilde{x}^\mu}{\partial x^\nu}$, the opposite way to the vector components. These transformation laws ensure that a scalar field created from the product of a vector field and a co-vector field, like $\boldsymbol{\omega} : \boldsymbol{X}$, is a Lorentz scalar not transforming under coordinate transformations. This can be seen from

$$\begin{aligned}
\tilde{\boldsymbol{\omega}} : \tilde{\boldsymbol{X}} &= \tilde{X}^\mu \tilde{\omega}_\mu, && (1.3.8)\\
&= X^\nu \frac{\partial \tilde{x}^\mu}{\partial x^\nu} \frac{\partial x^\rho}{\partial \tilde{x}^\mu} \omega_\rho, && (1.3.9)\\
&= X^\nu \frac{\partial x^\rho}{\partial x^\nu} \omega_\rho, && (1.3.10)\\
&= X^\nu \delta_\nu^{\ \rho} \omega_\rho, && (1.3.11)\\
&= X^\nu \omega_\nu, && (1.3.12)\\
&= \boldsymbol{\omega} : \boldsymbol{X}. && (1.3.13)
\end{aligned}$$

The general tensor transformation law can be derived easily from chaining multiple of the previous examples together, for example,

$$\tilde{T}^{\mu\nu\ldots}_{\quad\ \rho\sigma\ldots} = T^{\alpha\beta\ldots}_{\quad\ \gamma\delta\ldots} \left(\frac{\partial \tilde{x}^\mu}{\partial x^\alpha} \frac{\partial \tilde{x}^\nu}{\partial x^\beta}, \ldots \times \frac{\partial x^\gamma}{\partial \tilde{x}^\rho} \frac{\partial x^\delta}{\partial \tilde{x}^\sigma}, \ldots \right). \qquad (1.3.14)$$

Tensor Densities

A tensor density is the generalisation of a tensor field obeying the tensor transformation law in Eq. (1.3.14). One important example of a tensor density is the volume element $\sqrt{-g}$, this is a scalar density. This object does not have any indeces so at first glance may pass for a true scalar field. However, when a coordinate transformation $x^\mu \to \tilde{x}^\mu$ is applied we find that $\sqrt{-g} \to \sqrt{-\tilde{g}} \neq \sqrt{-g}$ but for a general scalar field ϕ we find $\phi \to \tilde{\phi} = \phi$; therefore $\sqrt{-g}$ cannot be a scalar field. This can be shown explicitly by look at the the determinant of the metric,

$$\sqrt{-\tilde{g}} = \sqrt{\det(-\tilde{g}_{\mu\nu})}, \tag{1.3.15}$$

$$= \sqrt{\det\left(-g_{\alpha\beta}\frac{\partial x^\alpha}{\partial \tilde{x}^\mu}\frac{\partial x^\beta}{\partial \tilde{x}^\nu}\right)}, \tag{1.3.16}$$

$$= \sqrt{-g}\det\left(\frac{\partial x^\alpha}{\partial \tilde{x}^\mu}\right), \tag{1.3.17}$$

and as can be seen, the volume element picks up a factor of the determinant of the Jacobean. A tensor density $\boldsymbol{\mathcal{T}}$ of weight w can be written in the form,

$$\boldsymbol{\mathcal{T}} = \sqrt{-g}^w \boldsymbol{T}, \tag{1.3.18}$$

where $\boldsymbol{T}$ is a tensor obeying the tensor transformation law. It should be noted that a tensor density of weight zero is a regular tensors and the weight of a tensor has nothing to do with the rank of the tensor.

Lie Derivatives of Tensor Densities

To calculate the Lie derivative of a tensor density, first the Lie derivative of $\sqrt{-g}$ should be calculated, and in order to calculate the Lie derivative of the volume element a preliminary result is needed. Following the definition of a Lie derivative in section 1.2.5 and setting $y^\mu = x^\mu + \epsilon\xi^\mu$, the determinant of the Jacobean matrix is,

$$\det\left(\frac{\partial y^\mu}{\partial x^\rho}\right) = \det\left(\delta^\mu_\rho + \epsilon\frac{\partial \xi^\mu}{\partial x^\rho}\right), \tag{1.3.19}$$

$$= \det\begin{pmatrix} 1+\epsilon\frac{\partial\xi^1}{\partial x^1} & \epsilon\frac{\partial\xi^1}{\partial x^2} & \epsilon\frac{\partial\xi^1}{\partial x^3} & \epsilon\frac{\partial\xi^1}{\partial x^4} \\ \epsilon\frac{\partial\xi^2}{\partial x^1} & 1+\epsilon\frac{\partial\xi^2}{\partial x^2} & \epsilon\frac{\partial\xi^2}{\partial x^3} & \epsilon\frac{\partial\xi^2}{\partial x^4} \\ \epsilon\frac{\partial\xi^3}{\partial x^1} & \epsilon\frac{\partial\xi^3}{\partial x^2} & 1+\epsilon\frac{\partial\xi^3}{\partial x^3} & \epsilon\frac{\partial\xi^3}{\partial x^4} \\ \epsilon\frac{\partial\xi^4}{\partial x^1} & \epsilon\frac{\partial\xi^4}{\partial x^2} & \epsilon\frac{\partial\xi^4}{\partial x^3} & 1+\epsilon\frac{\partial\xi^4}{\partial x^4} \end{pmatrix}, \tag{1.3.20}$$

$$= \left(1 + \epsilon\sum_i \frac{\partial \xi^i}{\partial x^i} + \mathcal{O}(\epsilon^2)\right), \tag{1.3.21}$$

$$= 1 + \epsilon\partial_\mu\xi^\mu + \mathcal{O}(\epsilon^2), \tag{1.3.22}$$

where four dimensions was used for explicitness, but the calculation works exactly the same in any number of dimensions. Using this result and the definition of a Lie derivative, $\mathcal{L}_\xi\sqrt{-g}$ evaluates to,

$$\mathcal{L}_\xi\sqrt{-g} = \lim_{\epsilon\to 0}\left(\frac{\Phi^*\sqrt{-\tilde{g}}\Big|_q - \sqrt{-g}\Big|_p}{\epsilon}\right), \tag{1.3.23}$$

$$= \lim_{\epsilon\to 0}\left(\frac{\sqrt{-\det\left(g_{\mu\nu}(y^\alpha)\frac{\partial y^\mu}{\partial x^\rho}\frac{\partial y^\nu}{\partial x^\sigma}\right)} - \sqrt{-g}(x^\alpha)}{\epsilon}\right), \tag{1.3.24}$$

$$= \lim_{\epsilon\to 0}\left(\frac{\sqrt{-g}(y^\alpha)\det\left(\frac{\partial y^\mu}{\partial x^\rho}\right) - \sqrt{-g}(x^\alpha)}{\epsilon}\right), \tag{1.3.25}$$

$$= \lim_{\epsilon\to 0}\left(\frac{\sqrt{-g}(y^\alpha)(1+\epsilon\partial_\mu\xi^\mu + \mathcal{O}(\epsilon^2)) - \sqrt{-g}(x^\alpha)}{\epsilon}\right), \tag{1.3.26}$$

$$= \lim_{\epsilon\to 0}\left(\frac{[\sqrt{-g}(x^\alpha) + \epsilon\xi^\mu\partial_\mu\sqrt{-g}(x^\alpha)](1+\epsilon\partial_\mu\xi^\mu + \mathcal{O}(\epsilon^2)) - \sqrt{-g}(x^\alpha)}{\epsilon}\right), \tag{1.3.27}$$

$$= \lim_{\epsilon\to 0}\left(\frac{\epsilon\xi^\mu\partial_\mu\sqrt{-g}(x^\alpha) + \epsilon\sqrt{-g}(x^\alpha)\partial_\mu\xi^\mu + \mathcal{O}(\epsilon^2))}{\epsilon}\right), \tag{1.3.28}$$

$$\mathcal{L}_\xi\sqrt{-g} = \xi^\mu\partial_\mu\sqrt{-g} + \sqrt{-g}\partial_\mu\xi^\mu. \tag{1.3.29}$$

Given that $\mathcal{L}_\xi\sqrt{-g}$ has been calculated, it is straightforeward to calculate the Lie derivarive of a tensor density $\boldsymbol{\mathcal{T}} = \sqrt{-g}^w\boldsymbol{T}$ of weight w, where $\boldsymbol{T}$ is a regular tensor, using the Liebnitz rule in Eq. (1.2.43). The Lie derivative is,

$$\mathcal{L}_\xi\boldsymbol{\mathcal{T}} = \sqrt{-g}^w\left(\mathcal{L}_\xi\boldsymbol{T} + w\boldsymbol{T}\left(\frac{1}{\sqrt{-g}}\xi^\mu\partial_\mu\sqrt{-g} + \partial_\mu\xi^\mu\right)\right). \tag{1.3.30}$$

As would be expected, setting $w = 0$ returns the regular Lie derivative of a tensor. This can also be written as,

$$\mathcal{L}_\xi\boldsymbol{\mathcal{T}} = \widetilde{\mathcal{L}}_\xi\boldsymbol{\mathcal{T}} + w\boldsymbol{\mathcal{T}}\partial_\mu\xi^\mu, \tag{1.3.31}$$

where $\widetilde{\mathcal{L}}_\xi$ is the differential operator equivalent to the Lie derivate of the same tensor but with weight zero.

1.3.2 The Covariant Derivative

There are many types of derivative on a manifold, all related to each other, that we care about in the context of General Relativity. The simplest is the partial derivative,

$$\partial_\mu = \frac{\partial}{\partial x^\mu}, \tag{1.3.32}$$

which works much the same as always. Two other derivatives are the exterior derivative[3] and the Lie derivative which is discussed in section 1.2.5.

The purpose of the covariant derivative, denoted ∇_μ, is to generalise the partial derivative to curved spaces (or curvilinear coordinates). The covariant derivative exactly reduces to the partial derivative (∂_μ) in flat space with cartesian coordinates. As suggested by the name, the covariant derivative of an object is covariant; it obeys the tensor transformation law in section 1.3.1. The covariant derivative uses

[3] The antisymmetric derivative of a differential n-form (totally antisymmetric co-tensor of rank n) that returns a differential $(n+1)$-form.

a vector field $\boldsymbol{X}$ to map a (p, q) tensor field $\boldsymbol{T}$ to a (p, q) tensor field $\boldsymbol{\nabla_X T}$. Requiring the covariant derivative of a tensor to return another tensor may sound pedantic but it allows the writing of physical differential equations that are covariant, i.e. that hold in all coordiante systems. Encoding the laws of physics with tensor differential equations is explored in more detail in section 1.4.3.

To be the analogue of the partial derivative, three properties of the covariant derivative are required,

$$\boldsymbol{\nabla}_{f\boldsymbol{X}+g\boldsymbol{Y}}\boldsymbol{T} = f\boldsymbol{\nabla_X T} + g\boldsymbol{\nabla_Y T}, \tag{1.3.33}$$

$$\boldsymbol{\nabla_X}(a\boldsymbol{T} + b\boldsymbol{W}) = a\boldsymbol{\nabla_X T} + b\boldsymbol{\nabla_X W}, \tag{1.3.34}$$

$$\boldsymbol{\nabla_X}(f\boldsymbol{T}) = f\boldsymbol{\nabla_X T} + \boldsymbol{T}\boldsymbol{\nabla_X} f, \tag{1.3.35}$$

where a and b are constants, f and g are functions and $\boldsymbol{T}$ and $\boldsymbol{W}$ are tensors of equal type. These are exactly the same as the conditions imposed on Lie derivatives in section 1.2.5. From now on the coraviant derivative $\boldsymbol{\nabla}_{\boldsymbol{e}_\mu}$ with respect to a basis vector $\boldsymbol{e}_\mu$ will be written as ∇_μ.

Lets start by finding the covariant derivative of a of a scalar field φ. The partial derivative $\partial_\mu\varphi$ obeys the tensor transformation law for a co-vector,

$$\frac{\partial}{\partial\tilde{x}^\mu}\tilde{\varphi} = \frac{\partial}{\partial\tilde{x}^\mu}\varphi, \tag{1.3.36}$$

$$= \frac{\partial x^\nu}{\partial\tilde{x}^\mu}\frac{\partial}{\partial x^\nu}\varphi, \tag{1.3.37}$$

and therefore the $\nabla_\mu\varphi = \partial_\mu\varphi$. Note that $\varphi = \tilde{\varphi}$ for any point p as a scalar remains unchanged in a coordinate transformation. Complications arise when taking the partial derivative of any other higher rank tensor; let's demonstrate this with a vector $\boldsymbol{X}$.

$$\frac{\partial}{\partial\tilde{x}^\mu}\tilde{X}^\alpha = \frac{\partial}{\partial\tilde{x}^\mu}\left(\frac{\partial\tilde{x}^\alpha}{\partial x^\beta}X^\beta\right), \tag{1.3.38}$$

$$= \frac{\partial x^\nu}{\partial\tilde{x}^\mu}\frac{\partial}{\partial x^\nu}\left(\frac{\partial\tilde{x}^\alpha}{\partial x^\beta}X^\beta\right), \tag{1.3.39}$$

$$= \underbrace{\frac{\partial\tilde{x}^\alpha}{\partial x^\beta}\frac{\partial x^\nu}{\partial\tilde{x}^\mu}}_{\text{Tensor transformation law}}\frac{\partial}{\partial x^\nu}X^\beta + X^\beta\frac{\partial x^\nu}{\partial\tilde{x}^\mu}\frac{\partial}{\partial x^\nu}\left(\frac{\partial\tilde{x}^\alpha}{\partial x^\beta}\right), \tag{1.3.40}$$

and as can be seen, only the first term on the right hand side should exist if the components $\partial_\mu X^\alpha$ were to obey the tensor transformation law.

The problem with performing differentiation on tensors is that it requires the comparison of tensors at two different (infinitessimaly close) tangent spaces. Lie derivatives circumvented this problem by comparing two two tangent planes with a pullback defined by a diffeomorphism. Another way of overcoming this problem is to consider how the coordinate basis vectors change over the manifold, not just the components. Defining the covariant derivative of the basis vector as

$$\boldsymbol{\nabla}_{\boldsymbol{e}_\rho}\boldsymbol{e}_\nu = \nabla_\rho\boldsymbol{e}_\nu := \Gamma^\mu{}_{\nu\rho}\boldsymbol{e}_\mu \tag{1.3.41}$$

where $\Gamma^\mu{}_{\nu\rho}$ is called the connection due to it defining a connection between neighbouring tangent space. The connection can be used to get the covariant derivative of the vector field $\boldsymbol{X} = X^\rho\boldsymbol{e}_\rho$,

$$\nabla_\rho(X^\nu\boldsymbol{e}_\nu) = (\partial_\rho X^\nu)\boldsymbol{e}_\nu + X^\nu(\nabla_\rho\boldsymbol{e}_\nu), \tag{1.3.42}$$

$$= (\partial_\rho X^\nu)\boldsymbol{e}_\nu + X^\nu\Gamma^\mu{}_{\nu\rho}\boldsymbol{e}_\mu, \tag{1.3.43}$$

$$= (\partial_\rho X^\mu + \Gamma^\mu{}_{\nu\rho}X^\nu)\boldsymbol{e}_\mu. \tag{1.3.44}$$

Note that on the first line above we used $\nabla_\rho X^\nu = \partial_\rho X^\nu$ as the X^ν are being treated as a set of scalar function coefficients multiplying the basis vectors $\boldsymbol{e}_\mu$. Strictly we should write the covariant derivative of $\boldsymbol{X}$ as,

$$\boldsymbol{\nabla X} = (\nabla X)_\sigma{}^\mu\boldsymbol{e}_\mu\otimes\boldsymbol{\theta}^\sigma, \tag{1.3.45}$$

but for convenience the coefficients $(\nabla X)_\sigma{}^\mu$ are usually denoted as,

$$\nabla_\sigma X^\mu = \partial_\sigma X^\mu + \Gamma^\mu{}_{\nu\sigma} X^\nu. \tag{1.3.46}$$

This is a slight abuse of notation as $\nabla_\sigma X^\mu$ might be understood as the covariant derivate of the components X^μ, but really it denotes the component $\boldsymbol{\theta}^\sigma \cdot (\boldsymbol{\nabla X}) \cdot \boldsymbol{e}_\mu$ where $\boldsymbol{\nabla X}$ is given in Eq. (1.3.45).

Given that the covariant derivative of a scalar reduces to the partial derivative we can see that,

$$\nabla_\rho(\boldsymbol{e}_\mu : \boldsymbol{\theta}^\nu) = 0, \tag{1.3.47}$$

and using the Liebnitz rule,

$$\begin{aligned}
\nabla_\rho(\boldsymbol{e}_\nu : \boldsymbol{\theta}^\mu) &= (\nabla_\rho \boldsymbol{e}_\nu) : \boldsymbol{\theta}^\mu + \boldsymbol{e}_\nu : (\nabla_\rho \boldsymbol{\theta}^\mu), && (1.3.48)\\
&= (\Gamma^\sigma{}_{\nu\rho} \boldsymbol{e}_\sigma) : \boldsymbol{\theta}^\mu + \boldsymbol{e}_\nu : (\nabla_\rho \boldsymbol{\theta}^\mu), && (1.3.49)\\
&= \Gamma^\mu{}_{\nu\rho} + \boldsymbol{e}_\nu : (\nabla_\rho \boldsymbol{\theta}^\mu), && (1.3.50)\\
\boldsymbol{e}_\nu : (\nabla_\rho \boldsymbol{\theta}^\mu) &= -\Gamma^\mu{}_{\nu\rho}, && (1.3.51)
\end{aligned}$$

therefore we must have,

$$\nabla_\rho \boldsymbol{\theta}^\mu = -\Gamma^\mu{}_{\nu\rho} \boldsymbol{\theta}^\nu. \tag{1.3.52}$$

In an identical way to before, we might ask what is the covariant derivative of a co-vector $\boldsymbol{\omega} = \omega_\alpha \boldsymbol{\theta}^\alpha$. The covariant derivative $\boldsymbol{\nabla\omega}$ can be found like,

$$\begin{aligned}
\nabla_\sigma \boldsymbol{\omega} &= \nabla_\sigma(\omega_\alpha \boldsymbol{\theta}^\alpha), && (1.3.53)\\
&= \partial_\sigma(\omega_\alpha)\boldsymbol{\theta}^\alpha + \omega_\alpha \nabla_\sigma \boldsymbol{\theta}^\alpha, && (1.3.54)\\
&= \partial_\sigma(\omega_\alpha)\boldsymbol{\theta}^\alpha - \omega_\alpha \Gamma^\alpha{}_{\nu\sigma} \boldsymbol{\theta}^\nu, && (1.3.55)\\
&= (\partial_\sigma \omega_\alpha - \omega_\nu \Gamma^\nu{}_{\alpha\sigma})\boldsymbol{\theta}^\alpha. && (1.3.56)
\end{aligned}$$

Again, we used $\nabla_\sigma \omega_\alpha = \partial_\sigma \omega_\alpha$ as the components ω_α are scalar coefficients of the basis co-vectors $\boldsymbol{\theta}^\alpha$. Similarly to earlier, from now on the components $(\nabla\omega)_{\sigma\alpha}$ are written as $\nabla_\sigma \omega_\alpha$ even though this is a mild abuse of notation.

The covariant derivative of a general tensor can be found by following the simple rule of adding a connection symbol term for each index, for example,

$$\nabla_\mu T^{\alpha\beta\ldots}_{\lambda\nu\ldots} = \partial_\mu T^{\alpha\beta\ldots}_{\lambda\nu\ldots} + \Gamma^\alpha{}_{\sigma\mu} T^{\sigma\beta\ldots}_{\lambda\nu\ldots} + \Gamma^\beta{}_{\sigma\mu} T^{\alpha\sigma\ldots}_{\lambda\nu\ldots} + \ldots - \Gamma^\sigma{}_{\lambda\mu} T^{\alpha\beta\ldots}_{\sigma\nu\ldots} - \Gamma^\sigma{}_{\nu\mu} T^{\alpha\beta\ldots}_{\lambda\sigma\ldots} - \ldots\ . \tag{1.3.57}$$

1.3.3 The Connection

In flat space we are used to the idea that the partial derivative commutes, i.e. $\partial_\mu \partial_\nu = \partial_\nu \partial_\mu$, and this is trivially true in curved space too. However, the covariant derivative does not generally commute, $\nabla_\mu \nabla_\nu \neq \nabla_\nu \nabla_\mu$. Applying $\nabla_\mu \nabla_\nu - \nabla_\nu \nabla_\mu$ to a scalar field φ gives,

$$\begin{aligned}
(\nabla_\mu \nabla_\nu - \nabla_\nu \nabla_\mu)\varphi &= \nabla_\mu \nabla_\nu \varphi - \nabla_\nu \nabla_\mu \varphi, && (1.3.58)\\
&= \nabla_\mu \partial_\nu \varphi - \nabla_\nu \partial_\mu \varphi, && (1.3.59)\\
&= (\partial_\mu \partial_\nu - \partial_\nu \partial_\mu)\varphi - \Gamma^\sigma{}_{\nu\mu} \partial_\sigma \varphi + \Gamma^\sigma{}_{\mu\nu} \partial_\sigma \varphi, && (1.3.60)\\
&= (\Gamma^\sigma{}_{\mu\nu} - \Gamma^\sigma{}_{\nu\mu})\partial_\sigma \varphi, && (1.3.61)
\end{aligned}$$

where we used the fact that $\nabla_\mu \varphi = \partial_\mu \varphi$ for a scalar field. This non-commutativity of derivatives on a scalar field is known as torsion.

Torsion

If a connection is torsion free then $(\nabla_\mu\nabla_\nu - \nabla_\nu\nabla_\mu)\varphi = 0$ which implies ${\Gamma^\sigma}_{\nu\mu} = {\Gamma^\sigma}_{\mu\nu}$. This leads to two important tensor identities; first the antisymetric derivative of a co-vector,

$$\nabla_\mu A_\nu - \nabla_\nu A_\mu = \partial_\mu A_\nu - \partial_\nu A_\nu - \underbrace{({\Gamma^\sigma}_{\nu\mu} - {\Gamma^\sigma}_{\mu\nu})}_{=0} A_\sigma, \tag{1.3.62}$$

$$\nabla_\mu A_\nu - \nabla_\nu A_\mu = \partial_\mu A_\nu - \partial_\nu A_\nu, \tag{1.3.63}$$

and the second identity,

$$\boldsymbol{\nabla_X Y} - \boldsymbol{\nabla_Y X} = (X^\mu \nabla_\mu Y^\nu - Y^\mu \nabla_\mu X^\nu)\boldsymbol{e}_\nu, \tag{1.3.64}$$

$$= (X^\mu \partial_\mu Y^\nu - Y^\mu \partial_\mu X^\nu + {\Gamma^\nu}_{\sigma\mu} X^\mu Y^\sigma - {\Gamma^\nu}_{\sigma\mu} Y^\mu X^\sigma)\boldsymbol{e}_\nu, \tag{1.3.65}$$

$$= (X^\mu \partial_\mu Y^\nu - Y^\mu \partial_\mu X^\nu + ({\Gamma^\nu}_{\sigma\mu} - {\Gamma^\nu}_{\mu\sigma}) X^\mu Y^\sigma)\boldsymbol{e}_\nu, \tag{1.3.66}$$

$$= (X^\mu \partial_\mu Y^\nu - Y^\mu \partial_\mu X^\nu)\boldsymbol{e}_\nu, \tag{1.3.67}$$

$$\boldsymbol{\nabla_X Y} - \boldsymbol{\nabla_Y X} = [\boldsymbol{X}, \boldsymbol{Y}]. \tag{1.3.68}$$

The commutator bracket $[\boldsymbol{X}, \boldsymbol{Y}]$ of two vectors $\boldsymbol{X}$ and $\boldsymbol{Y}$ is defined by,

$$[X^\mu \partial_\mu, Y^\nu \partial_\nu] = X^\mu \partial_\mu (Y^\nu \partial_\nu) - Y^\nu \partial_\nu (X^\mu \partial_\mu), \tag{1.3.69}$$

$$= X^\mu \partial_\mu Y^\nu - Y^\nu \partial_\nu (X^\mu)\partial_\mu + X^\mu Y^\nu \partial_\mu \partial_\nu - Y^\nu X^\mu \partial_\nu \partial_\mu, \tag{1.3.70}$$

$$= (X^\mu \partial_\mu Y^\nu - Y^\mu \partial_\mu X^\nu)\partial_\nu, \tag{1.3.71}$$

where the basis vector $\boldsymbol{e}_\mu$ has been written as ∂_μ with the intention of acting on a function f over the manifold $\mathcal{M}$.

Metric Compatibility

Another useful property that can be imposed on the connection is metric compatibility; this is $\nabla_\mu g_{\rho\sigma} = 0$, where $\boldsymbol{g}$ is the metric tensor, which immediately tells us $\nabla_\mu g^{\alpha\beta} = 0$ as,

$$\nabla_\mu \delta^\alpha_\rho = 0, \tag{1.3.72}$$

$$= \nabla_\mu (g^{\alpha\nu} g_{\nu\rho}), \tag{1.3.73}$$

$$= g_{\nu\rho} \nabla_\mu g^{\alpha\nu} + g^{\alpha\nu} \underbrace{\nabla_\mu g_{\nu\rho}}_{=0}, \tag{1.3.74}$$

which implies that $\nabla_\mu g^{\alpha\nu} = 0$. Demanding metric compatibility may seem a little arbitrary but turns out to have many nice algebraic properties such as the raising and lowering of indeces with the metric commuting with the covariant derivatives,

$$\nabla_\mu T^{\alpha\beta\ldots} = \nabla_\mu g^{\alpha\rho} {T_\rho}^{\beta\ldots} = g^{\alpha\rho} \nabla_\mu {T_\rho}^{\beta\ldots}, \tag{1.3.75}$$

and the derivative of the length of a vector $\boldsymbol{X}$,

$$\nabla_\alpha |\boldsymbol{X}|^2 = \nabla_\alpha (X^\mu X_\mu) = \nabla_\alpha (g_{\mu\nu} X^\mu X^\nu) = 2X^\mu \nabla_\alpha X_\mu = 2X_\mu \nabla_\alpha X^\mu. \tag{1.3.76}$$

The Levi Civita-Connection

As it turns out, a connection that obeys Eqs. (1.3.33,1.3.34 & 1.3.35), is both torsion-free and metric-compatible, can be demanded. This connection is called the Levi-Civita connection. The Levi-Civita connection will always be assumed from now and leads to teh following unique form of connection coefficients,

$${\Gamma^\rho}_{\mu\nu} = \frac{1}{2} g^{\rho\sigma} (\partial_\mu g_{\sigma\nu} + \partial_\nu g_{\mu\sigma} - \partial_\sigma g_{\nu\mu}), \tag{1.3.77}$$

which are also called Christoffel symbols of the second kind. It is also common to see the connection coefficients with the lowered index

$$\Gamma_{\sigma\mu\nu} = \frac{1}{2}(\partial_\mu g_{\sigma\nu} + \partial_\nu g_{\mu\sigma} - \partial_\sigma g_{\nu\mu}), \tag{1.3.78}$$

this is also called a Christoffel symbol of the first kind. It is very important to note that even though the connection symbols may look like a tensor they are not a tensor. This can easily be seen from applying the tensor transformation law to the Christoffel symbol of the first kind,

$$\begin{aligned}
2\tilde{\Gamma}_{\sigma\mu\nu} &= \tilde{\partial}_\mu \tilde{g}_{\sigma\nu} + \tilde{\partial}_\nu \tilde{g}_{\mu\sigma} - \tilde{\partial}_\sigma \tilde{g}_{\nu\mu}, && (1.3.79)\\
&= \frac{\partial x^\alpha}{\partial \tilde{x}^\mu}\partial_\alpha \left(\frac{\partial x^\beta}{\partial \tilde{x}^\sigma}\frac{\partial x^\gamma}{\partial \tilde{x}^\nu} g_{\beta\gamma}\right) + \frac{\partial x^\gamma}{\partial \tilde{x}^\nu}\partial_\gamma \left(\frac{\partial x^\beta}{\partial \tilde{x}^\sigma}\frac{\partial x^\alpha}{\partial \tilde{x}^\mu} g_{\alpha\beta}\right) - \frac{\partial x^\beta}{\partial \tilde{x}^\sigma}\partial_\beta \left(\frac{\partial x^\alpha}{\partial \tilde{x}^\mu}\frac{\partial x^\gamma}{\partial \tilde{x}^\nu} g_{\gamma\alpha}\right), && (1.3.80)\\
&= \frac{\partial x^\alpha}{\partial \tilde{x}^\mu}\frac{\partial x^\beta}{\partial \tilde{x}^\sigma}\frac{\partial x^\gamma}{\partial \tilde{x}^\nu}\left(\partial_\alpha g_{\beta\gamma} + \partial_\gamma g_{\alpha\beta} - \partial_\beta g_{\gamma\alpha}\right)\\
&\qquad + \frac{\partial x^\alpha}{\partial \tilde{x}^\mu} g_{\beta\gamma}\partial_\alpha \left(\frac{\partial x^\beta}{\partial \tilde{x}^\sigma}\frac{\partial x^\gamma}{\partial \tilde{x}^\nu}\right) + \frac{\partial x^\gamma}{\partial \tilde{x}^\nu} g_{\alpha\beta}\partial_\gamma \left(\frac{\partial x^\beta}{\partial \tilde{x}^\sigma}\frac{\partial x^\alpha}{\partial \tilde{x}^\mu}\right) - \frac{\partial x^\beta}{\partial \tilde{x}^\sigma} g_{\gamma\alpha}\partial_\beta \left(\frac{\partial x^\alpha}{\partial \tilde{x}^\mu}\frac{\partial x^\gamma}{\partial \tilde{x}^\nu}\right), && (1.3.81)\\
&= 2\frac{\partial x^\alpha}{\partial \tilde{x}^\mu}\frac{\partial x^\beta}{\partial \tilde{x}^\sigma}\frac{\partial x^\gamma}{\partial \tilde{x}^\nu}\Gamma_{\beta\alpha\gamma}\\
&\qquad + \frac{\partial x^\alpha}{\partial \tilde{x}^\mu} g_{\beta\gamma}\partial_\alpha \left(\frac{\partial x^\beta}{\partial \tilde{x}^\sigma}\frac{\partial x^\gamma}{\partial \tilde{x}^\nu}\right) + \frac{\partial x^\gamma}{\partial \tilde{x}^\nu} g_{\alpha\beta}\partial_\gamma \left(\frac{\partial x^\beta}{\partial \tilde{x}^\sigma}\frac{\partial x^\alpha}{\partial \tilde{x}^\mu}\right) - \frac{\partial x^\beta}{\partial \tilde{x}^\sigma} g_{\gamma\alpha}\partial_\beta \left(\frac{\partial x^\alpha}{\partial \tilde{x}^\mu}\frac{\partial x^\gamma}{\partial \tilde{x}^\nu}\right), && (1.3.82)\\
&= 2\frac{\partial x^\alpha}{\partial \tilde{x}^\mu}\frac{\partial x^\beta}{\partial \tilde{x}^\sigma}\frac{\partial x^\gamma}{\partial \tilde{x}^\nu}\Gamma_{\beta\alpha\gamma} + \Xi_{\sigma\mu\nu}. && (1.3.83)\\
& && (1.3.84)
\end{aligned}$$

As can be seen above, if $\Xi_{\sigma\mu\nu} = 0$ then the $\Gamma_{\sigma\mu\nu}$ would transform as an $(0, 3)$ tensor, however this is not the case and the existance of nonzero $\Xi_{\sigma\mu\nu}$ means the Christoffel symbol of first kind is not a tensor but instead a symbol. The non-tensor nature of the Christoffel symbol of first kind is sufficient to prove that the Christoffel symbol of second kind is also not a tensor.

Lie Derivatives in the Levi Civita Connection

The covariant derivative ∇, described in section 1.3.2 can replace all partial derivatives in a Lie derivative due to the connection symbols $\left(\Gamma^\mu{}_{\rho\sigma}\right)$ cancelling out.

A special example of a Lie derivative is of the metric tensor, $\boldsymbol{g}$, giving

$$\begin{aligned}
(\mathcal{L}_\xi g)_{\mu\nu} &= \xi^\rho \partial_\rho g_{\mu\nu} + g_{\rho\nu}\partial_\mu \xi^\rho + g_{\mu\rho}\partial_\nu \xi^\rho, && (1.3.85)\\
&= \xi^\rho \nabla_\rho g_{\mu\nu} + g_{\rho\nu}\nabla_\mu \xi^\rho + g_{\mu\rho}\nabla_\nu \xi^\rho, && (1.3.86)
\end{aligned}$$

where $\nabla_\rho g_{\mu\nu} = 0$ is assumed from metric compatibility, described in section 1.3.3. In the case the Lie derivative vanishes we get Killing's equation

$$\nabla_\mu \xi_\nu + \nabla_\nu \xi_\mu = 0 \tag{1.3.87}$$

and a vector field $\boldsymbol{\xi}$ satisfying Killing's equation is called a Killing vector. Killings equation will be very important in section **??**.

Normal Coordinates

Consider the set of all affinely parameterised geodesics, parameterised with λ, passing through the point p on a manifold $\mathcal{M}$. At p, each geodesic has a tangent vector $X^\mu\big|_p$. For all geodesics, define p to be the origin with $\lambda = 0$ and $x^\mu = 0$. Following a geodesic associated with $X^\mu\big|_p$ to a parameter value of λ will map to a new point q close to p for small enough λ. Normal coordinates $x^\mu(\lambda)$ at $q(\lambda)$ are defined such that $x^\mu(\lambda) = \lambda X^\mu\big|_p$. Given that $X^\mu\big|_p$ is constant, the geodesic equation, from Eq. (1.2.76), becomes

$$\frac{\mathrm{d}^2 x^\mu(\lambda)}{\mathrm{d}\lambda^2} + \Gamma^\alpha{}_{\mu\nu}\frac{\mathrm{d}x^\mu(\lambda)}{\mathrm{d}\lambda}\frac{\mathrm{d}x^\nu(\lambda)}{\mathrm{d}\lambda} = \Gamma^\alpha{}_{\mu\nu}X^\mu\big|_p X^\nu\big|_p = 0. \tag{1.3.88}$$

Using the Levi-civita connection, the connection symbol must be symmetric in lower two indeces and this implies $\Gamma^\alpha{}_{\mu\nu} = 0$ as the geodesic equation must hold for generic $X^\mu\big|_p$. From the definition of the covariant derivative,

$$\partial_\alpha g_{\mu\nu} = \nabla_\alpha g_{\mu\nu} + \Gamma^\beta{}_{\alpha\nu}g_{\mu\beta} + \Gamma^\beta{}_{\alpha\mu}g_{\beta\nu}, \tag{1.3.89}$$

which must vanish in normal coordintes as $\Gamma^\alpha{}_{\mu\nu} = 0$ and the Levi-Civita connection demands $\nabla_\alpha g_{\mu\nu} = 0$. Therefore, it is possible to construct a coordinate system that at one point p both $\partial_\alpha g_{\mu\nu} = 0$ and $\Gamma^\alpha{}_{\mu\nu} = 0$; importantly $\partial_\alpha\partial_\beta g_{\mu\nu} \neq 0$. As well as the metric's first derivative vanishing at p, it is also possible to demand that $g_{\mu\nu}\big|_p = \eta_{\mu\nu}$, the Minkowski metric. This can be done with a set of ${}^{(j)}X^\mu\big|_p$, one for each normal coordinate x^j, that satisfy

$$\boldsymbol{g}({}^{(j)}\boldsymbol{X}\big|_p, {}^{(k)}\boldsymbol{X}\big|_p) = \eta_{jk}. \tag{1.3.90}$$

1.3.4 Curvature Tensors

We have already seen that with the Levi-Civita connection, the commuted derivative of a scalar field vanishes. But taking the commuted derivative of a vector field $\boldsymbol{X}$ gives,

$$(\nabla_\mu\nabla_\nu - \nabla_\nu\nabla_\mu)X^\sigma = (\partial_\mu\nabla_\nu - \partial_\nu\nabla_\mu)X^\sigma + (\Gamma^\sigma{}_{\mu\rho}\nabla_\nu - \Gamma^\sigma{}_{\nu\rho}\nabla_\mu)X^\rho - \underbrace{(\Gamma^\rho{}_{\nu\mu} - \Gamma^\rho{}_{\mu\nu})}_{=0}\nabla_\rho X^\sigma, \tag{1.3.91}$$

$$= \underbrace{(\partial_\mu\partial_\nu - \partial_\nu\partial_\mu)}_{=0}X^\sigma + (\partial_\mu\Gamma^\sigma{}_{\nu\rho} - \partial_\nu\Gamma^\sigma{}_{\mu\rho})X^\rho + (\Gamma^\sigma{}_{\mu\rho}\nabla_\nu - \Gamma^\sigma{}_{\nu\rho}\nabla_\mu)X^\rho, \tag{1.3.92}$$

$$= (\partial_\mu\Gamma^\sigma{}_{\nu\rho} - \partial_\nu\Gamma^\sigma{}_{\mu\rho})X^\rho + (\Gamma^\sigma{}_{\mu\rho}\partial_\nu - \Gamma^\sigma{}_{\nu\rho}\partial_\mu)X^\rho + (\Gamma^\sigma{}_{\mu\rho}\Gamma^\rho{}_{\nu\lambda} - \Gamma^\sigma{}_{\nu\rho}\Gamma^\rho{}_{\mu\lambda})X^\lambda, \tag{1.3.93}$$

$$= X^\rho(\partial_\mu\Gamma^\sigma{}_{\nu\rho} - \partial_\nu\Gamma^\sigma{}_{\mu\rho}) + (\Gamma^\sigma{}_{\mu\rho}\Gamma^\rho{}_{\nu\lambda} - \Gamma^\sigma{}_{\nu\rho}\Gamma^\rho{}_{\mu\lambda})X^\lambda, \tag{1.3.94}$$

where one should note that whenever a term appears after a derivative here it is to be differentiated, even if it is outside a bracket. We can introduce the Riemann tensor here from

$$(\nabla_\mu\nabla_\nu - \nabla_\nu\nabla_\mu)X^\sigma = R^\sigma{}_{\rho\mu\nu}X^\rho, \tag{1.3.95}$$

and setting $\boldsymbol{X} = \boldsymbol{e}_\rho$, the coordinate basis vector associated with the x^ρ coordinate, the Riemann tensor can be written as

$$R^\sigma{}_{\rho\mu\nu} = \partial_\mu\Gamma^\sigma{}_{\nu\rho} - \partial_\nu\Gamma^\sigma{}_{\mu\rho} + \Gamma^\sigma{}_{\mu\lambda}\Gamma^\lambda{}_{\nu\rho} - \Gamma^\sigma{}_{\nu\lambda}\Gamma^\lambda{}_{\mu\rho}. \tag{1.3.96}$$

Symmetries of the Riemann Tensor

Now we will discuss the symmetries of the Riemann tensor. Firstly, from the definition of the Riemann tensor, it follows that $R^\sigma{}_{\rho\mu\nu} = -R^\sigma{}_{\rho\nu\mu}$; this can be written succinctly as $R^\sigma{}_{\rho[\mu\nu]} = 0$. The next symmetry of the Riemann tensor will prove easy to derive using normal coordinates (described in section 1.3.3) at a point p where $\Gamma = 0$ (but $\partial\Gamma \neq 0$) to get

$$R^\sigma{}_{\rho\mu\nu}\big|_p = \partial_\mu\Gamma^\sigma{}_{\nu\rho} - \partial_\nu\Gamma^\sigma{}_{\mu\rho}, \tag{1.3.97}$$

and it is simple to show that $R^\sigma_{[\rho\mu\nu]} = 0$ as

$$R^\sigma{}_{[\rho\mu\nu]}\big|_p = \partial_{[\mu}\Gamma^\sigma{}_{\nu\rho]} - \partial_{[\nu}\Gamma^\sigma{}_{\mu\rho]} = 0, \tag{1.3.98}$$

as the antisymmetrisation of any connection symbol like ${\Gamma^\sigma}_{[\nu\rho]} = 0$. Given that the tensor equation $R^\sigma_{[\rho\mu\nu]} = 0$ is true at p in normal coordinates then it is true in any coordinate system; ontop of this the point p was arbitrary so therefore $R^\sigma_{[\rho\mu\nu]} = 0$ holds globally.

The next symmetry of the Riemann tensor is $R_{\sigma\rho\mu\nu} = R_{\mu\nu\sigma\rho}$. We can prove this again using normal coordiantes at a point p; here derivatives of the metric and it's inverse vanish, but second derivatives do not. The proof of the symmetry is as follows,

$$\begin{aligned} R_{\sigma\rho\mu\nu}\big|_p &= g_{\lambda\sigma}\partial_\mu {\Gamma^\lambda}_{\nu\rho} - g_{\lambda\sigma}\partial_\nu {\Gamma^\lambda}_{\mu\rho}, && (1.3.99)\\ &= \partial_\mu g_{\lambda\sigma}{\Gamma^\lambda}_{\nu\rho} - \partial_\nu g_{\lambda\sigma}{\Gamma^\lambda}_{\mu\rho}, && (1.3.100)\\ &= \partial_\mu \Gamma_{\sigma\nu\rho} - \partial_\nu \Gamma_{\sigma\mu\rho}, && (1.3.101)\\ &= \frac{1}{2}\left(\partial_\mu\partial_\rho g_{\sigma\nu} - \partial_\mu\partial_\sigma g_{\rho\nu} + \partial_\nu\partial_\sigma g_{\rho\mu} - \partial_\nu\partial_\rho g_{\sigma\mu}\right), && (1.3.102) \end{aligned}$$

and it is a simple to show that this final expression doesn't change under swapping indeces $\sigma \leftrightarrow \mu$ and $\rho \leftrightarrow \nu$.

The final symmetry of the Riemann tensor is the Bianchi identity, $\nabla_{[\lambda}R_{\sigma\rho]\mu\nu}=0$. Using normal coordinates at a point p, we can write

$$\nabla_\lambda R_{\sigma\rho\mu\nu}\big|_p = \partial_\lambda R_{\sigma\rho\mu\nu}\big|_p \tag{1.3.103}$$

as all the christoffel symbols generated by the covariant derivative cancel and therefore

$$2\nabla_\lambda R_{\sigma\rho\mu\nu}\big|_p = \partial_\lambda\partial_\mu\partial_\rho g_{\sigma\nu} - \partial_\lambda\partial_\mu\partial_\sigma g_{\rho\nu} + \partial_\lambda\partial_\nu\partial_\sigma g_{\rho\mu} - \partial_\lambda\partial_\nu\partial_\rho g_{\sigma\mu}. \tag{1.3.104}$$

Antisymmetrising over λ, ρ and σ makes each term vanish as the triple partial derivates always contain two of the antisymmetrised indeces and must vanish.

To summarise, we have the following symmetries of the Riemann tensor;

$$\begin{aligned} R_{\sigma\rho[\mu\nu]} &= 0, && (1.3.105)\\ R_{\sigma\rho\mu\nu} &= R_{\mu\nu\sigma\rho}, && (1.3.106)\\ \nabla_{[\lambda}R_{\sigma\rho]\mu\nu} &= 0. && (1.3.107) \end{aligned}$$

The first two of these can be used together to give another useful relation $R_{[\sigma\rho]\mu\nu} = 0$.

Contractions of the Riemann Tensor

Now that we have explored the Riemann tensor, it is time to introduce the Ricci tensor and Ricci scalar. The Ricci tensor $R_{\mu\nu}$ is simply defined by the unique, non-zero self contraction (or trace) of the Riemann tensor,

$$R_{\rho\mu} := {R^\mu}_{\rho\mu\nu} = R_{\sigma\rho\mu\nu}g^{\sigma\mu}. \tag{1.3.108}$$

Contracting the the Riemann tensor with $g^{\mu\nu}$ or $g^{\sigma\rho}$ would give zero due to the antisymmetries of those indeces in the tensor. Any other contractions, such as with $g^{\rho\mu}$ can be shown to be exactly the same (upto a minus sign) as contracting with $g^{\sigma\mu}$ using the symmetries of the Riemann tensor. The symmetries of the Riemann tensor guarentee that the Ricci tensor itself is symmetric. We can contract the Ricci tensor with itself (the same as taking the trace with the metric) to give us the Ricci scalar R,

$$R = g^{\rho\nu}R_{\rho\nu}. \tag{1.3.109}$$

We can also take the trace of the Bianchi identity in Eq. (1.3.107) which gives us

$$\begin{aligned} g^{\lambda\mu}g^{\rho\nu}(\nabla_\lambda R_{\sigma\rho\mu\nu} + \nabla_\rho R_{\lambda\sigma\mu\nu} + \nabla_\sigma R_{\rho\lambda\mu\nu}) &= 0, && (1.3.110)\\ \nabla^\mu R_{\sigma\mu} + \nabla^\nu R_{\sigma\nu} - \nabla_\sigma R &= 0, && (1.3.111)\\ \nabla^\mu R_{\mu\sigma} - \frac{1}{2}\nabla_\sigma R &= 0. && (1.3.112) \end{aligned}$$

Defining the Einstein tensor $\boldsymbol{G}$,

$$G_{\mu\nu} := R_{\mu\nu} - \frac{1}{2} g_{\mu\nu} R, \tag{1.3.113}$$

and using the contracted Bianchi identity with $\boldsymbol{\nabla g} = 0$ from metric compatibility,

$$\begin{aligned} \nabla^{\mu} G_{\mu\nu} &= \nabla^{\mu} R_{\mu\nu} - \frac{1}{2} \left(g_{\mu\nu} \nabla^{\mu} R + R \nabla^{\mu} g_{\mu\nu} \right), && (1.3.114) \\ &= \nabla^{\mu} R_{\mu\nu} - \frac{1}{2} \nabla_{\nu} R, && (1.3.115) \\ &= 0. && (1.3.116) \end{aligned}$$

The Einstein tensor $G_{\mu\nu}$ therefore has a vanishing divergence $\nabla_{\mu} G^{\mu\nu} = 0$.

One more useful contraction of the Riemann tensor is with a second Riemann tensor which gives the Kretschmann scalar k,

$$k := R_{\mu\nu\rho\sigma} R^{\mu\nu\rho\sigma}. \tag{1.3.117}$$

Both k and R are scalar fields so they are a coordiante invariant curvature measure; however section 1.4.5 will have more use of the Kretschmann scalar.

1.3.5 The Divergence Theorem

There is a generalisation of the divergence theorem to non-flat spaces, using differential geometry, which will be extremely useful in section [REF]. First, we will have to find a convenient form of the divergence $\nabla_{\mu} X^{\mu}$ of a vector $\boldsymbol{X}$. Expanding the covariant deriative gives

$$\begin{aligned} \nabla_{\mu} X^{\mu} &= \partial_{\mu} X^{\mu} + \Gamma^{\mu}{}_{\mu\nu} X^{\nu}, && (1.3.118) \\ &= \partial_{\mu} X^{\mu} + \frac{1}{2} g^{\mu\rho} \left(\partial_{\mu} g_{\rho\nu} + \partial_{\nu} g_{\mu\rho} - \partial_{\rho} g_{\mu\nu} \right) X^{\nu}, && (1.3.119) \\ &= \partial_{\mu} X^{\mu} + \frac{1}{2} g^{\mu\rho} \partial_{\nu} g_{\mu\rho} X^{\nu}. && (1.3.120) \end{aligned}$$

To simplify any furthar, we need to prove a matrix identity for a symmetric real matrix $\boldsymbol{M}$ with determinant M,

$$M^{-1} \partial_{\mu} M = M^{-1}_{ij} \partial_{\mu} M_{ij} = \mathrm{Tr}(\boldsymbol{M}^{-1} \partial_{\mu} \boldsymbol{M}). \tag{1.3.121}$$

Simplifying the left hand side in terms of the eigenvalues λ_i of $\boldsymbol{M}$. Given that $M = \det\{\boldsymbol{M}\} = \prod_i \lambda_i$ we can easily write

$$\begin{aligned} M^{-1} \partial_{\mu} M &= \partial_{\mu} \ln(|M|), && (1.3.122) \\ &= \partial_{\mu} \ln \left(\left| \prod_i \lambda_i \right| \right), && (1.3.123) \\ &= \partial_{\mu} \sum_i \ln(|\lambda_i|), && (1.3.124) \\ &= \sum_i \lambda_k^{-1} \partial_{\mu} \lambda_k. && (1.3.125) \end{aligned}$$

Now we will show that the right hand side of Eq. (1.3.121) also equals this. To do this we start by decomposing $\boldsymbol{M}$ into a diagonal matrix $\boldsymbol{D}$ like

$$\begin{aligned} \boldsymbol{M} &= \boldsymbol{O}^{-1} \boldsymbol{D} \boldsymbol{O}, && (1.3.126) \\ \boldsymbol{M}^{-1} &= \boldsymbol{O}^{-1} \boldsymbol{D}^{-1} \boldsymbol{O}, && (1.3.127) \end{aligned}$$

then using the fact that $\mathrm{Tr}(\boldsymbol{AB}....\boldsymbol{CD}) = \mathrm{Tr}(\boldsymbol{DAB}....\boldsymbol{C})$ for matrices $\boldsymbol{A}$, $\boldsymbol{B}$, $\boldsymbol{C}$, ... and $\boldsymbol{D}$,

$$\begin{aligned}
\mathrm{Tr}(\boldsymbol{M}^{-1}\partial_\mu \boldsymbol{M}) &= \mathrm{Tr}(\boldsymbol{O}^{-1}\boldsymbol{D}^{-1}\boldsymbol{O}\partial_\mu(\boldsymbol{O}^{-1}\boldsymbol{DO})), && (1.3.128)\\
&= \mathrm{Tr}(\boldsymbol{D}^{-1}\partial_\mu \boldsymbol{D}) + \mathrm{Tr}(\boldsymbol{O}^{-1}\partial_\mu \boldsymbol{O}) + \mathrm{Tr}(\boldsymbol{O}\partial_\mu \boldsymbol{O}^{-1}), && (1.3.129)\\
&= \mathrm{Tr}(\boldsymbol{D}^{-1}\partial_\mu \boldsymbol{D}) + \mathrm{Tr}(\underbrace{\partial_\mu(\boldsymbol{O}^{-1}\boldsymbol{O})}_{=0}), && (1.3.130)\\
&= \mathrm{Tr}(\boldsymbol{D}^{-1}\partial_\mu \boldsymbol{D}). && (1.3.131)
\end{aligned}$$

Given that $\boldsymbol{D}$ is the diagonal matrix composed of the eigenvalues λ_i then it follow that,

$$\begin{aligned}
\boldsymbol{D} &= \mathrm{Diag}\{\lambda_1, \lambda_2, ..., \lambda_n\}, && (1.3.132)\\
\partial_\mu \boldsymbol{D} &= \mathrm{Diag}\{\partial_\mu\lambda_1, \partial_\mu\lambda_2, ..., \partial_\mu\lambda_n\}, && (1.3.133)\\
\boldsymbol{D}^{-1} &= \mathrm{Diag}\{\lambda_1^{-1}, \lambda_2^{-1}, ..., \lambda_n^{-1}\}, && (1.3.134)
\end{aligned}$$

then finally $\mathrm{Tr}(\boldsymbol{D}^{-1}\partial_\mu \boldsymbol{D})$ can be evaluated in terms of the λ_i as follows,

$$\begin{aligned}
\mathrm{Tr}(\boldsymbol{D}^{-1}\partial_\mu \boldsymbol{D}) &= \sum_{ij} D_{ij}^{-1}\partial_\mu D_{ij}, && (1.3.135)\\
&= \sum_i D_{ii}^{-1}\partial_\mu D_{ii}, && (1.3.136)\\
&= \sum_i \lambda_i^{-1}\partial_\mu \lambda_i, && (1.3.137)
\end{aligned}$$

which proves that Eq. (1.3.121) is true. Applying Eq. (1.3.121) to the metric $\boldsymbol{g}$ gives,

$$g^{\mu\rho}\partial_\nu g_{\mu\rho} = g^{-1}\partial_\nu g, \tag{1.3.138}$$

and the covariant divergence $\nabla_\mu X^\mu$ of a vector $\boldsymbol{X}$ simplifies to

$$\begin{aligned}
\nabla_\mu X^\mu &= \partial_\mu X^\mu + \frac{1}{2g}\partial_\mu g, && (1.3.139)\\
&= \frac{1}{\sqrt{|g|}}\partial_\mu\left(\sqrt{|g|}X^\mu\right), && (1.3.140)
\end{aligned}$$

which in the standard pseudo-Riemannian spacetime is often written

$$\boldsymbol{\nabla}\cdot\boldsymbol{X} = \nabla_\mu X^\mu = \frac{1}{\sqrt{-g}}\partial_\mu(\sqrt{-g}X^\mu). \tag{1.3.141}$$

This equation will have much use later in section [REF] where the divergence of a vector will be integrated over a finite n-dimensional volume M in $\mathcal{M}$. In order to do this, the divergence theorem of curved space is used, this is

$$\int_M \boldsymbol{\nabla}\cdot\boldsymbol{X}\sqrt{|{}^{(n)}g|}\,\mathrm{d}^n x = \sum_i \int_{\partial M_i} \boldsymbol{s}^{(i)}\cdot\boldsymbol{X}\sqrt{|{}^{(n-1)}g^{(i)}|}\,\mathrm{d}^{n-1}x, \tag{1.3.142}$$

where the surface of M is divided into a set of $(n-1)$-dimensional surfaces ∂M_i; for each of these surfaces there is an $(n-1)$-dimensional metric ${}^{(n-1)}\boldsymbol{g}^{(i)}$ with determinant ${}^{(n-1)}g^{(i)}$ and unit normal vector $\boldsymbol{s}^{(i)}$ with ${}^{(n-1)}\boldsymbol{g}^{(i)}(\boldsymbol{s}^{(i)}, \boldsymbol{s}^{(i)}) = \pm 1$. When dealing with a pseudo-Riemannian manifold, we need to take care of the direction of $\boldsymbol{s}^{(i)}$; in the case that $\boldsymbol{s}^{(i)}$ is timelike it should be in-directed, and if it's spacelike then it should be out-directed.

CHECK THE LAST STATEMENT

MAYBE DERIVE DIV THEOREM, OTHERWISE REFERENCE IT

1.4 Relativity

1.4.1 Special Relativity

In the nineteenth century, it was widely believed that the universe was permeated by an invisible luminous aether. It was thought that light travels at a fixed speed through this aether; the aether could be thought of as a universal rest frame. A consequnece of this is that moving towards/away from a light source would cause the speed of oncoming light to vary. With that line of thought one could measure the earths speed through the aether by setting up an interferometer experiment. An interferometer sends a light beam through a splitter, dividing the beam into two perpendicular paths. The two beams then reach a seperate mirror and are reflected to a half-mirror that recombines the two beams after they have travelled identical distance. If the time taken for the two beams to complete their identical length journeys differs then an interference pattern will be seen at a detector placed after the half-mirror due to the phase change between the two beams. In 1887, Michelson and Morley conducted their famous interferometer experiment to measure the earth's velocity through the aether. They expected to see interfernece when the different beams made differnet angles with the earths velocity through the aether. However, no matter which way they oriented the experiment there was no interference pattern. This implied that light moved at exactly the same speed in any direction; this is only possible if earth is in the rest frame of the aether, but this cannot possibly be true as the planet accelerates round a circular path around a sun that is following a bigger circular path and so on. This famous result demonstrated that the speed of light (in vacuum) was the same in any directions in all inertial (non-accelerating) frames - a result that defied newtonian mechanics. This was a big hint that a new theory of dynamics was needed.

In 1905, Einstein published "On the Electrodynamics of Moving Bodies" [1] which contained a description of Special Relativity (SR). SR is essentially the idea that the laws of physics (excluding gravity) are the same in any inertial rest frame. A consequence of this is that it is impossible to measure the velocity of your own rest frame and no inertial frame is special. One big problem with SR is that it does not properly describe gravity and thus describes an infinite vaccum universe; this is a problem that will be adressed in the next sections. SR alone contains many interesting results such as time dilation, length contraction and the inclusion of time into distance measures.

Minkowski Space

In Newtonian physics the metric of flat space, using cartesian coordiantes, is,

$$g_{ij} = \delta_{ij} = \begin{pmatrix} 1 & 0 & 0 \\ 0 & 1 & 0 \\ 0 & 0 & 1 \end{pmatrix}, \tag{1.4.1}$$

with line element,

$$\mathrm{d}s^2 = \delta_{ij}\mathrm{d}x^i\mathrm{d}x^j = \mathrm{d}x^2 + \mathrm{d}y^2 + \mathrm{d}z^2. \tag{1.4.2}$$

In SR, time is promoted to a dimension and the metric is over space and time (spacetime); this flat 4-dimensional spacetime is called Minkowski space. The spacetime metric has a single negative eigenvalue and hence negative determinant. In cartesian coordinates, the flat spacetime metric is,

$$g_{\mu\nu} = \eta_{\mu\nu} = \begin{pmatrix} -1 & 0 & 0 & 0 \\ 0 & 1 & 0 & 0 \\ 0 & 0 & 1 & 0 \\ 0 & 0 & 0 & 1 \end{pmatrix}, \tag{1.4.3}$$

and line element is,

$$\mathrm{d}s^2 = \eta_{\mu\nu}\mathrm{d}x^\mu\mathrm{d}x^\nu = -\mathrm{d}t^2 + \mathrm{d}x^2 + \mathrm{d}y^2 + \mathrm{d}z^2, \tag{1.4.4}$$

where the speed of light has been set to unity again. Having a metric over a 4-dimensional spacetime is a non-intuitive concept where time is included into geometry and paths through spacetime can have negative length.

Tranforming between two inertial frames moving at constant velocity with respect to each other is done with a *boost* in special relativity. Boosting from frame S with coordinates x^μ to $\tilde{S}$ with coordinates $\tilde{x}^\mu$ we can write,

$$\mathrm{d}\tilde{x}^\mu = \frac{\partial \tilde{x}^\mu}{\partial x^\nu}\mathrm{d}x^\nu = \Lambda^\mu{}_\nu \mathrm{d}x^\nu, \tag{1.4.5}$$

where we will call $\mathbf{\Lambda}$ the boost matrix. Considering a boost along the x direction with a speed of v,

$$\mathrm{d}\tilde{t} = \gamma(\mathrm{d}t - v\mathrm{d}x), \tag{1.4.6}$$
$$\mathrm{d}\tilde{x} = \gamma(\mathrm{d}x - v\mathrm{d}t), \tag{1.4.7}$$
$$\mathrm{d}\tilde{y} = \mathrm{d}y, \tag{1.4.8}$$
$$\mathrm{d}\tilde{z} = \mathrm{d}z, \tag{1.4.9}$$

where $\gamma = 1/\sqrt{1-v^2}$ is the Lorentz factor. This transformation may seem odd at first glance but ensures that every inertial frame agrees on the same speed of light in all directions. For boosts in general directions $\mathbf{\Lambda}$ should be rotated with a spatial rotation matrix using the tensor transformation law.

1.4.2 General Relativity

It is a well known result of Newtonian physics that in a rotating reference frame, with angular velocity ω, a test particle will experience three fictitious forces; the centrifugal force that grows with distance from the origin, the coriolis force that depends on the velocity of the test particle, and the Euler force depending on $\partial_t\omega$. From the point of view of an observer in the rotating frame a free test particle would appear to accelerate which is a violation of Newton's first law if there is no external force. The curved path followed by the particle in the rotating reference frame is of course a constant speed straight line in the non-rotating inertial frame, and therefore the particle follows a geodesic. It is possible (but very involved) to do a coordinate transformation from the inertial frame to the rotating frame and find the metric $\tilde{\eta}_{\mu\nu}$ of the rotating frame using the tensor transfoormation law; it would then be possible to compute the geodesics in the rotating frame using Eq. (1.2.76).

The gravitational force can also be described as a fictitious force. In a non-accelerating frame, the path of a particle moving without external force is seen to accelerate towards massive bodies. The presence of matter density causes geodesics to curve. This is a property also possesed by curved spaces; the paths followed by a free particle on a curved background is often curved itself. Einsteins idea to incorporate gravity into relativity was to change the flat spacetime of special relativity to a curved spacetime; this theory is general relativity. In general relativity inertial frames follow geodesics in curved space; inertial frames accelerate with gravity. The gravitational force is a fictitious force arising from departing from an inertial frame. This explains why an observer standing on earth experiences a reaction force, the frame of the observer is not following a geodesic (not an inertial frame) and therefore to counteract the fictitious gravitational force the ground must push back with a reaction force. The other viewpoint is that the observer must push off of the earth to deviate from their geodesic.

Worldlines and Causality

Consider a particle moving through spacetime, the motion can be described with coordinates like $x^\mu(\tau)$ which is called a worldline. Here τ denotes *proper time*, the time experienced by the particle following the worldline. The 4-velocity along a worldline is,

$$v^\mu(\tau) = \frac{\mathrm{d}x^\mu}{\mathrm{d}\tau}(\tau). \tag{1.4.10}$$

In general relativity, the line element $\mathrm{d}s$ elapsed along a coordinate interval $\mathrm{d}x^\mu$ is,

$$\mathrm{d}s^2 = g_{\mu\nu}\mathrm{d}x^\mu \mathrm{d}x^\nu, \tag{1.4.11}$$

and for a particle with 4-velocity $\boldsymbol{v}$ is,

$$\mathrm{d}s^2 = g_{\mu\nu}\frac{\mathrm{d}x^\mu}{\mathrm{d}\tau}\frac{\mathrm{d}x^\nu}{\mathrm{d}\tau}\mathrm{d}\tau^2 = g_{\mu\nu}v^\mu v^\nu \mathrm{d}\tau^2 = \boldsymbol{v}\cdot\boldsymbol{v}\,\mathrm{d}\tau^2. \tag{1.4.12}$$

As shown in section 1.2.8, if a worldline $x^\mu(\lambda)$ parameterised by λ is a geodesic then $g_{\mu\nu}\dot{x}^\mu\dot{x}^\nu$ is constant where the dot denotes a derivative with respect to λ. Equating $\lambda = \tau$ gives $\dot{x}^\mu = v^\mu$ which tells us that $\boldsymbol{v}\cdot\boldsymbol{v}$, or $|\boldsymbol{v}|^2$, is constant along a world line. If $|\boldsymbol{v}|^2 < 0$ then the geodesic is *timelike*; similarly if $|\boldsymbol{v}|^2 > 0$ then the geodesic is *spacelike*. In the special case that $|\boldsymbol{v}|^2 = 0$, the curve is called *null*. Physical massive particles must travel along timelike intervals and massless particles must travel along null ones. Information cannot travel faster than light (which follows null geodesics) and hence all spacelike intervals are intraversable. Given that $|\boldsymbol{v}|^2$ is a scalar, it is unchanged by a coordinate transformation, this means that all observers in all frames (and using any coordinate system) will agree on whether an interval is timelike, spacelike or null.

1.4.3 Physics in Curved Space

General relativity postulates that (locally) the laws of physics in a free falling frame are indistinguishable from special relativity. Any equation of motions that we want to hold in general relativity must agree with special relativity in the flat-space limit. As a general rule, if there is a law of physics expressed as a differential equation in Minkowski space that we want to use in curved space, we must replace all partial derivatives of fields with co-variant derivatives of tensor fields. This process is called the minimal coupling approach and is explored in more detail at the end of section 1.4.7.

The Wave Equation

To derive the curved space wave equation we start with the wave equation for a scalar field ϕ in Minkowski space,

$$\frac{1}{c^2}\frac{\partial^2}{\partial t^2}\phi(x^i,t) - \left(\frac{\partial^2}{\partial x^2} + \frac{\partial^2}{\partial y^2} + \frac{\partial^2}{\partial z^2}\right)\phi(x^i,t) = 0, \tag{1.4.13}$$

using cartesian coordinates and c as the speed of light which we will set to one. It should be noted that this equation can only be written down in one coordinate system, changing coordinate system would changing the explicit form of the equation of motion. In SR, using the language of tensor calculus, we can write this as,

$$\eta^{\mu\nu}\partial_\mu\partial_\nu\phi = 0, \tag{1.4.14}$$

where $\eta^{\mu\nu}$ is the inverse metric of flat space. To adapt this to curved space we follow the minimal coupling procedure and replace $\boldsymbol{\eta} \to \boldsymbol{g}$ and $\partial_\mu \to \nabla_\mu$ giving,

$$g^{\mu\nu}\nabla_\mu\nabla_\nu\phi = 0. \tag{1.4.15}$$

This equation is fully covariant as it is a contraction of a tensor with some covariant derivatives; it is a tensor differential equation. Writing the laws of physics as tensor equations is extremely useful as they can be written without reference to an explicit coordinate system. If a coordinate system is then picked, assuming knowledge of $g_{\mu\nu}$, then the wave equation becomes

$$g^{\mu\nu}\nabla_\mu\nabla_\nu\phi = g^{\mu\nu}\nabla_\mu\partial_\nu\phi = 0, \tag{1.4.16}$$
$$= g^{\mu\nu}\partial_\mu\partial_\nu\phi - g^{\mu\nu}\Gamma^\rho{}_{\mu\nu}\partial_\rho\phi, \tag{1.4.17}$$

in terms of partial derivatives and covariant derivatives.

Equation (1.4.15) is not the only tensor equation that returns Eq. (1.4.13) in the limit of flat space (and cartesian coordiantes). What is to stop us arbitrarily adding terms that vanish in the flat-space limit? For a simple example one is free to choose the wave equation to be,

$$g^{\mu\nu}\nabla_\mu\nabla_\nu\phi + f(\phi)R^n = 0, \tag{1.4.18}$$

for constant n, function f and the Ricci scalar R from section 1.3.4. This equation certainly returns the regular wave equation in the low curvature limit as $R \to 0$. Following the rules of minimal coupling, the general rule is to keep things simple and terms such as R which are proportional to second order derivaties of the metric are thought to be less dominant that terms such as $\Gamma^\mu{}_{\rho\sigma}$ which are proportional to first derivatives of the metric. Navigating this minefield of which terms to include in the laws of physics is tricky and can leads to the topic of modified gravity as discussed at the end of section 1.4.7, the next simplest theories beyond general relativity.

Electromagnetism

Electromagnetism can also be written in terms of tensor differential equations suitable for use in curved space. Traditionally, Maxwell's equations of electromagnetism are written as,

$$\begin{aligned}
\boldsymbol{\nabla}\cdot\boldsymbol{E} &= \frac{\rho}{\epsilon_0}, && (1.4.19)\\
\boldsymbol{\nabla}\cdot\boldsymbol{B} &= 0, && (1.4.20)\\
\boldsymbol{\nabla}\times\boldsymbol{E} + \frac{\mathrm{d}\boldsymbol{B}}{\mathrm{d}t} &= 0, && (1.4.21)\\
\boldsymbol{\nabla}\times\boldsymbol{B} - \frac{\mathrm{d}\boldsymbol{E}}{\mathrm{d}t} &= \mu_0\boldsymbol{J} && (1.4.22)
\end{aligned}$$

for charge density ρ, electric field $\boldsymbol{E}$, magnetic field $\boldsymbol{B}$ and current density $\boldsymbol{J}$. Note these differential equations are written using vector calculus in flat space, not differential geometry and tensor calculus; the bold faced fields are therefore 3-vectors. In spacetime, the current density and charge are promoted to a single 4-vector $j^\mu = \{\rho, j^i\}$ and the 6 degrees of freedom of the electromagnetic field are encoded in the components $F_{\mu\nu}$ of an antisymmetric tensor $\boldsymbol{F}$. The four electromagnetic potentials ϕ and A_i, defined by $E_i = -\partial_i\phi - \partial_t A_i$ and $\boldsymbol{B} = \boldsymbol{\nabla}\times\boldsymbol{A}$, are also combined into one 4-vector $A_\mu = \{-\phi, A_i\}$. In cartesian coordinates, the Electromagnetic field tensor $\boldsymbol{F}$ is,

$$F_{\mu\nu} = \nabla_\mu A_\nu - \nabla_\nu A_\nu = \partial_\mu A_\nu - \partial_\nu A_\nu, \tag{1.4.23}$$

where the swapping between $\partial_\mu \leftrightarrow \nabla_\mu$ is possible due to the cancellation of Christoffel symbols. To elucidate, in Minkowski space with Cartesian coordinates the field tensor is,

$$F_{\mu\nu} = \partial_\mu A_\nu - \partial_\nu A_\nu = \begin{pmatrix} 0 & E_x & E_y & E_z \\ -E_x & 0 & B_z & -B_y \\ -E_y & -B_z & 0 & B_x \\ -E_z & B_y & -B_x & 0 \end{pmatrix}. \tag{1.4.24}$$

The vector potential A_μ has a gauge transformation like $A_\mu \to A_\mu + \partial_\mu f$, for some scalar field f, that leaves the physically measureable field $F_{\mu\nu}$ unchanged,

$$\begin{aligned}
F_{\mu\nu} \to &\partial_\mu(A_\nu + \partial_\nu) - \partial_\nu(A_\mu + \partial_\mu), && (1.4.25)\\
&= \partial_\mu A_\nu - \partial_\nu A_\mu + \underbrace{\partial_\mu\partial_\nu f - \partial_\nu\partial_\mu f}_{=0}, && (1.4.26)\\
&= F_{\mu\nu}. && (1.4.27)
\end{aligned}$$

In curved space, the Maxwell Eqs. (1.4.19) and (1.4.22) in tensor form are,

$$\nabla_\mu F^{\mu\nu} = \mu_0 j^\nu, \tag{1.4.28}$$

as $\mu_0\epsilon_0 = c^{-2} = 1$ in natural units. The other two Maxwell Eqs. (1.4.20) and (1.4.21) are identically true from computing $\partial_{[\mu}F_{\alpha\beta]}$,

$$\partial_{[\mu}F_{\alpha\beta]} = \partial_\mu\partial_\alpha A_\beta - \partial_\mu\partial_\beta A_\alpha + \partial_\alpha\partial_\beta A_\mu - \partial_\alpha\partial_\mu A_\beta\partial_\beta\partial_\mu A_\alpha - \partial_\beta\partial_\alpha A_\mu, \tag{1.4.29}$$

$$\partial_{[\mu}F_{\alpha\beta]} = 0, \tag{1.4.30}$$

which is equivalent to $\nabla_{[\mu}F_{\alpha\beta]}$ due to the cancellation of Christoffel symbols.

The Stress-Energy-Momentum Tensor

At the heart of field theory in physics is the stress-energy-momentum tensor $\boldsymbol{T}$, also called the energy-momentum tensor or stress tensor for short. Roughly speaking, component T^{00} is energy density, components $T^{0i} = T^{i0}$ contain energy flux or momentum density and components $T^{ij} = T^{ji}$ contain momentum fluxes. The diagonal part of T^{ij} can also be though of as containing pressure and the off-diagonal terms containing shear stress. In flat space, the conservation of energy and momentum can be written as,

$$\partial_\mu T^{\mu\nu} = 0, \tag{1.4.31}$$

in the absence of external forces. Equation (1.4.31) is also called the continuity equation and can be split into two sets of familiar equations,

$$\partial_0 T^{00} = -\partial_i T^{i0}, \tag{1.4.32}$$

$$\partial_0 T^{0j} = -\partial_i T^{ij}, \tag{1.4.33}$$

where the first equation states *"The rate of change of energy density is equal and opposite to the divergence of energy flux density"* and the second equation states *"The rate of change of momentum density is equal and opposite to the divergence of momentum flux density"*.

The stress tensor is also very useful in curved space and the continuity equation becomes,

$$\nabla_\mu T^{\mu\nu} = \partial_\mu T^{\mu\nu} + \Gamma^\mu{}_{\mu\rho}T^{\rho\nu} + \Gamma^\nu{}_{\mu\rho}T^{\mu\rho} = 0, \tag{1.4.34}$$

where the partial derivative has been replaced with a covariant derivative in accordance with minimal coupling. This can be rewtitten using Eq. (1.3.141) as,

$$\partial_\mu(\sqrt{-g}T^{\mu\nu}) = -\sqrt{-g}\Gamma^\nu{}_{\mu\rho}T^{\mu\rho}, \tag{1.4.35}$$

$$\partial_\mu(\mathcal{T}^{\mu\nu}) = -\Gamma^\nu{}_{\mu\rho}\mathcal{T}^{\mu\rho}, \tag{1.4.36}$$

where the second equation writes the stress tensor as a tensor density $\boldsymbol{\mathcal{T}} = \sqrt{-g}\boldsymbol{T}$ making the equation resemble the flat space continuity equation more closely. This modification of traditional continuity of energy and momentum to curved spaces will be revisited in section **??**.

1.4.4 The Einstein Equation

We have already seen how the equations of motion for matter can be promoted to curved space; building on the vague notion of matter causing spacetime curvature it would be helpful to have a mathematical law saying how much curvature is caused by a given matter distribution. The first guess that Einstein arrived at was to write $R_{\mu\nu} = kT_{\mu\nu}$ for some constant k. The problem is that given $\nabla_\mu T^{\mu\nu} = 0$ is the generic equation of continuity for matter, it would imply $\nabla_\mu R^{\mu\nu}$ vanishes which is not generally true. As shown in Eq. (1.3.115), the Einstein tensor $G_{\mu\nu}$ does satisfy $\nabla_\mu G^{\mu\nu} = 0$; the next simplest guess at a physical law for spacetime curvature would be $G_{\mu\nu} = kT_{\mu\nu}$. Remarkebly this turns out to be correct and has succesfully described all gravitational physics to date. The Einstein equation,

$$R_{\mu\nu} - \frac{1}{2}g_{\mu\nu}R = \frac{8\pi G}{c^4}T_{\mu\nu}, \tag{1.4.37}$$

where $G_{\mu\nu} = R_{\mu\nu} - g_{\mu\nu}R/2$, is at the core of general relativity. This equation relates spacetime curvature, encoded in the Einstein tensor $G_{\mu\nu}$, to the matter distribution described by the stress tensor $T_{\mu\nu}$. This leads nicely to Wheeler's insightful one line summary of general relativity:

"Spacetime tells matter how to move; matter tells spacetime how to curve."

This desceptively simple equation can describe an infinite amount of vastly diverse spacetime geometries including regular flat Minkowski space, black holes, stars, planets, gravitational waves and even the entire universe; to properly describe the entire universe a small modification has to be made to this equation as shown in section 1.4.6. To be able to solve this equation in the presence of matter an equation of motion to dictate how matter moves is also required.

General Relativity in Vacuum

In the case of a vacuum spacetime with $T_{\mu\nu} = 0$, or one where the matter distribution is considered so small that it does not cause a spacetime curvature backreaction, the Einstein equation simplifies greatly to

$$G_{\mu\nu} = 0. \tag{1.4.38}$$

Taking the trace of the above equation and the definition of $G_{\mu\nu} = R_{\mu\nu} - g_{\mu\nu}R/2$, we see that,

$$g^{\mu\nu}G_{\mu\nu} = 0 = g^{\mu\nu}(R_{\mu\nu} - \frac{1}{2}Rg_{\mu\nu}) = R(1 - \frac{D}{2}), \tag{1.4.39}$$

where D is the number of spacetime dimensions. Clearly for $D \neq 2$ a vanishing einstein implies a vanishing Ricci scalar R; if the Ricci scalar vanishes then the Einstein equation in vacuum simplifies to

$$R_{\mu\nu} = 0. \tag{1.4.40}$$

1.4.5 Black Holes

As it turns out, vacuum General Relativity can describe more than just Minkowski space. Arguably the most important family of solutions to Einstein's equations in vacuum are black holes. The first black hole solution was found by Karl Schwarzschild, whos surname fittingly means "*black shield*" in German. This solution, known as the Schwarzschild solution, was discovered in 1916 with the intention of computing the spacetime curvature in the vacuum about a spherically symmetric mass such as stars and planets. The solution for $g_{\mu\nu}$ was assumed to take the following ansatz,

$$\mathrm{d}s^2 = g_{\mu\nu}\mathrm{d}x^\mu\mathrm{d}x^\nu = -A(r)\mathrm{d}t^2 + B(r)\mathrm{d}r^2 + r^2\left(\mathrm{d}\theta + \sin^2(\theta)\mathrm{d}\phi^2\right), \tag{1.4.41}$$

which is manifestly spherically symmetric and static; in the case $A(r) = B(r) = 1$ the solution is exactly Minkowski space in spherical polar coordinates. By solving the Einstein equation in vacuum ($R_{\mu\nu} = 0$) the following solution can be found,

$$g_{\mu\nu}\mathrm{d}x^\mu\mathrm{d}x^\nu = -\left(1 - \frac{2Gm}{rc^2}\right)\mathrm{d}t^2 + \left(1 - \frac{2Gm}{rc^2}\right)^{-1}\mathrm{d}r^2 + r^2\left(\mathrm{d}\theta + \sin^2(\theta)\mathrm{d}\phi^2\right). \tag{1.4.42}$$

This is known as the Schwarzschild solution. The constants G and c are included for completeness, but are equal to one in geometric units or Planck units. The Schwarzschild solution describes the spacetime about a non-spinning sphere of mass m and as $r \to \infty$ or $m \to 0$ we approach the vacuum Minkowski spacetime as desired. What Schwarzschild didn't realise before his untimely death was that his solution could infact be trusted down to vanishing radii and describes the eternal (or static), non-spinning black hole of mass m called the Schwarzschild black hole.

Many other black hole solutions have been found to date. These solutions include the spinning *Kerr* black hole, non-spinning electromagnetically charged *Reissner-Nordström* black hole and spinning electromagnetically charged *Kerr-Newman* black hole. Non asymptotically flat black holes in cosmological backgrounds have also been found. In modified gravity theories, briefly discussed in section 1.4.7, many exotic black hole solutions exist.

Polar-Areal Coordinates

The type of coordinates used in the Schwarzschild solution are called polar-areal coordinates; these are coordinates that satisfy $g_{\theta\theta} = r^2$, $g_{\phi\phi} = \sin^2(\theta)r^2$ and otherwise $g_{\mu\phi} = g_{\mu\theta} = 0$. Polar areal coordinates return a length of $2\pi r_0$ when integrating the length of a complete circle at fixed radius r_0. This can be calculated using Eq. (1.2.62) and integrating with respect to ϕ around a circle while keeping $t = t_0$, $r = r_0$ and $\theta = \pi/2$ constant,

$$\int_0^{2\pi} \sqrt{g_{\phi\phi}}\Big|_{t=t_0,r=r_0,\theta=\frac{\pi}{2}} \mathrm{d}\phi = r_0 \sin\left(\frac{\pi}{2}\right) \int_0^{2\pi} \mathrm{d}\phi = 2\pi r_0, \tag{1.4.43}$$

which is the same result at in regular flat space. Using Eq. (1.2.69) the surface area of a sphere with $t = t_0$, $r = r_0$ can be calculated like

$$\int_0^{\pi} \left[\int_0^{2\pi} \sqrt{g_{\phi\phi}g_{\theta\theta}}\Big|_{t=t_0,r=r_0} \mathrm{d}\phi\right] \mathrm{d}\theta = r_0^2 \int_0^{\pi} \left[\int_0^{2\pi} \mathrm{d}\phi\right] \sin^2(\theta)\,\mathrm{d}\theta = 4\pi r_0^2, \tag{1.4.44}$$

where $\sqrt{g_{\phi\phi}g_{\theta\theta}}$ is the determinant of the metric on the two-dimensional surface defined by $t = t_0$ and $r = r_0$. Both the circumference of a circle and the area of a sphere are the same as would be in flat space, this property comes from the metric ansatz in Eq. (1.4.41).

Coordinate Singularities and Physical Singularities

There is obviously some kind problem at radius $r_s = 2m$ (or $r_s = 2mG/c^2$ in S.I. units), known as the Schwarzschild radius, as g_{rr} diverges here. For physical planets and stars observed the radius of the object would be much larger than the Schwarzschild metric so the solution should not be trusted inside the object as it has been derived in vacuum. But in order to describe black holes we must consider radii down to $r = 0$. The problem at the Schwarzschild radius is due to the choice of coordinates and is not physically problematic. An easy way to show this is to compute a curvature scalar[4] and show that it is finite and smooth at $r = r_s$. The first choice of curvature scalar might be the Ricci scalar, but this is zero in vaccum so is not useful. Vaccum general relativity asserts that $R_{\mu\nu} = 0$, while that guarentees that $R = 0$ it does not guarentee that $R_{\mu\nu\rho\sigma} = 0$. Another curvature scalar is the Kretschmann scalar k, defined in Eq. (1.3.117), which does not generally vanish in vacuum. Calculating the Kretschmann scalar for the Schwarzschild metric gives,

$$k_{sc} = \frac{48m^2}{r^6}, \tag{1.4.45}$$

in polar-areal coordinates. As can be seen, k is continuous and infinitely differentiable at $r = 2m$. However, as $r \to 0$, $k \to \infty$ and there is a real coordinate independant singularity called a physical singularity.

To remove the coordinate singularity at $r = 2m$, new coordinate singularities can be introduced. One example is to use ingoing-Eddington-Finkelstein coordinates $\{v, s, \theta, \phi\}$ defined by

$$\frac{\mathrm{d}s}{\mathrm{d}r} = \left(1 - \frac{2m}{r}\right), \tag{1.4.46}$$

$$v = t + s, \tag{1.4.47}$$

[4]Scalar curvature invariants are useful as if they diverge in one coordinate system then they must diverge in all coordinate systems as they do not transform under coordinate transformations. It should be noted that $\sqrt{-g}$ is a scalar density and not a true scalar so is not a scalar curvature invariant.

which transforms the line element to,

$$g_{\mu\nu}x^{\mu}x^{\nu} = -\left(1 - \frac{2m}{r}\right)\mathrm{d}v^2 + 2\mathrm{d}v\mathrm{d}r + r^2\left(\mathrm{d}\theta + \sin^2(\theta)\mathrm{d}\phi^2\right), \tag{1.4.48}$$

and as can be seen the metric no longer diverges at $r = 2m$. Being careful to notice that now the metric is not diagonal, the metric determinant can be calculated, giving $\sqrt{-g} = r^2\sin(\theta)$. Given that the metric is finite and the metric determinant is non-zero at $r = 2m$, the metric inverse is guarenteed to be well behaved at $r = 2m$ aswell. It has been demonstrated that the coordinate singularity at $r = 2m$ in Schwarzschild polar-areal vanishes when using ingoing-Eddington-Finkelstein coordinates.

Throughout this section we have ignored the fact that the inverse metric also diverges as $\theta \to 0$ or $\theta \to \pi$, this is a coordinate singularity that is present in flat space (which is equivalent to the Schwarzshild spacetime with $m = 0$). This coordinate singularity arises in flat space due to the azimuthal angle ϕ being undefined at $\theta = 0$ and $\theta = \pi$. There are no physical singularities in flat space, as you might expect, and these coordinate singularities vanish when using cartesian coordinates.

Isotropic Coordinates

A coordinate system that will be very useful later on is the isotropic coordinate system. Isotropic coordinates are have the line element,

$$g_{\mu\nu}\mathrm{d}x^{\mu}\mathrm{d}x^{\nu} = -\Omega(r)^2\mathrm{d}t^2 + \Psi^2(r)\mathrm{d}s^2_{\text{flat}}, \tag{1.4.49}$$

where $\mathrm{d}s^2_{\text{flat}}$ is the flat space Euclidean line element. For example, in spherical polar and cartesian spatial coordinates, the isotropic line element becomes,

$$\begin{aligned} g_{\mu\nu}\mathrm{d}x^{\mu}\mathrm{d}x^{\nu} &= -\Omega(r)^2\mathrm{d}t^2 + \Psi^2(r)\left(\mathrm{d}r^2 + r^2\left(\mathrm{d}\theta^2 + \sin^2(\theta)\mathrm{d}\phi^2\right)\right), && (1.4.50)\\ &= -\Omega(r)^2\mathrm{d}t^2 + \Psi^2(r)\left(\mathrm{d}x^2 + \mathrm{d}y^2 + \mathrm{d}z^2\right), && (1.4.51)\end{aligned}$$

where $r^2 = x^2 + y^2 + z^2$.

The Schwarzschild black hole solution can also be expressed in isotropic coordinates,

$$= -\left(\frac{1 - \frac{m}{2r}}{1 + \frac{m}{2r}}\right)^2\mathrm{d}t^2 + \left(1 + \frac{m}{2r}\right)^4\mathrm{d}s^2_{\text{flat}}. \tag{1.4.52}$$

As $r \to \infty$ the line element reduces to the Minkowski space one. The radius $r = m/2$ has the same coordinate singularity that was seen in polar areal coordinates and this is the Schwarzschild radius in isotropic coordinates. At first glance one might think that there is also the same physical singularity at $r = 0$. However, if a new radial coordiante ξ is used, where $r = \frac{m^2}{4\xi}$, the line element becomes,

$$g_{\mu\nu}\mathrm{d}x^{\mu}x^{\nu} = -\left(\frac{1 - \frac{m}{2\xi}}{1 + \frac{m}{2\xi}}\right)^2\mathrm{d}t^2 + \left(1 + \frac{m}{2\xi}\right)^4\left(\mathrm{d}\xi^2 + \xi^2(\mathrm{d}\theta^2 + \sin^2(\theta)\mathrm{d}\phi^2)\right). \tag{1.4.53}$$

This is an intreaguing result, inverting the radial coordinate about $r = 2/m$ has returned an exactly identical metric. Given that at $r = \infty$ we have flat space this implies that at $\xi = \infty$ (or $r = 0$) there is another separate flat space, not the physical singularity that might have been expected. The black hole exterior $m/2 < r < \infty$ must be identical to the volume $m/2 < \xi < \infty$ (also written as $m/2 > r > 0$), hence there are two asymptotically flat universes joined by the surface $r = m/2$; this surface is the Einstein-Rosen bridge. The Einstein-Rosen bridge is in-traversable, to cross this brigde would require faster than light travel which is forbidden. The geometry of the isotropic black hole is shown in Fig. (1.2).

The reason that the physical singularity at $r = 0$ does not appear in isotropic coordinates is desceptively simple; in isotropic coordinates $r = 0$ does not correspond to the same point on the manifold as $r = 0$ does in the polar areal gauge for any value of t, θ or ϕ. Infact, the physical singularity of the black hole is outside of the patch on the manifold covered by isotropic coordinates. This can be illustrrated by computing the Kretschmann scalar in isotropic coordinates. Using isotropic radial coordinate ξ and polar areal radius r_p we can write,

$$\xi \left(1 + \frac{m}{2\xi}\right)^2 = r_p, \tag{1.4.54}$$

by comparing the dθ part of the line element. Substituting this into Eq. (1.4.45), the Kretschmann scalar in isotropic coordinates is,

$$k_{iso} = \frac{48m^2\xi^6}{\left(\xi + \frac{m}{2}\right)^{12}}. \tag{1.4.55}$$

This is finite for $0 \le \xi \le \infty$ and hence there is no physical singularity covered by isotropic coordinates.

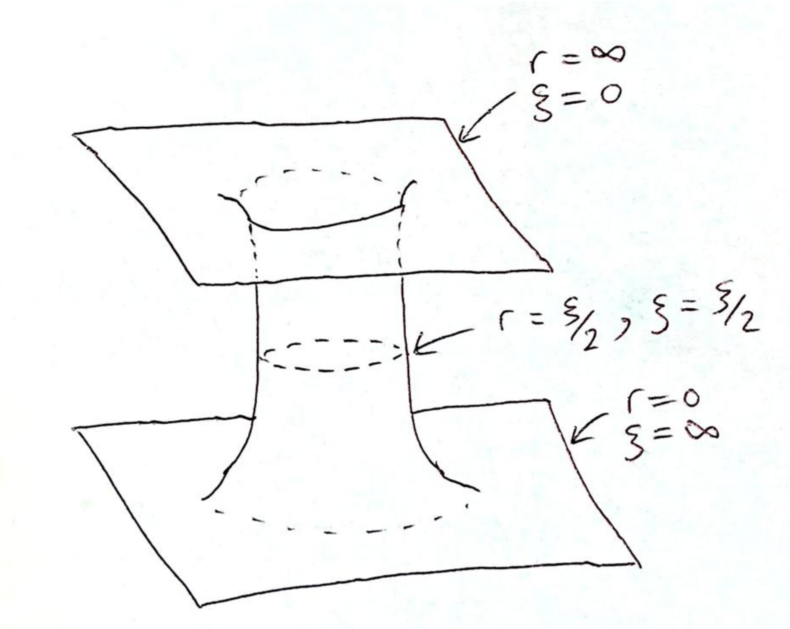

Figure 1.2: Diagram to demonstrate the spacetime covered by isotropic coordinates. There are two asymptotically flat ends joined by the Einstein-Rosen bridge at $r = \xi = m/2$.

Penrose Diagrams and the Causal Structure of the Schwarzschild Black Hole

NO9T SURE I NEED TO DISCUSS PENROSE DIAGRAMS HERE?

RANDOM TEXT RANDOM TEXT

RANDOM TEXT RANDOM TEXT RANDOM TEXT RANDOM TEXT RANDOM TEXT RANDOM TEXT RANDOM TEXT RANDOM TEXT

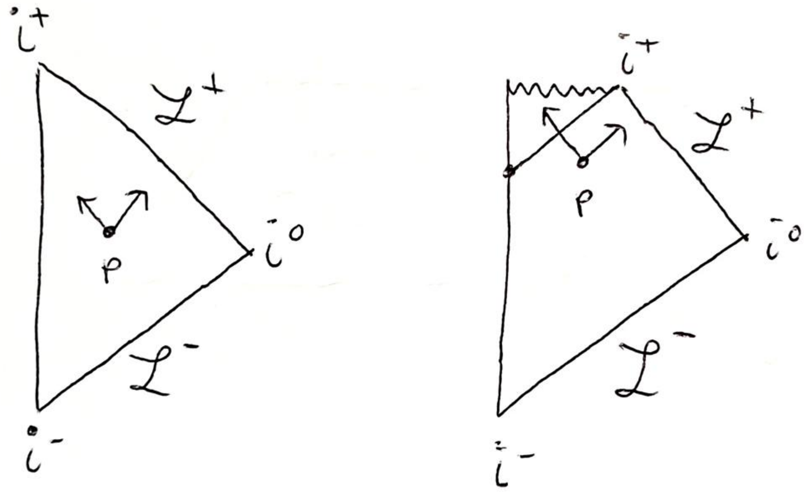

Figure 1.3: Diagram for proof of Penrose diagram of Minkowski space (left) and black hole formation from collapse (right). As shown from a point p, a null geodesic can fall into a black hole, but once inside can never return.

RANDOM TEXT RANDOM TEXT

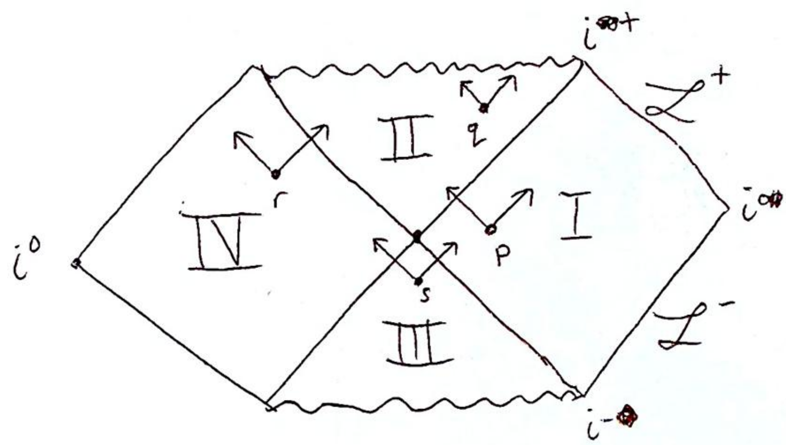

Figure 1.4: Penrose diagram for the maximal extension of the Schwarzschild spacetime of the eternal black hole.

RANDOM TEXT RANDOM TEXT

RANDOM TEXT RANDOM TEXT RANDOM TEXT RANDOM TEXT RANDOM TEXT RANDOM TEXT RANDOM TEXT RANDOM TEXT RANDOM TEXT RANDOM TEXT RANDOM TEXT RANDOM TEXT RANDOM TEXT RANDOM TEXT RANDOM TEXT RANDOM TEXT RANDOM TEXT

1.4.6 The Cosmological Constant

A discussion of general relativity is incomplete without discussing the cosmological constant Λ. At a geometric level, the cosmological constant encodes the homogeneous spacetime curvature in the absense of matter, and indeed setting $\Lambda \to 0$ (in vacuum) returns asymptotically flat vacuum general relativity. The cosmological constant is added into Einstein's equation, Eq. (1.4.37), with a term like $\Lambda g_{\mu\nu}$,

$$R_{\mu\nu} - \frac{1}{2}Rg_{\mu\nu} + \Lambda g_{\mu\nu} = \frac{8\pi G}{c^4}T_{\mu\nu}. \tag{1.4.56}$$

Each term still has a zero-divergence as $\nabla_\mu g_{\alpha\beta} = 0$ due to the Levi-Civita connection defined in section 1.3.3. The Einstein equation in vacuum becomes

$$R_{\mu\nu} - \frac{1}{2}Rg_{\mu\nu} + \Lambda g_{\mu\nu} = 0, \tag{1.4.57}$$

and the traced becomes

$$R = \frac{2D}{D-2}\Lambda \tag{1.4.58}$$

for D spacetime dimensions. This quite nicely shows us that in the limit $\Lambda = 0$ the normal vacuum GR solution $R = 0$ is returned. In the case $\Lambda \neq 0$ it describes a homogeneous curved universe with constant non-zero R.

Friedmann–Lemaître–Robertson–Walker Spacetime

To model the entire universe more realistically, an isotropic uniform fluid as added. A uniform matter distribution is often done with a perfect fluid with stress tensor,

$$T_{\mu\nu} = (\rho + P)u_\mu u_\nu + Pg_{\mu\nu}, \tag{1.4.59}$$

where ρ and P are the rest frame density and pressure. The fluid is taken to be at rest with $u^i = 0$ and $\boldsymbol{g}(\boldsymbol{u}, \boldsymbol{u}) = -1$. The line element takes the following ansatz,

$$\mathrm{d}s^2 = -\mathrm{d}t^2 + a^2(t)\gamma_{ij}\mathrm{d}x^i\mathrm{d}x^j, \tag{1.4.60}$$

where $a(t)$ is the scale factor of the universe and the spacelike metric $\boldsymbol{\gamma}$ is given by,

$$\gamma_{ij}\mathrm{d}x^i\mathrm{d}x^j = \begin{cases} \mathrm{d}r^2 + \sin^2(r)\left(\mathrm{d}\theta^2 + \sin^2(\theta)\mathrm{d}\phi^2\right) & , \text{ (closed)} \\ \mathrm{d}r^2 + r^2\left(\mathrm{d}\theta^2 + \sin^2(\theta)\mathrm{d}\phi^2\right) & , \text{ (flat)} \\ \mathrm{d}r^2 + \sinh^2(r)\left(\mathrm{d}\theta^2 + \sin^2(\theta)\mathrm{d}\phi^2\right) & , \text{ (hyperbolic)} \end{cases} \tag{1.4.61}$$

for either uniformly curved hyperbolic space, uniformly curved closed space or flat space. This spacetime is called the Friedmann–Lemaître–Robertson–Walker spacetime and the trace of Eintein's equation in four dimensions becomes,

$$R = 4\Lambda - 8\pi T, \tag{1.4.62}$$

where planck units are used and $T = T_{\mu\nu}g^{\mu\nu}$. It should be noted that R and T are constant over the entire spatial domain of the spacetime for a moment of time. This form of Einstein's equation makes it abundantly clear that the cosmological constant has the same effect on curvature as a uniform matter distribution. In the case $4\Lambda = 8\pi T$, Einstein's equation is once again $R = 0$ and can be solved with the flat metric of Minkowski (but now it is not in vacuum unless $T = \Lambda = 0$). If $8\pi T > 4\Lambda$, then the spatial hypersurface of the universe is closed and finite sized. Finally, if $4\Lambda > 8\pi T$ then the spatial hypersurface of the universe is open or hyperbolic; as a radial geodesics is followed, the amount of space grows faster than the r^2 as expected in flat space.

Putting the ansatz for the metric and stress tensor into the Einstein equation returns an ODE for $a(t)$. Along with an equation of state, $P(\rho)$, the continuity equation $\nabla_\mu T^{\mu\nu} = 0$ returns an ODE for $\rho(t)$. The two solutions $\rho(t)$ and $a(t)$, along with knowledge of whether the spatial time-slices are flat, closed or hyperbolic, fully specify the spacetime. These solutions cover many topics such as the big bang, inflation, universe expansion, bouncing cosmologies (ending with a big crunch) and also minkowksi space given the correct conditions.

1.4.7 The Lagrangean Formulation of General Relativity

A common procedure in theoretical physics is to encapsulate the solution space in an action functional S,

$$S = \int \mathcal{L}\sqrt{-g}\,\mathrm{d}x^4. \tag{1.4.63}$$

Using the calculus of variation on this action returns differential equations governing the system. As found by Hilbert [REF] the following lagrangean density $\mathcal{L} = R$, equal to the Ricci scalar, returns the vacuum Einstein equations under varying with respect to $g^{\mu\nu}$.

$$\begin{aligned}
\delta S &= \int \left[\sqrt{-g}(\delta R) + R(\delta\sqrt{-g})\right]\,\mathrm{d}x^4 && (1.4.64)\\
&= \int \left[\sqrt{-g}\delta(g^{\mu\nu}R_{\mu\nu}) - \frac{1}{2}\sqrt{-g}g_{\mu\nu}R(\delta g^{\mu\nu})\right]\,\mathrm{d}x^4 && (1.4.65)\\
&= \int \left[\sqrt{-g}g^{\mu\nu}(\delta R_{\mu\nu}) + \sqrt{-g}\left(R_{\mu\nu} - \frac{1}{2}Rg_{\mu\nu}\right)\delta g^{\mu\nu}\right]\,\mathrm{d}x^4 && (1.4.66)
\end{aligned}$$

where we used Eq. (1.3.138) to vary $\sqrt{-g}$. Remembering that the difference of two christoffel symbols such as,

$$\delta\Gamma^\lambda{}_{\mu\nu} = \Gamma^\lambda{}_{\mu\nu}|_{g^{\mu\nu}+\delta g^{\mu\nu}} - \Gamma^\lambda{}_{\mu\nu}|_{g^{\mu\nu}} \tag{1.4.67}$$

is a tensor, and using normal coordinates discussed in section 1.3.3 the left hand term of Eq. (1.4.66) becomes

$$\begin{aligned}
g^{\mu\nu}\delta R_{\mu\nu} &= g^{\mu\nu}\left(\partial_\lambda\delta\Gamma^\lambda{}_{\mu\nu} - \partial_\nu\delta\Gamma^\lambda{}_{\mu\lambda}\right), && (1.4.68)\\
&= g^{\mu\nu}\left(\nabla_\lambda\delta\Gamma^\lambda{}_{\mu\nu} - \nabla_\nu\delta\Gamma^\lambda{}_{\mu\lambda}\right), && (1.4.69)\\
&= \nabla_\lambda\left(g^{\mu\nu}\delta\Gamma^\lambda{}_{\mu\nu} - g^{\mu\lambda}\delta\Gamma^\nu{}_{\mu\nu}\right), && (1.4.70)\\
&= \nabla_\lambda X^\lambda. && (1.4.71)
\end{aligned}$$

The ability to transform the partial derivatives into covariant derivatives comes from using normal coordinates. Putting everything together, δS becomes

$$\begin{aligned}
\delta S &= \int \left[\nabla_\mu X^\mu + \left(R_{\mu\nu} - \frac{1}{2}Rg_{\mu\nu}\right)\right]\sqrt{-g}\,\mathrm{d}x^4, && (1.4.72)\\
&= \int_B X^\mu\hat{s}_\mu\sqrt{|^{(3)}g|}\mathrm{d}x^3 + \int\left[R_{\mu\nu} - \frac{1}{2}Rg_{\mu\nu}\right]\sqrt{-g}\,\mathrm{d}x^4, && (1.4.73)\\
& && (1.4.74)
\end{aligned}$$

where the integral over B represents the surface integral over the boundary of our spacetime with metric ${}^{(3)}g_{ij}$; on B $\delta g^{\mu\nu} \to 0$ and therefore $X^\mu \to 0$. Setting $\mathrm{d}S = 0$ implies

$$R_{\mu\nu} - \frac{1}{2}Rg_{\mu\nu} = 0, \tag{1.4.75}$$

which is the vacuum Einstein equation.

Non-Vacuum Spacetimes

Matter is often added into a spacetime at the level of the lagrangean with a term $\frac{16\pi G}{c^4}\mathcal{L}_m$. The cosmological constant can be added in exactly the same way with $\mathcal{L}_\Lambda$. The total lagrangean becomes,

$$S = \int \left(R + \frac{16\pi G}{c^4}\mathcal{L}_m + \mathcal{L}_\Lambda \right) \sqrt{-g}\, \mathrm{d}x^4. \tag{1.4.76}$$

As we have already seen earlier in this section, the variation of R with respect to the inverse metric components $g^{\mu\nu}$ returns the vacuum Einstein equation; adding the two new terms from $\mathcal{L}_m$ and $\mathcal{L}_\Lambda$, setting $\delta S = 0$ gives different equation

$$R_{\mu\nu} - \frac{1}{2}Rg_{\mu\nu} + \frac{16\pi G}{c^4}\frac{1}{\sqrt{-g}}\frac{\delta(\mathcal{L}_m\sqrt{-g})}{\delta g^{\mu\nu}} + \frac{1}{\sqrt{-g}}\frac{\delta(\mathcal{L}_\Lambda\sqrt{-g})}{\delta g^{\mu\nu}} = 0. \tag{1.4.77}$$

Comparing the $\mathcal{L}_\Lambda$ term to the Einstein equation with cosmological constant in Eq. (1.4.56) we must have

$$g_{\mu\nu}\Lambda = \frac{1}{\sqrt{-g}}\frac{\delta(\mathcal{L}_\Lambda\sqrt{-g})}{\delta g^{\mu\nu}}, \tag{1.4.78}$$

$$= \mathcal{L}_\Lambda \frac{1}{\sqrt{-g}}\frac{\delta(\sqrt{-g})}{\delta g^{\mu\nu}} + \frac{\delta(\mathcal{L}_\Lambda)}{\delta g^{\mu\nu}}, \tag{1.4.79}$$

$$= -\frac{1}{2}g_{\mu\nu}\mathcal{L}_\Lambda + \frac{\delta(\mathcal{L}_\Lambda)}{\delta g^{\mu\nu}}, \tag{1.4.80}$$

$$\tag{1.4.81}$$

which is solved by $\mathcal{L}_\Lambda = -2\Lambda$. Comparing the matter term instead returns another definition of the stress tensor,

$$T_{\mu\nu} := -\frac{2}{\sqrt{-g}}\frac{\delta(\mathcal{L}_m\sqrt{-g})}{\delta g^{\mu\nu}}, \tag{1.4.82}$$

$$= -2\frac{\delta\mathcal{L}_m}{\delta g^{\mu\nu}} + g_{\mu\nu}\mathcal{L}_m. \tag{1.4.83}$$

Collecting these results, the full lagrangean is,

$$\mathcal{L} = R + \frac{16\pi G}{c^4}\mathcal{L}_m - 2\Lambda, \tag{1.4.84}$$

or in Planck units,

$$\mathcal{L} = R + 16\pi\mathcal{L}_m - 2\Lambda. \tag{1.4.85}$$

The form of $\mathcal{L}_m$ is problem specific, depending on the type of matter. The equation of motion of the matter, described by a set of fields ϕ_i, and their partial derivatives with respect to x^μ is,

$$\sqrt{-g}\frac{\delta\mathcal{L}}{\delta\phi_i} - \partial_\mu\left(\sqrt{-g}\frac{\delta\mathcal{L}}{\delta\partial_\mu\phi_i}\right) = 0. \tag{1.4.86}$$

If the ϕ_i are scalar fields then the equation of motion simplifies, using Eq. (1.3.141), to

$$\frac{\delta\mathcal{L}}{\delta\phi_i} - \nabla_\mu\left(\frac{\delta\mathcal{L}}{\delta\nabla_\mu\phi_i}\right) = 0. \tag{1.4.87}$$

Modified Theories of Gravity

The Lagrangean formulation of general relativity is especially useful for the more theoretical apects of general relativity such as exotic matter and modified gravity. General relativity is not thought of as the "correct" or "final" theory of gravity. It is a classical field theory so cannot describe particles or quantum mechanics. To date no sucessful quantisation of general relativity has been done. Another problem with general relativity is that at the centre of black holes there are singularities; a similar singularity exists for the Coulomb force of a point particle. The Coulomb force singularity is resolved by quantum field theory (QFT); it is thought a similar thing may happen in a quantum field theory for gravity but it is currently unknown.

Theories such as string theory and loop quantum gravity have attempt to describe a quantum theory of gravity but are notoriously difficult to derive observable effects from. Many modified gravity theories aim to describe the first deviation from general relativity towards a quantum gravity. It is thought that deviations from general relativity might be seen in extremely high curvature regimes.

Currently there is no conclusive experimental evidence of deviations from general relativity.

At the level of the lagrangean, minimal coupling means to write down the simplest lagrangean possible - without coupling between matter fields and Ricci curvature. As an example, the action for the minimally coupled scalar field ψ in curved space is,

$$S_\psi = \int \left(aR - bg^{\mu\nu}\partial_\mu\psi\partial_\nu\psi\right)\sqrt{-g}\,\mathrm{d}^4x, \tag{1.4.88}$$

for constants a and b. Extra coupling terms between matter and curvature could be added, for instance the action,

$$S_f = \int \left(aRf(\psi) - bg^{\mu\nu}\partial_\mu\psi\partial_\nu\psi\right)\sqrt{-g}\,\mathrm{d}^4x, \tag{1.4.89}$$

for some function f; note that if f is constant then this action is the minimally coupled wave sf asdf. Varying S_f with respect to $g^{\mu\nu}$ gives a modified Einstein equation,

$$f(\psi)R_{\mu\nu} - \frac{1}{2}Rf(\psi)g_{\mu\nu} + R\frac{\delta f}{\delta g^{\mu\nu}}(\psi) = \frac{b}{a}\left(\nabla_\mu\psi\nabla_\nu\psi - \frac{1}{2}g_{\mu\nu}g^{\rho\sigma}\nabla_\rho\psi\nabla_\sigma\psi\right), \tag{1.4.90}$$

where a new type of term $R\frac{\delta f}{\delta g^{\mu\nu}}(\psi)$ coupling gravity and matter has arisen; note this becomes the regular Einstein equation for a spacetime with a real massless scalar field ψ if f is constant. Varying S_f with respect to ψ instead gives the modified wave equation,

$$g^{\mu\nu}\nabla_\mu\nabla_\nu\psi + \frac{a}{b}R\frac{\partial f}{\partial\psi} = 0, \tag{1.4.91}$$

which is equivalent to Eq. (1.4.18); note that this returns the regular curved space wave equation if $\partial f/\partial\psi = 0$ and the regular wave equation in the flat-space limit.

other popular methods of modifying gravity include higher poowers of curvature such as the gauss bonnet ...

1.4.8 STUFF

finish modified gravity and a lightnight fast introduction to penrose diagrms (probably onyl mention krustal skzeres coords or ref them?)

Chapter 2

Numerical Relativity and Boson Stars

2.1 Numerical Relativity

2.1.1 Spacetime Foliation

Einstein's equation is a classical field equation which, along with an equation of motion for any matter, governs the dynamics of spacetime curvature,

$$R_{\mu\nu} - \frac{1}{2}Rg_{\mu\nu} = \frac{8\pi G}{c^4}T_{\mu\nu}. \tag{2.1.1}$$

The above version is fully covariant, agnostic of the definition of time, and many solutions are known analytically, for instance Black Hole geometries. When the system of interest becomes more complicated, such as the case of orbiting objects which will be discussed later, finding an analytic expression becomes impossible. For low energy dynamics, Newtonian theory, post-Newtonian theory and perturbation theory can make more progress; however this work focuses on the highly nonlinear regime where Numerical relativity is truly the only hope to solve Einstein's equations. To do this it is common to split the 4-dimensional spacetime into 3+1 dimensions, evolving a 3-dimensional manifold (maybe with matter) on a computer along the final 4th dimension. To do this we need to define a suitable hypersurface $\Sigma \in \mathcal{M}$ where $\mathcal{M}$ is the 4-dimensional manifold representing the entire spacetime. This is usually done by demanding the hypersurface Σ_t be the set of points $p \in \mathcal{M}$ where some scalar function $f : \mathcal{M} \mapsto \mathbb{R}$ satisfies $f(p) = t$. This hypersurface should be a Cauchy surface, intersecting all causal curves only once, or a partial Cauchy surface which intersects all causal curves at most once. Generally we will choose a partial Cauchy surface covering a finite region of Σ_t due to the finite memory of computers. However, by picking certain compactified coordinates it is possible to use a Cauchy surface [REF]. A foliation $\mathcal{F}$ is then the union of a set of Σ_t for some range of the parameter t,

$$\mathcal{F} = \cup_t(\Sigma_t) \subseteq \mathcal{M}. \tag{2.1.2}$$

This means we should be careful to pick a parameter t such that the foliation is not self intersecting for the parameter range that covers the region of $\mathcal{M}$ that we are interested in simulating. The time coordinate in a suitable coordinate system works in many cases; it also gives the physical interpretation of Σ_t being an instance of time. Now we should define unit normal vector $\boldsymbol{n}$ to Σ_t,

$$n^\mu = -\frac{\nabla^\mu t}{\sqrt{|g_{\mu\nu}\nabla^\mu t \nabla^\nu t|}} \quad \& \quad n_\mu = -\frac{dt_\mu}{\sqrt{|g_{\mu\nu}\nabla^\mu t \nabla^\nu t|}}, \tag{2.1.3}$$

where $\mathrm{d}t_\mu$ is the differential form exterior derivative of $\partial_\mu t$. For simplicity we define the lapse function α to be

$$\alpha := \frac{1}{\sqrt{|g_{\mu\nu}\nabla^\mu t \nabla^\nu t|}}. \tag{2.1.4}$$

giving us $n_\mu = -\alpha \mathrm{d}t_\mu$ as well as the normal evolution vector $m_\mu = \alpha n_\mu$. Defining two infinitessimaly close points $p \in \Sigma_t$ and $q \in \Sigma_{t'}$ where $q^\mu = p^\mu + m^\mu \delta t$ we see,

$$t(q) = t(p^\mu + m^\mu \delta t) = t(p) + \frac{\partial t}{\partial x^\mu} m^\mu \delta t = t(p) + \mathrm{d}t_\mu m^\mu \delta t = t(p) + \delta t, \tag{2.1.5}$$

showing that m^μ points between the two same neighbouring hypersurfaces for any point $p \in \Sigma_t$; therefore when creating evolution equations we should care about Lie derivates $\mathcal{L}_m$ along m^μ rather than $\mathcal{L}_n$.

2.1.2 The 3+1 Decomposition

With the notion of a spacetime foliation we should define how to project tensors onto Σ_t; clearly scalars need no projecting. Following the ideas of section 1.2.4 we can split a vector $X^\mu \boldsymbol{e}_\mu = X^\mu_\parallel \boldsymbol{e}_\mu + X^\mu_\perp \boldsymbol{e}_\mu$

into components tangent or normal to Σ_t we define the orthogonal projector $\perp^\mu_\nu$ and parallel projector $-n^\mu n_\nu$,

$$X^\mu_\parallel = \left[\delta^\mu_\nu + n^\mu n_\nu\right] X^\mu = \perp^\mu_\nu X^\nu, \tag{2.1.6}$$
$$X^\mu_\perp = -n^\mu n_\nu X^\nu. \tag{2.1.7}$$

Considering scalars such as $\phi = w_\mu X^\mu$ or $\psi = T^{\mu\nu} w_\mu w_\nu$, and remembering scalars don't vary under projection, it is simple to show that any tensor T can be projected by contracting a projection operator $\perp$ on any free index,

$$T_\parallel{}^{ij\ldots}{}_{kl\ldots} = \mathcal{T}^{ij\ldots}{}_{kl\ldots} = \perp^i_\mu \perp^j_\nu \perp^\rho_k \perp^\sigma_l \cdots T^{\mu\nu\ldots}{}_{\rho\sigma\ldots}. \tag{2.1.8}$$

We can find the 3-metric $\gamma_{\mu\nu}$ of Σ_t by projecting $g_{\mu\nu}$,

$$\gamma_{ij} = \perp^\mu_i \perp^\nu_j g_{\mu\nu} = g_{\mu\nu} + n_\mu n_\nu \quad \rightarrow \quad \gamma^i_j = \perp^i_j, \tag{2.1.9}$$

and we find it is equivalent to the projector $\perp$; this had to be the case as $\perp_{ij} \mathrm{d}x^i \mathrm{d}x^j$ gives the line element along Σ_t. With this machinery we can define the extrinsic curvature tensor $\mathcal{K}_{ij}$ representing curvature due to the choice of spacetime foliation; it could be nonzero for certain foliations of Minkowski space. It is not the same as the 3-Ricci tensor $\mathcal{R}_{ij}$ which is due to genuine spacetime curvature of $\mathcal{M}$ regardless of foliation. The extrinsic curvature tensor is defined the following way,

$$\mathcal{K}_{ij} = \mathcal{K}_{ji} := -\perp^\mu_i \perp^\nu_j \nabla_\mu n_\nu = -\perp^\mu_i \nabla_\mu n_j = -\nabla_i n_j - n_i a_j, \tag{2.1.10}$$
$$\mathcal{K} = \mathcal{K}^i_i = -\boldsymbol{\nabla} \cdot \boldsymbol{n}, \tag{2.1.11}$$

where $a_i = \boldsymbol{n} \cdot \boldsymbol{\nabla} n_i$ is called the Eularian acceleration; it should be noted $\mathcal{K}_{ij}$ is symmetric. It can also be shown to take the following form,

$$\mathcal{K}_{ij} = -\frac{1}{2}\mathcal{L}_n \gamma_{ij} = -\frac{1}{2\alpha}\mathcal{L}_m \gamma_{ij}, \tag{2.1.12}$$

which gives the intuitive explanation of $\mathcal{K}_{ij}$ being the rate of change of the 3-metric γ_{ij} with respect to the foliation. The next object we should discuss is the projected covariant 3-derivative $\mathcal{D}_i$. This is the covariant derivative belonging to Σ_t and hence it's arguments should be tensors belonging to Σ_t. This means we can define it as so,

$$\mathcal{T}^{ij\ldots}{}_{kl\ldots} = \perp^i_\mu \perp^j_\nu \perp^\rho_k \perp^\sigma_l \cdots T^{\mu\nu\ldots}{}_{\rho\sigma\ldots}, \tag{2.1.13}$$
$$\mathcal{D}_m \mathcal{T}^{ij\ldots}{}_{kl\ldots} := \perp^\mu_m \perp^i_\mu \perp^j_\nu \perp^\rho_k \perp^\sigma_l \cdots \nabla_\mu \mathcal{T}^{\mu\nu\ldots}{}_{\rho\sigma\ldots}. \tag{2.1.14}$$

A simple example is the derivative of a vector $X^i \boldsymbol{e}_i \in \mathcal{T}(\Sigma_t)$,

$$\mathcal{D}_i X^j = \partial_i X^j + \Upsilon^i{}_{jk} X^k, \tag{2.1.15}$$
$$\Upsilon^i{}_{jk} = \frac{1}{2}\gamma^{il}\left[\partial_j \gamma_{lk} + \partial_k \gamma_{jk} - \partial_l \gamma_{jk}\right], \tag{2.1.16}$$

where $\Upsilon^i{}_{jk}$ is the Christoffel symbol of Σ_t. Another useful example is a^μ which can be equated to,

$$a_\mu = \boldsymbol{n} \cdot \boldsymbol{\nabla} n_\mu = \mathcal{D}_\mu \ln \alpha = \frac{1}{\alpha}\mathcal{D}_\mu \alpha, \tag{2.1.17}$$

and allows us to evaluate the Lie derivative of the projector $\perp^i_j$,

$$\mathcal{L}_m \perp^i_j = \alpha n^k \nabla_k \perp^i_j + \perp^i_k \nabla_j \alpha n^k - \perp^k_j \nabla_k \alpha m^i, \tag{2.1.18}$$
$$= \alpha n^k \nabla_k \left[n^i n_j\right] + \alpha \nabla_j n^i - \left[\alpha K^i_j + n^i \mathcal{D}_j \alpha\right], \tag{2.1.19}$$
$$= 0. \tag{2.1.20}$$

The result $\mathcal{L}_m \perp^i_j = 0$ is incredibly important, it tells us that the projector commutes with $\mathcal{L}_m$ and as a result any tensor $\boldsymbol{T}$ which when projected onto Σ_t, written $\boldsymbol{\mathcal{T}}$, satisfies

$$\mathcal{L}_m \mathcal{T}^{ij\ldots}{}_{kl\ldots} = \perp^i_\mu \perp^j_\nu \perp^\rho_k \perp^\sigma_l \mathcal{L}_m T^{\mu\nu\ldots}{}_{\rho\sigma\ldots}. \tag{2.1.21}$$

In other words, evolving a projected tensor along integral curves of m leaves the tensor parallel to Σ_t.

2.1.3 Gauss, Codazzi and Ricci Equations

The projections of the 4-dimensional curvature tensors into a combination of 3-dimensional curvature tensors and $\boldsymbol{\mathcal{K}}$ is very useful as it captures all the degrees of freedom of the 4-dimensional Riemann tensor in terms of variables on Σ_t. This property is crucial when numerically simulating a single time slice Σ_t as we only have access to variables on Σ_t.

The Gauss Equations

From the definition of the Riemann tensor in section 1.3.4 we know,

$$[\mathcal{D}_i\mathcal{D}_j - \mathcal{D}_j\mathcal{D}_i]v^k = \mathcal{R}^k{}_{mij}v^m, \tag{2.1.22}$$

$$[\nabla_\alpha\nabla_\beta - \nabla_\beta\nabla_\alpha]v^\gamma = R^\gamma{}_{\lambda\alpha\beta}v^\lambda, \tag{2.1.23}$$

where the vector $v^m =\perp^m_\rho v^\rho$ is tangent to Σ_t. Expanding the $\mathcal{D}$'s in terms of ∇'s gives,

$$\mathcal{D}_i\mathcal{D}_j v^k =\perp^\mu_i\perp^\sigma_j\perp^k_\xi \nabla_\mu(\perp^\nu_\sigma\perp^\xi_\rho \nabla_\nu v^\rho), \tag{2.1.24}$$

and using the following properties; impotence of projections $\perp^i_\mu\perp^\mu_j=\perp^i_j$, null projection of orthogonal vectors $\perp(\boldsymbol{n}) = 0$, metric compatibility $\nabla_\mu \perp^i_j= n_j\nabla_\mu n^i + n^i\nabla_\mu n_j$ and Eq. (2.1.10) for $\mathcal{K}_{ij}$ we obtain the Gauss relation,

$$\perp^\mu_i\perp^\nu_j\perp^k_\rho\perp^\sigma_l R^\rho{}_{\sigma\mu\nu} = \mathcal{R}^k{}_{lij} + \mathcal{K}^k_i\mathcal{K}_{lj} - \mathcal{K}^k_j\mathcal{K}_{il}. \tag{2.1.25}$$

Contracting over i, k above and relabelling indices we get the contracted Gauss relation,

$$\perp^\mu_i\perp^\nu_j R_{\mu\nu} + \gamma_{i\mu}n^\nu \perp^\rho_j n^\sigma R^\mu{}_{\nu\rho\sigma} = \mathcal{R}_{ij} + \mathcal{K}\mathcal{K}_{ij} - \mathcal{K}^k_j\mathcal{K}_{ik}. \tag{2.1.26}$$

Contracting again and realising $R_{\mu\nu\rho\sigma}n^\mu n^\nu n^\rho n^\sigma = 0$ from antisymmetry in indeces 0 and 1 or 2 and 3 in the Riemann tensor, gives the scalar Gauss equation,

$$R + 2R_{\mu\nu}n^\mu n^\nu = \mathcal{R} + \mathcal{K}^2 - \mathcal{K}_{ij}\mathcal{K}^{ij}. \tag{2.1.27}$$

The Codazzi Equations

The Codazzi relations are derived from a different start point. Instead of projecting the Riemann tensor fully onto Σ_t with projection operators $\perp$ and a spacelike vector $\boldsymbol{v}$, it is now projected with a timelike vector $\boldsymbol{n}$,

$$[\nabla_\alpha\nabla_\beta - \nabla_\beta\nabla_\alpha]n^\gamma = R^\gamma{}_{\lambda\alpha\beta}n^\lambda, \tag{2.1.28}$$

and again projecting to Σ_t with three projection operators. The following relations are used

$$\nabla_j n^k = -\mathcal{K}^k{}_j - a^k n_j, \tag{2.1.29}$$

$$\perp^i_\mu\perp^j_\nu\perp^\rho_k \nabla_i\nabla_j n^k = -\mathcal{D}_i\mathcal{K}^k{}_j + a^k\mathcal{K}_{ij}, \tag{2.1.30}$$

which lead immediately to the Codazzi relation,

$$\perp^\mu_i\perp^\nu_j\perp^k_\rho n^\sigma R^\rho{}_{\sigma\mu\nu} = \mathcal{D}_j\mathcal{K}^k{}_i - \mathcal{D}_i\mathcal{K}^k{}_j, \tag{2.1.31}$$

and the contracted Codazzi relation,

$$\perp^\mu_i n^\nu R_{\mu\nu} = \mathcal{D}_i\mathcal{K} - \mathcal{D}_\mu\mathcal{K}^\mu{}_i. \tag{2.1.32}$$

The Ricci Equation

Finally we turn our attention to the Ricci equation, the projection of the Riemann tensor twice onto Σ_t and twice contracting with $\boldsymbol{n}$. This is done by projecting Eq (2.1.28) with two projectors $\perp$ and one timelike $\boldsymbol{n}$. If we contract with n^γ then the antisymmetry in the first two Riemann tensor indeces would identically gie to zero, therefore the unique choice (upto a minus sign) is to project with n^β,

$$R_{\gamma\lambda\alpha\beta}n^\lambda n^\beta = n^\beta \left[\nabla_\alpha\nabla_\beta - \nabla_\beta\nabla_\alpha\right] n_\gamma, \tag{2.1.33}$$

and project the remaining free indeces with $\perp$ like,

$$\perp_i^\gamma \perp_j^\alpha \; R_{\gamma\lambda\alpha\beta}n^\lambda n^\beta = \perp_i^\gamma \perp_j^\alpha \; n^\beta \left[\nabla_\alpha\nabla_\beta - \nabla_\beta\nabla_\alpha\right] n_\gamma. \tag{2.1.34}$$

Rearanging Eqs. (2.1.10) and (2.1.17),

$$\nabla_\sigma n_\mu = -\mathcal{K}_{\mu\sigma} - n_\sigma \mathcal{D}_\mu \ln(\alpha), \tag{2.1.35}$$

which can be used to expand the right hand side of Eq. (2.1.36),

$$\begin{aligned}
\perp_i^\gamma \perp_j^\alpha \; R_{\gamma\lambda\alpha\beta}n^\lambda n^\beta =& \perp_i^\gamma \perp_j^\alpha \; n^\beta \left[-\nabla_\alpha \mathcal{K}_{\gamma\beta} + \nabla_\beta \mathcal{K}_{\gamma\alpha}\right] && (2.1.36)\\
&+ \perp_i^\gamma \perp_j^\alpha \; n^\beta \left[-\nabla_\alpha(n_\beta \mathcal{D}_\gamma \ln(\alpha)) + \nabla_\beta(n_\alpha \mathcal{D}_\gamma \ln(\alpha))\right], \\
=& \perp_i^\gamma \perp_j^\alpha \; n^\beta n^\sigma \nabla_\sigma \mathcal{K}_{\gamma\alpha} + \perp_\gamma^i \perp_j^\alpha \; \mathcal{K}_{\gamma\beta}\nabla_\alpha n^\beta && (2.1.37)\\
&+ \perp_i^\gamma \perp_j^\alpha \; n^\beta \left[-n_\beta \nabla_\alpha(\mathcal{D}_\gamma \ln(\alpha)) + n_\alpha \nabla_\beta \mathcal{D}_\gamma \ln(\alpha) + (\mathcal{D}_\gamma \ln(\alpha))\nabla_\beta n_\alpha\right], \\
=& \perp_i^\gamma \perp_j^\alpha \; n^\beta n^\sigma \nabla_\sigma \mathcal{K}_{\gamma\alpha} - \mathcal{K}_{ik}\mathcal{K}^k{}_j && (2.1.38)\\
&+ \mathcal{D}_j\mathcal{D}_i \ln(\alpha) + \mathcal{D}_i \ln(\alpha)\mathcal{D}_j \ln(\alpha), \\
=& \perp_i^\gamma \perp_j^\alpha \; n^\beta n^\sigma \nabla_\sigma \mathcal{K}_{\gamma\alpha} - \mathcal{K}_{ik}\mathcal{K}^k{}_j + \frac{1}{\alpha}\mathcal{D}_j\mathcal{D}_i\alpha, && (2.1.39)
\end{aligned}$$

where $\boldsymbol{n}^2 = -1$, $\perp_i^\mu \; n_\mu = 0$, $\mathcal{D}_\alpha \ln\alpha = n^\beta \nabla_\beta n_\alpha$ from Eq. (2.1.17) and $n^\beta \nabla_\alpha n_\beta = 0$ were used. This expression can be simplified by calculating the Lie derivative of $\boldsymbol{\mathcal{K}}$,

$$\begin{aligned}
\mathcal{L}_m \mathcal{K}_{ij} =& \perp_i^\mu \perp_j^\nu \; \mathcal{L}_m \mathcal{K}_{\mu\nu}, && (2.1.40)\\
=& \alpha \perp_i^\mu \perp_j^\nu \; \mathcal{L}_n \mathcal{K}_{\mu\nu}, && (2.1.41)\\
=& \alpha \perp_i^\mu \perp_j^\nu \left[\alpha \boldsymbol{n}\cdot\boldsymbol{\nabla}\mathcal{K}_{\mu\nu} + 2\mathcal{K}_{k(\nu}\nabla_{\mu)}n^k\right], && (2.1.42)\\
=& \alpha \perp_i^\mu \perp_j^\nu \; n^\sigma \nabla_\sigma \mathcal{K}_{\mu\nu} - 2\alpha \mathcal{K}_{ik}\mathcal{K}^k{}_j, && (2.1.43)
\end{aligned}$$

where the results $\mathcal{L}_m \boldsymbol{\mathcal{K}} = \alpha \mathcal{L}_n \boldsymbol{\mathcal{K}}$ from Eq. (2.1.12), $\mathcal{L}_m \mathcal{K}_{\alpha\beta} \in \Sigma_t$ from Eq. (2.1.21) and Eq. (2.1.10) were used. Putting everything together we arrive at the Ricci equation,

$$\perp_i^\mu \perp_j^\nu \; n^\rho n^\sigma R_{\mu\rho\nu\sigma} = \frac{1}{\alpha}\mathcal{L}_m \mathcal{K}_{ij} + \frac{1}{\alpha}\mathcal{D}_j\mathcal{D}_i\alpha + \mathcal{K}_{ik}\mathcal{K}^k{}_j. \tag{2.1.44}$$

This is the final contraction of the Riemann tensor that can be made with $\perp$ and $\boldsymbol{n}$ as any projections with three or more contractions with $\boldsymbol{n}$ would identically give zero due to the symmetries of the Riemann tensor.

2.1.4 Decomposition of Einstein's Equation

To evolve General Relativity numerically we must project the Einstein Equation into 3+1 dimensions. Relations between three and four dimensional geometric objects have been derived above and will be used to decompose the Einstein tensor $G_{\mu\nu} = R_{\mu\nu} - g_{\mu\nu}R/2$ from the left hand side of Eq. (2.1.1). The second component, for simulating non-vacumm spacetimes, is the 3+1 decomposition of the Stress tensor

T_{ab}. We contract twice with $\boldsymbol{n}$, then once with $\boldsymbol{n}$ while projecting onto Σ_t and finally twice projecting onto Σ_t to get an energy, momentum and stress-like split,

$$\rho = \boldsymbol{T}(\boldsymbol{n}, \boldsymbol{n}) = T_{\mu\nu} n^\mu n^\nu, \tag{2.1.45}$$
$$\mathcal{S}_i = -\boldsymbol{T}(\boldsymbol{n}, \cdot) = - \perp_i^\mu n^\nu T_{\mu\nu}, \tag{2.1.46}$$
$$\mathcal{S}_{ij} = \perp_i^\mu \perp_j^\nu T_{\mu\nu}, \tag{2.1.47}$$

and by construction,

$$T_{\mu\nu} = \rho n_\mu n_\nu + \mathcal{S}_\mu n_\nu + \mathcal{S}_\nu n_\mu + \mathcal{S}_{\mu\nu}. \tag{2.1.48}$$

With this and the Gauss-Codazzi equations of section 2.1.3 we can project the Einstein equation. Lets first look at the scalar equation,

$$G_{\mu\nu} n^\mu n^\nu = R_{\mu\nu} n^\mu n^\nu + \frac{1}{2} R = 8\pi\rho, \tag{2.1.49}$$

and equating the geometric terms to the scalar Gauss equation we get the Hamiltonian constraint, $\mathcal{H} = 0$,

$$\mathcal{H} = \mathcal{K}_{\mu\nu}\mathcal{K}^{\mu\nu} - \mathcal{K}^2 - \mathcal{R} + 16\pi\rho = 0. \tag{2.1.50}$$

Now looking at the once projected part we see,

$$\perp_i^\mu n^\nu G_{\mu\nu} = \perp_i^\mu n^\nu R_{\mu\nu} = -8\pi\mathcal{S}_i, \tag{2.1.51}$$

and substituting the geometric terms for the contracted Codazzi relation we get the momentum constraint, $\mathcal{P}_i = 0$,

$$\mathcal{P}_i = \mathcal{D}_i\mathcal{K} - \mathcal{D}_j\mathcal{K}_i^j + 8\pi\mathcal{S}_i = 0. \tag{2.1.52}$$

Finally, the space-space projection gives the 6 evolution PDE's. This time start with the trace reversed Einstein Equation

$$R_{\mu\nu} = 8\pi \left[T_{\mu\nu} - \frac{1}{2} T g_{\mu\nu} \right], \tag{2.1.53}$$
$$\perp_i^\mu \perp_j^\nu R_{\mu\nu} = 8\pi \left[\mathcal{S}_{ij} - \frac{1}{2}(\mathcal{S} - \rho)\gamma_{ij} \right], \tag{2.1.54}$$

where we used $T = [\gamma^{\mu\nu} - n^\mu n^\nu] T_{\mu\nu} = \mathcal{S} - \rho$. Project the Ricci tensor, we use the contracted Gauss equation but replace the term with $R^\mu{}_{\nu\rho\sigma}$ with the Ricci equation in Eq. (2.1.44). Rearranging gives a normal evolution for the extrinsic curvature,

$$\mathcal{L}_m\mathcal{K}_{ij} = -\mathcal{D}_j\mathcal{D}_i\alpha + \alpha \left[\mathcal{R}_{ij} + \mathcal{K}\mathcal{K}_{ij} - 2\mathcal{K}_i^k\mathcal{K}_{kj} + 4\pi \left[\gamma_{ij} \left[\mathcal{S} - \rho \right] - 2\mathcal{S}_{ij} \right] \right]. \tag{2.1.55}$$

Along with the definition of $\mathcal{K}_{ij}$ in Eq. (2.1.12),

$$\mathcal{L}_m\gamma_{ij} = -2\alpha\mathcal{K}_{ij}, \tag{2.1.56}$$

this gives the normal evolution equations for γ_{ij} and $\mathcal{K}_{ij}$. In 4 or n spacetime dimensions the normal evolution equations contain 6 or $\frac{n^2-n}{2}$ differential equations, the Hamiltonian constraint is a single differential equation, the momentum constraint contains 3 or $n-1$ differential equations and the Einstein equation contains 10 or $\frac{n^2+n}{2}$ differential equations. In four spacetime dimensions this corresponds to 6 evolution equations and 4 constraint equations over the surface Σ_t.

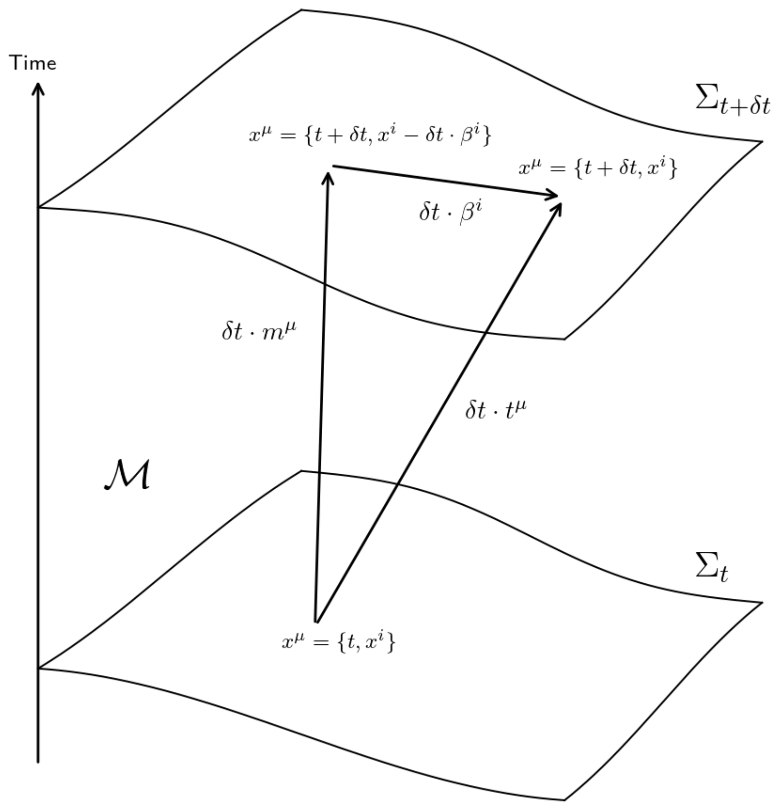

2.1.5 Foliation Adapted Coordinates

Picking coordinates in general relativity introduces a large gauge freedom which allows us to use a level set of the time coordinate $x^0 = t$ to define our foliation hypersurfaces Σ_t. The other three coordinates x^i for $i \in [1, 2, 3]$ can be used to span each hypersurface Σ_t however we define. It is conventional to split the normal evolution vector m^μ into time t^μ and space parts β^μ,

$$t^\mu = (1, 0, 0, 0)\,, \tag{2.1.57}$$

$$\beta^\mu = \left(0, -\beta^1, -\beta^2, -\beta^3\right), \tag{2.1.58}$$

such that,

$$m^\mu = t^\mu - \beta^\mu = (\partial_0)^\mu - \beta^i(\partial_i)^\mu, \tag{2.1.59}$$

$$m^\mu = \left(1, -\beta^1, -\beta^2, -\beta^3\right). \tag{2.1.60}$$

We can view t^μ as the (not necessarily causal) worldline for a simulation gridpoint, hence we would like to evolve our PDE's along t^μ on a computer. In other words, integral curves of t^μ must have constant spatial coordiantes on Σ_t. Equation (2.1.60), along with the definitions $\boldsymbol{m} = \alpha\boldsymbol{n}$ and $\boldsymbol{n}^2 = -1$, specify n^μ and n_μ,

$$n^\mu = \frac{1}{\alpha}\left(1, -\beta^1, -\beta^2, -\beta^3\right), \tag{2.1.61}$$

$$n_\mu = -\alpha\,(1, 0, 0, 0)\,. \tag{2.1.62}$$

The decomposed metric can be calculated, using the property that $\boldsymbol{\beta}$ is tangent to Σ_t and orthogonal to $\boldsymbol{m}$,

$$g_{00} = \boldsymbol{g}(\boldsymbol{\partial}_0, \boldsymbol{\partial}_0) = \boldsymbol{g}(\boldsymbol{m} + \beta^i \boldsymbol{\partial}_i, \boldsymbol{m} + \beta^j \boldsymbol{\partial}_j) = \boldsymbol{g}(\boldsymbol{m}, \boldsymbol{m}) + \beta^i \beta_j \langle \boldsymbol{\partial}_i, \mathbf{d}\boldsymbol{x}^j \rangle = -\alpha^2 + \beta^i \beta_i, \tag{2.1.63}$$
$$g_{0i} = \boldsymbol{g}(\boldsymbol{\partial}_0, \boldsymbol{\partial}_i) = \boldsymbol{g}(\boldsymbol{m} + \beta^j \boldsymbol{\partial}_j, \boldsymbol{\partial}_i) = \beta^j \boldsymbol{g}(\boldsymbol{\partial}_j, \boldsymbol{\partial}_i) = \beta_i, \tag{2.1.64}$$
$$g_{ij} = \boldsymbol{g}(\boldsymbol{\partial}_i, \boldsymbol{\partial}_j) = \boldsymbol{\gamma}(\boldsymbol{\partial}_i, \boldsymbol{\partial}_j) = \gamma_{ij}. \tag{2.1.65}$$

This is commonly called the $3+1$ ADM metric [REF] and α, β^i are referred to the lapse and shift vector in this context. The line element and metric are commonly written as,

$$\mathrm{d}s^2 = -\alpha^2 \mathrm{d}t^2 + \gamma_{ij} \left[\mathrm{d}x^i + \beta^i \mathrm{d}t\right] \left[\mathrm{d}x^j + \beta^j \mathrm{d}t\right], \tag{2.1.66}$$
$$g_{\mu\nu} = \begin{pmatrix} -\alpha^2 + \beta^i \beta_i & \beta_i \\ \beta_j & \gamma_{ij} \end{pmatrix}, \tag{2.1.67}$$
$$g^{\mu\nu} = \frac{1}{\alpha^2} \begin{pmatrix} -1 & \beta^i \\ \beta^j & \alpha^2 \gamma^{ij} - \beta^i \beta^j \end{pmatrix}, \tag{2.1.68}$$

and using Cramers rule for metric determinant,

$$g^{00} = \frac{\det\{\gamma_{ij}\}}{\det\{g_{\mu\nu}\}}, \tag{2.1.69}$$

we get the important relationship,

$$\sqrt{-g} = \alpha \sqrt{\gamma}, \tag{2.1.70}$$

where g and γ are the determinants of $g_{\mu\nu}$ and γ_{ij} respectively.

2.1.6 ADM Equations

Now that we have some coordinates suitable for the spacetime foliation we can find the Arnowitt-Deser-Misner (ADM) evolution equations for $\mathcal{K}_{ij}$ and γ_{ij}. First simplifying the Lie derivative $\mathcal{L}_t$ along t^μ using,

$$\mathcal{L}_t \boldsymbol{T} = \partial_t \boldsymbol{T}, \tag{2.1.71}$$

for any tensor $\boldsymbol{T}$ as $\partial_\nu t^\mu = 0$. This can be used to expand the Lie derivative along m^μ,

$$\mathcal{L}_m = \mathcal{L}_t - \mathcal{L}_\beta = \partial_t - \mathcal{L}_\beta, \tag{2.1.72}$$

and the ADM equations can be written by substituting $\mathcal{L}_m \to \partial_t - \mathcal{L}_\beta$ in the normal evolution equations in section 2.1.4 for $\boldsymbol{\mathcal{K}}$ and $\boldsymbol{\gamma}$. The ADM equations are,

$$\partial_t \mathcal{K}_{ij} = \mathcal{L}_\beta \mathcal{K}_{ij} - \mathcal{D}_j \mathcal{D}_i \alpha + \alpha \left[\mathcal{R}_{ij} + \mathcal{K} \mathcal{K}_{ij} - 2\mathcal{K}_i^k \mathcal{K}_{kj} + 4\pi \left[\gamma_{ij} \left[\mathcal{S} - \rho\right] - 2\mathcal{S}_{ij}\right]\right], \tag{2.1.73}$$
$$\partial_t \gamma_{ij} = \mathcal{L}_\beta \gamma_{ij} - 2\alpha \mathcal{K}_{ij}. \tag{2.1.74}$$

Unfortunately, these PDE's turn out to be ill-posed [REF]; this means that the time evolution of these equations does not depend smoothly on the initial data.

2.1.7 BSSN

To tackle the ill-posedness of the ADM equations in section 2.1.6 the Baumgarte-Shapiro-Shibata-Nakamura (BSSN) formalism [REF] is introduced. The first step in BSSN is to decompose the 3-metric into the conformal metric $\tilde{\gamma}_{ij}$ and the conformal factor χ,

$$\tilde{\gamma}_{ij} = \chi \gamma_{ij}, \tag{2.1.75}$$
$$\det\{\tilde{\gamma}_{ij}\} = \tilde{\gamma} = \chi^3 \gamma = 1, \tag{2.1.76}$$

with the above being the convention used in GRChombo described in section 3.2.1. Other conventions include factors such as $\tilde{\gamma}_{ij} = \psi^{-4}\gamma_{ij}$ or $\tilde{\gamma}_{ij} = e^{-\phi}\gamma_{ij}$. Along with this the extrinsic curvature $\mathcal{K}_{ij}$ is conformally decomposed with χ and modified to be trace free,

$$\tilde{A}_{ij} = \chi \left[\mathcal{K}_{ij} - \frac{1}{3}\mathcal{K}\gamma_{ij}\right], \tag{2.1.77}$$

so that $\tilde{A}_{ij}\gamma^{ij} = 0$. During an evolution the conditions $\operatorname{tr}\tilde{A}_{ij} = 0$ and $\tilde{\gamma} = 1$ are enforced which are observed to improve numerical stability; it is unclear why this works beyond heuristic arguments. As discussed later in section 2.1.10, the definition of $\chi = \gamma^{-1/3}$ is good for black hole simulations where $\gamma \to \infty$ but $\chi \to 0$. For example the isotropic schwarzschild metric has,

$$\gamma = \left[1 + \frac{M}{2r}\right]^{12}, \tag{2.1.78}$$

$$\chi = \left[\frac{r}{\frac{M}{2} + r}\right]^{4}. \tag{2.1.79}$$

The next step is to introduce the conformal connection functions as auxiliary variables,

$$\tilde{\Upsilon}^i = \tilde{\gamma}^{jk}\tilde{\Upsilon}^i{}_{jk} = -\partial_i\tilde{\gamma}^{ij}, \tag{2.1.80}$$

$$\tilde{\Upsilon}^i{}_{jk} = \frac{1}{2}\tilde{\gamma}^{il}\left[\partial_j\tilde{\gamma}_{kl} + \partial_k\tilde{\gamma}_{lj} - \partial_l\tilde{\gamma}_{jk}\right] = \Upsilon^i{}_{jk} + \left[\delta^i_j\partial_k + \delta^i_k\partial_j - \gamma^{il}\gamma_{jk}\partial_l\right]\ln\sqrt{\chi}, \tag{2.1.81}$$

where $\Gamma^i{}_{jk}$ are the christoffel symbols of Σ_t as shown in Eq. (2.1.16). This reduces the set of vacuum evolution variables to $\{\chi, \tilde{\gamma}_{ij}, \mathcal{K}, \tilde{\mathcal{A}}_{ij}, \tilde{\Upsilon}^i\}$. It is conventional to use $-\partial_i\tilde{\gamma}^{ij}$ to evaluate the conformal connection coefficients when they appear in the RHS of an equation, but $\partial_j\tilde{\Upsilon}^i$ is calculated by differentiating the evolution variable $\tilde{\Upsilon}^i$. One final necessity, not included in the CCZ4 formulation discussed later, is to add multiples of the constraint equations (in section 2.1.4) to the evolution equations to change the characteristic matrix and improve stability.

The BSSN formalism is not the only way to find a well-posed set of evolution equations for general relativity. Another strongly hyperbolic formalism is the generalised harmonic gauge [?] with,

$$\Box x^\mu = H^\mu, \tag{2.1.82}$$

for some functions H^μ.

I AM CONSIDERING JUST REMOVING THE HYPERBOLCOI GAUGE BIT AS I DONT USE IT BUT I GUESS IT DOES NO HARM - MIGHT DELETE LATER

2.1.8 Z4 Formalism

The Z4 formalism [?] generalises the Einstein equation to include an unphysical field Z_μ, along with damping terms parameterised by κ_1, κ_2,

$$R_{\mu\nu} + \nabla_\mu Z_\nu + \nabla_\nu Z_\mu - \kappa_1\left[n_\mu Z_\nu + n_\nu Z_\mu - [1+\kappa_2]g_{\mu\nu}n^\alpha Z_\alpha\right] = 8\pi G\left[T_{\mu\nu} - \frac{1}{2}Tg_{\mu\nu}\right]. \tag{2.1.83}$$

Of course regular General Relativity is returned setting $Z_\mu = 0$. It is shown in [REF] that achieving $Z_\mu = 0$ whilst dynamically evolving Z_μ is equivalent to solving the constraints. Z_μ is subjected to a wave equation, transporting constraint violation off the computational domain. It can be shown that the system is driven to $Z_\mu = 0$ for $k_1 > 0$ and $k_2 < -1$. It is much cheaper to evolve the variables Z_μ, driven to zero, than to perform four elliptic solves for the constraints $\{\mathcal{H}, \mathcal{M}^i\}$ on each timestep.

MAYBE I SHOULD START THE Z4 DISCUSSION FROM THE LAGRANGEAN (A BIT MORE TOP DOWN APPROACH).

2.1.9 CCZ4

Joining BSSN with Z4 gives the CCZ4 formalism. The additional modifications,

$$\Theta = -n \cdot Z = -\alpha Z^0, \tag{2.1.84}$$

$$\hat{\Upsilon}^i = \tilde{\Upsilon}^i + \frac{2\gamma^{ij} Z_j}{\chi}, \tag{2.1.85}$$

are made, leaving us with the following set of vacuum evolution variables $\{\chi, \tilde{\gamma}_{ij}, \mathcal{K}, \tilde{\mathcal{A}}_{ij}, \hat{\Upsilon}^i, \Theta\}$. Notably the pair of variables $\mathcal{R}_{ij} + \mathcal{D}_{(i} Z_{j)}$, and traced version $\mathcal{R} + \boldsymbol{\mathcal{D}} \cdot \boldsymbol{Z}$, always appear together; separately they ruin strong hyperbolically but together they do not. The evolution equations can now be found in the CCZ4 scheme by doing a 3+1 decomposition of the Z4 modified Einstein equation in Eq. (2.1.83) and following the BSSN formalism. To illustrate this, the equation of motion for χ is derived. Using Eqs. (1.3.121) and (2.1.56) with $\chi^{-3} = \gamma$,

$$\mathcal{L}_m \gamma = \gamma \gamma^{ij} \mathcal{L}_m \gamma_{ij} = -2\gamma\alpha\gamma^{ij} \mathcal{K}_{ij} = -2\gamma\alpha\mathcal{K}. \tag{2.1.86}$$

This can be used to simplify the Lie derivative of χ,

$$\begin{aligned}
\mathcal{L}_m \chi &= \mathcal{L}_{\partial_t} \chi - \mathcal{L}_\beta \chi, && (2.1.87)\\
&= (\partial_t)^i \partial_i \chi + \omega\chi\partial_i (\partial_t)^i - \beta^i \partial_i \chi - \omega\chi\partial_i \beta^i, && (2.1.88)\\
&= \partial_t \chi - \beta^i \partial_i \chi + \frac{2}{3}\chi\partial_i \beta^i, && (2.1.89)\\
\mathcal{L}_m \chi &= \mathcal{L}_m \gamma^{-\frac{1}{3}}, && (2.1.90)\\
&= -\frac{1}{3}\gamma^{-\frac{4}{3}} \mathcal{L}_m \gamma, && (2.1.91)\\
&= \frac{2}{3}\gamma^{-\frac{1}{3}} \alpha\mathcal{K}, && (2.1.92)\\
&= \frac{2}{3}\chi\gamma\alpha\mathcal{K}, && (2.1.93)
\end{aligned}$$

where Eq. (1.3.31)was used with $\boldsymbol{\mathcal{T}} = \chi$ as χ is a scalar density of weight $\omega = -2/3$. Re-arranging gives the equation of motion for χ,

$$\partial_t \chi = \beta^i \partial_i \chi + \frac{2\chi}{3}\left[\alpha\mathcal{K} - \partial_i \beta^i\right]. \tag{2.1.94}$$

A similar process returns the CCZ4 equations but care should be taken to include the Z4 terms where they are needed. The complete list of CCZ4 equations used in simulations with GRChombo [REF] are given below.

$$\partial_t \chi = \beta^i \partial_i \chi + \frac{2\chi}{3}\left[\alpha \mathcal{K} - \partial_i \beta^i\right] \tag{2.1.95}$$

$$\partial_t \tilde{\gamma}_{ij} = \beta^k \partial_k \tilde{\gamma}_{ij} + \tilde{\gamma}_{kj}\partial_i \beta^k + \tilde{\gamma}_{ik}\partial_j \beta^k - \frac{2}{3}\tilde{\gamma}_{ij}\partial_k \beta^k - 2\alpha \tilde{\mathcal{A}}_{ij} \tag{2.1.96}$$

$$\begin{aligned}\partial_t \mathcal{K} &= \beta^k \partial_k \mathcal{K} + \alpha\left[\mathcal{R} + 2\boldsymbol{\mathcal{D}}\cdot \boldsymbol{Z} + \mathcal{K}\left[\mathcal{K} - 2\Theta\right]\right] - 3\alpha\kappa_1\left[1+\kappa_2\right]\Theta \\ &\quad - \chi\tilde{\gamma}^{kl}\mathcal{D}_k\mathcal{D}_l\alpha + 4\pi G\alpha\left[\mathcal{S} - 3\rho\right]\end{aligned} \tag{2.1.97}$$

$$\begin{aligned}\partial_t \tilde{\mathcal{A}}_{ij} &= \beta^k \partial_k \tilde{\mathcal{A}}_{ij} + \chi\left[\alpha\left[\mathcal{R}_{ij} + 2\mathcal{D}_{(i}Z_{j)} - 8\pi G\mathcal{S}_{ij}\right] - \mathcal{D}_i\mathcal{D}_j\alpha\right]^{TF} \\ &\quad + \tilde{\mathcal{A}}_{ij}\left[\alpha\left[\mathcal{K} - 2\Theta\right] - \frac{2}{3}\mathcal{K}^2\right] + 2\tilde{\mathcal{A}}_{k(i}\partial_{j)}\beta^k - 2\alpha\tilde{\gamma}^{kl}\tilde{\mathcal{A}}_{ik}\tilde{\mathcal{A}}_{lj}\end{aligned} \tag{2.1.98}$$

$$\partial_t \Theta = \beta^k\partial_k\Theta + \frac{1}{2}\alpha\left[\mathcal{R} + 2\boldsymbol{\mathcal{D}}\cdot\boldsymbol{Z} - \tilde{\mathcal{A}}_{kl}\tilde{\mathcal{A}}^{kl} + \frac{2}{3}\mathcal{K}^2 - 2\Theta\mathcal{K}\right] - \kappa_1\alpha\Theta\left[2+\kappa_2\right] - Z^k\partial_k\alpha - 8\pi G\alpha\rho \tag{2.1.99}$$

$$\begin{aligned}\partial_t \hat{\Upsilon}^i &= \beta^k\partial_k\hat{\Upsilon}^i + \frac{2}{3}\left[\partial_k\beta^k\left[\tilde{\Upsilon}^i + 2\kappa_3\frac{Z^i}{\chi}\right] - 2\alpha\mathcal{K}\frac{Z^j}{\chi}\right] - 2\alpha\kappa_1\frac{Z^i}{\chi} \\ &\quad + 2\tilde{\gamma}^{ij}\left[\alpha\partial_j\Theta - \Theta\partial_j\alpha\right] - 2\tilde{\mathcal{A}}^{ij}\partial_j\alpha - \alpha\left[\frac{4}{3}\tilde{\gamma}^{ij}\partial_j\mathcal{K} + 3\tilde{\mathcal{A}}^{ij}\frac{\partial_j\chi}{\chi}\right] \\ &\quad - \left[\tilde{\Upsilon}^j + 2\kappa_3\frac{Z^j}{\chi}\right]\partial_j\beta^i + 2\alpha\tilde{\Upsilon}^i{}_{jk}\tilde{\mathcal{A}}^{jk} + \tilde{\gamma}^{jk}\partial_j\partial_k\beta^i + \frac{1}{3}\tilde{\gamma}^{ij}\partial_k\partial_j\beta^k - 16\pi G\alpha\tilde{\gamma}^{ij}\mathcal{S}_j\end{aligned} \tag{2.1.100}$$

$$\partial_t\varphi = \beta^k\partial_k\varphi - \alpha\Pi \tag{2.1.101}$$

$$\partial_t\Pi = \beta^k\partial_k\Pi - \chi\tilde{\gamma}^{ij}\partial_i\varphi\partial_j\alpha + \alpha\left[\chi\tilde{\Upsilon}^k\partial_k\varphi + \frac{1}{2}\tilde{\gamma}^{lk}\partial_k\chi\partial_l\varphi - \chi\tilde{\gamma}^{ij}\partial_i\partial_j\varphi + \mathcal{K}\Pi + V'\varphi\right] \tag{2.1.102}$$

Note that Eqs. (2.1.101) and (2.1.102) are for the 3+1 Klein-Gordon equation which will be derived later in section 2.2.3. Also to be noted, in the CCZ4 equations there is an additional parameter κ_3 premultiplying terms in the evolution of $\hat{\Upsilon}^i$ which experimentally were found to ruin numerical stability for black hole simulations []. Setting $\kappa_3 < 1$ stabilises the simulation but at the cost of covariance. Later on it was realised that setting $\kappa_3 = 1$ and $\alpha\kappa_1 \to \kappa_1$ retains covariance as well as numerical stability [REF].

The CCZ4 scheme proves useful in my simulations for a few reason. Firstly, any initial data that does not satisfy the constraints will generally not do so along evolution either when using BSSN. Given that superposition of solutions in GR does not generally give a new solution, but does approximate one for separated compact objects, all the simulated binaries considered in this work will have non constraint satisfying initial data. The use of the CCZ4 scheme will also help simulations satisfy the constraints even if they initially satisfy them; one reason being that finite resolution imposes some small deviation from the continuum solution. More importantly, the use of adaptive mesh refinement (discussed in section 3.2.1) introduces large interpolation errors into the simulation at the boundary of the different grid resolution levels. Finally, the Sommerfeld boundary conditions (discussed in section 3.1.2) used are inexact in GR and will introduce small errors at the boundary that ruin constraint satisfaction. In all above cases, the CCZ4 system forces the evolution towards constraint satisfaction, despite the numerical errors and approximations.

2.1.10 Gauge Conditions

The lapse α and shift β^i are freely specifiable on a hypersurface Σ_t being gauge variables, however they must be chosen carefully along with a suitable initial Cauchy surface Σ_{t_0} and initial data. Σ_{t_0} should be a smooth non-intersecting Cauchy surface as described in section 2.1.1 and contain smooth initial data. It is also wise to avoid singularities (both coordinate and physical) on this surface. As an example, consider the simulation of a single Schwarzschild black hole. Figure 2.1 (left) shows how an initial Cauchy surface could extend to the singularity for ingoing Eddington-Finkelstein coordinates. In this work Σ_{t_0} is chosen to be in the isotropic gauge as in figure 2.1 (right); not only does this allow trivial swapping between spherical polar and Cartesian (used in the simulation) coordinates but also provides an initial Cauchy surface free of singularities and easy to compute. However, for a poor choice of lapse function, even a well chosen Σ_{t_0} can advance to the singularity in finite simulation time.

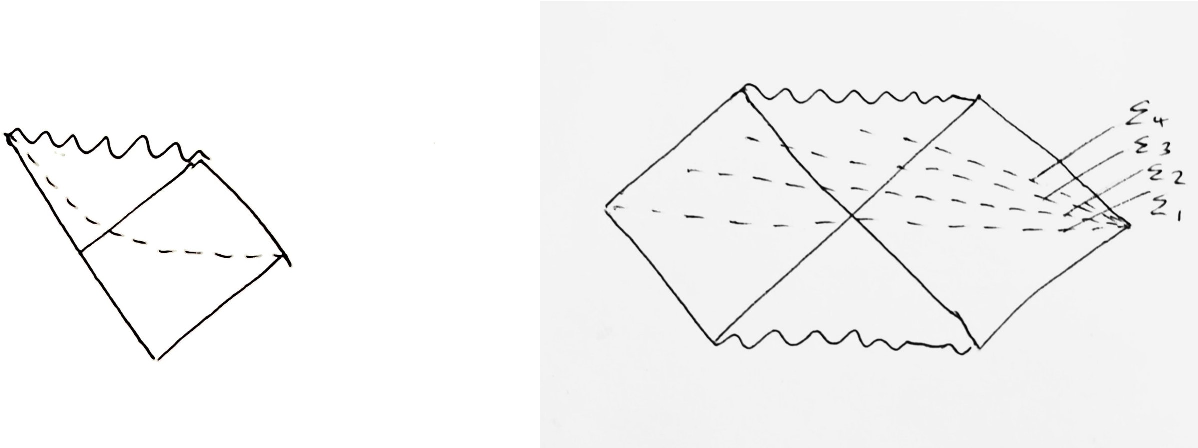

Figure 2.1: Penrose Diagrams, Σ_{t_0} dashed, Left: Ingoing Eddington-Finkelstein Coordinates, Right: Isotropic Coordinates.

Lapse Gauge Conditions

The simplest lapse choice would be to enforce $\alpha = 1$, called geodesic slicing, with the hypersurface following intergral curves of n^μ; given that geodesics can converge this can lead to hypersurface self-intersection which breaks the definition of a Cauchy surface and the simulation will likely fail. Another problem is that a black hole singularity can be reached in finite simulation time. Geodesic slicing can be modified to the maximal slicing condition which keeps the volume element $\sqrt{-g}$ constant along geodesics. This means as $\gamma \to \infty$ nearing a singularity $\alpha \to 0$ from Eq. (2.1.70), causing the hypersurface to advance more slowly before a singularity is reached as demonstrated in Fig. (2.2). This property is called singularity avoiding and is crucial for numerical stability unless using excision[1]. Maximal slicing can be implemented by forcing $\mathcal{K} = \partial_t \mathcal{K} = 0 \; \forall t$ which requires a slow elliptic solve for α at each timestep. Instead α is promoted to an evolution variable and is evolved along with every other simulation variable. To do this we can pick an algebraic slicing condition of the Bona-Masso type,

$$\mathcal{L}_m \alpha = \partial_t \alpha - \beta^i \partial_i \alpha = -\alpha^2 f(\alpha) \mathcal{K}. \tag{2.1.103}$$

Using this with $f = 2\alpha^{-1}$ gives,

$$\mathcal{L}_m \alpha = \partial_t \alpha - \beta^i \partial_i \alpha = -2\alpha \mathcal{K}, \tag{2.1.104}$$

which is called 1+log slicing; this is very common in Numerical Relativity codes. In practice 1+log slicing is strongly singularity avoiding reaching $\alpha = 0$ before the singularity. This is modified in the CCZ4 scheme to,

$$\partial_t \alpha = -2\alpha \left[\mathcal{K} - 2\Theta\right] + \beta^i \partial_i \alpha. \tag{2.1.105}$$

In the absence of the CCZ4 formulation and using gaussian normal coordinates $\beta^i = 0$, the 1+log slicing condition reduces to,

$$\alpha = 1 + \ln \gamma, \tag{2.1.106}$$

giving the slicing condition it's name.

[1]Excision is the practice of cutting singularities out of a simulation while supplying suitable boundary conditions about the excised region

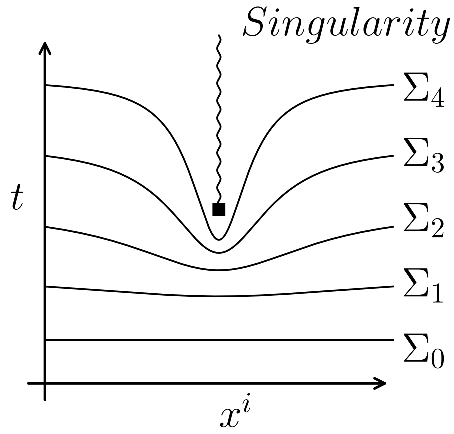

Figure 2.2: Diagram showing the time evolution of a hypersurface using a singularity avoiding lapse gauge condition. The vertical squiggled line represents a physical singularty that is formed at some point in spacetime, potentially from the collapse of matter to a black hole.

Shift Gauge Conditions

The simplest choice for the shift vector would be $\beta^i = 0$ but this causes great stretching and shearing of Σ_t in the neghbourhood of a singularity as in Fig. (2.2); the effect of this is that neighbouring gridpoints have large differences in field values leading to inaccurate and unstable evolutions. Another negative side effect is that the computational domain can fall inside an event horizon in black hole simulations. To counteract this we want to pick a shift vector that minimises hypersurface shear σ_{ij} which can be defined as [REF] [ref 1977 smarr and york],

$$\sigma_{ij} := \perp_i^{\mu} \perp_j^{\nu} \left[\nabla_{(\mu} n_{\nu)} - \frac{1}{3} \gamma^{ab} \nabla_{(a} n_{b)} \gamma_{\mu\nu} \right], \tag{2.1.107}$$

where σ_{ij} is tracefree corresponding to shearing rather than inflation or expansion. Minimising the total shear Σ,

$$\Sigma = \int \sigma_{ij} \sigma^{ij} \sqrt{\gamma}\, \mathrm{d}x^3, \tag{2.1.108}$$

with respect to β^i leads to an elliptic PDE to be solved for each β^i at each time step that minimises shear,

$$\delta\Sigma = 0 \rightarrow \mathcal{D}_i \sigma^{ij} = 0. \tag{2.1.109}$$

This is known as the minimal shift condition. As before, promoting β^i to be evolution variables is computationally cheaper that solving a set of PDE's at each time step. A very common choice is to promote the elliptic PDE for β^i into a hyperbolic equation via introducing a $\partial_t^2 \beta^i$ term and an artificial damping term parameterised by η. This becomes a damped wave equation and is supposed to transport away any part of β^i which does not satisfy $\mathcal{D}_i \sigma^{ij} = 0$. This works well with Sommerfeld (outgoing wave) boundary conditions given in section 3.1.2. The standard Gamma driver shift condition is,

$$\partial_t \beta^i = F B^i, \tag{2.1.110}$$

$$\partial_t B^i = \partial_t \tilde{\Gamma}^i - \eta B^i, \tag{2.1.111}$$

where $F = 3/4$ and $\eta = 1$.

Moving Puncture Gauge

The moving puncture gauge is the combination of the 1+log slicing lapse condition in Eq. 2.1.104 and the Gamma driver shift condition in Eqs. (2.1.110) and (2.1.111). The moving puncture gauge lead to a breakthrough in numerical relativity, allowing for the first successful simulation of a back hole binary [REF]. Even though $\chi \to 0$, or $\gamma \to \infty$, at the centre of a black hole, as long as the black hole singulary (also called the puncture) does not start on a gridpoint then no field values diverge and the simulation can run. This can be safeguarded by setting a minimum value for χ, such as $\chi = 10^{-4}$. Even thought it is unphysical to modify a physical variable, any errors this causes are localised to well within the event horizon and as a result do not propogate away from the puncture.

Not only does the moving puncture gauge safely allow for the divergence of fields at the puncture, but it causes the puncture to move; hence the name *moving* puncture gauge. Near the puncture, the lapse α becomes vanishingly small and the 1+log slicing condition in Eq. (2.1.104) becomes,

$$\partial_t \alpha = \beta^i \partial_i \alpha, \tag{2.1.112}$$

which causes the puncture to move.

2.2 Mathematical Modelling of Boson Stars

2.2.1 Action

The Boson Stars considered are a complex Klein Gordon Scalar field, φ, minimally coupled to gravity. The action is the Einstein-Hilbert vacuum action plus the matter action for curved space,

$$S = \int_{\mathcal{M}} \left[\mathcal{L}_{EH} + \mathcal{L}_M\right] \sqrt{-g}\, \mathrm{d}x^4, \tag{2.2.1}$$

$$\mathcal{L}_{EH} = \frac{1}{16\pi G} R, \tag{2.2.2}$$

$$\mathcal{L}_M = -\frac{1}{2} g^{\mu\nu} \nabla_\mu \varphi^* \nabla_\nu \varphi - \frac{1}{2} V(|\varphi|^2), \tag{2.2.3}$$

Here V is the Klein-Gordon potential and it's effect on boson stars is discussed in []. Some common choices of poteantials are,

$$V = \frac{m^2 c^2}{\hbar^2} |\varphi|^2, \tag{2.2.4}$$

$$V = \frac{m^2 c^2}{\hbar^2} |\varphi|^2 + \frac{1}{2} \Lambda_4 |\varphi|^4, \tag{2.2.5}$$

$$V = \frac{m^2 c^2}{\hbar^2} |\varphi|^2 \left(1 - \frac{|\varphi|^2}{2\sigma^2}\right)^2, \tag{2.2.6}$$

where $\hbar$ and c are given for completeness but will be set to unity from now on. Considering only the m^2 term, which corresponds to the squared mass of the particle in the quantum theory, we get a massive wave equation linear in φ, leading to so called mini Boson stars. Having $\Lambda_4 \neq 0$ gives self-interacting stars which have a nonlinear wave equation corresponding to particle creation and annihilation at the quantum level; self interacting potentials can include higher order terms in φ such as $|\varphi|^6$, $|\varphi|^8$ and more. These self interacting potentials tend to have star solutions with a higher density. Finally, Eq. (2.2.6) describes the solitonic potential, giving rise to boson stars with compactnesses comparable to neutron stars.

Varying the action with respect to the metric and scalar field return the Einstein Field equations and the Klein Gordon equation of curved space respectively,

$$R_{\mu\nu} - \frac{1}{2} R g_{\mu\nu} = \frac{8\pi G}{c^4} T_{\mu\nu}, \tag{2.2.7}$$

$$g^{\mu\nu} \nabla_\mu \nabla_\nu \varphi = \frac{\partial V}{\partial |\varphi|^2} \varphi. \tag{2.2.8}$$

Collectively these are known as the Einstein-Klein-Gordon (EKG) equations. From Eq. (1.4.83), the boson-specific stress energy tensors are,

$$T_{\mu\nu} := -2 \frac{\delta \mathcal{L}_M}{\delta g^{\mu\nu}} + g_{\mu\nu} \mathcal{L}_M, \tag{2.2.9}$$

$$T_{\mu\nu} = \frac{1}{2} \nabla_\mu \varphi^* \nabla_\nu \varphi + \frac{1}{2} \nabla_\nu \varphi^* \nabla_\mu \varphi - \frac{1}{2} g_{\mu\nu} \left[g^{\alpha\beta} \nabla_\alpha \varphi^* \nabla_\beta \varphi + V\right]. \tag{2.2.10}$$

Studying neutron stars requires the fermionic, or ordinary fluid, stress tensor $\boldsymbol{T}_F$;

$$T_F^{\mu\nu} = \left[\rho c^2 + P\right] \frac{u^\mu u^\nu}{c^2} + P g^{\mu\nu} + 2u^{(\mu} q^{\nu)} + \pi^{\mu\nu} + \dots\,. \tag{2.2.11}$$

The continuity equation from Eq. (1.4.34), $\nabla_\nu T^{\mu\nu} = 0$, returns the highly nonlinear relativistic Navier-Stokes equations of curved space. The viscosity term $\pi^{\mu\nu}$ and heat flux q^μ are often omitted for simplicity. The remaining variables ρ, P and u^μ are the fluid density, pressure and worldline tangent. Just as in flat space, the Navier-Stokes equations can develop shockwaves and the use of sophisticated shock capturing schemes is required, unlike the linear Klein-Gordon equation which is linear in the principal part.

2.2.2 Solitons

A soliton is a wave that exhibits particle-like behaviour. More precisely, in classical field theory, a soliton is a field or set of fields in a localised configuration that can travel at constant speed but not disperse. For our purposes, we look for solitons in the Einstein-Klein-Gordon (EKG) system which are self gravitating localised scalar field and metric configurations. In the case of the real scalar field it was shown by [REF] that there are no long lived stars; however promoting the field to a complex scalar we can find a spherically symmetric stationary soliton with the following scalar field,

$$\varphi = \Phi(r)e^{i\omega t}, \tag{2.2.12}$$

in spherical polar coordinates $x^\mu \in \{t, r, \theta, \phi\}$. Traditionally, the polar areal gauge has been used for the metric's ansatz,

$$g_{\mu\nu}\mathrm{d}x^\mu \mathrm{d}x^\nu = -a^2(r)\mathrm{d}t^2 + b^2(r)\mathrm{d}r^2 + r^2\left[\mathrm{d}\theta^2 + \sin^2\theta \mathrm{d}\phi^2\right], \tag{2.2.13}$$

where the boundary condition $b^2(0) = 1$ is demanded to avoid a conical singularity at the origin. However an isotropic gauge is more useful for simulations due to easier conversion to cartesian space-coordinates, for more information on isotropic coordinates see section 1.4.5. The polar areal solution must then be transformed into an isotropic solution. Alternatively, the approach taken in this report, is to start with an isotropic ansatz,

$$g_{\mu\nu}\mathrm{d}x^\mu \mathrm{d}x^\nu = -\Omega^2(r)\mathrm{d}t^2 + \Psi^2(r)\mathrm{d}\boldsymbol{x}^2, \tag{2.2.14}$$

where $\mathrm{d}\boldsymbol{x}^2$ denotes the euclidean 3D line element; this changes between spherical polar or cartesian coordinates trivially. This ends up being slightly harder to solve for numerically, but no conversion to isotropic coordinates is needed afterwards.

To get a set of ODE's to solve for the functions $\{\Omega(r), \Psi(r), \Phi(r)\}$ we must turn to the Einstein Equation and Klein Gordon Equation. The Einstein Equations for $\{\mu, \nu\} = \{0,0\}, \{1,1\}, \{2,2\}$ are the only components that give unique non-zero equations in spherical symmetry; they are,

$$\frac{\Omega^2\left[r\Psi'^2 - 2\Psi\left[r\Psi'' + 2\Psi'\right]\right]}{r\Psi^4} = 4\pi G\left[\Omega^2\left[\frac{P'^2}{\Psi^2} + V\right] + \omega^2 P^2\right], \tag{2.2.15}$$

$$\frac{2\Psi\Psi'\left[r\Omega' + \Omega\right] + r\Omega\Psi'^2 + 2\Psi^2\Omega'}{r\Psi^2\Omega} = 4\pi G\left[P'^2 - \Psi^2 V + \frac{\omega^2 P^2\Psi^2}{\Omega^2}\right], \tag{2.2.16}$$

$$r\left[-\frac{r\Psi'^2}{\Psi^2} + \frac{r\Psi'' + \Psi'}{\Psi} + \frac{r\Omega'' + \Omega'}{\Omega}\right] = -4\pi G r^2\Psi^2\left[\frac{P'^2}{\Psi^2} + V - \frac{\omega^2 P^2}{\Omega^2}\right]. \tag{2.2.17}$$

The Einstein tensor $G_{\mu\nu} = R_{\mu\nu} - \frac{1}{2}Rg_{\mu\nu}$ (left above) and the stress tensor $T_{\mu\nu}$ (right above) were obtained with a private, self written Mathematica notebook. Substituting the metric ansatz Eq. (2.2.14) and the field ansatz Eq. (2.2.12) into Eq. (2.2.8), the Klein Gordon equation becomes,

$$g^{\mu\nu}\nabla_\mu\nabla_\nu\varphi = \frac{\partial V}{\partial|\varphi|^2}\varphi, \tag{2.2.18}$$

$$\frac{1}{\sqrt{-g}}\partial_\mu\left[\sqrt{-g}g^{\mu\nu}\partial_\nu\Phi(r)e^{i\omega t}\right] = \frac{\partial V}{\partial|\varphi|^2}\Phi(r)e^{i\omega t}, \tag{2.2.19}$$

$$\Phi'' = \Phi\Psi^2\left[V' - \frac{\omega^2}{\Omega^2}\right] - \Phi'\left[\frac{\Omega'}{\Omega} + \frac{\Psi'}{\Psi} + \frac{2}{r}\right]. \tag{2.2.20}$$

Simplifying the Einstein Equations and combinig with the Klein Gordon equation we get three ODE's to solve; the EKG system has been reduced to two second order ODE's and a first order ODE,

$$\Omega' = \frac{\Omega}{r\Psi' + \Psi}\left[2\pi G r\Psi\left[\Phi'^2 - \Psi^2 V + \frac{\omega^2\Phi^2\Psi^2}{\Omega^2}\right] - \Psi' - \frac{r\Psi'^2}{2\Psi}\right], \tag{2.2.21}$$

$$\Psi'' = \frac{\Psi'^2}{2\Psi} - \frac{2\Psi'}{r} - 2\pi G\left[V\Psi^3 + \Phi'^2\Psi + \frac{\omega^2\Phi^2\Psi^3}{\Omega^2}\right], \tag{2.2.22}$$

$$\Phi'' = \Phi\Psi^2\left[V' - \frac{\omega^2}{\Omega^2}\right] - \Phi'\left[\frac{\Omega'}{\Omega} + \frac{\Psi'}{\Psi} + \frac{2}{r}\right]. \tag{2.2.23}$$

This is turned into a set of five first order ODE's to numerically integrate from $r = 0$ out to large radius. Note that if we had used the polar areal ansatz in Eq. (2.2.13) the equation for Φ would also be first order; reducing the EKG system to four first order ODE's.

2.2.3 3+1 Klein Gordon System

Now let's project the Klein Gordon equation in a 3+1 split to get the evolution equations. The first step is to turn the second order Klein-Gordon equation into two first order ones

$$\mathcal{L}_m\varphi = ..., \tag{2.2.24}$$
$$\mathcal{L}_m\Pi = ..., \tag{2.2.25}$$

where Π is the foliation dependant definition of conjugate momentum to the complex scalar field,

$$\Pi := -\mathcal{L}_n\varphi. \tag{2.2.26}$$

Decomposing the Klein Gordon Equation,

$$\nabla^\mu\nabla_\mu\varphi = V'\varphi = \frac{1}{\sqrt{-g}}\partial_\mu\left[\sqrt{-g}\left[\gamma^{\mu\nu} - n^\mu n^\nu\right]\partial_\nu\varphi\right] = \frac{1}{\sqrt{-g}}\partial_\mu\left[\sqrt{-g}\left[\mathcal{D}^\mu\varphi - n^\mu\mathcal{L}_n\varphi\right]\right]. \tag{2.2.27}$$

The term with $\mathcal{D}^\mu$ simplifies like,

$$\frac{1}{\sqrt{-g}}\partial_\mu\left[\sqrt{-g}\mathcal{D}^\mu\varphi\right] = \frac{1}{\alpha\sqrt{\gamma}}\partial_\mu\left[\alpha\sqrt{\gamma}\mathcal{D}^\mu\varphi\right] = \mathcal{D}_\mu\mathcal{D}^\mu\varphi + \mathcal{D}^\mu\varphi\,\partial_\mu\ln\alpha, \tag{2.2.28}$$

and the remainder becomes,

$$-\frac{1}{\sqrt{-g}}\partial_\mu\left[\sqrt{-g}n^\mu\mathcal{L}_n\varphi\right] = -\left[\nabla\cdot n + n\cdot\partial\right]\mathcal{L}_n\varphi = -\mathcal{K}\Pi + \mathcal{L}_n\Pi. \tag{2.2.29}$$

Combining these results, the full Klein Gordon system is constructed,

$$\mathcal{L}_m\Pi = -\mathcal{D}^\mu\varphi\,\partial_\mu\alpha + \alpha\left[\mathcal{K}\Pi - \mathcal{D}_\mu\mathcal{D}^\mu\varphi + V'\varphi\right], \tag{2.2.30}$$
$$\mathcal{L}_m\varphi = -\alpha\Pi. \tag{2.2.31}$$

The final matter term we must decompose is the Klein-Gordon stress tensor in Eq. (2.2.10) with Eqs. (2.1.45), (2.1.46) and (2.1.47).

$$\rho = n^\mu n^\nu T_{\mu\nu} = \frac{1}{2}|\Pi|^2 + \frac{1}{2}\gamma^{ij}\mathcal{D}_i\varphi^*\mathcal{D}_j\varphi + \frac{1}{2}V(|\varphi|^2), \tag{2.2.32}$$

$$S_i = -\perp_i^\mu n^\nu T_{\mu\nu} = \frac{1}{2}\left[\Pi^*\mathcal{D}_i\varphi + \Pi\mathcal{D}_i\varphi^*\right], \tag{2.2.33}$$

$$S_{ij} = \perp_i^\mu\perp_j^\nu T_{\mu\nu} = \mathcal{D}_{(i}\varphi\mathcal{D}_{j)}\varphi^* - \frac{1}{2}\left[\gamma^{ij}\mathcal{D}_i\varphi\mathcal{D}_j\varphi^* - |\Pi|^2 + V(|\varphi|^2)\right]. \tag{2.2.34}$$

2.2.4 Klein Gordon's Noether Charge

For the complex scalar field, we have the U(1) symmetry,

$$\varphi \to \varphi e^{i\epsilon} \approx \varphi + i\epsilon\varphi, \tag{2.2.35}$$
$$\varphi^* \to \varphi^* e^{-i\epsilon} \approx \varphi^* - i\epsilon\varphi^*, \tag{2.2.36}$$

which leaves the Lagrangian unchanged and therefore the total action. The associated conserved current j and current density $\mathcal{J}$ are then,

$$j^\mu = \frac{\delta\mathcal{L}}{\delta\nabla_\mu\varphi}\delta\varphi + \frac{\delta\mathcal{L}}{\delta\nabla_\mu\varphi^*}\delta\varphi^*, \tag{2.2.37}$$
$$j^\mu = ig^{\mu\nu}\left[\varphi\nabla_\nu\varphi^* - \varphi^*\nabla_\nu\varphi\right], \tag{2.2.38}$$

where the current satisfies the continuity equation,

$$\nabla_\mu j^\mu = 0. \tag{2.2.39}$$

Using Eq. (1.3.141), the continuity equation can be re-written as,

$$\nabla_\mu j^\mu = \frac{1}{\sqrt{-g}}\partial_\mu\left(\sqrt{-g}j^\mu\right) = \frac{1}{\sqrt{-g}}\partial_\mu\mathcal{J}^\mu = 0, \tag{2.2.40}$$

where $\mathcal{J}^\mu = \sqrt{-g}j^\mu$ is the current expressed as a tensor density. Therefore,

$$\partial_\mu\mathcal{J}^\mu = 0, \tag{2.2.41}$$

is also true and even in curved space the current $\boldsymbol{\mathcal{J}}$ obeys a conservation equation; this means there must be some conserved charge $\mathcal{Q}$ associated with the current. Integrating Eq. (2.2.41) over a manifold $\mathcal{M}$ gives,

$$\int_\mathcal{M}\nabla_\mu j^\mu\sqrt{-g}\,\mathrm{d}x^4 = 0, \tag{2.2.42}$$
$$\int_\mathcal{M}\partial_\mu\left[\sqrt{-g}j^\mu\right]\mathrm{d}x^4 = 0, \tag{2.2.43}$$
$$\int_\mathcal{M}\partial_\mu\mathcal{J}^\mu\mathrm{d}x^4 = 0, \tag{2.2.44}$$
$$\int_{t_0}^{t_1}\left[\int_{\Sigma_t}\partial_0\mathcal{J}^0\mathrm{d}x^3\right]\mathrm{d}t = -\int_{t_0}^{t_1}\left[\int_{\Sigma_t}\partial_i\mathcal{J}^i\mathrm{d}x^3\right]\mathrm{d}t, \tag{2.2.45}$$
$$\int_{t_0}^{t_1}\left[\int_{\Sigma_t}\partial_0\mathcal{J}^0\mathrm{d}x^3\right]\mathrm{d}t = -\int_{t_0}^{t_1}\left[\int_{\partial\Sigma_t}\hat{s}_i\mathcal{J}^i\mathrm{d}x^2\right]\mathrm{d}t, \tag{2.2.46}$$
$$\int_{t_0}^{t_1}\left[\int_{\Sigma_t}\partial_0\mathcal{J}^0\mathrm{d}x^3\right]\mathrm{d}t = 0, \tag{2.2.47}$$

where the flat space divergence theorem was used and $\hat{\boldsymbol{s}}$ is the flat space normal to $\partial\Sigma_t$, the boundary of Σ_t. The term containing $\hat{s}_i\mathcal{J}^i$ integrates to zero over $\partial\Sigma_t$ due to $\mathcal{J}$ vanishing on $\partial\Sigma_t$. The $\mathcal{J}^0$ term can be simplified by permuting the time derivative using,

$$\partial_0\int_{\Sigma_t}\mathcal{J}^0\mathrm{d}x^3 = \int_{\Sigma_t}\partial_0\mathcal{J}^0\mathrm{d}x^3 + \lim_{\Delta x^0\to 0}\left[\frac{1}{\Delta x^0}\int_{\Delta\Sigma_t}\left[\mathcal{J}^0 + \Delta x^0\partial_0\mathcal{J}^0\right]\mathrm{d}x^3\right], \tag{2.2.48}$$

where the last term vanishes as $\mathcal{J}$ vanishes near $\partial\Sigma$, and Eq. (2.2.47) becomes,

$$\int_{t_0}^{t_1}\left[\partial_0\int_{\Sigma_t}\mathcal{J}^0\mathrm{d}x^3\right]\mathrm{d}t = 0, \tag{2.2.49}$$

and the formula for the conserved charge Q can be read off as,

$$\partial_0 Q = 0, \tag{2.2.50}$$

$$Q = \int_{\Sigma_t} \mathcal{J}^0 \mathrm{d}x^3. \tag{2.2.51}$$

The charge density $\mathcal{Q}$ is defined as,

$$Q := \int_{\Sigma_t} \mathcal{Q}\sqrt{\gamma}\,\mathrm{d}x^3, \tag{2.2.52}$$

$$\mathcal{Q} = \frac{\mathcal{J}^0}{\sqrt{\gamma}} = \frac{\sqrt{-g}j^0}{\sqrt{\gamma}} = \alpha j^0, \tag{2.2.53}$$

where Eq. (2.1.70), saying $\sqrt{-g} = \alpha\sqrt{\gamma}$, was used. Finally we get an expression for the total Noether charge $N = Q$,

$$N = i\int_{\Sigma_t} \sqrt{-g}\left[\varphi\nabla^0\varphi^* - \varphi^*\nabla^0\varphi\right]\mathrm{d}x^3. \tag{2.2.54}$$

Using $\sqrt{-g} = \alpha\sqrt{\gamma}$ again and $\alpha\nabla^0\varphi = -n_\mu\nabla^\mu\varphi = \Pi$ from Eq. (2.2.26) we get the following neat formula,

$$N = i\int_{\Sigma_t} \left[\varphi\Pi^* - \varphi^*\Pi\right]\sqrt{\gamma}\,\mathrm{d}x^3. \tag{2.2.55}$$

Equivalently, the Noether charge density $\mathcal{N}$ is ,

$$\mathcal{N} = i\left(\varphi\Pi^* - \varphi^*\Pi\right). \tag{2.2.56}$$

The ideas of this section, concerning conserved charges are extended in section **??** with applications to continuity equations in energy, momentum, angular momentum and noether charges for spin-1 Proca fields. The results of this section have all been derived for an infinite volume where only a charge density $\mathcal{Q}$ needs be considered. Section **??** considers continuity equations in a finite volume V so must also consider the flux density $\mathcal{F}$ of conserved particles through ∂V (the boundary of V) and the source density $\mathcal{S}$ (creation and destruction of $\mathcal{Q}$) in V.

2.2.5 Boosted Boson Stars and Black Holes

Let us now consider a moving star, this corresponds to boosting a stationary soliton solution. There is no unique way of doing this as any coordinate transformation that reduces to a Minkowski spacetime boost at large radius is valid. All the degrees of freedom we have can be absorbed into a coordinate gauge choice so it makes sense to choose the trivial, constant valued boost, with rapidity $\chi = \operatorname{arctanh}(v)$ for a velocity v, from Special Relativity. Using Cartesian coordinates, the boost matrix $\mathbf{\Lambda}$ for a boost in the x direction is,

$$\Lambda^\mu_\nu = \exp\begin{pmatrix} 0 & -\chi & 0 & 0 \\ -\chi & 0 & 0 & 0 \\ 0 & 0 & 1 & 0 \\ 0 & 0 & 0 & 1 \end{pmatrix} = \begin{pmatrix} \cosh(\chi) & -\sinh(\chi) & 0 & 0 \\ -\sinh(\chi) & \cosh(\chi) & 0 & 0 \\ 0 & 0 & 1 & 0 \\ 0 & 0 & 0 & 1 \end{pmatrix}, \tag{2.2.57}$$

as discussed in section 1.4.1. Declaring the boosted frame and lab frame (in which the star is moving) to have coordinates x^μ and $\tilde{x}^\mu$,

$$\tilde{x}^\mu = [\Lambda^{-1}]^\mu{}_\nu x^\nu, \tag{2.2.58}$$

where both x^μ and $\tilde{x}^\mu$ agree on an origin. The metric transforms via the tensor transformation law like,

$$\tilde{g}_{\mu\nu}(\tilde{x}^\sigma) = \frac{\partial x^\alpha}{\partial\tilde{x}^\mu}\frac{\partial x^\beta}{\partial\tilde{x}^\nu}g_{\alpha\beta}(\tilde{x}^\sigma) = \Lambda^\alpha{}_\mu\Lambda^\beta{}_\nu g_{\alpha\beta}(\tilde{x}^\sigma), \tag{2.2.59}$$

where the inverse boost matrix $\mathbf{\Lambda}^{-1}$ can be found simply by $\mathbf{\Lambda}^{-1}(\chi) = \mathbf{\Lambda}(-\chi)$ which is equivalent to a boost in the opposite direction. We choose the boosted soliton's initial Cauchy surface to be the level set of $\tilde{t} = 0$, an instance of time in the lab frame. The coordinates and metric transform as,

$$x^\mu = \{t, x, y, z\} = \{\tilde{t}\cosh(\chi) + \tilde{x}\sinh(\chi), \tilde{x}\cosh(\chi) + \tilde{t}\sinh(\chi), \tilde{y}, \tilde{z}\}, \tag{2.2.60}$$

$$g_{\mu\nu} = \text{diag}\{-\Omega^2, \Psi^2, \Psi^2, \Psi^2\}, \tag{2.2.61}$$

$$\tilde{g}_{\mu\nu} = \begin{pmatrix} -\Omega^2\cosh^2(\chi) + \Psi^2\sinh^2(\chi) & \sinh(\chi)\cosh(\chi)\left[\Omega^2 - \Psi^2\right] & 0 & 0 \\ \sinh(\chi)\cosh(\chi)\left[\Omega^2 - \Psi^2\right] & \Psi^2\cosh^2(\chi) - \Omega^2\sinh^2(\chi) & 0 & 0 \\ 0 & 0 & \Psi^2 & 0 \\ 0 & 0 & 0 & \Psi^2 \end{pmatrix}, \tag{2.2.62}$$

as the star is at rest using coordinates x^μ rather than $\tilde{x}^\mu$. Comparing this boosted metric to the $3+1$ decomposed metric in Eq. (2.1.67) we can read off the shift vector $\tilde{\beta}_i$, the 3-metric $\tilde{\gamma}_{ij}$ and obtain the lapse and metric determinant,

$$\tilde{\alpha}^2 = \frac{\Psi^2\Omega^2}{\Psi^2\cosh^2(\chi) - \Omega^2\sinh^2(\chi)}, \tag{2.2.63}$$

$$\tilde{\gamma} = \det\tilde{\gamma}_{ij} = \Psi^4\left[\Psi^2\cosh^2(\chi) - \Omega^2\sinh^2(\chi)\right]. \tag{2.2.64}$$

Finally, the conformal 3-metric with unit determinant is,

$$\bar{\gamma}_{ij} = \tilde{\gamma}^{-\frac{1}{3}}\begin{pmatrix} \Psi^2\cosh^2(\chi) - \Omega^2\sinh^2(\chi) & 0 & 0 \\ 0 & \Psi^2 & 0 \\ 0 & 0 & \Psi^2 \end{pmatrix}, \tag{2.2.65}$$

where normally $\tilde{\gamma}_{ij}$ is the conformal 3-metric, but to avoid confusion it is denoted $\bar{\gamma}_{ij}$ in this section. Turning our attention to the matter fields now we only need to change the coordinate dependance, like $\varphi(x) \to \varphi(\tilde{x})$, given that φ and Π are (complex) scalar fields. Given that $\tilde{t} = 0$ describes a time slice in the lab frame (where the star has non-zero velocity), $t = \tilde{x}\sinh(\chi)$ in the rest frame and we get the following boosted complex scalar field,

$$\varphi = \Phi(r)e^{i\omega\tilde{x}\sinh(\chi)}, \tag{2.2.66}$$

where r is the radius in the boosted frame; $r = \sqrt{\tilde{x}^2\cosh^2(\chi) + \tilde{y}^2 + \tilde{z}^2}$. Note the field is modulated by an oscillatory phase now with wavenumber $k = \omega\tilde{x}\sinh(\chi)$; nodal planes in $\text{Re}(\varphi)$ appear perpendicular to velocity. The conjugate momentum $\tilde{\Pi}$, defined in Eq. (2.2.26), in the rest frame it becomes,

$$\tilde{\Pi}(\tilde{x}^\mu) = -\mathcal{L}_{\tilde{n}}\varphi(\tilde{x}^\mu) = -\frac{1}{\tilde{\alpha}}\tilde{m}\cdot\tilde{\partial}\varphi = -\frac{1}{\tilde{\alpha}}\left[\tilde{\partial}_0 - \tilde{\beta}^i\tilde{\partial}_i\right]\Phi(r)e^{i\omega t}. \tag{2.2.67}$$

Inconveniently we cannot simply evaluate $\tilde{\Pi}$ in the boosted frame as this has a different spacetime foliation and the normal vector $\boldsymbol{n} \neq \tilde{\boldsymbol{n}}$ is genuinely changed; not just transforming components under coordinate transformation. Explicitly writing the contravariant components of the shift vector,

$$\tilde{\beta}^i = \left(\frac{\sinh(\chi)\cosh(\chi)\left[\Omega^2 - \Psi^2\right]}{\Psi^2\cosh^2(\chi) - \Omega^2\sinh^2(\chi)}, 0, 0\right), \tag{2.2.68}$$

and using the following derivative formulae,

$$\partial_{\tilde{t}} = \cosh(\chi)\partial_t + \sinh(\chi)\partial_x, \tag{2.2.69}$$

$$\partial_{\tilde{x}} = \cosh(\chi)\partial_x + \sinh(\chi)\partial_t, \tag{2.2.70}$$

$$\partial_t\varphi = \Phi\partial_t e^{i\omega t} = i\omega\Phi e^{i\omega t}, \tag{2.2.71}$$

$$\partial_x\varphi = \frac{\partial r}{\partial x}\Phi' e^{i\omega t} = \frac{x}{r}\Phi' e^{i\omega t}, \tag{2.2.72}$$

we get an expression for the conjugate momentum of a boosted star. Again, setting $\tilde{t} = 0$ gives the conjugate momentum on the surface $\tilde{t} = 0$ to be used as initial conditions,

$$\widetilde{\Pi} = -\frac{1}{\tilde{\alpha}}\left[\left[\sinh(\chi) - \tilde{\beta}^1\cosh(\chi)\right]\frac{\tilde{x}\cosh(\chi)}{r}\Phi' + i\omega\left[\cosh(\chi) - \tilde{\beta}^1\sinh(\chi)\right]\Phi\right]e^{i\omega\tilde{x}\sinh(\chi)}. \tag{2.2.73}$$

The penultimate ingredient is the intrinsic curvature $\tilde{\boldsymbol{K}}$, defined in Eq. (2.1.10). Similarly to the conjugate momentum, the definition of $\tilde{\boldsymbol{K}}$ depends on the spacetime foliation so using $K_{ij} = 0$ in the stars rest frame and using the tensor transformation to conclude that $\tilde{K}_{ij} = 0$ in the rest frame (where the star moves) is incorrect. Instead the components $\tilde{K}_{ij}$ must be calculated from scratch with the correct normal vector $\boldsymbol{n}$ like,

$$\widetilde{\mathcal{K}}_{\mu\nu} := -\frac{1}{2}\mathcal{L}_{\tilde{n}}\tilde{\gamma}_{\mu\nu} = -\frac{1}{2\tilde{\alpha}}\mathcal{L}_{\tilde{m}}\tilde{\gamma}_{\mu\nu} = -\frac{1}{2\tilde{\alpha}}\left[\tilde{m}\cdot\tilde{\partial}\tilde{\gamma}_{ij} + \tilde{\gamma}_{ik}\tilde{\partial}_j\tilde{m}^k + \tilde{\gamma}_{jk}\tilde{\partial}_i\tilde{m}^k\right]. \tag{2.2.74}$$

A private, self written mathematica script gives the following explicit form for the components of $\tilde{K}_{ij}$,

$$\alpha^{-1}\widetilde{\mathcal{K}}_{xx} = \cosh^2(\chi)\sinh(\chi)\frac{x}{r}\frac{\left[v^2\Omega^2\Omega' + \Psi\Omega\Psi' - 2\Psi^2\Omega'\right]}{\Psi^2\Omega}, \tag{2.2.75}$$

$$\alpha^{-1}\widetilde{\mathcal{K}}_{xy} = \cosh(\chi)\sinh(\chi)\frac{y}{r}\frac{\left[\Omega\Psi' - \Psi\Omega'\right]}{\Psi\Omega}, \tag{2.2.76}$$

$$\alpha^{-1}\widetilde{\mathcal{K}}_{xz} = \cosh(\chi)\sinh(\chi)\frac{z}{r}\frac{\left[\Omega\Psi' - \Psi\Omega'\right]}{\Psi\Omega}, \tag{2.2.77}$$

$$\alpha^{-1}\widetilde{\mathcal{K}}_{yy} = -\sinh(\chi)\frac{x}{r}\frac{\Psi'}{\Psi}, \tag{2.2.78}$$

$$\widetilde{\mathcal{K}}_{zz} = \widetilde{\mathcal{K}}_{yy}, \tag{2.2.79}$$

where the $\{x, y, z\}$ need to be expanded in terms of $\{\tilde{x}, \tilde{y}, \tilde{z}\}$ and $r = \sqrt{x^2 + y^2 + z^2}$.

The final object needed is the three-dimensional connection symbols $\Upsilon^i{}_{jk}$, these are calculated numerically after the initial data is loaded in using the definition from Eq. (1.3.77),

$$\Upsilon^i_{jk} = \frac{1}{2}\gamma^{im}\left(\partial_k\gamma_{jm} + \partial_j\gamma_{mk} - \partial_m\gamma_{jk}\right). \tag{2.2.80}$$

The boost formalism described here can apply this to the Black Hole spacetime by an identical procedure setting,

$$\varphi = 0, \tag{2.2.81}$$

$$\Pi = 0, \tag{2.2.82}$$

$$\Omega = \frac{1 - \frac{M}{2r}}{1 + \frac{M}{2r}}, \tag{2.2.83}$$

$$\Psi = \left[1 + \frac{M}{2r}\right]^2, \tag{2.2.84}$$

corresponding to the isotropic Schwarzschild black hole given in section 1.4.5.

MIGHT JUST DELETE THIS SECTION

2.2.6 Spherical Harmonics in Curved Space DO I KEEP THIS SECTION? MAYBE JUST FOR INTERPITING SOME SIMS

Spherical harmonics are an orthonormal function basis for the surface of a sphere. They arise when looking for solutions to the 3D spherical polar laplacian

$$\nabla^2\varphi = \frac{1}{\sqrt{|g|}}\partial_\mu\left(\sqrt{|g|}g^{\mu\nu}\partial_\nu\varphi\right), \quad \mu,\nu \in \{1,2,3\}. \tag{2.2.85}$$

On the hypersurface $r = 1$ we get the following metric

$$g_{\mu\nu} = \begin{pmatrix} 1 & 0 \\ 0 & \sin^2\theta \end{pmatrix}, \tag{2.2.86}$$

and on this surface the spherical harmonics $Y_{lm}(\theta,\phi)$ satisfy the following condition.

$$\mathcal{D}_\mu\mathcal{D}^\mu Y_{lm}(\theta,\phi) = -l(l+1)Y_{lm}(\theta,\phi), \quad x^\mu \in \{\theta,\phi\} \tag{2.2.87}$$

This means we can take any spherically symmetric and static metric with $g_{\phi\phi} = \sin^2\theta g_{\theta\theta}$ and replace the angular part of the wave equation with $l(l+1)$. For a spherically symmetric spacetime this gives the Klein Gordon equation for scalar hair.

$$\nabla_\mu\nabla^\mu\varphi = V'\varphi, \quad \varphi = T(t)R(r)Y_{lm}(\theta,\phi) \tag{2.2.88}$$

$$\varphi^{-1}\nabla_\mu\nabla^\mu\varphi = g^{tt}\frac{\ddot{T}}{T} + \frac{1}{R\sqrt{|g|}}\partial_r\left(\sqrt{|g|}g^{rr}\partial_r R\right) - l(l+1)g^{\theta\theta} \tag{2.2.89}$$

This is a second order ODE for the radial profile R and is an eigenvalue problem for ω if we assume $T = e^{i\omega t}$. Assuming $T = e^{-kt}$ can be done on-top of the black hole metric () and requires the assumption of no back reaction of the scalar field on the metric; this gives an eigenvalue problem in k instead. This leads to the following ODE for the radial profile.

$$\frac{1}{R\sqrt{|g|}}\partial_r\left(\sqrt{|g|}\Psi^{-4}\partial_r R\right) = k^2\frac{\Omega^2}{\Psi^2} + \frac{l(l+1)}{r^2\Psi^4} + V' \tag{2.2.90}$$

Simulations shown later involve boson stars of mass M and black holes of mass $M \to 10M$; these simulations often produce scalar hair about these black holes that is orders of magnitude less massive than the boson stars. In this regime the above equation is assumed relevant.

MAYBE JUST USE THIS SECTION TO TALK ABOUT THE COLLISIONS THAT MAYBE SEEM TO FOLLOW THIS RULE ... SAY HOW EVEN THOUGHT ITS NOT REALLY SPHERICALLY SYMMETRIC MAYBE IT CAN BE APPROXIMATES BY THIS? AND WE CAN'T USE SUPERPOSISION OF SOLUTIONS REALLY

Chapter 3

Numerical Methods and GRChombo

3.1 Numerical Methods

3.1.1 Numerical Discretisation of Spacetime

The are many ways to time evolve a field theory on a spatial surface. Some popular numerical methods include spectral methods, fourrier methods, finite element models and finite volume methods [MAYBE ADD REFS?]. The method used throughout this work is the finite difference framework. This models a continuous spacetime with a discrete lattice of points; usually this lattice is cubic or cuboidal. A field $\phi(x^\mu)$ on a manifold $\mathcal{M}$ is expressed as a set of discrete values ϕ^n_{ijk}, for integer $\{n, i, j, k\}$, one a set of discrete lattice points with coordinates $(x^n_{ijk})^\mu$. In cartesian coordinates $(x^n_{ijk})^\mu = \{n\Delta t, i\Delta x, j\Delta y, k\Delta z\}$ where Δt, Δx, Δy and Δz represent the grid spacing. In the limit that the grid spacing tends to zero, the lattice and discretised fields perfectly model the continuum. For a detailed introduction to numerical methods the reader is directed to [2].

To calculate gradients on a lattice, we can consider a two dimensional manifold spanned by coordinates $\{t, x\}$. We can no longer employ the traditional definition of $\mathrm{d}f/\mathrm{d}x$,

$$\frac{\mathrm{d}f}{\mathrm{d}x} := \lim_{\delta x \to 0} \left(\frac{f(x + \delta x) - f(x)}{\delta x} \right), \tag{3.1.1}$$

as there no longer exists two points x and $x + \delta x$ that are infinitessimally close to each other. Derivatives are now calculated by comparing gridpoints a finite distance from each other. To elucidate this idea, a formula for the second derivative is calculated. First we pick five lattice points, equally spaced by Δx, with coordinates $\{x_{-2}, x_{-1}, x_0, x_1, x_2\}$, and writing $f(x_i) = f_i$. Then using the well known formula for the taylor expansion of a function about a point x_0,

$$f(x) = f(x_0) + (x - x_0)f'(x_0) + \frac{(x - x_0)^2}{2!} f''(x_0) + \frac{(x - x_0)^3}{3!} f'''(x_0) + \ldots, \tag{3.1.2}$$

we can write,

$$f_2 \approx f_0 + 2\Delta x f'_0 + 2(\Delta x)^2 f''_0 + \frac{4}{3}(\Delta x)^3 f'''_0 + \frac{2}{3}(\Delta x)^4 f''''_0, \tag{3.1.3}$$

$$f_1 \approx f_0 + \Delta x f'_0 + \frac{1}{2}(\Delta x)^2 f''_0 + \frac{1}{6}(\Delta x)^3 f'''_0 + \frac{1}{24}(\Delta x)^4 f''''_0, \tag{3.1.4}$$

$$f_0 \approx f_0, \tag{3.1.5}$$

$$f_{-1} \approx f_0 - \Delta x f'_0 + \frac{1}{2}(\Delta x)^2 f''_0 - \frac{1}{6}(\Delta x)^3 f'''_0 + \frac{1}{24}(\Delta x)^4 f''''_0, \tag{3.1.6}$$

$$f_{-2} \approx f_0 - 2\Delta x f'_0 + 2(\Delta x)^2 f''_0 - \frac{4}{3}(\Delta x)^3 f'''_0 + \frac{2}{3}(\Delta x)^4 f''''_0, \tag{3.1.7}$$

where the taylor expansions are truncated at terms of order $(\Delta x)^4$. The equations above can be inverted to give,

$$\left.\frac{\mathrm{d}^2 f}{\mathrm{d}x^2}\right|_{x_0} := f''_0 = \frac{-f_2 + 16f_1 - 30f_0 + 16f_{-1} - f_{-2}}{12(\Delta x)^2}, \tag{3.1.8}$$

and an approximation for the second derivative using a discrete sum of neighbouring points, also called a stencil, has been obtained. Adding terms of order $(\Delta x)^5$ would not affect the result as the pairs of terms $\{f_2, f_{-2}\}$ and $\{f_1, f_{-1}\}$ appear in equal amounts; therefore Eq. (3.1.8) is correct upto a taylor expansion of order $(\Delta x)^6$. Given that f''_0 appears with a $(\Delta x)^2$ and Eq. (3.1.8) is correct untill terms of order $(\Delta x)^6$, then the expression is accurate up to fourth order. Any other derivate to any order accuracy (in any dimension) can be calculated in a similar fashion. In the limit that the grid spacing $\Delta x \to 0$ the approximations for the derivatives approach the exact contiuum limit with higher order accurate stencils approach the continuum limit more quickly.

3.1.2 Boundary Conditions

Another artefact of evolving field equations over a volume on a computer is that the volume must have finite size; a computer does not have infinite memory to store an infinite amount of gridpoints. The usual way to deal with this problem is to enforce an algebraic condition on the fields on a surface surrounding the region of interest. Alternatively, an infinite volume can be modeled if coordinates are used which compactify the volume to some finite region, this corresponds to the grid spacing Δx diverging or resolution becoming infintely low quality towards the boundary.

Common boundary conditions include Dirichlet (fixed value), Von-Neumann (fixed derivative) or some mix of these conditions. It is common to re-categorize boundary conditions into sub-categories with informative names such as reflective, periodic or symmetric.

As an example in one spatial dimension, symmetric boundary conditions for a field ϕ about a point x_n could be implemented by creating extra *ghost cells* beyond the desired simulation domain with coordinates $\{x_{n+1}, x_{n+2}, x_{n+3}, ...\}$ and setting,

$$\phi_{n+1} = \phi_{n-1}, \quad \phi_{n+2} = \phi_{n-2}, \quad \phi_{n+3} = \phi_{n-3}, \quad \dots, \tag{3.1.9}$$

where $\phi_i = \phi(x_i) = \phi(i * \Delta x)$. These extra ghost cells allow the calculation of derivatives at x_n using stencils, as shown in section 3.1.1; without these ghost cells the stencil would not be able to access points x_m where $m > n$. The number of ghost cells should be chosen to be the minimum required to allow the calculation of derivcative stencils at each point in the simulation domain. The desired location of the boundary condition does not have to coincide with a gridpoint. As an example, modifying the symmetric boundary condition to be centered on $x_n + \Delta x/2$ instead results in,

$$\phi_{n+1} = \phi_n, \quad \phi_{n+2} = \phi_{n-1}, \quad \phi_{n+3} = \phi_{n-2}, \quad \dots. \tag{3.1.10}$$

Generic boundary conditions can be imposed by assigning values to ghost cells similarly to above. Although the examples given in this section are in one dimension, the ideas generalise to arbitrary dimensions.

Sommerfeld Boundary Conditions

A very useful type of boundary condition is the Sommerfeld boundary condition [3], used to approximate an outgoing wave being transmitted through the boundary condition. Sommerfeld boundary condtions can be derived from studying the solution to the wave equation in spherical symmetry in flat space,

$$-\frac{1}{v^2}\partial_t^2\Psi + \gamma^{ij}\mathcal{D}_i\mathcal{D}_j\Psi = -\frac{1}{v^2}\partial_t^2\Psi + \frac{1}{\sqrt{-\gamma}}\partial_i\left(\sqrt{\gamma}\gamma^{ij}\partial_j\Psi\right) = -\partial_t^2\Psi + \frac{1}{r^2}\partial_r\left(r^2\partial_r\Psi\right) = 0, \tag{3.1.11}$$

for some field Ψ with wavespeed v. In spherical polar coordinates, $\gamma^{ij} = \mathrm{diag}\{1, r^{-2}, r^{-2}\mathrm{cosec}^2(\theta)\}$. Equation (3.1.11) has an outgoing wave solution,

$$\Psi(r,t) = \Psi_\infty + \frac{A}{r}\psi(r - vt), \tag{3.1.12}$$

for an asymptotic value Ψ_∞ and arbitrary constant A. In differential form this can be written as,

$$\frac{1}{v}\partial_t\Psi + \partial_r\Psi + \frac{1}{r}(\Psi - \Psi_\infty) = 0. \tag{3.1.13}$$

The equation of motion for Ψ can be used to write ∂_t in terms of spatial derivatives and field values giving the new boundary condition which can be applied numerically as a regular mixed type boundary condition.

In general relativity, Sommerfeld boundary conditions are commonly used with $v = c = 1$ (the speed of light) to avoid reflections of matter and gravitational waves from the boundary of a simulation. It should be noted that Sommerfeld boundary conditions are approximate in general relativity for a number of reasons.

- Sommerfeld boundary conditions were derived in spherical symmetry and flat space; spacetimes often asymptote to spherically symmetric flat space, but this is only approximately true for finite radii.
- Matter doesn't always obey a wave equation or propogate at the speed of light.
- Gravitational waves only obey a linear wave equation under special circumstances such as specific wave shapes [BRILL WAVES?] and small amplitude waves in flat space.

It has been found experimentally in my work that ensuring the boundary conditions are sufficiently far away from any compact objects is very important in maintaining accuracy of the simulation when using Sommerfeld boundary conditions.

3.1.3 The Method of Lines

Assuming adequate boundary conditions are in place, the time evolution of initial data ϕ^n_{ijk} covering a spacelike computational grid can be done by applying a time integration scheme to the PDE governing the field $\phi(x^\mu)$. There are many ways to do this and the reader is directed to [2] for a comprehensive introduction. A common and simple method is the method of lines (MoL).

The MoL reduces the dimensionality of the PDE problem to set of ODE's in time at each gridpoint (with coordinate $\boldsymbol{x}_{ijk}$). Spatial derivatives are treated as a function on each gridpoint; their evaluation is done using the derivative stencils described in section 3.1.1. For example, consider the partial differential equation,

$$\partial_t \phi(\boldsymbol{x}, t) = \hat{O}\phi(\boldsymbol{x}, t) + f(\phi, \boldsymbol{x}, t), \tag{3.1.14}$$

where $\hat{O}$ is some spatial derivative operator, f is a function and $\boldsymbol{x}$ are spacelike coordinates. Using the MoL, the operator $\hat{O}$ is discretised on a grid like,

$$\hat{O}\phi(\boldsymbol{x}, t) \Rightarrow (O\phi)_{ijk}(t), \tag{3.1.15}$$

where $(O\phi)_{ijk}(t) \approx \hat{O}\phi(\boldsymbol{x}_{ijk}, t)$ is a sum of field values at neighbouring gridpoints generated by the method of finite differences. Discretising the function f on the grid gives the following ODE for each gridpoint with spatial indeces $\{i, j, k\}$,

$$\partial_t \phi_{ijk}(t) = (\hat{O}\phi)_{ijk}(t) + f_{ijk}(\phi, t) = F_{ijk}(\phi, t), \tag{3.1.16}$$

where $F_{ijk}(\phi, t)$ is treated as the discretisation of a continuum function $F(\phi, \boldsymbol{x}, t)$.

3.1.4 Integration of ODE's

To perform the time evolution of the ODE (3.1.16), we need to pick a time integration method for an ODE. The obvious choice might be to discretise the time integral like,

$$\partial_t \phi^n_{ijk} = \frac{\phi^{n+1}_{ijk} - \phi^n_{ijk}}{\Delta t}, \tag{3.1.17}$$

where Δt is the time-step of evolution. This can be substituted into Eq. (3.1.16) to give,

$$\phi^{n+1}_{ijk} = \phi^n_{ijk} + F^n_{ijk}\Delta t, \tag{3.1.18}$$

which is an explicit scheme; the desired future field values ϕ^{n+1}_{ijk} is given by an explicit formula in terms of the previous values ϕ^m_{ijk}. This is known as the Eular method and is often unstable; it can be shown to be completely unstable no matter how small Δt is taken to be for $F^n_{ijk} = A\phi^n_{ijk}$ for positive constant A. There is nothing stopping us instead writing,

$$\phi^{n+1}_{ijk} - F^{n+1}_{ijk}\Delta t = \phi^n_{ijk}, \tag{3.1.19}$$

which is known as an implicit scheme as the desired future field values ϕ_{ijk}^{n+1} is given by an implicit equation. This is called the backwards Eular method and is often stable, but only first order accurate in time. This can be improved to the second order accurate Crank-Nicolson method,

$$\phi_{ijk}^{n+1} - \frac{1}{2}F_{ijk}^{n+1}\Delta t = \phi_{ijk}^{n} + \frac{1}{2}F_{ijk}^{n}\Delta t, \tag{3.1.20}$$

but is still implicit in ϕ_{ijk}^{n}. The problem with implicit methods is that the F_{ijk}^{n+1} are some combination of the ϕ_{ijk}^{n+1} at $\boldsymbol{x}_{ijk}$ and multiple other neighbouring gridpoints to $\boldsymbol{x}_{ijk}$; the number of gridpoints increases with higher order accurate spatial derivatives. Solving the set of simultanious equations in Eq. (3.1.20), for example, requires the inverting of a very big (albeit sparse) matrix whose size scales with the number of gridpoints. This can be done in a single step if the F_{ijk}^{n} are linear in ϕ^{n}. For non-linear ODE's the F_{ijk}^{n} are non-linear in ϕ_{ijk}^{n}; in the best case one can linearise Eq. (3.1.20) and the ϕ_{ijk}^{n+1} can be solved with an iterative method, in the worst the implicit scheme is impossible to solve.

A stable and explicit method can be obtained by seeking a higher order accurate time derivative. In a similar fashion to the derivation of Eq. (3.1.8), one can write,

$$\phi_{ijk}^{n} = \phi_{ijk}^{n}, \tag{3.1.21}$$

$$\phi_{ijk}^{n-1} = \phi_{ijk}^{n} - \Delta t\dot{\phi}_{ijk}^{n} + \frac{1}{2}(\Delta t)^2\ddot{\phi}_{ijk}^{n}, \tag{3.1.22}$$

$$\phi_{ijk}^{n-2} = \phi_{ijk}^{n} - 2\Delta t\dot{\phi}_{ijk}^{n} + 2(\Delta t)^2\ddot{\phi}_{ijk}^{n}, \tag{3.1.23}$$

where the dot represents a time derivative and the taylor expansion has been given up to $(\Delta t)^2$ terms. Rearranging, these give

$$\partial_t\phi_{ijk}^{n} = \frac{-3\phi_{ijk}^{n} + 4\phi_{ijk}^{n-1} - \phi_{ijk}^{n-2}}{6\Delta t}. \tag{3.1.24}$$

Substituting this into Eq. (3.1.16) gives an explicit equation for ϕ_{ijk}^{n},

$$\phi_{ijk}^{n} = \frac{4}{3}\phi_{ijk}^{n-1} - \frac{1}{3}\phi_{ijk}^{n-2} - 2F_{ijk}\Delta t, \tag{3.1.25}$$

where the index n has been omitted from F_{ijk} as is can be replaced with any combination of F_{ijk}^{n}, F_{ijk}^{n} and F_{ijk}^{n} such as $F_{ijk}^{n} = \frac{4}{3}F_{ijk}^{n-1} - \frac{1}{3}F_{ijk}^{n-2}$. Even thought this method is explicit it requires two sets of initial data, ϕ_{ijk}^{n-1} and ϕ_{ijk}^{n-2}.

MAYBE CUT THIS BIT SHORT AT EQ 3.1.24
MAYBE I EVEN JUST SKIP THIS FROM "A STABLE AND EXPLICIT METHOD ...." AND GO STRAIGHT TO RK4?

The Runge Kutta Method

The Runge-Kutta method is an explicit ODE integration scheme that can be made accurate to arbitrary order in Δt. For an ODE of the form,

$$\frac{\mathrm{d}\phi}{\mathrm{d}t} = F(\phi, t), \tag{3.1.26}$$

the widely used fourth order accurate Runge-Kutta (RK4) method first calculates four intermediate gradients $\{k_1, k_2, k_3, k_4\}$,

$$k_1 = F(\phi, t), \tag{3.1.27}$$

$$k_2 = F(\phi + \frac{1}{2}k_1\Delta t, t + \frac{1}{2}\Delta t), \tag{3.1.28}$$

$$k_3 = F(\phi + \frac{1}{2}k_2\Delta t, t + \frac{1}{2}\Delta t), \tag{3.1.29}$$

$$k_4 = F(\phi + k_3\Delta t, t + \Delta t). \tag{3.1.30}$$

These are then summed in a way that calculates $\phi(t+\Delta t)$ from $\phi(t)$ removing errors upto and including $(\Delta t)^4$ terms,

$$\phi(t+\Delta t) = \phi(t) + \frac{1}{6}\left(k_1 + 2k_2 + 2k_3 + k_4\right)\Delta t + \mathcal{O}(\Delta t^5). \tag{3.1.31}$$

A similar procedure can be done for any desired accuracy with higher order methods becoming quite involved. The simplicity of this RK4 scheme along with it's robustness has no doubt led to it being oe of the most popular methods for integrating ODEs. Lower order Runge-Kutta methods also exist, for example the first order RK1 method which is equivalent to the Eular method in Eq. (3.1.18). Another common Runge-Kutta method is the second order accurate RK2 method also called the midpoint method.

3.2 GRChombo

3.2.1 Overview of GRChombo

GRChombo [4] [5] is an open-source fully non-linear Numerical Relativity (NR) code built on top of Chombo, a PDE solver with adaptive mesh refinement (AMR). GRChombo is written in C++ making extensive use of templating, classes and object oriented programming. GRChombo also supports vectorisation and parallelisation with OpenMP and MPI for efficient scaling to large problems suitable for use on supercomputer clusters. Current public examples of GRChombo include a black hole binary with seperate spins, a single kerr black hole and a compact real scalar configuration.

The AMR in Chombo relies on the Berger-Oliger style AMR [6] with block-structured Berger-Rigoutsos grid generation [7]. The labelling of which regions to regrid, called tagging, is specifiable by the user. A common tagging criterion (used in this work) is to define a gradient sensitive quantity $\aleph$ in terms of a grid variable ψ,

$$\aleph = \Delta x \sqrt{\frac{\left|\sum_{ij}(\partial_i\partial_j\psi)(\partial_i\partial_j\psi)\right|}{\left|\sum_k(\partial_k\psi)(\partial_k\psi)\right| + \epsilon}}, \tag{3.2.1}$$

for grid spacing Δx and small positive constant ϵ to avoid division by zero. Some threshold ψ_0 is prespecified and any gridpoint where $\aleph > \psi_0$ is flagged (or tagged) for regridding. If a box[1] has a greater fraction of its cells tagged than the *fill_ratio* parameter then the box will be covered by the next AMR level; in this work *fill_ratio* $= 0.7$. The reason for premultiplying by Δx is so that as the grid spacing gets smaller on deeper levels the tagging criterion is not flagged unless gradients become more extreme.

In order to evolve a spatial hypersurface with the Einstein equation, GRChombo uses either the BSSN formalism [8] [9] described in section 2.1.7 or the CCZ4 formalism [10] [11]. A summary of the CCZ4 formulation is given in section 2.1.9 along with the equations of motion used in this work. The conformal factor used is $\chi = \gamma^{-\frac{1}{3}}$ where γ is the metric determinant from Eq. (2.1.9) on the three dimensional hypersurface Σ_t. The time evolution scheme is the method of lines 3.1.3 using 4'th order spatial derivatives 3.1.1 and runge kutta 4'th order time integration 3.1.4. While 6'th order spatial derivatives have been implemented, they are not used in this work due to their increasing the number of ghost cells needed. Kreiss-Oliger dissipation [12] is used to supress high frequency noise occuring from interpolation, regridding of AMR and high field gradients inside black hole regions. As described in section 2.1.10, the moving puncture gauge with conformal factor χ is used to evolve moving black hole singularities.

The code can use Sommerfeld, periodic, reflective and extrapolating boundary conditions. Simulations in this work all use some combination of Sommerfeld boundary conditions for boundaries far away and reflective boundary conditions in a plane of symmetry. Headon collision of identical objects can use *octant* symmetry, three planes of symmetry on the planes $x = 0$, $y = 0$ and $z = 0$. This means one only needs to simulate the region $x > 0$, $y > 0$ and $z > 0$ with reflective boundary conditions on

[1]Each AMR level is subdivided by cuboids, often of side lengths 8, 16, or 32 gridpoints, called boxes. These boxes can be evolved forewards one time step without sharing memory making them compatible with MPI.

the symmetry planes; the overall problem size (or number of gridpoints) reduces by a factor of eight. Similarly, headon collisions of non-similar objects can use *quadrant* symmetry, reducing the problem size by four. A general inspiral of two dissimilar compact obejcts has one plane of symmetry, the plane of inspiral; *bitant* symmetry can be used to half the problem size. For all the pre-mentioned symmetries, a suitable rest frame must be used aligning with the symmetries of the initial data. Boundary conditions are discussed in more detail in section 3.1.2.

A selection of diagnostic tools have been included into GRChombo. These include, but are not limited to, black hole horizon finders, gravitational wave extraction and the calculation for ADM mass, ADM momentum, Noether charges and energy-momentum densities and fluxes. The diagnostic for the angular momentum density and flux are the result of section **??**.

While GRChombo can be used to simulate traditional spacetimes, such as binary black hole inspirals [13], it excells at simulating novel and theoretical physics due to its adaptable code and AMR. The advantage of AMR is that regions needing higher resolution are assigned (and de-assigned) dynamically during run time; this requires no a-priori knowledge or pre-determined grid structure unlike other NR codes. [DO I LIST OTHER CODES HERE?] AMR is especially useful for matter simulations that can develop features requiring higher resolution in places a human may not expect making pre-specified mesh refinement hard to use. GRChombo has also sucessfully simulated ring-like configurations [REF] [THOMAS,JOSU] and inhomogeneous spacetimes [REF] [PAU, KATY ...] which would be tricky with a conventional pre-specified grid structure. GRChombo has been designed to be straight forward to modify making it an excellent choice for exotic matter, modified gravity theories and higher dimensional spacetimes.

DO I NEED THE REFERENCES LEFT IN CAP LOCKS?

Simulation Units

GRChombo defaults to geometric units with $c = G = 1$, but the value of Newton's gravitational constant G can be changed if desired. Plancks constant does not arise in vaccum General Relativity, but does appear when the Klein Gordon equation for a scalar fields as in section 2.2.1. Following the conventions of section 1.1.3, Planks reduced constant $\hbar$ is also set to unity and Planck units are used.

As given in section 2.2.1, the Lagrangean for a self-interacting boson star is proportional to,

$$g^{\mu\nu}\partial_\mu\varphi\partial_\nu\bar{\varphi} + m^2|\varphi|^2 + \frac{1}{2}\Lambda_4|\varphi|^4, \tag{3.2.2}$$

in natural units; of course setting $\Lambda_4 = 0$ returns a mini boson star. For a constant κ, Setting $m \to \kappa m$ with $\varphi \to \kappa^{-1}\varphi$, $x^\mu \to \kappa^{-1}x^\mu$[2] and $\Lambda_4 \to \kappa^4\Lambda_4$ leaves the Lagrangean unchanged. Similarly for the solitonic boson star with lagrangean,

$$g^{\mu\nu}\partial_\mu\varphi\partial_\nu\bar{\varphi} + m^2|\varphi|^2\left(1 - \frac{|\varphi|^2}{2\sigma^2}\right), \tag{3.2.3}$$

the total Lagrangean is unchanged under $m \to \kappa m$, $x^\mu \to \kappa^{-1}x^\mu$ and $\sigma \to \kappa^{-1}\sigma$. This means that changing the boson particle mass m gives a solution of the same equation but with rescaled coordinates, field values and scalar field parameters. To account for this one parameter freedom, from now on the coordinates $\hat{x}^\mu = x^\mu \cdot m$, scalar field $\hat{\varphi} = \varphi \cdot m$ and solitonic parameter $\hat{\sigma} = \sigma \cdot m$ will be used; the circumflex over these units will now be dropped for convenience. This is equivalent to setting $m = 1$; if boson stars with particle mass other than $m = 1$ are desired they can be obtained by rescaling the appropriate solution of the $m = 1$ Klein-Gordon equation.

[2]It has been assumed that the coordinates x^μ have the dimension of length such as cartesian coordinates; instead we can demand that $g^{\mu\nu}\partial_\mu\partial_\mu \to \kappa^2 g^{\mu\nu}\partial_\mu\partial_\mu$ which is generally true even for dimensionless coordinates such as angles.

3.2.2 Boson Star Initial Data

We now seek to solve the EKG ODE's (2.2.21), (2.2.22) and (2.2.23) numerically to obtain initial data for a single static boson star. The system can be reduced to a set of five first order ODE's with five boundary conditions. For a physical star we would like to impose $\Phi(0) = \Phi_c$, $\Phi'(0) = 0$, $\Phi(r \to \infty) \to 0$, $\Omega'(0) = 0$, $\Omega(r \to \infty) \to 1$, $\Psi'(0) = 0$ and $\Psi(r \to \infty) \to 1$ to be regular at the origin and match the Schwarzschild vacuum solution at large radius; however this is seven boundary conditions and we can only impose five. The condition $\Omega(0)' = 0$ cannot be specified as Eq. (2.2.21) is first order in derivatives of Ω but given that r and Ψ' both vanish at the origin then Ω' must also vanish at the origin automatically. One more boundary condition can be removed by asking for the boson star solution to match the isotropic Schwarzschild solution in Eq. (1.4.52) at large radius and therefore,

$$\Omega_\infty = \left(\frac{1 - \frac{M_{\text{BS}}}{2r}}{1 + \frac{M_{\text{BS}}}{2r}} \right) \quad \& \quad \Psi_\infty = \left(1 + \frac{M_{\text{BS}}}{2r} \right)^2 \tag{3.2.4}$$

where M_{BS} can be interpreted as the mass of the boson star; this mass will not enter the boundary condition so can be safely ignored. Combining the two equations above gives

$$\sqrt{\Psi_\infty}\,(1 + \Omega_\infty) = 2 \tag{3.2.5}$$

for a vacuum spacetime. Imposing the single condition $\sqrt{\Psi(\infty)}\,(1 + \Omega(\infty)) = 2$, rather than both $\Omega(\infty) = 1$ and $= \Psi(\infty) = 1$, then gives asymptotic flatness in just one boundary condition. One final point of importance is the frequency ω turns the Klein-Gordon ODE into an eigenvalue problem, admitting only discrete values of ω.

The problem has now been reduced to five ODE's with the following five boundary conditions,

$$\{\Phi(0), \Phi'(0), \Psi'(0), \Omega(0), \sqrt{\Psi(\infty)}\,(1 + \Omega(\infty))\,; \omega\} = \{\Phi_c, 0, 0, \Omega_0, 2; \omega_0\}, \tag{3.2.6}$$

subjected to the condition of an eigenvalue $\omega = \omega_0$. The first attempt to find the radial profile $\{\Phi(r), \Omega(r), \Psi(r)\}$ of the boson star was to use a relaxation method as it trivially incorporates the above two-point boundary conditions. In practice this method did not work well with the eigenvalue problem in ω. Unlike with a shooting method, there was no obvious way of telling whether the guess ω was larger or smaller than the correct value. Even if this problem were overcome, a numerical solution with relaxation is computationally slow, even with Successive Over-Relaxation [14]; perhaps a multigrid method could work here but a simpler method was used.

Shooting Method

To find the initial data for a single Boson star, a c++ script was written using the RK4 method in section 3.1.4 to integrate the EKG system taking five initial conditions, and eigenvalue guess ω_0,

$$\{\Phi(0), \Phi'(0), \Psi(0), \Psi'(0), \Omega(0); \omega\} = \{\Phi_c, 0, \Psi_c, 0, \Omega_0; \omega_0\}. \tag{3.2.7}$$

Unfortunately Ω_0 and Ψ_c are unknown apriori, but guessing any values reasonably close to untity, such as $\omega_0 = 0.5$ and $\Psi_c = 2$, still give a boson star. This will generally result in the following asymptotic metric,

$$g_{\mu\nu}(r \to \infty) \to \text{diag}(-A^2, B^2, B^2, B^2), \tag{3.2.8}$$

for constant A and B.

Before we discuss how to find the correct value of ω, there is a subtle numerical problem to adress. Using spherical polar coordinates in flat space, the Klein-Gordon equation (2.2.8) with $V = m^2|\varphi|^2$ and ansatz

$\varphi = \Phi_{flat}(r)e^{\mathrm{i}\omega t}$ reduces to,

$$\frac{1}{\sqrt{-g}}\partial_\mu\left(\sqrt{-g}g^{\mu\nu}\partial_\nu\right)\varphi = \frac{\partial V}{\partial|\varphi|^2}\varphi, \tag{3.2.9}$$

$$\partial_t\left(g^{tt}\partial_t\right)\Phi_{flat}(r)e^{\mathrm{i}\omega t} + \frac{1}{r^2}\partial_r\left(r^2 g^{rr}\partial_r\right)\Phi_{flat}(r)e^{\mathrm{i}\omega t} = m^2\Phi_{flat}(r)e^{\mathrm{i}\omega t}, \tag{3.2.10}$$

$$\omega^2\Phi_{flat}(r) + \frac{1}{r^2}\partial_r\left(r^2\partial_r\right)\Phi_{flat}(r) = m^2\Phi_{flat}(r), \tag{3.2.11}$$

$$\tag{3.2.12}$$

where $\sqrt{-g} = r^2\sin(\theta)$, $g^{tt} = -1$ and $g^{rr} = 1$. This has general solution,

$$\Phi_{flat}(r) = \frac{1}{r}\left(C_1 e^{-r\sqrt{m^2-\omega^2}} + C_2 e^{r\sqrt{m^2-\omega^2}}\right), \tag{3.2.13}$$

for the amplitude $\Phi_{flat}(r)$ specified by two constants C_1 and C_2. Due to finite resolution during numerical integration, at large radius C_2 will never be exactly zero and will eventually grow (along increasing radius) and spoil the numerical integration; even though this behavour was derived in flat space it is still present in curved space with spherical symmetry - especially at such large radius that space is approximately flat. In practice, the scalar field Φ decays to some small[3] value and is effectively zero within numerical noise. At this point the coefficient C_2 is excited by noise and starts to grow exponentially. At a radius r_* when the growing mode is deemed to be dominating, usually detected by an axis crossing ($\Phi(r_*) = 0$) or a turning point ($\Phi'(r_*) = 0$), the conditions $\Phi(r > r_*) = \Phi'(r > r_*) = 0$ are enforced during integration. This creates a vacuum for $r > r_*$ and the spacetime is equivalent to the Schwarzschild spacetime. After this radius, an exponentially growing stepsize is used to reach radii of order 10^8 to 10^{10} and the values $A = \Omega_\infty = \sqrt{-g_{00}}$ and $B = \Psi_\infty = \sqrt{g_{ii}}$ can be read off.

Interval bisection was used to find the correct value of ω, ω_0, to machine precision; for the ground state we can tell that $\omega > \omega_0$ if $\Phi(r)$ develops a turning point before an axis crossing and $\omega < \omega_0$ if $\Phi(r)$ develops an axis crossing before a turning point. To find the n'th excited state, which has n axis crossing for $\Phi(r)$ and $\Phi(r \to \infty) \to 0$, a similar scheme is followed to find the eigenvalue ω_n. If $\Phi(r)$ has $n+1$ axis crossings then $\omega > \omega_n$ and if $\Phi(r)$ has n axis crossings followed by a turning point then $\omega < \omega_n$. This method of doing a numerical integration and iteratively restarting to get closer to the target solution is known as a shooting method.

Putting everything together, a boson star solution with eigen value ω_0 (or ω_n for excited stars) and asymptotic metric Eq. (3.2.8) can be obtained. To find a star with asymptotic metric $\eta_{\mu\nu}$ of flat space, the initial conditions are iteratively improved like $\Omega_c \to \Omega_c/\Omega_\infty$ and $\Psi_c \to \Psi_c/\Psi_\infty$; the interval bisection for ω is then restarted. This is iterated three to five times which leaves $A = \Omega_\infty = 1$ and $B = \Psi_\infty = 1$ to high precision and the isotropic boson star profile has been created. This whole process requires a few seconds runtime for a high resolution 200,000 grid-point simulation on a regular laptop.

Figure 3.2a shows the numerically obtained radial profile of a mini boson star ($\Lambda = 0$) and an excited mini boson star. Note two mass definitions are plotted; the ADM mass (calculated as a function of finite r) and the aspect mass [REF] [I THINK I NEED TO WRITE OUT THIS SOMEWHERE ITS ONLY A FEW LINES]. Polytropic fluid stars were also simulated as a preliminary test of the code; they are much easier to create not needing to solve an eigenvalue problem and don't have an asymptotically growing mode. Figure (3.3a) shows how the ADM mass of boson stars varies with central amplitude $\Phi(0)$ and r_{99}, the radius which $\Phi(r_{99}) = \Phi(0)/100$. It should be noted that the mini boson star (with $\Lambda = 0$) case agrees with the known maximum mass, the Kaup limit [15] $M_{max} \approx 0.633 M_{PL}^2 m^{-1}$ with the highest measured mass being $M_{max} = 0.63299(3) M_{PL}^2 m^{-1}$ corresponding to a central amplitude of $\sqrt{4\pi G}\Phi(0)_{max} = 0.271(0)$.

[3]Small meaning roughly twenty orders of magnitude smaller than the central density $\Phi(0)$ for a mini boson star. This gets a little less small for dense solitonic stars but it still a good approximation to zero.

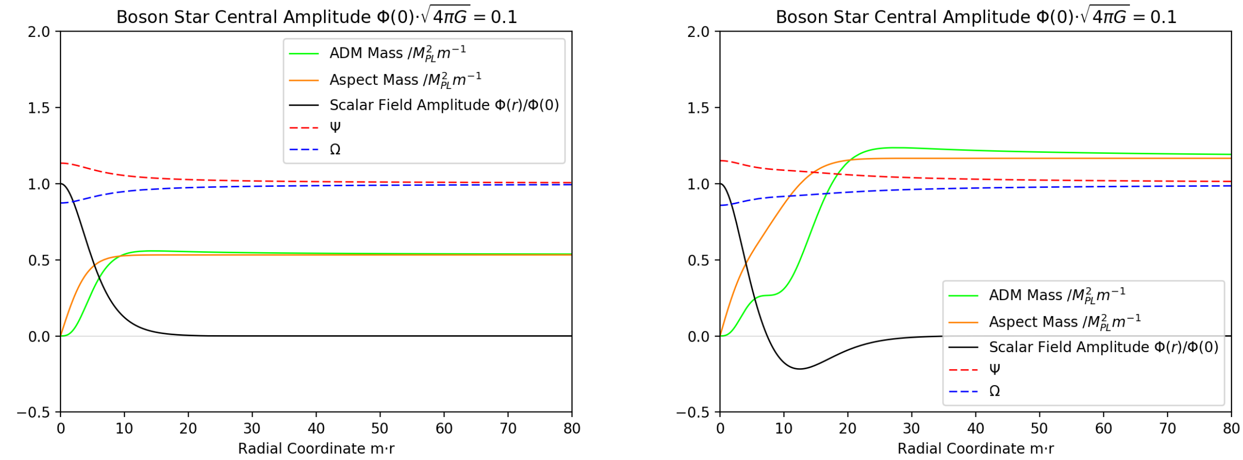

Figure 3.1: Boson Star radial profile, Left: Ground state, Right: 1st Excited state

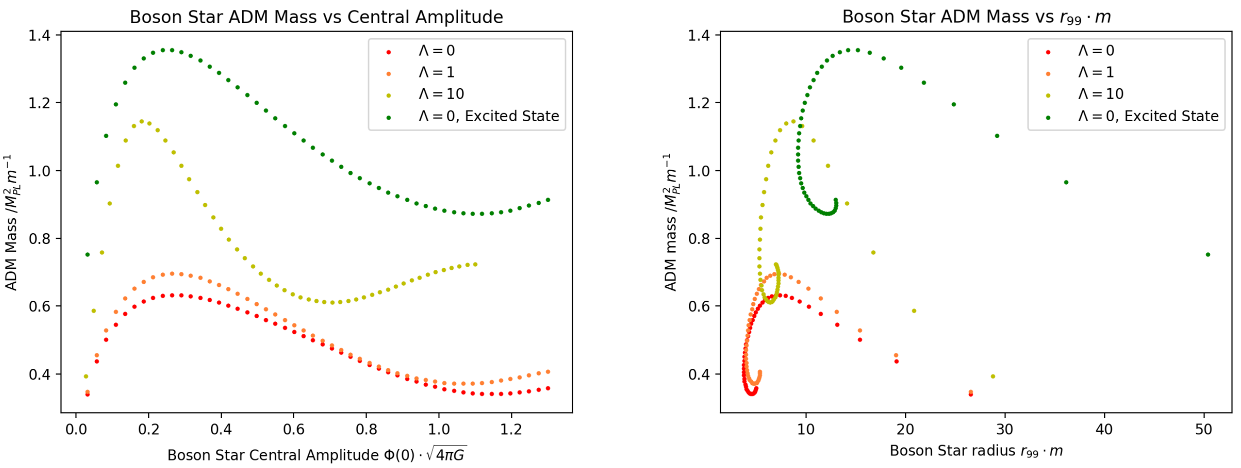

Figure 3.2: Boson star trends, Left: ADM mass vs $\Phi(0)$, Right: ADM mass vs r_{99}

While many different boson stars have been made to test the initial data code, all the following evolutions use the same boson star with parameters $\Lambda = 0$, $\sqrt{4\pi G}\Phi(0) = 0.1 \rightarrow \Phi(0) \approx 0.0282$ and ADM mass $M = 0.532(7)$. This is as the stars are heavy enough to form black holes under collisions and large deformations, but stable enough to not collapse to a black hole for moderate perturbations.

3.2.3 Single Star Evolution

As a check that the initial from section 3.2.2 is correct, a mini boson star with central density $\Phi(0) = 0.02820$ is evolved in time in three spatial dimensions. The simulation has a physical domain size $L = 1024$ with $N = 320$ gridpoints on AMR level zero with grid spacing $\Delta x = 3.2 \cdot m$. The AMR is allowed upto six extra levels; the finest level (level six) has a grid spacing of $\Delta x = 0.05 \cdot m$. The star is supposed to remain in the centre of the grid and not change as it is a rest frame soliton; this is observed through evolution with GRChombo. Figure (3.4a) shows the global maximum value of $|\varphi|$ and Fig. (3.4b) shows the total integral of the Noether charge N over the grid. As can be seen, $|\varphi|_{max}$ is constant to $\sim 0.7\%$ and N is conserved to the $\sim 0.07\%$ level untill time $t = 350 \cdot m$.

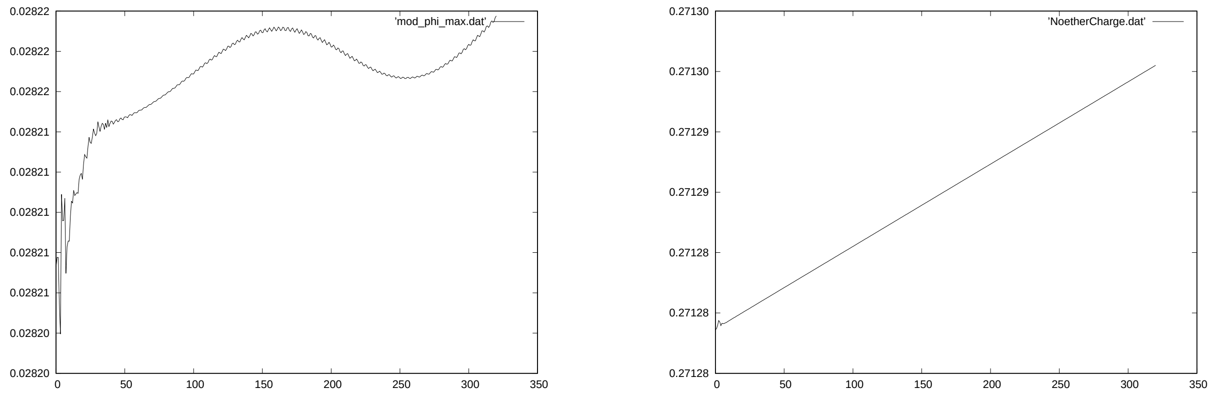

Figure 3.3: Left: Maximum of $|\varphi|$ during evolution, Right: Total integrated Noether charge N.

3.2.4 Superposition of Initial Data

In order to simulate a spacetime consisting of two stars (or a star and a black hole) we must choose a way of superposing the initial data of two objects, centred at $x^{(1)}$ and $x^{(2)}$. For some field $\psi^{(j)}$ associated with the compact object at $x^{(j)}$,

$$\psi^{(j)} = \psi(x - x^{(j)}), \tag{3.2.14}$$

where ψ refers to the object centred about the origin. Taking two compact objects with fields φ, Π, γ_{ij}, $\mathcal{K}_{ij}$, α and β^i, a naive superposition scheme was chosen;

$$\varphi = \varphi^{(1)} + \varphi^{(2)}, \tag{3.2.15}$$

$$\Pi = \Pi^{(1)} + \Pi^{(2)}, \tag{3.2.16}$$

$$\mathcal{K}^i_j = \mathcal{K}^{(1)}{}^i_j + \mathcal{K}^{(2)}{}^i_j, \tag{3.2.17}$$

$$\gamma_{\mu\nu} = \gamma^{(1)}_{\mu\nu} + \gamma^{(2)}_{\mu\nu}, \tag{3.2.18}$$

$$\beta_i = \beta^{(1)}_i + \beta^{(2)}_i, \tag{3.2.19}$$

$$\alpha = \sqrt{\alpha^2_{(1)} + \alpha^2_{(2)} - 1}, \tag{3.2.20}$$

$$\chi = \det\left\{\gamma^{(1)}_{\mu\nu} + \gamma^{(2)}_{\mu\nu}\right\}^{-1/3}, \tag{3.2.21}$$

where the super-scripts $^{(1)}$ and $^{(2)}$ refer to the separate compact objects. The extrinsic curvature is chosen to be superposed with mixed indeces so that it implies the trace $\mathcal{K}$ is also superposed. If one of the compact objects is a black hole the lapse $\alpha \to 0$ on the horizon; this is circumvented by setting,

$$\alpha = \sqrt{\chi}, \tag{3.2.22}$$

ensuring that the lapse is real and non-negative for a all of Σ_t.

Superposing two solutions in general relativity usually no longer satisfies the Einstein equation, the Hamiltonian constraint Eq. (2.1.50) and momentum contraints Eq. (2.1.52) are violated. For asymptotically flat compact objects, the constraint violation reduces to zero as the object separation tends to inifinity. In the case of finite separations, the CCZ4 scheme in section 2.1.9 aims to drive the constraint violation towards zero and hence a true solution of Einstein's equation. The collisions of compact objects in section(S) 3.2.5 use this naive superposition scheme. Section [REF] [MALAISE PAPER SECTION] explores a technique to improve the naive superposition of compact objects.

3.2.5 Collisions of Boson Stars

Both a headon collision and a grazing collision of two bosons stars are simulated using the superposition scheme given in section 3.2.4. The two stars are identical, each has a central density of $\Phi(0) = 0.02820$ and an ADM mass $M = 0.532(7)$. The stars are placed at positions $x^i = \pm\{40, 0, 0\}$ in the headon case and $x^i = \pm\{40, 8, 0\}$ in the grazing case and are boosted together with respective velocities $v^i = \mp\{0.1, 0, 0\}$ in both cases. A speed of $v = 0.1$ corresponds to a rapidity of $\psi = 0.1003353$ (4 s.f.). The simulations have a physical domain size of $L = 512$ with $N = 256$ gridpoints on AMR level zero, this gives a coarse grid resolution of $\Delta x = 2$. There are up to five extra AMR levels giving a finest grid resolution of $\Delta x = 1/16$.

Headon Collision

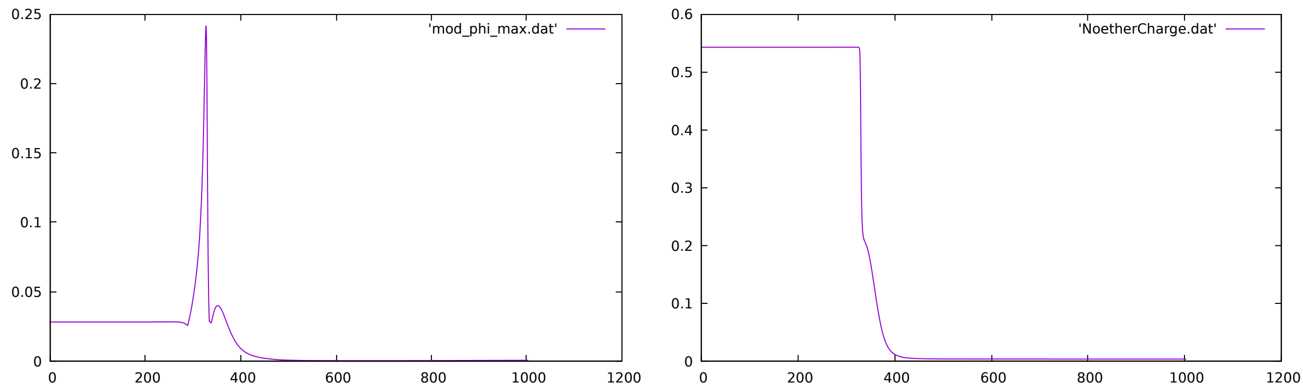

Figure 3.4: Left: Maximum of $|\varphi|$ during evolution, Right: Total integrated Noether charge N.

Figure (3.5a) shows $|\varphi|_{max}$, the global maximum value of $|\varphi|$, and the total Noether charge N as a function of time for the headon collision. At time $t \approx 289 \cdot m$, $|\varphi|_{max}$ rapidly increases and collapses to a black hole. At time $t \approx 327 \cdot m$, there is a temporal maximum in $|\varphi|_{max}$ as the resolution limit of the simulation is reached and the scalar field is dissipated by the Kreiss-Oliger dissipation mentioned in section 3.2.1. This dissipation can also be seen in the Noether charge plot at a time of $t \approx 326 \cdot m$ where the total charge that should remain constant but begins to fall. The lack of sufficient resolution inside the black hole is not problematic for the external simulation; the errors accumulated are trapped inside the event horizon. Fig. (3.5a) shows that the total Noether charge rapidly decays to zero as it falls into the black hole and is dissipated due to finite resolution effects.

The gravitational wave extraction at radius $r = 140 \cdot m$ is given in figure 3.6a. A spin-weighted spherical harmonic decomposition of the Newman-Penrose scalar Ψ_4 [REF] [DO I NEED TO REF THIS?] has been done and the $m, l = 2, 0$ and $m, l = 2, 2$ modes are plotted.

The dynamics of the two boson stars are shown in Fig. (3.9a) which plots the scalar field modulus $|\varphi|$ on the x, y plane. The stars collide at at time $275 \cdot m < t < 300 \cdot m$; the collision time of two point masses (with the same initial conditions) has been simulated in Newtonian gravity giving a collision time of $t = 287.6 \cdot m$. Soon after collision, an overdensity of scalar field is developed which subsequently collapses to a black hole. The black hole then accretes the surrouding scalar field; the scalar field can be seen to be composed of higher order spherical harmonic modes at later times. DO I MENTIONT THIS IS BECAUSE HIGHER ORDER MODES HAVE SLWOER DECAY RATE? I THINK I HAVE SHOWN THIS

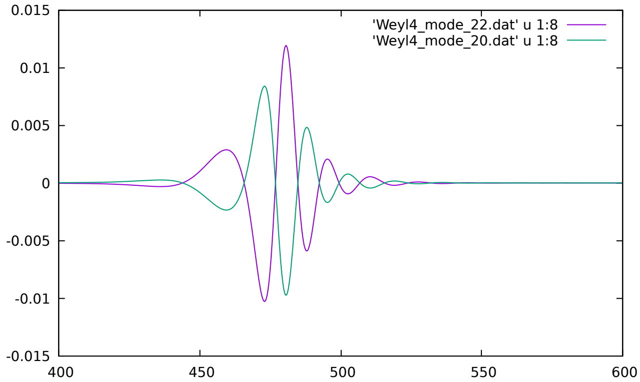

Figure 3.5: Gravitational wave signal of the headon boson star collision. The $m, l = 2, 2$ and $m, l = 2, 0$ spin weighted spherical harmonic modes of the Ψ_4 Newman-Penrose scalar are given.

Grazing Collision

Figure (3.7a) plots $|\varphi|_{max}$ and the total Noether charge (N) versus time for the grazing collision. At time $t \approx 309 \cdot m$, $|\varphi|_{max}$ rapidly increases and a black hole is soon formed. The black hole is assumed to be spinning due to the collapsing matter containing angular momentum. At time $t \approx 356 \cdot m$ there is a temporal maximum in $|\varphi|_{max}$; similarly to the headon collision, this is caused by diverging resolution requirements towards the black hole centre and usually does not affect the exterior spacetime. Consequently, the Noether charge plot shows a fall in charge at a time of $t \approx 355 \cdot m$; for a well resolved simulation N should remain constant.

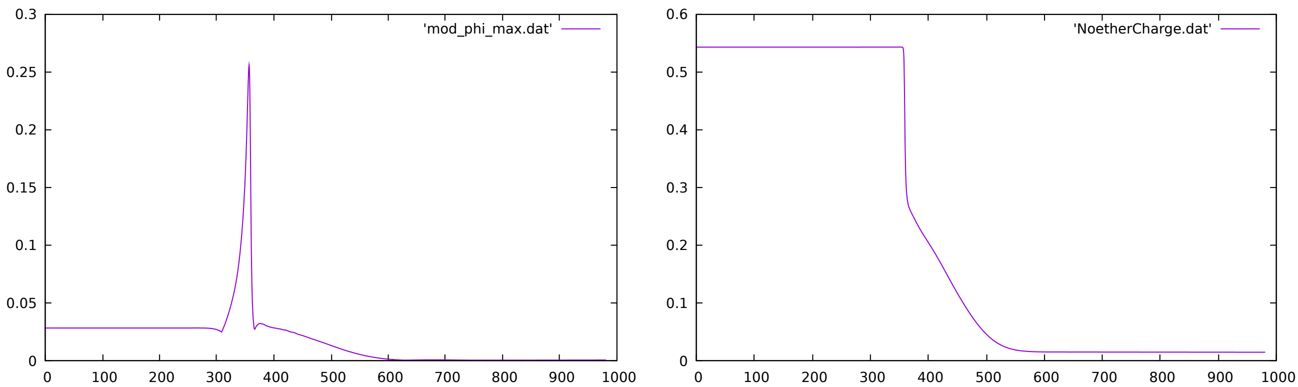

Figure 3.6: Left: Maximum of $|\varphi|$ during evolution, Right: Total integrated Noether charge N.

A simulation of the grazing collision with point masses has been done using Newtons laws. The time taken for closest approach (with separation $s = 2.33 \cdot m$) is $t = 315.8 \cdot m$; at this separation the finite sized stars would collide. Snapshots of the grazing boson star collision using numerical relativity are shown in Fig. (3.10a) plotting the scalar field modulus $|\varphi|$ on the x, y plane. The stars collide at time $300 \cdot m < t < 325 \cdot m$ which is in good agreement with the Newtonian approximation. Soon after collision, an overdensity of scalar field develops and collapses to a black hole; this black hole is thought to be spinning due to the angular momentum of the collapsing matter. The black hole subsequently accretes most of the surrouding scalar field leaving a quasi-long-lived rotating toroidal scalar field configuration surrounding the black hole. This late time toroidal scalar field configuration will be referred to as a *toroidal wig* due to it being "fake" hair. The late time toroidal wig seems to settle to a rotationally symmetric configuration, with no quadrupole moment, and does not emit a gravitational wave signal; this can be seen in the figure 3.8a which plots the $m, l = 2, 2$ and $m, l = 2, 0$ modes of Ψ_4.

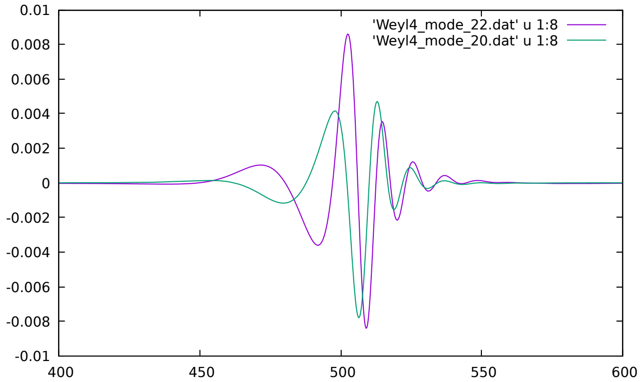

Figure 3.7: Gravitational wave signal of the grazing boson star collision. The $m, l = 2, 2$ and $m, l = 2, 0$ spin weighted spherical harmonic modes of the Ψ_4 Newman-Penrose scalar are given.

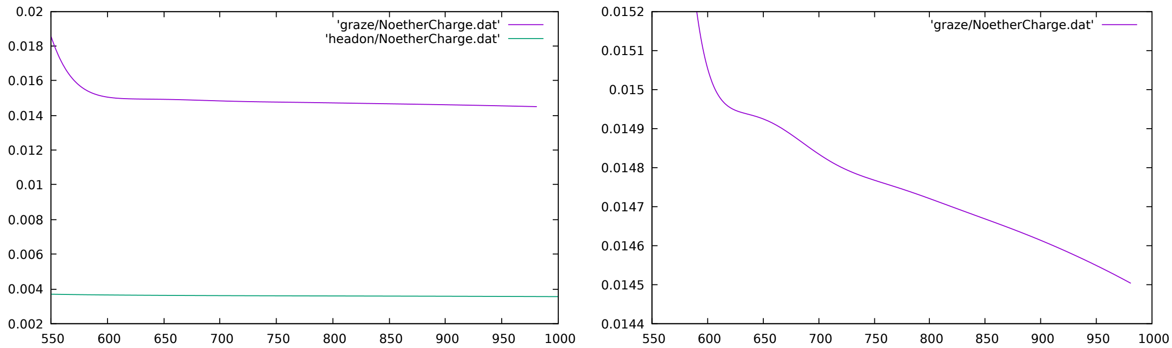

Figure 3.8: Left: Comparison of late time Noether charge N between headon collision and grazing collision of two boson stars. Right: Late time plot of the Noether charge of the grazing collision only.

Figure (3.9a) shows the late time Noether charge of the grazing and headon collisions. In contrast to the headon collision, the decay of N in the grazing case is slower and reaches a value approximately 7 times greater. Using linear extrapolation, the Noether charge of the grazing collision decays to zero at time $t \approx 12500$ and hence the toroidal wig has an approximate lifespan of 12000 time units.

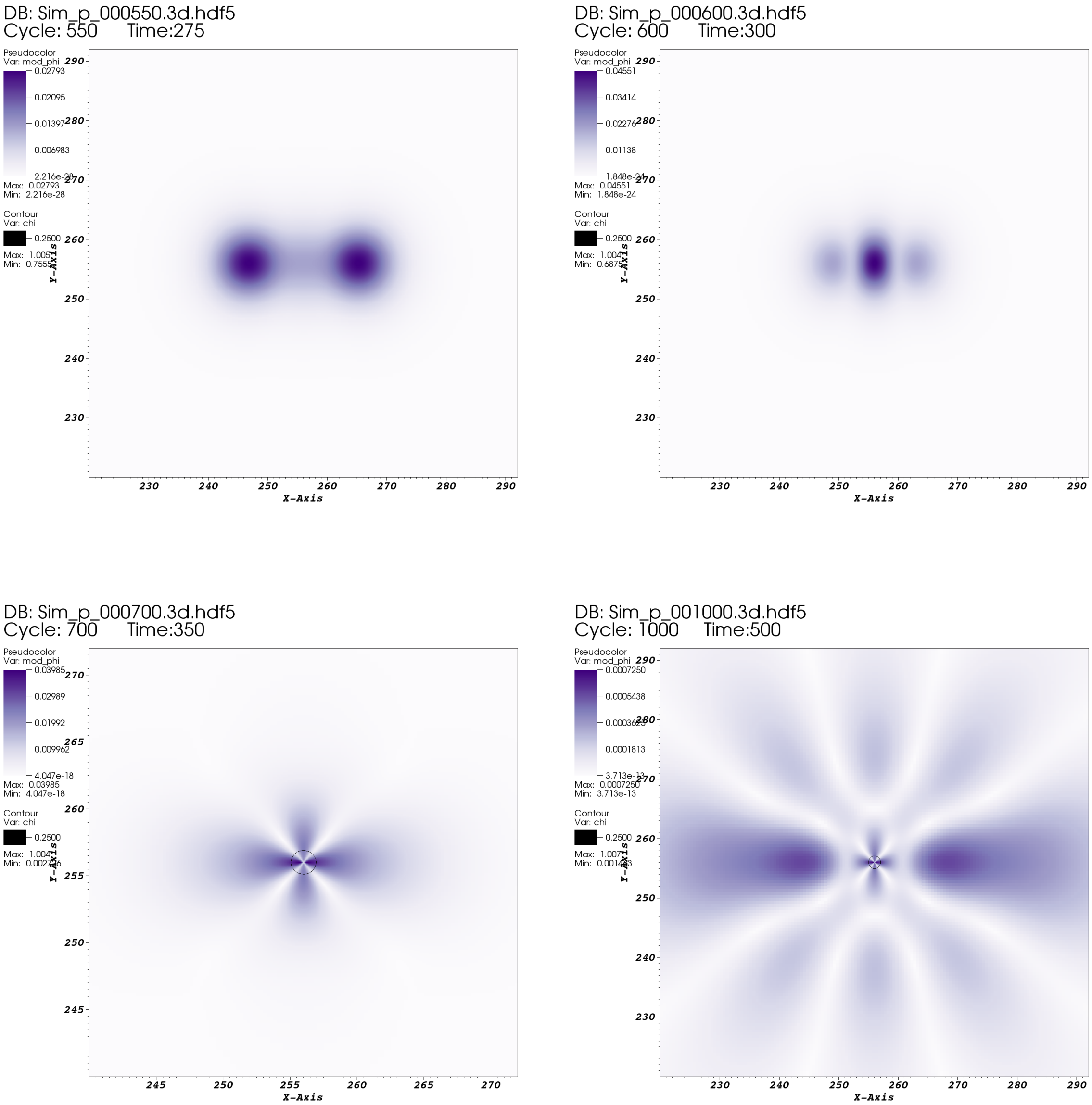

Figure 3.9: Field plots of $|\varphi|$ during evolution at four different times. Time $t = 275 \cdot m$ and $t = 300 \cdot m$ show snapshots momentarily before and after star collision. Time $t = 350 \cdot m$ shows the scalar field accreting into the recently formed black hole. Time $t = 500 \cdot m$ shows the scalar field surrounding the black hole a little later; noteably the amplitude is lower. Both the plots of $t = 350 \cdot m$ and $t = 500 \cdot m$ have a contour plot of $\chi = 0.25$ acting as a very approximate marker for the event horizon. The Newtonian estimate of collision time is $t = 287.6 \cdot m$.

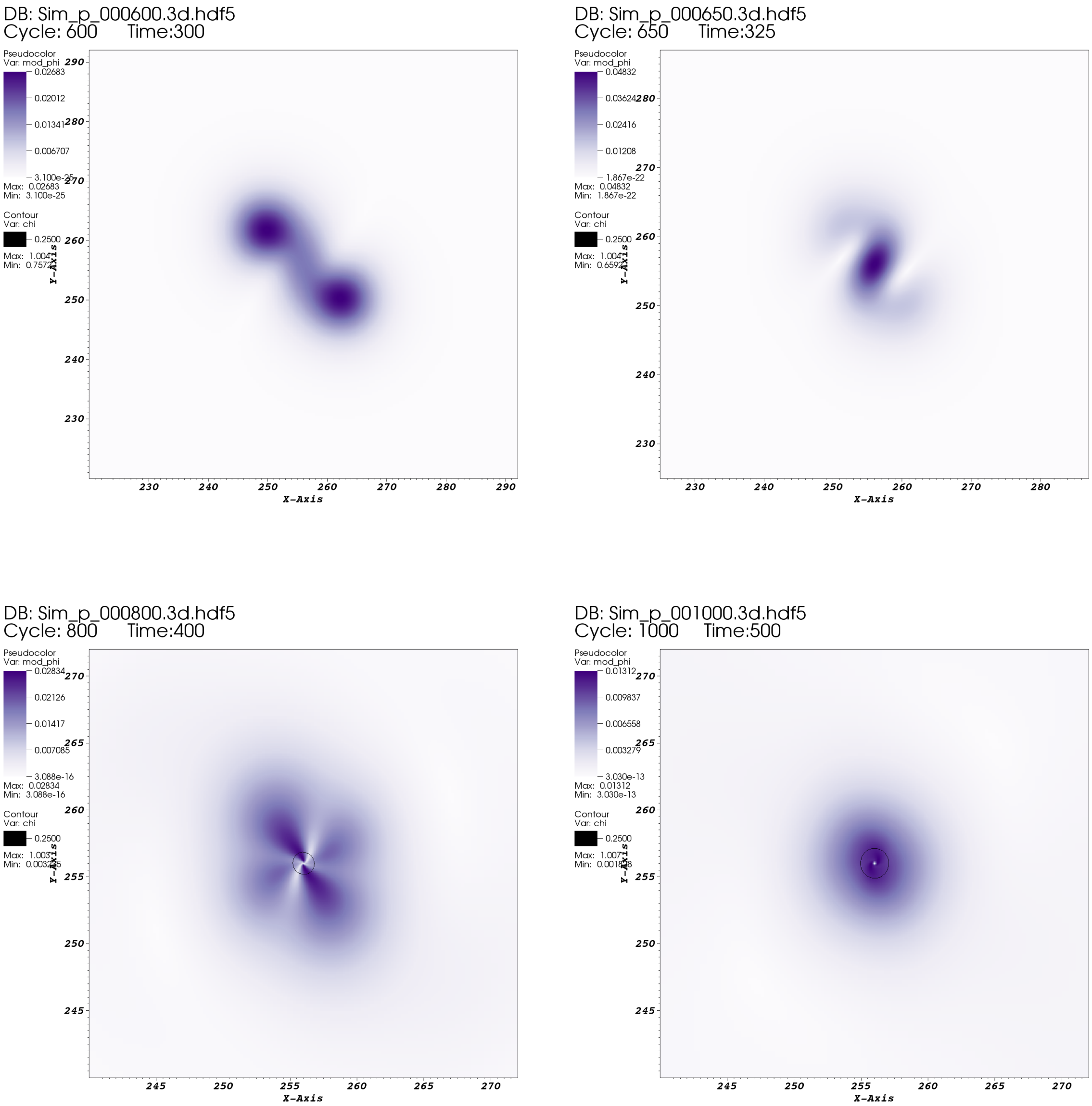

Figure 3.10: Field plots of $|\varphi|$ during evolution at four different times for the grazing boson star collision. Time $t = 300 \cdot m$ and $t = 325 \cdot m$ show snapshots momentarily before and after the collision. The Newtonian estimate of collision time is $t = 315.8 \cdot m$. Time $t = 400 \cdot m$ shows the scalar field accreting into the recently formed black hole. Time $t = 500 \cdot m$ shows the scalar field surrounding the black hole a little later; this is called a *toroidal wig*. Both the plots of $t = 400 \cdot m$ and $t = 500 \cdot m$ display a contour plot of $\chi = 0.25$ acting as a very approximate marker for the event horizon.

Chapter 4

MALAISE PAPER

Through numerical simulations of boson-star head-on collisions, we explore the quality of binary initial data obtained from the superposition of single-star spacetimes. Our results demonstrate that evolutions starting from a plain superposition of individual boosted boson-star spacetimes are vulnerable to significant unphysical artefacts. These difficulties can be overcome with a simple modification of the initial data suggested in [16] for collisions of oscillatons. While we specifically consider massive complex scalar field boson star models up to a 6th-order-polynomial potential, we argue that this vulnerability is universal and present in other kinds of exotic compact systems and hence needs to be addressed.

4.1 Introduction

The rise of gravitational-wave (GW) physics as an observational field, marked by the detection of GW150914 [17] and followed by about 50 further compact binary events [18, 19] over the past years, has opened up unprecedented opportunities to explore gravitational phenomena. From tests of general relativity [20, 21, 22, 23, 24, 25] to the exploration of BH populations [26, 27, 28, 29, 30] or charting the universe with independent new methods [31, 32], GW astronomy offers potential for revolutionary insight into long-standing open questions; for a review see [33]. Some answers, such as the association of a soft gamma-ray burst with the neutron star merger GW170817 [34, 35] have already raised our understanding to new levels. GW physics furthermore establishes new concrete links to other fields of research, most notably to particle and high-energy physics and the exploration of the dark sector of the universe [36, 33]. Two important ingredients of this remarkable connection are the characteristic interaction of fundamental fields with compact objects through superradiance [37] and their capacity to form compact objects through an elaborate balance between the intrinsically dispersive character of the fields and their self-gravitation. The latter feature has given rise to the hypothesis of a distinct class of compact objects as early as the 1950s [38]. In contrast to their well known fermionic counterparts – stars, white dwarfs or neutron stars – these compact objects are composed of bosonic particles or fields and, hence, commonly referred to as *Boson Stars* (BS). GW observations provide the first systematic approach to search for populations of these objects or to constrain their abundance. As with all other GW explorations, the success of this exploration is heavily reliant on the availability of accurate theoretical predictions for the anticipated GW signals. This type of calculation, using numerical relativity techniques [39], is the topic of this work.

The idea of bosonic stars dates back to Wheeler's 1955 study of gravitational-electromagnetic entities or *geons* [38]. By generalising from real to complex-valued fundamental fields, it is even possible to obtain genuinely stationary solutions to the Einstein-matter equations. First established for spin 0 or scalar fields [40, 41, 42], this idea has more recently been extended to spin 1 or vector (aka *Proca* [1]) fields [43] as well as wider classes of scalar BSs [44, 45]. In the wake of the dramatic progress of numerical relativity in the simulations of black holes (BHs) [46, 47, 48] (see [49] for a review), the modelling of BSs and binary systems involving BSs has rapidly gathered pace.

The first BS models computed in the 1960s consisted of a massive but non-interacting complex scalar field φ. This class of stationary BSs, commonly referred to as *mini boson stars*, consists of a one parameter family of ground-state solutions characterised by the central scalar-field amplitude that reveals a stability structure analogous to that of Tolman-Oppenheimer-Volkoff [50, 51] stars: a stable and an unstable branch of ground-state solutions are separated by the configuration with maximal mass [52, 53, 54]. For each ground-state model, there furthermore exists a countable hierarchy of excited states with $n > 0$ nodes in the scalar profile [55, 56, 57]. Numerical evolutions of these excited BSs demonstrate their unstable character, but also reveal significant variation in the instability time scales [58].

Whereas mini BS models are limited in terms of their maximum compactness, self-interacting scalar fields

[1]Even though the term "boson star" generally applies to compact objects formed of any bosonic fields, it is often used to specifically denote stars made up of a *scalar* field. Stars composed of vector fields, in contrast, are most commonly referred to as *Proca* stars. Unless specified otherwise, we shall accordingly assume the term boson star to imply scalar-field matter.

can result in significantly more compact stars, even denser than neutron stars [59, 60, 61, 62]. This raises the intriguing question whether compact BS binaries may reveal themselves through characteristic GW emission analogous to that from BHs or NSs [63]. Recent studies conclude that this may well be within the grasp of next-generation GW detectors and, in the case of favourable events, even with advanced LIGO [64, 65, 66].

One of the characteristic properties of BSs is the quantised nature of their spin. The linearised Einstein equations in the slow-rotation limit lead to a two-dimensional Poisson equation that does not admit everywhere regular solutions except for trivial constants; in consequence BSs cannot rotate perturbatively [67]. By relaxing the slow-rotation approximation, Schunck and Mielke [68] computed the first (differentially) rotating BSs and found that these solutions have an integer ratio of angular momentum to particle number. The structure of spinning BS models has been studied extensively over the years [69, 70, 71, 72, 73, 74, 75, 76, 77]. The quantised nature of the angular momentum also applies to Proca and *Dirac* (spin $\frac{1}{2}$) stars [78], but numerical studies of the formation of rotating stars have revealed a striking difference between the scalar and vector case: while collapsing scalar fields shed all their angular momentum through an axisymmetric instability, the collapse of vector fields results in spinning Proca stars with no indication of an instability [79, 65]. This observation is supported by analytic calculations [80], but the instability may be quenched by self-interaction terms in the potential function or in the Newtonian limit [81]. For further reviews of the structure and dynamics of single BSs, we note the reviews [82, 83, 84, 85].

The first simulations of BS binaries have considered the head-on collision of configurations with phase differences between the constituent stars or opposite frequencies [86]; see also [87, 88]. The phase or frequency differences manifest themselves most pronouncedly in the dynamics and GW emission at late times around merger. These collisions result in either a BH, a non-rotating BS or a near-annihilation of the scalar field in the case of opposite frequencies. BS binaries with orbital angular momentum generate a GW signal qualitatively similar to that of BH binaries during the inspiral phase, but exhibit a much more complex structure around merger [89, 90]. In agreement with the above mentioned BS formation studies, the BS inspirals also seem to avoid the formation of spinning BSs, although they may settle down into single nonrotating BSs.

In spite of the rapid progress of this field, the computation of GW templates for BSs still lags considerably behind that of BH binaries, both in terms of precision and coverage of the parameter space. Clearly, the presence of the matter fields adds complexity to this challenge, but also alleviates some of the difficulties through the non-singular character of the BS spacetimes. The first main goal of our study is to highlight the substantial risk of obtaining spurious physical results due to the use of overly simplistic initial data constructed by plain superposition of single-BS spacetimes. Our second main goal is to demonstrate how an astonishingly simple modification of the superposition procedure, first identified by Helfer *et al.* [16] for oscillatons, overcomes most of the problems encountered with plain superposition. We summarise our main findings as follows.

1. An adjustment of the superposition procedure, given by Eq. (4.2.3), results in a significant reduction of the constraint violations inherent to the initial data; see Fig. 4.3.

2. In the head-on collision of mini BS binaries with rather low compactness, we observe a significant drop of the radiated GW energy with increasing distance d if we use plain superposition. This physically unexpected dependence on the initial separation levels off only for rather large $d \gtrsim 150\,M$, where M denotes the Arnowitt-Deser-Misner (ADM) mass [91]. In contrast, the total radiated energy computed from the evolution of our adjusted initial data displays the expected behaviour over the entire studied range $75.5\,M \leq d \leq 176\,M$: a very mild increase in the radiated energy with d. In the limit of large $d \gtrsim 150\,M$, both types of simulations agree within numerical uncertainties; see upper panel in Fig. 4.6.

3. In collisions of highly compact BSs with solitonic potentials, the radiated energy is largely in-

dependent of the initial separations for both initial data types, but for plain superposition we consistently obtain $\sim 10\,\%$ more radiation than for the adjusted initial data; see bottom panel in Fig. 4.6. Furthermore, we find plain superposition to result in a slightly faster infall. The most dramatic difference, however, is the collapse into individual BHs of both BSs well before merger if we use plain superposition. No such collapse occurs if we use adjusted initial data. Rather, these lead to the expected near-constancy of the central scalar-field amplitude of the BSs throughout most of the infall; see Fig. 4.9.

4. We have verified through evolutions of single boosted BSs that the premature collapse into a BH is closely related to the spurious metric perturbation (4.2.2) that arises in the plain superposition procedure. Artificially adding the same perturbation to a single BS spacetime induces an unphysical collapse of the BS that is in qualitative and quantitative agreement with that observed in the binary evolution starting with plain superposition; see Fig. 4.9.

The detailed derivation of these results begins in Sec. **??** with a review of the formalism and the computational framework of our BS simulations. We discuss in more detail in Sec. 4.2 the construction of initial data through plain superposition and our modification of this method. In Sec. 4.3, we compare the dynamics of head-on collisions of mini BSs and highly compact solitonic BS binaries starting from both types of initial data. We note the substantial differences in the results thus obtained and argue why we regard the results obtained with our modification to be correct within numerical uncertainties. We summarise our findings and discuss future extensions of this work in Sec. 4.4.

Throughout this work, we use units where the speed of light and Planck's constant are set to unity, $c = \hbar = 1$. We denote spacetime indices by Greek letters running from 0 to 3 and spatial indices by Latin indices running from 1 to 3.

4.1.1 TODO

4.1.2 Boson Star Initial Data

The initial data for our time evolution are based on single stationary BS solutions in spherical symmetry as discussed in section 2.2.2. Using spherical polar isotropic coordinates the line element can be written as

$$\mathrm{d}s^2 = -e^{2\Phi}\mathrm{d}t^2 + \psi^4\delta_{ij}\mathrm{d}x^i\mathrm{d}x^j\,. \tag{4.1.1}$$

where Φ and ψ are functions of r only. The metric can be compared to the metric of the isotropic schwarzschild metric by setting,

$$\psi(r) = \left(1 + \frac{m(r)}{2r}\right), \tag{4.1.2}$$

and defining a function $m(r)$ describing the mass inside a given radius r. At large radius the boson star spacetime approaches the vaccum black hole spacetime, $m(r)$ is constant and $m(\infty)$ gives the ADM mass of an isolated boson star. It turns out convenient to express the complex scalar field in terms of amplitude and frequency,

$$\varphi(t,r) = A(r)e^{\mathrm{i}\omega t}\,, \qquad \omega = \text{const} \in \mathbb{R}\,, \tag{4.1.3}$$

as shown in section 2.2.2. The scalar field potentials used for the stars are,

$$V_{\text{min}} = A^2\,, \tag{4.1.4}$$

$$V_{\text{sol}} = A^2\left(1 - 2\frac{A^2}{\sigma_0^2}\right)^2, \tag{4.1.5}$$

taken from Eqs. (2.2.4) and (2.2.6) for a mini boson star and a solitonic boson star respectively; clearly setting $\sigma_0 \to \infty$ gives $V_{\text{min}} = V_{\text{sol}}$.

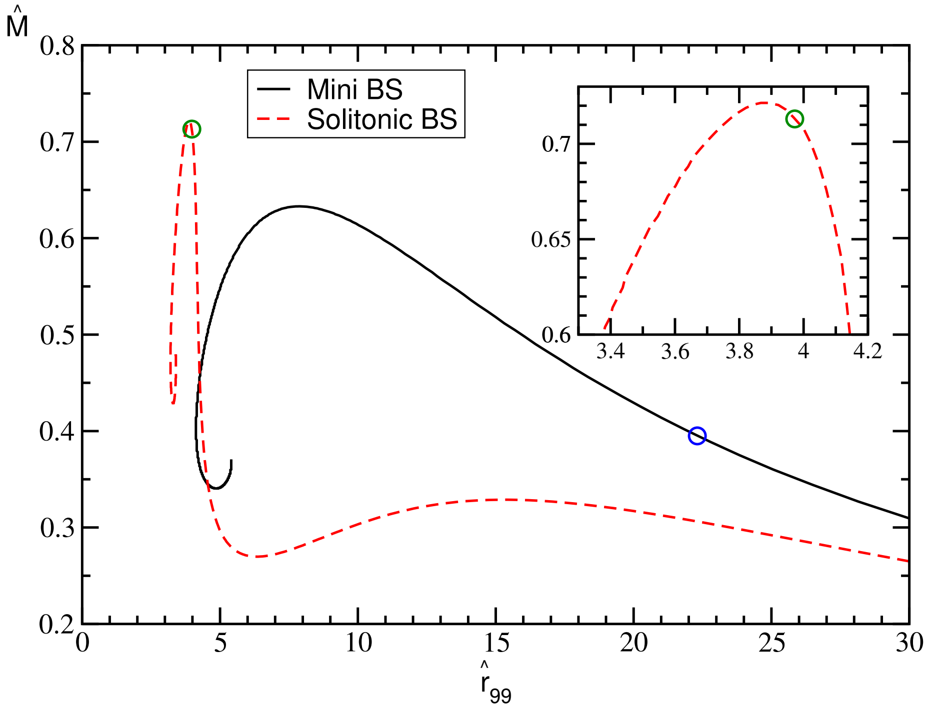

Figure 4.1: One parameter families of mini BSs (black solid) with potential $\hat{V}_{\rm min}$ and solitonic BSs (red dashed) with potential $\hat{V}_{\rm sol}$ and $\hat{\sigma}_0 = 0.2$ as given in Eqs. (4.1.4) and (4.1.5). In Sec. 4.3 we simulate head-on collisions of two specific models marked by the circles and with parameters listed in Table 4.1.

Model	A_0	σ_0	$m \cdot M_{\rm BS}$	ω/m	$m \cdot r_{99}$	$\max \frac{m(r)}{r}$
mini	0.0124	∞	0.395	0.971	22.31	0.0249
soli	0.17	0.2	0.713	0.439	3.98	0.222

Table 4.1: Parameters of the two single, spherically symmetric ground state BS models employed for our simulations of head-on collisions. Up to the rescaling with the scalar mass m, each BS is determined by the central amplitude A_0 of the scalar field and the potential parameter σ_0 of Eq. (4.1.5). The mass $M_{\rm BS}$ of the boson star, the scalar field frequency ω, the areal radius r_{99} containing 99 % of the total mass $M_{\rm BS}$ and the compactness, defined here as the maximal ratio of the mass function $m(r)$ to radius, represent the main features of the stellar model.

Following the conventions of [REF] MAKE THE PLANK UNITS AND BOSON MASS CONVENTIONS WORK

For a given potential, the solutions computed with this method form a one-parameter family characterised by the central scalar field amplitude A_0. In Fig. 4.1 we display two such families for the potentials (4.1.4) and (4.1.5) with $\sigma_0 = 0.2$ in the mass-radius diagram using the areal radius r_{99} containing 99 % of the BS's total mass. In that figure, we have also marked by circles two specific models, one mini BS and one solitonic BS, which we use in the head-on collisions in Sec. 4.3 below. We have chosen these two models to represent one highly compact and one rather squishy BS; note that both models are located to the right of the maximal $M(r)$ and, hence, stable stars. Their parameters and properties are summarised in Table 4.1.

TALK ABOUT THE BOOSTS HERE!

MAYBE ADD PLOT OF SOLITONIC STAR VS MINI BOSON STAR HERE TOO

4.2 Boson-star binary initial data

The single BS models constructed according to the procedure of the previous section are exact solutions of the Einstein equations, affected only by a numerical error that we can control by increasing the resolution, the size of the computational domain and the degree of precision of the floating point variable type employed. The construction of binary initial data is conceptually more challenging due to the non-linear character of the Einstein equations; the superposition of two individual solutions will, in general, not constitute a new solution. Instead, such a superposition incurs some violation of the constraint equations (??), (??). The purpose of this section is to illustrate how we can substantially reduce the degree of constraint violation with a relatively simple adjustment in the superposition. Before introducing this "trick", we first summarise the superposition as it is commonly used in numerical simulations.

4.2.1 Simple superposition of boson stars

The most common configuration involving more than one BS is a binary system, and this is the scenario we will describe here. We note, however, that the method generalises straightforwardly to any number of stars. Let us then consider two individual BS solutions with their centres located at $x^i_{\rm A}$ and $x^i_{\rm B}$, velocities $v^i_{\rm A}$ and $v^i_{\rm B}$. The two BS spacetimes are described by the 3+1 (ADM) variables $\gamma^{\rm A}_{ij}$, $\alpha_{\rm A}$, $\beta^i_{\rm A}$ and $K^{\rm A}_{ij}$, the scalar field variables $\varphi_{\rm A}$ and $\Pi_{\rm A}$, and likewise for star B. We can construct from these individual solutions an approximation for a binary BS system via the pointwise superposition

$$
\begin{aligned}
\gamma_{ij} &= \gamma^{\rm A}_{ij} + \gamma^{\rm B}_{ij} - \delta_{ij}\,, \qquad & K_{ij} &= \gamma_{m(i}\left[K^{\rm A}_{j)n}\gamma^{nm}_{\rm A} + K^{\rm B}_{j)n}\gamma^{nm}_{\rm B}\right]\,, \\
\varphi &= \varphi_{\rm A} + \varphi_{\rm B}\,, & \Pi &= \Pi_{\rm A} + \Pi_{\rm B}\,.
\end{aligned}
\tag{4.2.1}
$$

One could similarly construct a superposition for the lapse α and shift vector β^i, but their values do not affect the physical content of the initial hypersurface. In our simulations we instead initialise them by $\alpha = \sqrt{\chi}$ and $\beta^i = 0$.

A simple superposition approach along the lines of Eq. (4.2.1) has been used in numerous studies of BS as well as BH binaries including higher-dimensional BHs [86, 89, 92, 93, 90, 94]. For BHs and higher-dimensional spacetimes in particular, this leading-order approximation has proved remarkably successful and in some limits a simple superposition is exact, such as infinite initial separation, in Brill-Lindquist initial data for non-boosted BHs[7] [95] or in the superposition of Aichelburg-Sexl shockwaves [96] for head-on collisions of BHs at the speed of light. It has been noted in Helfer *et al.* [16], however, that this simple construction can result in spurious low-frequency amplitude modulations in the time evolution of binary oscillatons (real-scalar-field cousins of BSs); cf. their Fig. 7. Furthermore, they have proposed a straightforward remedy that essentially eliminates this spurious modulation. As we will see in the next section, the repercussions of the *simple superposition* according to Eqs. (4.2.1) can be even more dramatic for BS binaries, but they can be cured in the same way as in the oscillaton case. We note in this context that BSs may be more vulnerable to superposition artefacts near their centres due to the lack of a horizon and its potentially protective character in the superposition of BHs.

The key problem of the construction (4.2.1) is the equation for the spatial metric γ_{ij}. This is best illustrated by considering the centre $x^i_{\rm A}$ of star A. In the limit of infinite separation, the metric field of its companion star B becomes $\gamma^{\rm B}_{ij} \to \delta_{ij}$. This is, of course, precisely the contribution we subtract in the third term on the right-hand-side and all would be well. In practice, however, the BSs start from initial positions $x^i_{\rm A}$ and $x^i_{\rm B}$ with finite separation $d = ||x^i_{\rm A} - x^i_{\rm B}||$ and we consequently perturb the metric at star A's centre by

$$
\delta\gamma_{ij} = \gamma^{\rm B}_{ij}(x^i_{\rm A}) - \delta_{ij} \tag{4.2.2}
$$

away from its equilibrium value $\gamma^{\rm A}_{ij}(x^i_{\rm A})$. This metric perturbation can be interpreted as a distortion of the volume element $\sqrt{\gamma}$ at the centre of star A. More specifically, the volume element at star A's

[7] Note that for Brill-Lindquist one superposes the conformal factor ψ rather than ψ^4 as in the method discussed here.

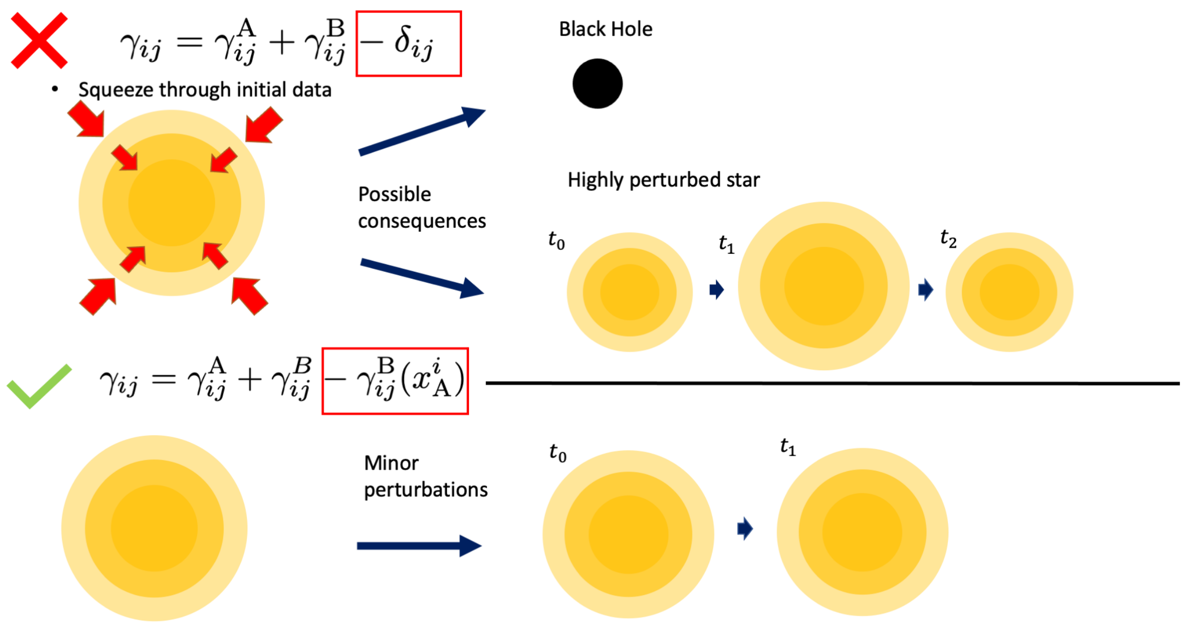

Figure 4.2: Graphical illustration of the spurious dynamics that may be introduced by the simple superposition procedure (4.2.1). *Upper panel*: The spurious increase in the volume element mimics a squeezing of the stellar core that effects a pulsation of the star or may even trigger gravitational collapse to a BH. *Lower panel*: No such squeezing occurs with the adjusted superposition (4.2.3), and the binary evolution starts with approximately unperturbed stars.

centre is enhanced by $\mathcal{O}(1)\,\%$ for initial separations $\mathcal{O}(100)\,M$ and likewise for the centre of star B (by symmetry); see appendix A of Ref. [16] for more details.[8] The energy density ρ, on the other hand, is barely altered by the presence of the other star, because of the exponential fall-off of the scalar field. The leading-order error therefore consists in a small excess mass that has been added to each BS's central region. We graphically illustrate this effect in the upper half of Fig. 4.2 together with some of the possible consequences. As we will see, this qualitative interpretation is fully borne out by the phenomenology we observe in the binaries' time evolutions.

Finally, we would like to emphasise that, while evaluating the constraint violations is in general a good rule of thumb to check whether the field configuration is a solution of the system, it does *not* inform one whether it is *the intended* solution; a system with some constraint violation may have drifted closer to a different, unintended solution. In the present case, in addition to the increased constraint violation, the constructed BS solutions possess significant excitations. Thus, while applying a constraint damping system like conformal Z4 [97, 98] may eventually drive the system to a solution, it may no longer be what was originally intended to be the initial condition of an unexcited BS star.

4.2.2 Improved superposition

The problem of the simple superposition is encapsulated by Eq. (4.2.2) and the resulting deviation of the volume elements at the stars' centres away from their equilibrium values. At the same time, the equation presents us with a concrete recipe to mitigate this error: we merely need to replace in the simple superposition (4.2.1) the first relation $\gamma_{ij} = \gamma_{ij}^{\rm A} + \gamma_{ij}^{B} - \delta_{ij}$ by

$$\boxed{\gamma_{ij} = \gamma_{ij}^{\rm A} + \gamma_{ij}^{\rm B} - \gamma_{ij}^{\rm B}(x_{\rm A}^i) = \gamma_{ij}^{\rm A} + \gamma_{ij}^{\rm B} - \gamma_{ij}^{\rm A}(x_{\rm B}^i)\,.} \tag{4.2.3}$$

[8]Due to the slow decay of this effect $\propto 1/\sqrt{d}$ [16], a simple cure in terms of using larger d is often not practical.

Label	star A	star B	v	initial data	d/M
`mini`	mini	mini	0.1	plain	75.5, 101, 126, 151, 176
`+mini`	mini	mini	0.1	adjusted	75.5, 101, 126, 151, 176
`soli`	soli	soli	0.1	plain	16.7, 22.3, 27.9, 33.5, 39.1
`+soli`	soli	soli	0.1	adjusted	16.7, 22.3, 27.9, 33.5, 39.1

Table 4.2: The four types of BS binary head-on collisions simulated in this study. The individual BSs A and B are given either by the mini or solitonic model of Table 4.1, and start with initial velocity v directed towards each other. The initial data is constructed either by plain superposition (4.2.1) or by adjusting the superposed data according to Eq. (4.2.3). For each type of binary, we perform five collisions with initial separations d listed in the final column.

The two expressions on the right-hand side are indeed equal thanks to the symmetry of our binary: its constituents have equal mass, no spin and their velocity components satisfy $v^i_{\rm A}v^j_{\rm A} = v^i_{\rm B}v^j_{\rm B}$ for all i, $j = 1, 2, 3$ in the centre-of-mass frame. Equation (4.2.3) manifestly ensures that at positions $x^i_{\rm A}$ and $x^i_{\rm B}$ we now recover the respective star's equilibrium metric and, hence, volume element. We graphically illustrate this improvement in the bottom panel of Fig. 4.2.

A minor complication arises from the fact that the resulting spatial metric does not asymptote towards δ_{ij} as $R \to \infty$. We accordingly impose outgoing Sommerfeld boundary conditions on the asymptotic background metric $2\delta_{ij} - \gamma^{\rm A}_{ij}(x^i_{\rm B})$; in a set of test runs, however, we find this correction to result in very small changes well below the simulation's discretisation errors.

Finally, we note that the leading-order correction to the superposition as written in Eq. (4.2.3) does not work for asymmetric configurations with unequal masses or spins. Generalising the method to arbitrary binaries requires the subtraction of a spatially varying term rather than a constant $\gamma^{\rm B}_{ij}(x^i_{\rm A}) = \gamma^{\rm A}_{ij}(x^i_{\rm B})$ or δ_{ij}. Such a generalisation may consist, for example, of a weighted sum of the terms $\gamma^{\rm A}_{ij}(x^i_{\rm B})$ and $\gamma^{\rm B}_{ij}(x^i_{\rm A})$. Leaving this generalisation for future work, we will focus on equal-mass systems in the remainder of this study and explore the degree of improvement achieved with Eq. (4.2.3).

4.3 Models and results

For our analysis of the two types of superposed initial data, we will now discuss time evolutions of binary BS head-on collisions. A head-on collision is characterised by the two individual BS models and three further parameters, the initial separation in units of the ADM mass, d/M, and the initial velocities $v_{\rm A}$ and $v_{\rm B}$ of the BSs. We perform all our simulations in the centre-of-mass frame, so that for equal-mass binaries, $v_{\rm A} = -v_{\rm B}v$. One additional parameter arises from the type of superposition used for the initial data construction: we either use the "plain" superposition of Eq. (4.2.1) or the "adjusted" method (4.2.3).

For all our simulations, we set $v = 0.1$; this value allows us to cover a wide range of initial separations without the simulations becoming prohibitively long. The BS binary configurations summarised in Table 4.2 then result in four sequences of head-on collisions labelled `mini`, `+mini`, `soli` and `+soli`, depending in the nature of the constituent BSs and the superposition method. For each sequence, we vary the BSs initial separation d to estimate the dependence of the outcome on d. First, however, we test our interpretation of the improved superposition (4.2.3) by computing the level of constraint violations in the initial data.

4.3.1 Initial constraint violations

As discussed in Sec. 4.2.1 and in Appendix A of Ref. [16], the main shortcoming of the plain superposition procedure consists in the distortion of the volume element near the individual BSs' centres and the

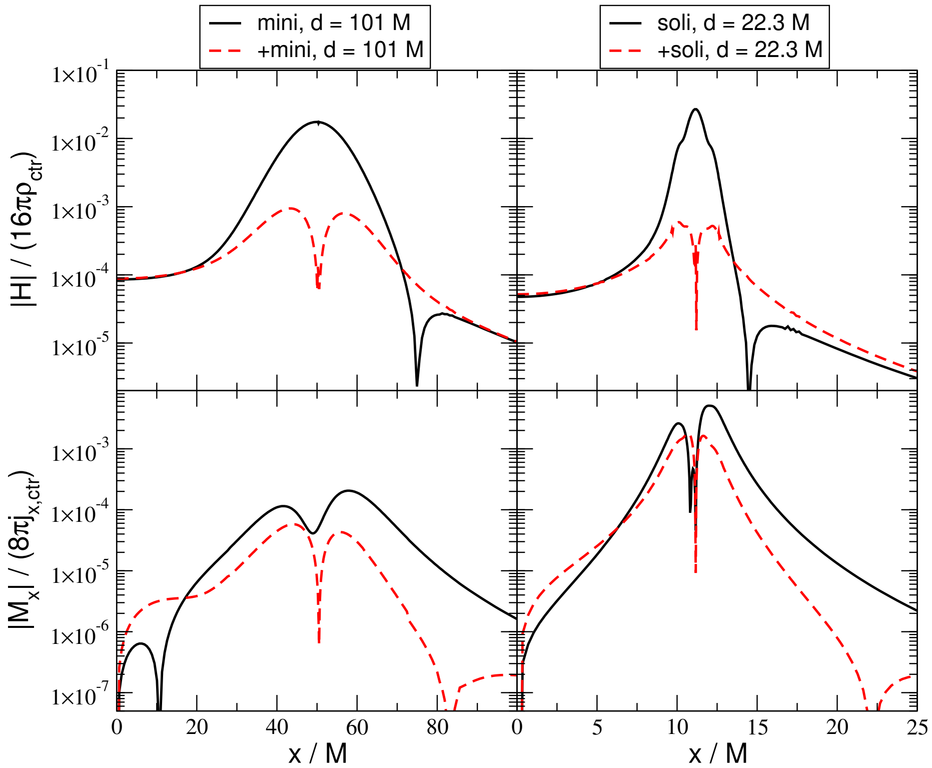

Figure 4.3: Upper row: The Hamiltonian constraint violation $\mathcal{H}$ – Eq. (**??**) – normalised by the respective BS's central energy density $16\pi\rho_{\rm ctr}$ is plotted along the collision axis of the binary configurations `mini`, `+mini` with $d = 101\,M$ (left) and `soli`, `+soli` with $d = 22.3\,M$ (right). The degree of violations is substantially reduced in the BS interior by using the improved superposition (4.2.3) for `+mini` and `+soli` relative to their plain counterparts; the maxima of $\mathcal{H}$ have dropped by over an order of magnitude in both cases. Bottom row: The same analysis for the momentum constraint $\mathcal{M}_x$ normalised by the central BS's momentum density $8\pi j_x$. Here the improvement is less dramatic, but still yields a reduction by a factor of a few in the BS core.

resulting perturbation of the mass-energy inside the stars away from their equilibrium values. If this interpretation is correct, we would expect this effect to manifest itself in an elevated level of violation of the Hamiltonian constraint (**??**) which relates the energy density to the spacetime curvature. Put the other way round, we would expect our improved method (4.2.3) to reduce the Hamiltonian constraint violation. This is indeed the case as demonstrated in the upper panels of Fig. 4.3 where we plot the Hamiltonian constraint violation of the initial data along the collision axis for the configurations `mini` and `+mini` with $d = 101\,M$ and the configurations `soli` and `+soli` with $d = 22.3\,M$.

In the limit of zero boost velocity $v = 0$, this effect is even tractable through an analytic calculation which confirms that the improved superposition (4.2.3) ensures $\mathcal{H} = 0$ at the BS's centres in isotropic coordinate; see 4.5 for more details.

Our adjustment (4.2.3) also leads to a reduction of the momentum constraint violations of the initial data, although the effect is less dramatic here. The bottom panels of Fig. 4.3 display the momentum constraint $\mathcal{M}_x$ of Eq. (**??**) along the collision axis normalised by the momentum density $8\pi j_x$; we see a reduction by a factor of a few over large parts of the BS interior for the modified data `+mini` and `+soli`.

The overall degree of initial constraint violations is rather small in all cases, well below 0.1 % for our adjusted data. These data should therefore also provide a significantly improved initial guess for a full constraint solving procedure. We leave such an analysis for future work and in the remainder of the work

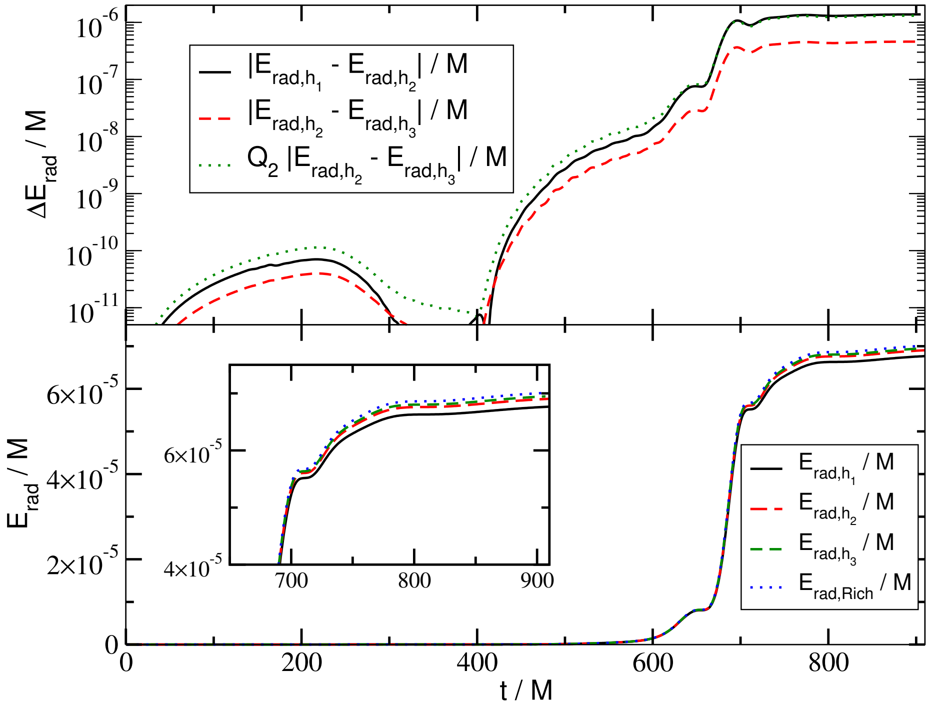

Figure 4.4: Convergence analysis for the GW energy extracted at $R_{\rm ex} = 252\,M$ from the head-on collision `+mini` of Table 4.1 with $d = 101\,M$. For the resolutions $h_1 = M/6.35$, $h_2 = M/9.53$ and $h_3 = 12.70$ (on the innermost refinement level), we obtain convergence close to second order (upper panel). The numerical error, obtained by comparing our results with the second-order Richardson extrapolated values (bottom panel), is 0.9 % (1.6 %, 3.6 %) for our high (medium, coarse) resolutions.

explore the impact of the adjustment (4.2.3) on the physical results obtained from the initial data's time evolutions.

4.3.2 Convergence and numerical uncertainties

In order to put any differences in the time evolutions into context, we need to understand the uncertainties inherent to our numerical simulations. For this purpose, we have studied the convergence of the GW radiation generated by the head-on collisions of mini and solitonic BSs.

Figure 4.4 displays the convergence of the radiated energy $E_{\rm rad}$ as a function of time for the `+mini` configuration with $d = 101\,M$ of Table 4.1 obtained for grid resolutions $h_1 = M/6.35$, $h_2 = M/9.53$ and $h_3 = M/12.70$ on the innermost refinement level and corresponding grid spacings on the other levels. The functions $E_{\rm rad}(t)$ and their differences are shown in the bottom and top panel, respectively, of Fig. 4.4 together with an amplification of the high-resolution differences by the factor $Q_2 = 2.86$ for second-order convergence. The observation of second-order convergence is compatible with the second-order ingredients of the Lean code, prolongation in time and the outgoing radiation boundary conditions. We believe that this dominance is mainly due to the smooth behaviour of the BS centre as compared with the case of black holes [99]. By using the second-order Richardson extrapolated result, we determine the discretisation error of our energy estimates as 0.9 % for h_3 which is the resolution employed for all remaining mini BS collisions. We have performed the same convergence analysis for the plain-superposition counterpart `mini` and for the dominant $(\ell, m) = (2, 0)$ multipole of the Newman-Penrose scalar of both configurations and obtained the same convergence and very similar relative errors.

In Fig. 4.5, we show the same convergence analysis for the solitonic collision `+soli` with $d = 22.3\,M$ and resolutions $h_1 = M/22.9$, $h_2 = M/45.9$, $h_3 = M/68.8$. We observe second-order convergence during merger and ringdown and slightly higher convergence in the earlier infall phase. For the uncertainty

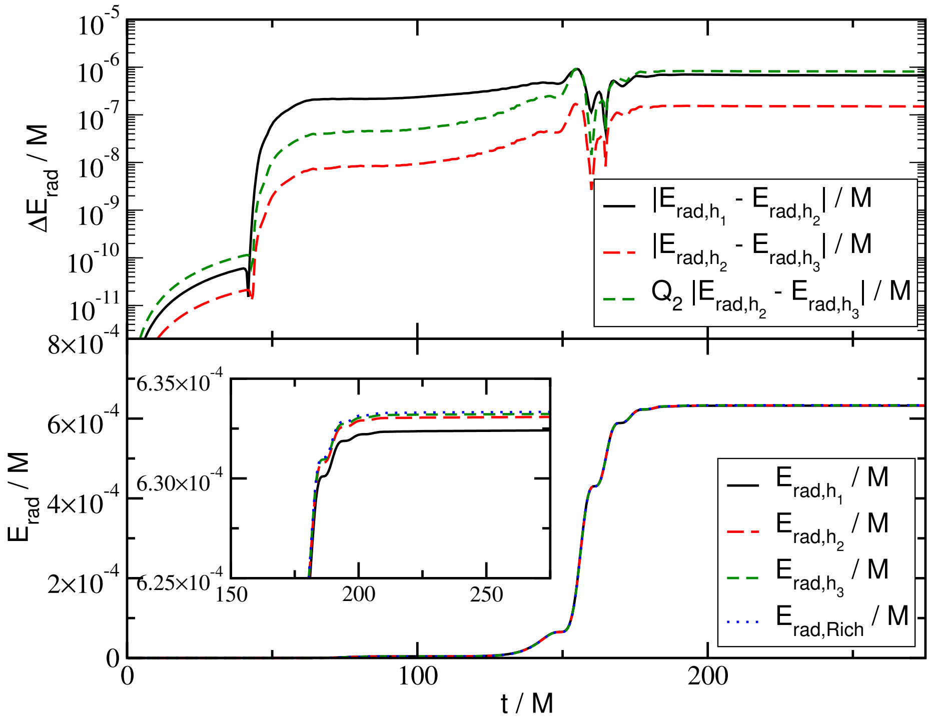

Figure 4.5: Convergence analysis as in Fig. 4.4 but for the configuration `+soli` of Table 4.1 with $d = 22.3\,M$ and resolutions $h_1 = M/22.9$, $h_2 = M/45.9$ and $h_3 = M/68.8$. The numerical error, obtained by comparing our results with the second-order Richardson extrapolated values (bottom panel), is 0.03 % (0.07 %, 0.6 %) for our high (medium, coarse) resolutions.

estimate we conservatively use the second-order Richardson extrapolated result and obtain a discretisation error of about 0.07 % for our medium resolution h_2 which is the value we employ in our solitonic production runs. Again, we have repeated this analysis for the plain `soli` counterpart and the $(2, 0)$ GW multipole observing the same order of convergence and similar uncertainties. Our error estimate for the solitonic configurations is rather small in comparison to the mini BS collisions and we cannot entirely rule out a fortuitous cancellation of errors in our simulations. From this point on, we therefore use a conservative discretisation error estimate of 1 % for all our BS simulations.

A second source of uncertainty in our results is due to the extraction of the GW signal at finite radii rather than $\mathcal{I}^+$. We determine this error by extracting the signal at multiple radii, fitting the resulting data by the series expansion $f = f_0 + f_1/r$, and comparing the result at our outermost extraction radius with the limit f_0. This procedure results in errors in $E_{\rm rad}$ ranging between 0.5 % and 3 %. With the upper range, we arrive at a conservative total error budget for discretisation and extraction of about 4 %. As a final test, we have repeated the `mini` and `+mini` collisions for $d = 101\,M$ with the independent GRChombo code [100, 101] using the CCZ4 formulation [98] and obtain the same results within ≈ 1.5 %. Bearing in mind these tests and a 4 % error budget, we next study the dynamics of the BS head-on collisions with and without our adjustment of the initial data.

4.3.3 Radiated gravitational-wave energy

For our first test, we compute the total radiated GW energy for all our head-on collisions focusing in particular on its dependence on the initial separation d of the BS centres. In this estimate we exclude any spurious or "junk" radiation content of the initial data by starting the integration at $t = R_{\rm ex} + 40\,M$. Unless specified otherwise, all our results are extracted at $R_{\rm ex} = 300\,M$ for mini BS collisions and $R_{\rm ex} = 84\,M$ for the solitonic binaries.

The main effect of increasing the initial separation is a reduction of the (negative) binding energy of the

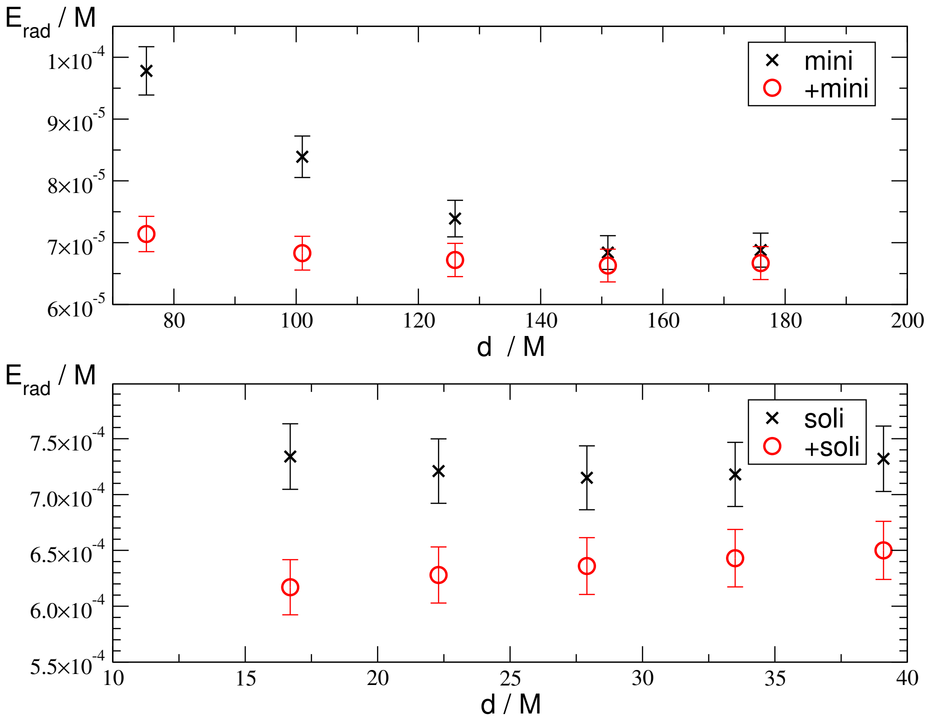

Figure 4.6: The GW energy $E_{\rm rad}$ generated in the head-on collision of mini (upper panel) and solitonic (lower panel) BS binaries starting with initial separation d and velocity $v = 0.1$ towards each other. For comparison, a non-spinning, equal-mass BH binary colliding head-on with the same boost velocity $v = 0.1$ radiates $E_{\rm rad} = 6.0 \times 10^{-4}\,M$ [94].

binary and a corresponding increase of the collision velocity around merger. In the large d limit, however, this effect becomes negligible. For the comparatively large initial separations chosen in our collisions, we would therefore expect the function $E_{\rm rad}$ to be approximately constant, possibly showing a mild increase with d. The mini BS collisions shown as black $\times$ symbols in the upper panel of Fig. 4.6 exhibit a rather different behaviour: the radiated energy rapidly decreases with d and only levels off for $d \gtrsim 150\,M$. We have verified that the excess energy for smaller d is not due to an elevated level of junk radiation which consistently contribute well below $0.1\,\%$ of $E_{\rm rad}$ in all our mini BS collisions and has been excluded from the results of Fig. 4.6 anyway. The `+mini` BS collisions, in contrast, results in an approximately constant $E_{\rm rad}$ with a total variation approximately at the level of the numerical uncertainties. For $d \gtrsim 150\,M$, both types of initial data yield compatible results, as is expected. The key benefit of our adjusted initial data is that they provide reliable results even for smaller initial separations suitable for starting BS inspirals.

The discrepancy is less pronounced for the head-on collisions of solitonic BS collisions; both types of initial data result in approximately constant $E_{\rm rad}$. They differ, however, in the predicted amount of radiation at a level that is significant compared to the numerical uncertainties. As we will see below, this difference is accompanied by drastic differences in the BS's dynamics during the long infall period. We furthermore note that the mild but steady increase obtained for the adjusted `+soli` agrees better with the physical expectations.

The differences in the total radiated GW energy also manifest themselves in different amplitudes of the $(2, 0)$ multipole of the Newman-Penrose scalar Ψ_4. This is displayed in Figs. 4.7 and 4.8 where we show the GW modes for the mini and solitonic collisions, respectively. The most prominent difference between the results for plain and adjusted initial data is the significant variation of the amplitude of the $(2, 0)$ mode in the plain mini BS collisions in the upper panel of Fig. 4.7. In contrast, the differences in the amplitudes in Fig. 4.8 for the solitonic collisions are very small. In fact, the differences in the

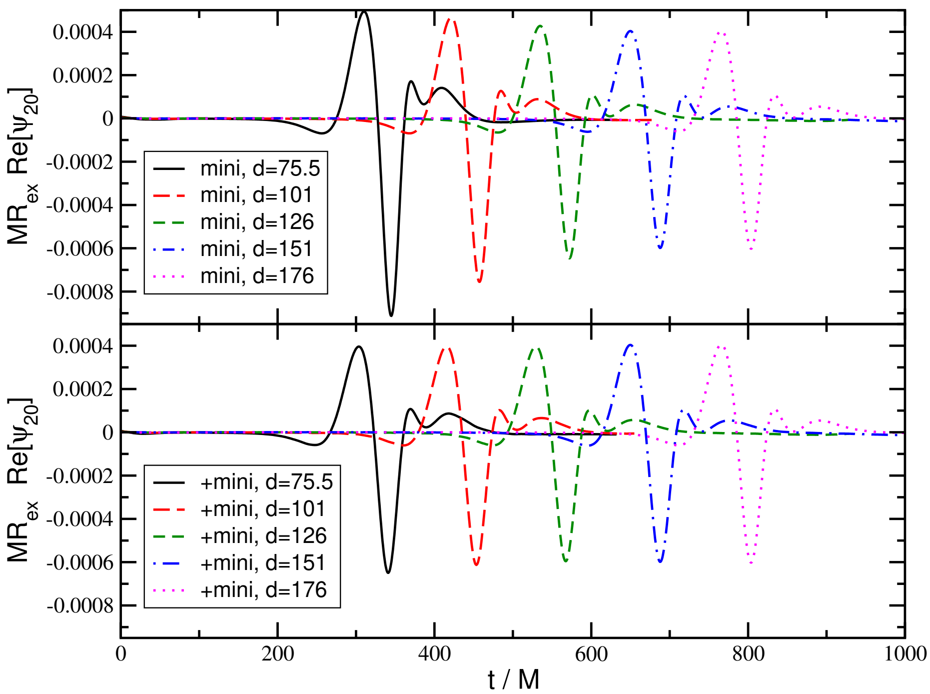

Figure 4.7: The $(2,0)$ mode of the Newman-Penrose scalar for the mini boson star collisions of Table 4.1.

radiated energy of the `soli` and `+soli` collisions mostly arise from a minor stretching of the signal for the `soli` case; this effect is barely perceptible in Fig. 4.8 but is amplified by the integration in time when we calculate the energy. Finally, we note the different times of arrival of the main pulses in Fig. 4.8; especially for larger initial separation, the merger occurs earlier for the `soli` configurations than for their adjusted counterparts `+soli`. We will discuss this effect together with the evolution of the scalar field amplitude in the next subsection.

4.3.4 Evolution of the scalar amplitude and gravitational collapse

The adjustment (4.2.3) in the superposition of oscillatons was originally developed in Ref. [16] to reduce spurious modulations in the scalar field amplitude; cf. their Fig. 7. In our simulations, this effect manifests itself most dramatically in the collisions of our solitonic BS configurations `soli` and `+soli`. From Fig. 4.1, we recall that the single-BS constituents of these binaries are stable, but highly compact stars, located fairly close to the instability threshold. We would therefore expect them to be more sensitive to spurious modulations in their central energy density. This is exactly what we observe in all time evolutions of the `soli` configurations starting with plain-superposition initial data. As one example, we show in Fig. 4.9 the scalar amplitude at the individual BS centres and the BS trajectories as functions of time for the `soli` and `+soli` configurations starting with initial separation $d = 22.3\,M$. Let us first consider the `soli` configuration using plain superposition displayed by the solid (black) curves. In the upper panel of Fig. 4.9, we clearly see that the scalar amplitude steadily increases, reaching a maximum around $t \approx 30\,M$ and then rapidly drops to a near-zero level. Our interpretation of this behaviour as a collapse to a BH is confirmed by the horizon finder which reports an apparent horizon of irreducible mass $m_{\rm irr} = 0.5\,M$ just before the scalar field amplitude collapses; the time of the first identification of an apparent horizon is marked by the vertical dotted black line at $t \approx 30\,M$. For reference we plot in the bottom panel the trajectory of the BS centres along their collision (here the x) axis. In agreement with the horizon mass $m_{\rm irr} = 0.5\,M$, the trajectory clearly indicates that around $t \approx 30\,M$, the BSs are still far away from merging into a single BH; in units of the ADM mass, the individual BS radius is $r_{99} = 2.78\,M$. We interpret this early BH collapse as a spurious feature due to the use of plain superposition in the initial data construction. This behaviour is also seen in the case of the real scalar field oscillatons in [16].

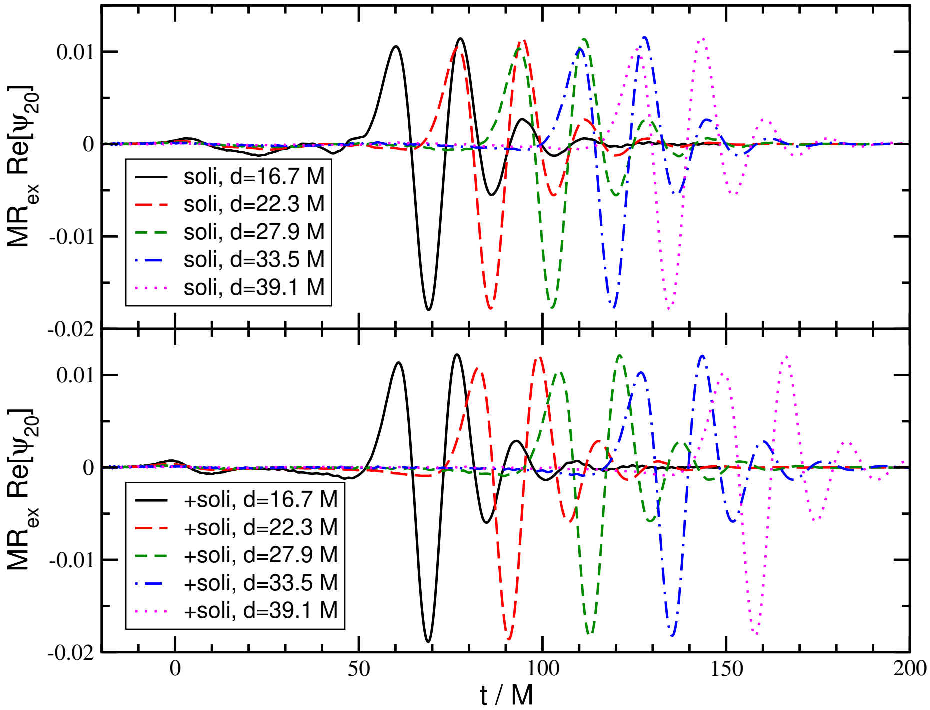

Figure 4.8: The $(2, 0)$ mode of the Newman-Penrose scalar for the solitonic boson star collisions of Table 4.1.

We have tested this hypothesis with the evolution of the adjusted initial data. These exhibit a drastically different behaviour in the collision `+soli` displayed by the dashed (red) curves in Fig. 4.9. Throughout most of the infall, the central scalar amplitude is constant, it increases mildly when the BS trajectories meet near $x = 0$, and then rapidly drops to zero. Just as the maximum amplitude is reached, the horizon finder first computes an apparent horizon, now with $m_{\rm irr} = 0.99\,M$, as expected for a BH resulting from the merger; see the vertical red line in the figure.

As a final test of our interpretation, we compare the behaviour of the binary constituents with that of single BSs boosted with the same velocity $v = 0.1$. As expected, the scalar field amplitude at the centre of such a single BS remains constant within high precision, about $\mathcal{O}(10^{-5})$, on the timescale of our collisions. We have then repeated the single BS evolution by poisoning the initial data with the very same term (4.2.2) that is also added near a single BS's centre by the plain-superposition procedure. The resulting scalar amplitude at the centre of this poisoned BS is shown as the dash-dotted (blue) curve in Fig. 4.9 and nearly overlaps with the corresponding curve of the `soli` binary. Furthermore, the poisoned single BS collapses into a BH after nearly the same amount of time as indicated by the vertical blue dotted curve in the figure[5]. Clearly this behaviour of the single boosted BS is unphysical, and strongly indicates that the plain superposition of initial data introduces the same unphysical behaviour to our `soli` binary constituents. We have repeated this analysis for our entire sequence of `soli` binaries with very similar results: the individual BSs always collapse to distinct BHs about $\Delta t \approx 50\,M$ before the binary merger.

Finally, the trajectories in the bottom panel of Fig. 4.9 indicate that the BS merger occurs a bit later for the `+soli` case than its plain-superposition counterpart `soli`. This is indeed a systematic effect we see for all initial separations d and which agrees with the different arrival times of the peak GW signals that we have already noticed in Fig. 4.8. We do not have a rigorous explanation of this effect, but note that the two trajectories in Fig. 4.9 start diverging right at the time of spurious BH formation in the

[5]Recall that this BS model is stable but fairly close to the stability threshold in Fig. 4.1 and therefore does not require a large perturbation to be toppled over the edge.

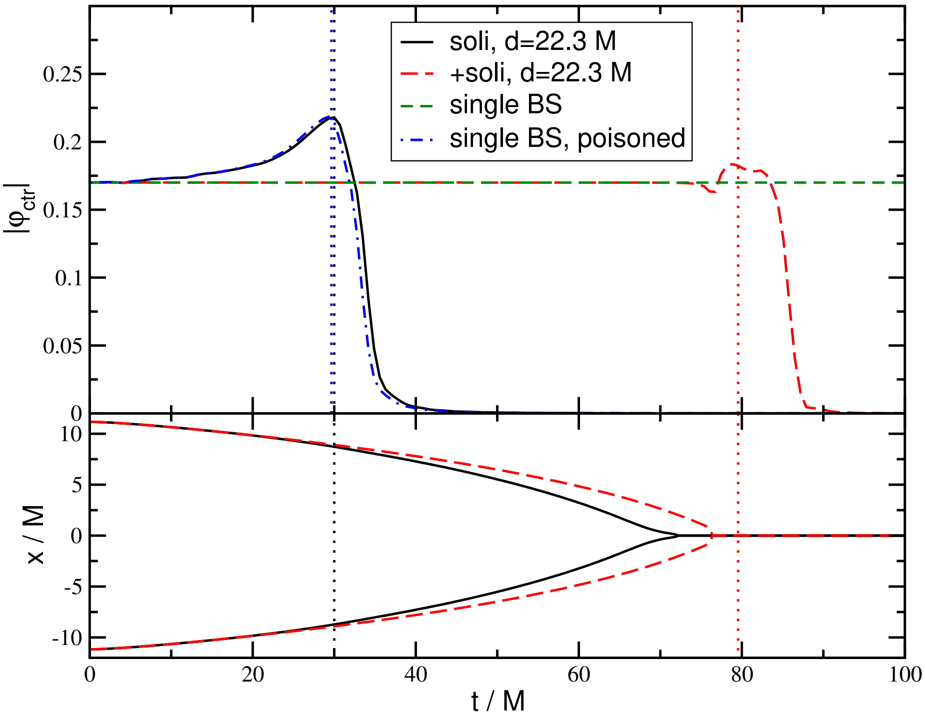

Figure 4.9: The central scalar-field amplitude $|\varphi_{\rm ctr}|$ as a function of time for one BS in the head-on collisions of solitonic BSs with distance $d = 22.3\,M$ (black solid and red long-dashed) as well as a single BS spacetime with the same parameters (green dashed) and the same single BS spacetime "poisoned" with the metric perturbation (4.2.2) that would arise in a simple superposition (see text for details). The dotted vertical lines mark the first location of an apparent horizon in the simulation of the same colour; as expected, no horizon ever forms in the evolution of the unpoisoned single BS. In the bottom panel, we show for reference the coordinate trajectories of the BS centres as obtained from locally Gauss-fitting the scalar profile. Around merger this procedure becomes inaccurate, so that the values around $t \approx 70\,M$ should be regarded as qualitative measures, only.

`soli` binary. Perhaps some of the binding energy in BS collisions is converted into deformation energy rather than simply kinetic energy of the stars' centres of mass, slowing down the infall compared to the BH case[6]. Another explanation may consider the generally repulsive character of the scalar field which endows it with support against gravitational collapse. When the infalling BSs collapse to BHs, the scalar field essentially disappears as a potentially repulsive ingredient and the ensuing collision is sped up. Whatever ultimately generates this effect, the key observation of our study is that even rather mild imperfections in the initial data can drastically affect the physical outcome of the time evolution.

4.4 Conclusions

We have simulated head-on collisions of equal-mass, non-spinning boson stars and the GW radiation generated in the process. The main focus of our study is the construction of BS binary initial data and the ensuing impact of systematic errors on the physical results of the simulations. In particular, we have contrasted the relatively common method of plain superposition according to Eq. (4.2.1) with the adjusted procedure (4.2.3) first identified in Ref. [16] for oscillatons.

Our results demonstrate that the adjustment (4.2.3) in the construction of initial data leads to major improvements in the initial constraint violations and the time evolutions of binary BS collisions. In contrast, we find that the use of plain superposition for BS binary initial data may not only result in quantitatively wrong physical diagnostics but can even result in completely spurious physical behaviour such as premature gravitational collapse. In spite of the great simplicity of the adjustment (4.2.3) and its success in overcoming the most severe errors in the ensuing evolution, it is not free of shortcomings. (i) In its present form, the adjustment only works for a restricted class of binaries, namely equal-mass systems with no spin and velocity vectors satisfying $v^i_{\rm A}v^j_{\rm A} = v^i_{\rm B}v^j_{\rm B}$. (ii) Even with the adjustment, the initial data contain some residual constraint violations; it should therefore primarily be regarded as an improved initial guess for a constraint solving procedure rather than the "real deal" in its own right. These shortcomings clearly point towards the most urgent generalisations of our work, overcoming the symmetry restrictions and adding a numerical constraint solver.

Acknowledgments

CAN REMOVE THIS LATER PROBABLY

We thank Andrew Tolley, Serguei Ossokine and Richard Brito for fruitful discussions. This work is supported by STFC Consolidator Grant Nos. ST/V005669/1 and ST/P000673/1, NSF-XSEDE Grant No. PHY-090003, STFC Capital Grant Nos. ST/P002307/1, ST/R002452/1, STFC Operations Grant No. ST/R00689X/1 (project ACTP 186), PRACE Grant No. 2020225359, and DIRAC RAC13 Grant No. ACTP238. Computations were performed on the San Diego Supercomputing Center's clusters Comet and Expanse, the Texas Advanced Supercomputing Center's Stampede2, the Cambridge Service for Data Driven Discovery (CSD3) system, Durham COSMA7 system and the Juwels cluster at GCS@FZJ, Germany. T.H. is supported by NSF Grants No. PHY-1912550 and AST-2006538, NASA ATP Grants No. 17-ATP17-0225 and 19-ATP19-0051, NSF-XSEDE Grant No. PHY-090003, and NSF Grant PHY-20043. This work has received funding from the European Union's Horizon 2020 research and innovation programme under the Marie Skłodowska-Curie grant agreement No. 690904. This research project was conducted using computational resources at the Maryland Advanced Research Computing Center (MARCC). The authors acknowledge the Texas Advanced Computing Center (TACC) at The University of Texas at Austin for providing HPC resources that have contributed to the research results reported within this paper. URL: http://www.tacc.utexas.edu [103]

[6]We note that the relativistic Love numbers (which measure the tidal deformability) of non-rotating BHs are zero [102].

4.5 Analytic treatment of the Hamiltonian constraint- MIGHT REMOVE

CAN REMOVE THIS LATER PROBABLY For the case of two non-boosted BSs, we can analytically compute the Hamiltonian constraint violation at the stars' centres. Let us consider for this purpose the metric ansatz (**??**). From this line element, we directly extract the spatial metric

$$\gamma^{A}_{ij} = \psi^4_{\mathrm{A}} \delta_{ij} \,. \tag{4.5.1}$$

for a non-boosted BS at position x^i_{A}. This metric is time-independent, so that for zero shift vector the extrinsic curvature vanishes, $K^{\mathrm{A}}_{ij} = 0$. For the second binary member, we likewise obtain a metric γ^{B}_{ij} and extrinsic curvature $K^{\mathrm{B}}_{ij} = 0$, now centred at position x^i_{B}.

For sufficiently large initial separation $d = ||x^i_{\mathrm{B}} - x^i_{\mathrm{A}}||$, the exponential falloff of the scalar field implies

$$\begin{aligned} \phi_{\mathrm{A}}(x_{\mathrm{B}}) &= \phi_{\mathrm{B}}(x_{\mathrm{A}}) \approx 0 \,, \\ \Pi_{\mathrm{A}}(x_{\mathrm{B}}) &= \Pi_{\mathrm{B}}(x_{\mathrm{A}}) \approx 0 \,. \end{aligned} \tag{4.5.2}$$

The superposition of the two stars' scalar fields results in

$$\varphi = \varphi_{\mathrm{A}} + \varphi_{\mathrm{B}} \,, \qquad\qquad \Pi = \Pi_{\mathrm{A}} + \Pi_{\mathrm{B}} \,, \tag{4.5.3}$$

and, combined with Eqs. (4.5.2),

$$\begin{aligned} \rho(x_{\mathrm{A}}) &= \rho_A(x_{\mathrm{A}}) \,, \\ \rho(x_{\mathrm{B}}) &= \rho_B(x_{\mathrm{B}}) \,. \end{aligned} \tag{4.5.4}$$

The single BS spacetimes are solutions to the Einstein equations; by using Eq. (4.5.1), their individual Hamiltonian constraints (**??**) simplify to

$$\mathcal{H}_{\mathrm{A}} = 8\delta^{ij}\partial_i\partial_j\psi_{\mathrm{A}} + 16\pi\psi^5_{\mathrm{A}}\rho_{\mathrm{A}} = 0 \,, \tag{4.5.5}$$

and likewise for star B.

Next, we construct a binary spacetime by superposing the metric which leads to

$$\psi^4 = \psi^4_{\mathrm{A}} + \psi^4_{\mathrm{B}} - c^4 \,, \tag{4.5.6}$$

where c is a constant which we keep arbitrary for the moment. For the Hamiltonian constraint of the superposed spacetime at the centre of star A, we find

$$\begin{aligned} \mathcal{H}(x^i_{\mathrm{A}}) &= 8\delta^{ij}\partial_i\partial_j\psi_{\mathrm{A}}(x^i_{\mathrm{A}}) + 8\delta^{ij}\partial_i\partial_j\psi_{\mathrm{B}}(x^i_{\mathrm{A}}) \\ &\quad + 16\pi \left[\psi_A(x^i_{\mathrm{A}})^4 + \psi_{\mathrm{B}}(x^i_{\mathrm{A}})^4 - c^4\right]^{5/4} \rho(x^i_{\mathrm{A}}) \,. \end{aligned} \tag{4.5.7}$$

We can now choose the constant c in accordance with the "trick" in Eq. (4.2.3), namely

$$c = \psi_B(x^i_A) \,, \tag{4.5.8}$$

and the constraint simplifies to

$$\begin{aligned} \mathcal{H}(x^i_{\mathrm{A}}) &= 8\delta^{ij}\partial_i\partial_j\psi_{\mathrm{A}}(x^i_{\mathrm{A}}) + 8\delta^{ij}\partial_i\partial_j\psi_{\mathrm{B}}(x^i_{\mathrm{A}}) \\ &\quad + 16\pi\psi_{\mathrm{A}}(x^i_{\mathrm{A}})^4 \rho(x^i_{\mathrm{A}}) \,. \end{aligned} \tag{4.5.9}$$

By Eq. (4.5.5), the derivative of the conformal factor ψ_{A} cancels out the density ρ_{A}, so that

$$\mathcal{H}(x^i_{\mathrm{A}}) = 8\delta^{ij}\partial_i\partial_j\psi_{\mathrm{B}}(x^i_{\mathrm{A}}) \,. \tag{4.5.10}$$

Using the analogue of Eq. (4.5.5) for star B, we trade the right-hand side for the energy density,

$$\mathcal{H}(x^i_{\mathrm{A}}) = -16\pi\psi_{\mathrm{B}}(x^i_{\mathrm{A}})^4 \rho_{\mathrm{B}}(x^i_{\mathrm{A}}) \,. \tag{4.5.11}$$

For sufficiently large separation d of the stars, however, this vanishes by Eq. (4.5.2) which is the result we wished to compute. By symmetry, we likewise obtain $\mathcal{H}(x^i_{\mathrm{B}}) = 0$, which concludes our calculation.

Chapter 5

STUFF TO DO

einstein summation conventions? and upstiars/downstairs incedes in conventions

check tensor vs tensor field

3+1 stress tensor is wrong for klein gordon?

add a sections with intro reading such as books alcubbiere baumgarte, adn GR stuff like sean caroll, tong, harvey ..

PUT A NICE FIGURE ON EACH CHAPTER PAGE?

CODE DEV? LIKE INITIAL DATA AND RANDOM SIMS IVE DONE ESPECIALLY WITH BLACK HOLES, MAYBE AN INITIAL DATA SECTION THEN FOLOWED BY MALAISE?

rename the sections maybe, or maybe not. is NUmerical relativity the best name for section that has no numerics and just does a 3+1 spacetime split?

ADD TO CONVENTIONS THAT LATE LATIN INDECES (I,J,K,...) SYMBOLISE 3D OBJECTS IN 4D SPACE ASWELL AS 3D OBJECST IN 3D SPACE

BOX IMPORTANT EQS? MAYBE NOT.

CHECK THE 3+1 SPLIT STRESS TENSOR AGREES WITH PAPERS ...

CHECK CURLY VS SMOOTH BRACKETS FOR SETS AND VECTORS ALL OVER

REF THE ADM METRIC?

make a note of the dx form notation but don't go into depth, maybe hint at intergating over a mfold?

maybe put BSSN and onwards in the GRCHOMBO SECTION? OR A CODE SECTION? and keep the first half as the adm decomposiiton section?

MAYBE ADD Z4 LAGRANGEAN OR UNDERSTAND IT BETTER? LOOK AT MARKUS/KATY THESIS?

CHECK CONVENTIONS ARE OBEYED IN INTRO NR BOSON Q MALAISE OTHER SECTRIONS...

MAKE SOME UNIFORM CONVENTION FOR STRESS TENSOR, MAYBE RHO FOR ENERGY DENSITY MAYBE EPSILON? SIMILAR FOR THE MOMENTA AND THE PROJECTED TENSOR? its in the ccz4 equations too ...

fig or Fig in figure referneceing?

DECIDE ON A FACTOR OF 16PI IN TEH MATTER LAGRANGEAN OF GR BETWEEN THE INTRO SECTION AND THE LATER SECTION. PROBABLY USE R/16PI RATHER THAN 16PI*MATTER ...

standardise complex phi, bar or star for conjugate? or dagger??

MAKE SURE I CREDIT MIREN FOR THE TIME EVOLUTION OF THE SCALAR FIELD

SORT OUT MY RANDOM USE OF ITALICS

IF SR SECTION GETS BOOSTS, MUST REFERENCE THEM FROM THE BOOSTED STARS SECTION

IF THE MASS RESCALING THING (M) IS EXPLAINED IN THE GRCHOMBO SECTION MAYBE IT CAN BE REMOVED IN THE Q PAPER SECTION?

Bibliography

Bibliography

[1] A. Einstein *et al.*, “On the electrodynamics of moving bodies,” *Annalen der physik*, vol. 17, no. 10, pp. 891–921, 1905.

[2] Press, William H. and Teukolsky, Saul A. and Vetterling, William T. and Flannery, Brian P., *Numerical recipes in C (2nd ed.): the art of scientific computing.* New York, NY, USA: Cambridge University Press, 1992.

[3] M. Alcubierre, B. Brügmann, P. Diener, M. Koppitz, D. Pollney, E. Seidel, and R. Takahashi, “Gauge conditions for long-term numerical black hole evolutions without excision,” *Phys. Rev. D*, vol. 67, p. 084023, 2003. gr-qc/0206072.

[4] T. Andrade, L. A. Salo, J. C. Aurrekoetxea, J. Bamber, K. Clough, R. Croft, E. de Jong, A. Drew, A. Duran, P. G. Ferreira, P. Figueras, H. Finkel, T. França, B.-X. Ge, C. Gu, T. Helfer, J. Jäykkä, C. Joana, M. Kunesch, K. Kornet, E. A. Lim, F. Muia, Z. Nazari, M. Radia, J. Ripley, P. Shellard, U. Sperhake, D. Traykova, S. Tunyasuvunakool, Z. Wang, J. Y. Widdicombe, and K. Wong, “Grchombo: An adaptable numerical relativity code for fundamental physics,” *Journal of Open Source Software*, vol. 6, no. 68, p. 3703, 2021.

[5] K. Clough, P. Figueras, H. Finkel, M. Kunesch, E. A. Lim, and S. Tunyasuvunakool, “Grchombo: numerical relativity with adaptive mesh refinement,” *Classical and Quantum Gravity*, vol. 32, no. 24, p. 245011, 2015.

[6] M. J. Berger and J. Oliger, “Adaptive mesh refinement for hyperbolic partial differential equations,” *Journal of computational Physics*, vol. 53, no. 3, pp. 484–512, 1984.

[7] M. Berger and I. Rigoutsos, “An algorithm for point clustering and grid generation,” *IEEE Transactions on Systems, Man, and Cybernetics*, vol. 21, no. 5, pp. 1278–1286, 1991.

[8] M. Shibata and T. Nakamura, “Evolution of three-dimensional gravitational waves: Harmonic slicing case,” *Phys. Rev. D*, vol. 52, pp. 5428–5444, 1995.

[9] T. W. Baumgarte and S. L. Shapiro, “Numerical integration of einstein’s field equations,” *Physical Review D*, vol. 59, no. 2, p. 024007, 1998.

[10] C. Gundlach, G. Calabrese, I. Hinder, and J. M. Martín-García, “Constraint damping in the z4 formulation and harmonic gauge,” *Classical and Quantum Gravity*, vol. 22, no. 17, p. 3767, 2005.

[11] D. Alic, C. Bona-Casas, C. Bona, L. Rezzolla, and C. Palenzuela, “Conformal and covariant formulation of the z4 system with constraint-violation damping,” *Phys. Rev. D*, vol. 85, p. 064040, Mar 2012.

[12] H.-O. Kreiss and J. Oliger, *Methods for the approximate solution of time dependent problems.* No. 10, International Council of Scientific Unions, World Meteorological Organization, 1973.

[13] M. Radia, U. Sperhake, E. Berti, and R. Croft, "Anomalies in the gravitational recoil of eccentric black-hole mergers with unequal mass ratios," *Physical Review D*, vol. 103, no. 10, p. 104006, 2021.

[14] A. Hadjidimos, "Successive overrelaxation (sor) and related methods," *Journal of Computational and Applied Mathematics*, vol. 123, no. 1-2, pp. 177–199, 2000.

[15] D. J. Kaup, "Klein-gordon geon," *Phys. Rev.*, vol. 172, pp. 1331–1342, Aug 1968.

[16] T. Helfer, E. A. Lim, M. A. G. Garcia, and M. A. Amin, "Gravitational Wave Emission from Collisions of Compact Scalar Solitons," *Phys. Rev. D*, vol. 99, no. 4, p. 044046, 2019.

[17] B. P. Abbott *et al.*, "Observation of Gravitational Waves from a Binary Black Hole Merger," *Phys. Rev. Lett.*, vol. 116, no. 6, p. 061102, 2016.

[18] B. P. Abbott *et al.*, "GWTC-1: A Gravitational-Wave Transient Catalog of Compact Binary Mergers Observed by LIGO and Virgo during the First and Second Observing Runs," *Phys. Rev. X*, vol. 9, no. 3, p. 031040, 2019.

[19] R. Abbott *et al.*, "GWTC-2: Compact Binary Coalescences Observed by LIGO and Virgo During the First Half of the Third Observing Run," *Phys. Rev. X*, vol. 11, p. 021053, 2021.

[20] E. Berti *et al.*, "Testing General Relativity with Present and Future Astrophysical Observations," *Class. Quant. Grav.*, vol. 32, p. 243001, 2015.

[21] B. P. Abbott *et al.*, "Tests of general relativity with GW150914," *Phys. Rev. Lett.*, vol. 116, no. 22, p. 221101, 2016.

[22] B. Abbott *et al.*, "Tests of General Relativity with GW170817," *Phys. Rev. Lett.*, vol. 123, no. 1, p. 011102, 2019.

[23] B. Abbott *et al.*, "Tests of General Relativity with the Binary Black Hole Signals from the LIGO-Virgo Catalog GWTC-1," *Phys. Rev. D*, vol. 100, no. 10, p. 104036, 2019.

[24] R. Abbott *et al.*, "Tests of general relativity with binary black holes from the second LIGO-Virgo gravitational-wave transient catalog," *Phys. Rev. D*, vol. 103, no. 12, p. 122002, 2021.

[25] C. J. Moore, E. Finch, R. Buscicchio, and D. Gerosa, "Testing general relativity with gravitational-wave catalogs: the insidious nature of waveform systematics," 3 2021.

[26] D. Trifirò, R. O'Shaughnessy, D. Gerosa, E. Berti, M. Kesden, T. Littenberg, and U. Sperhake, "Distinguishing black-hole spin-orbit resonances by their gravitational wave signatures. II: Full parameter estimation," *Phys. Rev. D*, vol. 93, no. 4, p. 044071, 2016. arXiv:1507.05587 [gr-qc].

[27] K. Belczynski *et al.*, "Evolutionary roads leading to low effective spins, high black hole masses, and O1/O2 rates for LIGO/Virgo binary black holes," *Astron. Astrophys.*, vol. 636, p. A104, 2020.

[28] R. Abbott *et al.*, "Population Properties of Compact Objects from the Second LIGO-Virgo Gravitational-Wave Transient Catalog," *Astrophys. J. Lett.*, vol. 913, no. 1, p. L7, 2021.

[29] V. Baibhav, D. Gerosa, E. Berti, K. W. K. Wong, T. Helfer, and M. Mould, "The mass gap, the spin gap, and the origin of merging binary black holes," *Phys. Rev. D*, vol. 102, no. 4, p. 043002, 2020.

[30] D. Gerosa and M. Fishbach, "Hierarchical mergers of stellar-mass black holes and their gravitational-wave signatures," 5 2021.

[31] B. P. Abbott *et al.*, "A gravitational-wave standard siren measurement of the Hubble constant," *Nature*, vol. 551, no. 7678, pp. 85–88, 2017.

[32] B. P. Abbott *et al.*, "A Gravitational-wave Measurement of the Hubble Constant Following the Second Observing Run of Advanced LIGO and Virgo," *Astrophys. J.*, vol. 909, no. 2, p. 218, 2021.

[33] L. Barack *et al.*, "Black holes, gravitational waves and fundamental physics: a roadmap," *Class. Quant. Grav.*, vol. 36, no. 14, p. 143001, 2019.

[34] B. P. Abbott *et al.*, "GW170817: Observation of Gravitational Waves from a Binary Neutron S+tar Inspiral," *Phys. Rev. Lett.*, vol. 119, no. 16, p. 161101, 2017.

[35] B. P. Abbott *et al.*, "Gravitational Waves and Gamma-rays from a Binary Neutron Star Merger: GW170817 and GRB 170817A," *Astrophys. J.*, vol. 848, no. 2, p. L13, 2017.

[36] V. Cardoso, L. Gualtieri, C. Herdeiro, and U. Sperhake, "Exploring New Physics Frontiers Through Numerical Relativity," *Living Rev. Relativity*, vol. 18, p. 1, 2015. arXiv:1409.0014 [gr-qc].

[37] R. Brito, V. Cardoso, and P. Pani, "Superradiance," *Lect. Notes Phys.*, vol. 906, pp. pp.1–237, 2015.

[38] J. A. Wheeler, "Geons," *Phys. Rev.*, vol. 97, pp. 511–536, 1955.

[39] T. W. Baumgarte and S. L. Shapiro, *Numerical Relativity: Starting from Scratch.* Cambridge University Press, 2 2021.

[40] D. A. Feinblum and W. A. McKinley, "Stable States of a Scalar Particle in Its Own Gravational Field," *Phys. Rev.*, vol. 168, no. 5, p. 1445, 1968.

[41] D. J. Kaup, "Klein-Gordon Geon," *Phys. Rev.*, vol. 172, pp. 1331–1342, 1968.

[42] R. Ruffini and S. Bonazzola, "Systems of selfgravitating particles in general relativity and the concept of an equation of state," *Phys. Rev.*, vol. 187, pp. 1767–1783, 1969.

[43] R. Brito, V. Cardoso, C. A. R. Herdeiro, and E. Radu, "Proca stars: Gravitating Bose–Einstein condensates of massive spin 1 particles," *Phys. Lett.*, vol. B752, pp. 291–295, 2016.

[44] M. Alcubierre, J. Barranco, A. Bernal, J. C. Degollado, A. Diez-Tejedor, M. Megevand, D. Nunez, and O. Sarbach, "ℓ-Boson stars," *Class. Quant. Grav.*, vol. 35, no. 19, p. 19LT01, 2018.

[45] M. Choptuik, R. Masachs, and B. Way, "Multioscillating Boson Stars," *Phys. Rev. Lett.*, vol. 123, no. 13, p. 131101, 2019.

[46] F. Pretorius, "Evolution of Binary Black-Hole Spacetimes," *Phys. Rev. Lett.*, vol. 95, p. 121101, 2005. gr-qc/0507014.

[47] M. Campanelli, C. O. Lousto, P. Marronetti, and Y. Zlochower, "Accurate Evolutions of Orbiting Black-Hole Binaries without Excision," *Phys. Rev. Lett.*, vol. 96, p. 111101, 2006. gr-qc/0511048.

[48] J. G. Baker, J. Centrella, D.-I. Choi, M. Koppitz, and J. van Meter, "Gravitational-Wave Extraction from an inspiraling Configuration of Merging Black Holes," *Phys. Rev. Lett.*, vol. 96, p. 111102, 2006. gr-qc/0511103.

[49] U. Sperhake, "The numerical relativity breakthrough for binary black holes," *Class. Quant. Grav.*, vol. 32, no. 12, p. 124011, 2015.

[50] R. C. Tolman, "Static Solutions of Einstein's Field Equations for Spheres of Fluid," *Phys. Rev.*, vol. 55, pp. 364–373, 1939.

[51] J. R. Oppenheimer and G. M. Volkoff, "On Massive Neutron Cores," *Phys. Rev.*, vol. 55, pp. 374–381, 1939.

[52] J. D. Breit, S. Gupta, and A. Zaks, "Cold Bose Stars," *Phys. Lett. B*, vol. 140, pp. 329–332, 1984.

[53] M. Gleiser and R. Watkins, "Gravitational Stability of Scalar Matter," *Nucl. Phys. B*, vol. 319, pp. 733–746, 1989.

[54] E. Seidel and W.-M. Suen, "Dynamical Evolution of Boson Stars. 1. Perturbing the Ground State," *Phys. Rev. D*, vol. 42, pp. 384–403, 1990.

[55] T. D. Lee and Y. Pang, "Nontopological solitons," *Phys. Rept.*, vol. 221, pp. 251–350, 1992.

[56] P. Jetzer, "Boson stars," *Phys. Rept.*, vol. 220, pp. 163–227, 1992.

[57] A. R. Liddle and M. S. Madsen, "The Structure and formation of boson stars," *Int. J. Mod. Phys. D*, vol. 1, pp. 101–144, 1992.

[58] J. Balakrishna, E. Seidel, and W.-M. Suen, "Dynamical evolution of boson stars. 2. Excited states and selfinteracting fields," *Phys. Rev. D*, vol. 58, p. 104004, 1998.

[59] M. Colpi, S. L. Shapiro, and I. Wasserman, "Boson Stars: Gravitational Equilibria of Selfinteracting Scalar Fields," *Phys. Rev. Lett.*, vol. 57, pp. 2485–2488, 1986.

[60] T. D. Lee, "Soliton Stars and the Critical Masses of Black Holes," *Phys. Rev. D*, vol. 35, p. 3637, 1987.

[61] F. E. Schunck and D. F. Torres, "Boson stars with generic selfinteractions," *Int. J. Mod. Phys. D*, vol. 9, pp. 601–618, 2000.

[62] B. Hartmann, B. Kleihaus, J. Kunz, and I. Schaffer, "Compact Boson Stars," *Phys. Lett. B*, vol. 714, pp. 120–126, 2012.

[63] J. C. Bustillo, N. Sanchis-Gual, A. Torres-Forné, J. A. Font, A. Vajpeyi, R. Smith, C. Herdeiro, E. Radu, and S. H. W. Leong, "GW190521 as a Merger of Proca Stars: A Potential New Vector Boson of+ 8.7×10^{-13} eV," *Phys. Rev. Lett.*, vol. 126, no. 8, p. 081101, 2021.

[64] N. Sennett, T. Hinderer, J. Steinhoff, A. Buonanno, and S. Ossokine, "Distinguishing Boson Stars from Black Holes and Neutron Stars from Tidal Interactions in Inspiraling Binary Systems," *Phys. Rev. D*, vol. 96, no. 2, p. 024002, 2017.

[65] F. Di Giovanni, N. Sanchis-Gual, P. Cerdá-Durán, M. Zilhão, C. Herdeiro, J. A. Font, and E. Radu, "Dynamical bar-mode instability in spinning bosonic stars," *Phys. Rev. D*, vol. 102, no. 12, p. 124009, 2020.

[66] A. Toubiana, S. Babak, E. Barausse, and L. Lehner, "Modeling gravitational waves from exotic compact objects," *Phys. Rev. D*, vol. 103, no. 6, p. 064042, 2021.

[67] Y. Kobayashi, M. Kasai, and T. Futamase, "Does a boson star rotate?," *Phys. Rev. D*, vol. 50, pp. 7721–7724, 1994.

[68] F. E. Schunck and E. W. Mielke, "Rotating boson star as an effective mass torus in general relativity," *Phys. Lett.*, vol. A249, pp. 389–394, 1998.

[69] F. D. Ryan, "Spinning boson stars with large selfinteraction," *Phys. Rev. D*, vol. 55, pp. 6081–6091, 1997.

[70] S. Yoshida and Y. Eriguchi, "Nonaxisymmetric boson stars in Newtonian gravity," *Phys. Rev. D*, vol. 56, pp. 6370–6377, 1997.

[71] S. Yoshida and Y. Eriguchi, "Rotating boson stars in general relativity," *Phys. Rev. D*, vol. 56, pp. 762–771, 1997.

[72] S. Yoshida and Y. Eriguchi, "New static axisymmetric and nonvacuum solutions in general relativity: Equilibrium solutions of boson stars," *Phys. Rev. D*, vol. 55, pp. 1994–2001, 1997.

[73] F. E. Schunck and E. W. Mielke, "Boson stars: Rotation, formation, and evolution," *Gen. Rel. Grav.*, vol. 31, p. 787, 1999.

[74] B. Kleihaus, J. Kunz, and M. List, "Rotating boson stars and Q-balls," *Phys. Rev. D*, vol. 72, p. 064002, 2005.

[75] B. Kleihaus, J. Kunz, M. List, and I. Schaffer, "Rotating Boson Stars and Q-Balls. II. Negative Parity and Ergoregions," *Phys. Rev. D*, vol. 77, p. 064025, 2008.

[76] B. Kleihaus, J. Kunz, and S. Schneider, "Stable Phases of Boson Stars," *Phys. Rev. D*, vol. 85, p. 024045, 2012.

[77] L. G. Collodel, B. Kleihaus, and J. Kunz, "Excited Boson Stars," *Phys. Rev. D*, vol. 96, no. 8, p. 084066, 2017.

[78] C. Herdeiro, I. Perapechka, E. Radu, and Ya. Shnir, "Asymptotically flat spinning scalar, Dirac and Proca stars," *Phys.Lett.B*, vol. 797, p. 134845, 2019.

[79] N. Sanchis-Gual, F. Di Giovanni, M. Zilhão, C. Herdeiro, P. Cerdá-Durán, J. A. Font, and E. Radu, "Nonlinear Dynamics of Spinning Bosonic Stars: Formation and Stability," *Phys. Rev. Lett.*, vol. 123, no. 22, p. 221101, 2019.

[80] A. S. Dmitriev, D. G. Levkov, A. G. Panin, E. K. Pushnaya, and I. I. Tkachev, "Instability of rotating Bose stars," *Phys. Rev. D*, vol. 104, no. 2, p. 023504, 2021.

[81] N. Siemonsen and W. E. East, "Stability of rotating scalar boson stars with nonlinear interactions," *Phys. Rev. D*, vol. 103, no. 4, p. 044022, 2021.

[82] E. W. Mielke and F. E. Schunck, "Boson stars: Early history and recent prospects," in *Recent developments in theoretical and experimental general relativity, gravitation, and relativistic field theories. Proceedings, 8th Marcel Grossmann meeting, MG8, Jerusalem, Israel, June 22-27, 1997. Pts. A, B*, pp. 1607–1626, 1997.

[83] E. W. Mielke and F. E. Schunck, "Boson stars: Alternatives to primordial black holes?," *Nucl. Phys. B*, vol. 564, pp. 185–203, 2000.

[84] B. C. Mundim, *A Numerical Study of Boson Star Binaries.* PhD thesis, British Columbia U., 2010.

[85] S. L. Liebling and C. Palenzuela, "Dynamical Boson Stars," *Living Rev. Rel.*, vol. 15, p. 6, 2012.

[86] C. Palenzuela, I. Olabarrieta, L. Lehner, and S. L. Liebling, "Head-on collisions of boson stars," *Phys. Rev. D*, vol. 75, p. 064005, 2007.

[87] M. W. Choptuik and F. Pretorius, "Ultra Relativistic Particle Collisions," *Phys. Rev. Lett.*, vol. 104, p. 111101, 2010. arXiv:0908.1780 [gr-qc].

[88] M. Bezares, C. Palenzuela, and C. Bona, "Final fate of compact boson star mergers," *Phys. Rev. D*, vol. 95, no. 12, p. 124005, 2017.

[89] C. Palenzuela, L. Lehner, and S. L. Liebling, "Orbital Dynamics of Binary Boson Star Systems," *Phys. Rev. D*, vol. 77, p. 044036, 2008.

[90] C. Palenzuela, P. Pani, M. Bezares, V. Cardoso, L. Lehner, and S. Liebling, "Gravitational Wave Signatures of Highly Compact Boson Star Binaries," *Phys. Rev. D*, vol. 96, no. 10, p. 104058, 2017.

[91] R. Arnowitt, S. Deser, and C. W. Misner, "The dynamics of general relativity," in *Gravitation an introduction to current research* (L. Witten, ed.), pp. 227–265, John Wiley, New York, 1962.

[92] M. Shibata, H. Okawa, and T. Yamamoto, "High-velocity collisions of two black holes," *Phys. Rev. D*, vol. 78, p. 101501(R), 2008. arXiv:0810.4735 [gr-qc].

[93] H. Okawa, K.-i. Nakao, and M. Shibata, "Is super-Planckian physics visible? Scattering of black holes in 5 dimensions," *Phys. Rev. D*, vol. 83, p. 121501(R), 2011. arXiv:1105.3331 [gr-qc].

[94] U. Sperhake, W. Cook, and D. Wang, "The high-energy collision of black holes in higher dimensions," *Phys. Rev. D*, vol. 100, no. 10, p. 104046, 2020.

[95] D. R. Brill and R. W. Lindquist, "Interaction Energy in Geometrostatics," *Phys. Rev.*, vol. 131, pp. 471–476, 1963.

[96] P. C. Aichelburg and R. U. Sexl, "On the Gravitational field of a massless particle," *Gen. Rel. Grav.*, vol. 2, pp. 303–312, 1971.

[97] S. Bernuzzi and D. Hilditch, "Constraint violation in free evolution schemes: Comparing BSSNOK with a conformal decomposition of Z4," *Phys. Rev. D*, vol. 81, p. 084003, 2010.

[98] D. Alic, C. Bona-Casas, C. Bona, L. Rezzolla, and C. Palenzuela, "Conformal and covariant formulation of the Z4 system with constraint-violation damping," *Phys. Rev. D*, vol. 85, p. 064040, 2012. arXiv:1106.2254 [gr-qc].

[99] S. Husa, J. A. González, M. D. Hannam, B. Brügmann, and U. Sperhake, "Reducing phase error in long numerical binary black hole evolutions with sixth order finite differencing," *Class. Quant. Grav.*, vol. 25, p. 105006, 2008. arXiv:0706.0740 [gr-qc].

[100] K. Clough, P. Figueras, H. Finkel, M. Kunesch, E. A. Lim, and S. Tunyasuvunakool, "GRChombo : Numerical Relativity with Adaptive Mesh Refinement," *Class. Quant. Grav.*, vol. 32, no. 24, p. 245011, 2015. arXiv:1503.03436 [gr-qc].

[101] M. Radia, U. Sperhake, K. Clough, A. Drew, E. A. Lim, and J. L. Ripley, "Numerical relativity with adaptive mesh refinement:obtaining accurate+ results with grchombo." in preparation.

[102] T. Binnington and E. Poisson, "Relativistic theory of tidal Love numbers," *Phys. Rev. D*, vol. 80, p. 084018, 2009.

[103] D. Stanzione, J. West, R. T. Evans, T. Minyard, O. Ghattas, and D. K. Panda, "Frontera: The evolution of leadership computing at the national science foundation," in *Practice and Experience in Advanced Research Computing*, PEARC '20, (New York, NY, USA), p. 106–111, Association for Computing Machinery, 2020.

[104] blank